Observation of oscillations of atmospheric neutrinos with the IceCube Neutrino Observatory

Von der Fakultät für Mathematik, Informatik und Naturwissenschaften
der RWTH Aachen University zur Erlangung des akademischen Grades
eines Doktors der Naturwissenschaften genehmigte Dissertation

vorgelegt von

Diplom-Physiker
Sebastian Euler

aus Viersen.

Berichter: Univ.-Prof. Dr. Christopher Wiebusch
Prof. Dr. Elisa Resconi

Tag der mündlichen Prüfung: 04. Februar 2014

Contents

List of Figures

List of Tables

1 Introduction

Neutrino oscillations have become one of the most important research topics in particle physics since their discovery 15 years ago [48]. Only recently, the discovery of a non-zero mixing angle θ_{13} [17] has added momentum to the field, as it significantly facilitates investigations of the mass hierarchy or CP violation in the neutrino sector. In the last year also the large-volume neutrino telescopes ANTARES [23] and IceCube [3] have reported their results on the oscillations of atmospheric muon neutrinos and have thus joined the community of experiments studying neutrino oscillations. The precision of their results is not yet competitive, but their sheer size and the consequently enormous statistics give rise to the expectation of a competitive measurement in the future. This thesis describes an analysis that was done on IceCube data taken with the nearly complete detector in the years 2010/2011. It employs an event selection that is based on the idea of using the outer layers of IceCube as an active veto against the background of atmospheric muons and that achieves the necessary background rejection of more than 6 orders of magnitude while keeping a high-statistics sample of several thousands of muon neutrinos. In contrast to the earlier IceCube analysis, which used only the zenith angle, it then performs a 2-dimensional likelihood fit on reconstructed zenith angle and energy and improves upon the earlier measurements of the mixing angle θ_{23} and the mass difference Δm^2_{32}.

This thesis is organized as follows: Chapter 2 presents the theory of neutrino oscillations and summarizes our current knowledge about neutrinos and their flavor oscillations. Chapter 3 introduces the IceCube Neutrino Observatory and its components, and explains the neutrino detection process. The actual analysis is presented in Chapter 4, which discusses the data selection, and in particular in Chapter 5, which explains in detail the analysis procedure, the likelihood method used, and the systematic effects that are considered. Chapter 6 then presents the results, before Chapter 7, finally, gives an outlook to future improvements.

[48] Y. Fukuda et al. Evidence for oscillation of atmospheric neutrinos. *Phys. Rev. Lett.*, 81:1562–1567, Aug 1998. DOI: 10.1103/PhysRevLett.81.1562

[17] Y. Abe et al. Indication of Reactor $\bar{\nu}_e$ Disappearance in the Double Chooz Experiment. *Phys. Rev. Lett.*, 108:131801, Mar 2012. DOI: 10.1103/PhysRevLett.108.131801

[23] S. Adrián-Martínez et al. Measurement of atmospheric neutrino oscillations with the ANTARES neutrino telescope. *Physics Letters B*, 714(2-5):224–230, 2012. DOI: 10.1016/j.physletb.2012.07.002

[3] M. G. Aartsen et al. Measurement of Atmospheric Neutrino Oscillations with IceCube. *Phys. Rev. Lett.*, 111:081801, Aug 2013. DOI: 10.1103/PhysRevLett.111.081801

2 Neutrino oscillations

2.1 Neutrinos

The neutrino was first postulated by Wolfgang Pauli in 1930. The continuous energy spectrum of beta decay electrons could only be explained by another particle taking part in the process and carrying away energy. Because of the tiny interaction cross sections, the new particle was first thought to be undetectable. Fortunately, this turned out to be wrong, although it took more than 25 years from the postulation to the discovery by Frederick Reines[1] and Clyde Cowan in 1956 [43]. Since then, many experiments have studied the neutrino's properties.

According to our current knowledge, the neutrino is an elementary particle, a lepton with spin 1/2. It is electrically neutral and it comes in three different flavors – ν_e, ν_μ, and ν_τ – corresponding to the charged leptons. It interacts only by the weak force, by exchange of a W boson (*charged current, CC*) or Z boson (*neutral current, NC*). Figures 2.1 and 2.2 show Feynman diagrams for CC and NC neutrino interactions with matter. The interaction cross sections are typically very small, on the order of $\sim 10^{-38}\,\mathrm{cm}^2$, which makes large and expensive detectors necessary.

[1] who was awarded the Nobel Prize in 1995 for this discovery

[43] C. L. Cowan, F. Reines, F. B. Harrison, H. W. Kruse, and A. D. McGuire. Detection of the Free Neutrino: a Confirmation. *Science*, 124(3212):103–104, 1956. DOI: 10.1126/science.124.3212.103

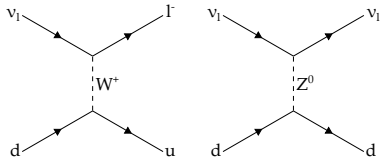

Figure 2.1: Feynman diagrams for neutrino interactions with quarks, CC (left) and NC (right).

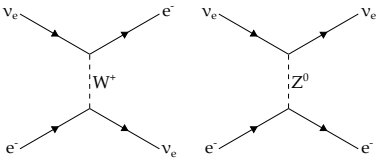

Figure 2.2: Feynman diagrams for neutrino interactions with electrons, CC (left) and NC (right).

[22] P. A. R. Ade et al. Planck 2013 results. XVI. Cosmological parameters. *Submitted to A&A*

[2] **Ka**rlsruhe **Tri**tium **N**eutrino

2.1.1 Neutrino mass

The neutrino is not massless; this fact is closely connected with the observation of neutrino oscillations, as will be discussed below. It is, however, very light compared to all other known particles: current limits on the sum of the three neutrino masses – for example derived from measurements of the cosmic microwave background by the Planck satellite [22] – are in the range below 1 eV. A direct measurement of the mass of the electron antineutrino is attempted by the KATRIN[2] experiment, which will measure the energy of electrons from the beta decay of tritium:

$$^3\mathrm{H} \longrightarrow {}^3\mathrm{He} + \mathrm{e}^- + \overline{\nu}_e\,.$$

For massless neutrinos, the electron energy spectrum is expected to reach up to 18.6 keV, the maximum energy of this beta decay. For a non-zero neutrino mass, deviations occur near the end point of the spectrum, and the maximum electron energy becomes $E_{e,\mathrm{max}} =$

18.6 keV $- m_{\overline{\nu}_e}$. Figure 2.3 shows the expected electron spectrum for three different neutrino masses. While a precursor experiment has set a limit of $m_{\overline{\nu}_e} < 2.2\,\text{eV}$ [37], KATRIN is expected to reach a precision of about 0.2 eV [103]. The measurements are planned to start 2015.

[37] J. Bonn et al. The Mainz neutrino mass experiment. *Nuclear Physics B - Proceedings Supplements*, 91:273–279, 2001. DOI: 10.1016/S0920-5632(00)00951-8

[103] J. Wolf. The KATRIN neutrino mass experiment. *Nucl.Instrum.Meth. A*, 623(1):442–444, 2010. DOI: 10.1016/j.nima.2010.03.030

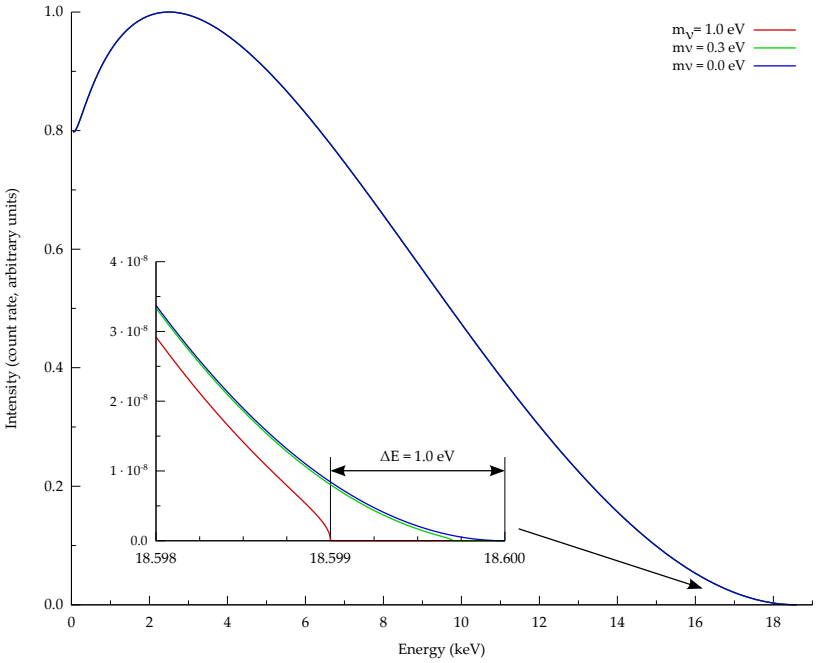

Figure 2.3: Expected energy spectrum of the electrons from the tritium beta decay for different neutrino masses [101].

Also not settled is the question if neutrinos are Majorana or Dirac particles, i.e. if they are their own antiparticles or not. Support for the Majorana nature of neutrinos might come from the *seesaw mechanism* [81], which yields a natural explanation for the smallness of the neutrino masses, and requires the neutrinos to be Majorana fermions. It assumes the mass matrix of the neutrinos to be of the form

$$A = \begin{pmatrix} 0 & m \\ m & M \end{pmatrix},$$

with m being the Dirac mass terms, and $M \gg m$ the Majorana mass. The eigenvalues of this matrix are

$$\lambda_\pm = \frac{M \pm \sqrt{M^2 + 4m^2}}{2}.$$

These eigenvalues give the masses of the physical neutrinos:

$$m_{\text{light}} = \lambda_- \approx -\frac{m^2}{M},$$
$$m_{\text{heavy}} = \lambda_+ \approx M.$$

The larger m_{heavy} becomes, the smaller is m_{light}, thus the name of this mechanism. Reasonable values of m and M are on the order of the electroweak scale ($m \approx 10^2\,\text{GeV}$) and the GUT scale ($M \approx 10^{15}\,\text{GeV}$), leading naturally to a mass of the light neutrinos of around 0.01 eV [75]. Of course, this approach implicates the existence of

[81] P. Minkowski. $\mu \to e\gamma$ at a rate of one out of 10^9 muon decays? *Physics Letters B*, 67(4):421–428, 1977. DOI: 10.1016/0370-2693(77)90435-X

[75] M. Lindner, T. Ohlsson, and G. Seidl. Seesaw mechanisms for Dirac and Majorana neutrino masses. *Phys. Rev. D*, 65:053 014, 2002. DOI: 10.1103/PhysRevD.65.053014

another sort of very heavy neutrinos. Until now, these have not been observed, but their existence would not necessarily be in conflict with any experimental results, and in fact could also explain certain other observations (see Section 2.6).

The observation of the *neutrinoless double-beta decay* ($0\nu\beta\beta$) would mean that neutrinos are indeed Majorana fermions. In an ordinary double-beta decay ($2\nu\beta\beta$), two neutrons are converted into protons under emission of two electrons and two $\overline{\nu}_e$. If the neutrino is a Majorana fermion, the two neutrinos can annihilate and the decay occurs under emission of only two electrons. Figures 2.4 and 2.5 show Feynman diagrams of the two processes. Since the mean lifetime of the double-beta decay is typically much larger than that of the ordinary beta decay, it is only observable in nuclei for which the standard beta decay is forbidden. A popular isotope used by many experiments is ^{76}Ge, which decays to ^{76}Se. The $0\nu\beta\beta$ decay rate is proportional to the Majorana mass M and therefore gives rise to another possibility to determine the neutrino mass [99].

Until now, no experiment has convincingly observed a neutrinoless double-beta decay. Part of the Heidelberg-Moscow collaboration claimed an observation of $0\nu\beta\beta$ events with a significance of more than $6\,\sigma$ [68], but this lead to controversial discussion in the field. The GERDA[3] experiment is currently taking data. In a first result, they find no excess of events beyond the expected background, disfavoring the older Heidelberg-Moscow claim. They calculate a lifetime of the $0\nu\beta\beta$ process of $T_{1/2} > 2.1 \cdot 10^{25}$ years at 90% confidence level, and consequently an upper limit on the ν_e mass of $0.2 - 0.4\,\text{eV}$ [24]. With more data to come, they will increase their sensitivity by another order of magnitude.

[99] C. Weinheimer and K. Zuber. Neutrino Masses. *Annalen der Physik*, 525:565–575, 2013. DOI: 10.1002/andp.201300063

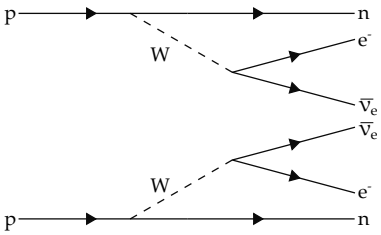

Figure 2.4: Feynman diagram for the ordinary double-beta decay ($2\nu\beta\beta$).

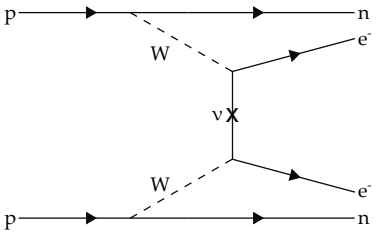

Figure 2.5: Feynman diagram for the neutrinoless double-beta decay ($0\nu\beta\beta$).

[68] H. V. Klapdor-Kleingrothaus and I. V. Krivosheina. The evidence for the observation of $0\nu\beta\beta$ decay: The identification of $0\nu\beta\beta$ events from the full spectra. *Modern Physics Letters A*, 21(20):1547–1566, 2006. DOI: 10.1142/S0217732306020937

[3] **Ger**manium **D**etector **A**rray

[24] M. Agostini et al. Results on neutrinoless double beta decay of ^{76}Ge from GERDA Phase I. *Phys. Rev. Lett.*, 111:122 503, Sep 2013. DOI: 10.1103/PhysRevLett.111.122503

2.2 ATMOSPHERIC NEUTRINOS

The Earth is continuously exposed to a bombardment of high-energy particles from space. These *cosmic rays* were discovered as early as 1912 by Victor Hess[4], but the question of their origin is still unresolved. However, their properties and in particular their interactions with the Earth's atmosphere have been studied extensively. They consist mainly of protons (about 85%), helium nuclei (11%) and a small amount of heavier nuclei and electrons [107]. Their energy spectrum, shown in Figure 2.7, has been observed over more than 10 orders of magnitude and the measured fluxes span more than 30 orders of magnitude. In large parts, the energy spectrum follows a simple power law, $\mathrm{d}N/\mathrm{d}E \propto E^{-\gamma}$, with $\gamma \approx 2.7$ [107]. Newer measurements suggest a value closer to $\gamma \approx 2.65$ [105], which is therefore used as the default value in this work. Only at much higher energies than the range of interest for the analysis in this thesis, the spectrum steepens around 3 PeV (the *knee*) and flattens again at about 3 EeV (the *ankle*). Recent results indicate that the spectrum between the knee and the ankle does not follow a single power law, but shows considerable structure, with the spectral index fluctuating around $\gamma = 3.0$ [6].

[4] Nobel Prize 1936

[107] K. Zuber. *Neutrino Physics*. Series in high energy physics, cosmology, and gravitation. Taylor & Francis, 2012

[105] Y. S. Yoon et al. Cosmic-ray Proton and Helium Spectra from the First CREAM Flight. *The Astrophysical Journal*, 728(2):122, 2011

[6] M. G. Aartsen et al. Measurement of the cosmic ray energy spectrum with IceTop-73. *Phys. Rev. D*, 88:042 004, Aug 2013. DOI: 10.1103/PhysRevD.88.042004

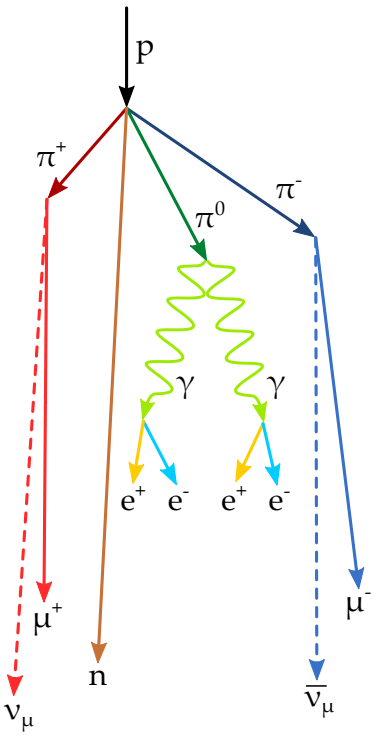

Figure 2.6: Sketch of an air shower.

[49] T. K. Gaisser. *Cosmic Rays and Particle Physics*. Cambridge University Press, 1990

The total spectrum, measured by various experiments, is shown in Figure 2.7.

When a cosmic-ray particle enters the Earth's atmosphere, it will collide with an air molecule. In this collision, the nucleon is destroyed and many new particles are produced, which in turn collide with other air molecules, resulting in an extended cascade of particles and electromagnetic radiation, a so-called *air shower*. A basic sketch of such a shower is shown in Figure 2.6. These air showers are the production site of *atmospheric neutrinos*. Atmospheric ν_μ are the signal source used to measure neutrino oscillations in the analysis presented here. Atmospheric ν_e, on the other hand, contribute to the background of the analysis. To understand the atmospheric neutrino flux is thus of fundamental importance.

In the primary cosmic-ray interaction, mainly pions (and, at higher energy, kaons) are produced. If the pions do not interact again, they decay into photons (in the case of π^0) and into muons and neutrinos (in the case of the charged pions). The muons decay into neutrinos, as well. For an initial π^+, the complete decay chain is

$$\begin{aligned} p + N \rightarrow\ & \pi^+ + X \\ \pi^+ \rightarrow\ & \mu^+ + \nu_\mu \\ & \mu^+ \rightarrow e^+ + \nu_e + \overline{\nu}_\mu\,, \end{aligned} \tag{2.1}$$

and accordingly for π^-. Similar considerations apply to kaons [49]. From this decay chain, a generic flavor ratio ($\nu_e : \nu_\mu : \nu_\tau$) of 1:2:0 can be read off immediately. Note that except for a very small contribution from the decay of charmed mesons ($D_s^+ \rightarrow \tau^+\nu_\tau$ and similar for D_s^-), which only occurs at much higher energies, no atmospheric ν_τ flux is expected! Hence, atmospheric ν_τ can only arise from neutrino oscillations, which are described in Section 2.3.

The shapes of the energy and zenith angle distributions of atmospheric neutrinos are governed by the interplay of interaction and decay of the parent particles: if these interact before they decay, no neutrinos are produced. Above 1 GeV the muon decay length becomes larger than the height in which they are produced, and the muons largely do not decay, but reach the ground. For the energy range relevant for this oscillation analysis (between $\sim$ 10 GeV and 100 GeV), the neutrino flux from pions and kaons is most relevant. This so-called *conventional neutrino flux* can be calculated from the initial cosmic-ray flux [56]. It can be expressed as a function of neutrino energy E_ν and zenith angle θ_ν and the constants $A_{\pi\nu}$, $B_{\pi\nu}$, $A_{K\nu}$, and $B_{K\nu}$, which have individual values for ν_μ, $\overline{\nu}_\mu$, ν_e, and $\overline{\nu}_e$ [49]:

$$\begin{aligned} \frac{\mathrm{d}N_\nu}{\mathrm{d}E_\nu} = \Phi_0 \cdot E_\nu^{-\gamma} \cdot \Bigg(& \frac{A_{\pi\nu}}{1 + B_{\pi\nu} E_\nu \cos\theta_\nu / \epsilon_\pi} \\ & + \frac{A_{K\nu}}{1 + B_{K\nu} E_\nu \cos\theta_\nu / \epsilon_K} \Bigg)\,, \end{aligned} \tag{2.2}$$

The term $\Phi_0 \cdot E_\nu^{-\gamma}$ stands for the primary cosmic-ray flux. The first of the two summands describes the contribution from pions, and the second the contribution from kaons. Above $\epsilon_\pi = 115$ GeV, the pions are

[56] M. Honda, T. Kajita, K. Kasahara, S. Midorikawa, and T. Sanuki. Calculation of atmospheric neutrino flux using the interaction model calibrated with atmospheric muon data. *Phys. Rev. D*, 75:043 006, Feb 2007. DOI: 10.1103/PhysRevD.75.043006

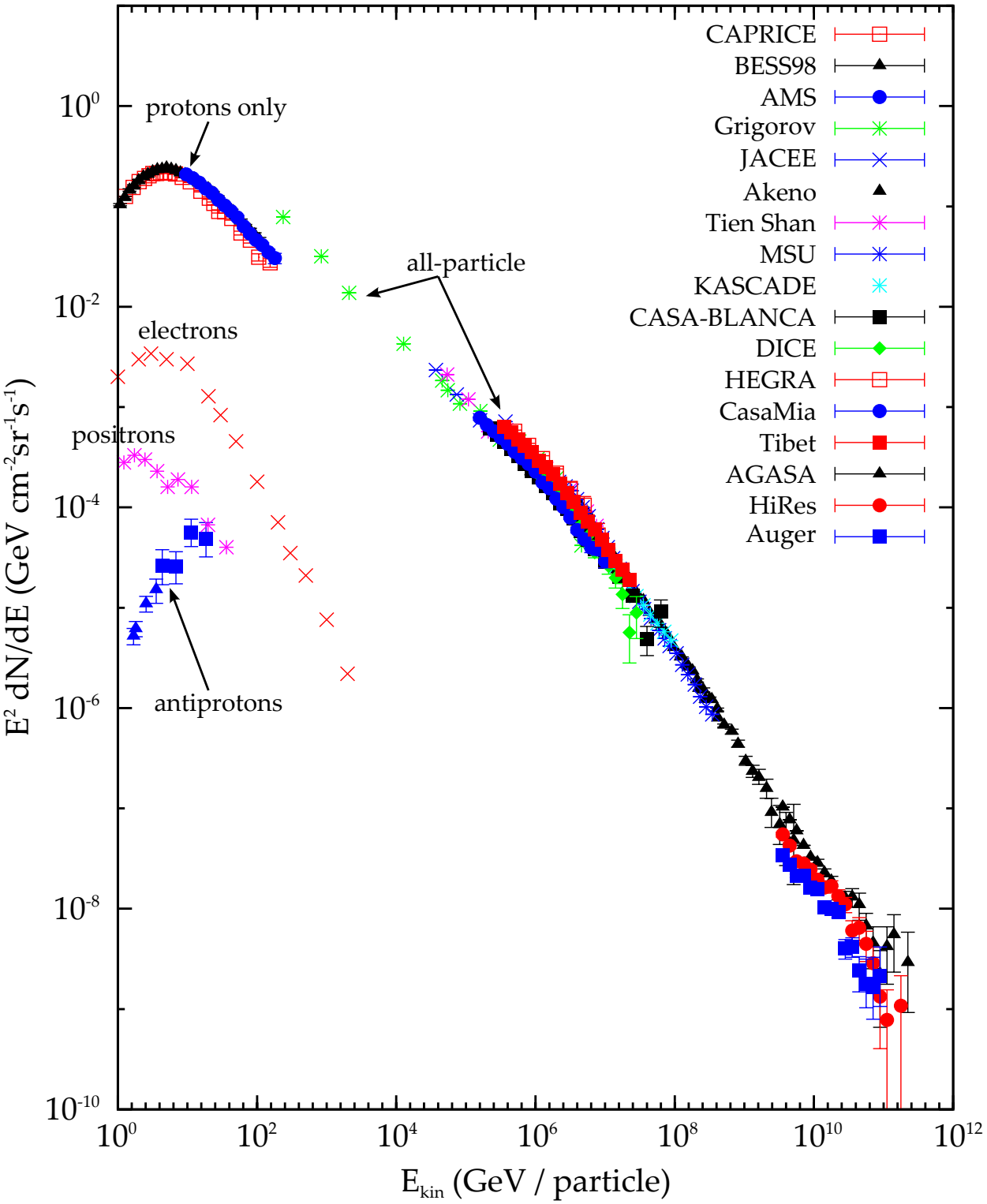

Figure 2.7: The cosmic-ray spectrum, measured by various experiments. At low energies the individual contributions from (anti-)protons, electrons, and positrons are shown, and at higher energies the all-particle spectrum [50].

more likely to interact instead of decaying. The neutrino flux at high energies stems thus mainly from kaon decays. The corresponding energy for kaons, above which interaction is more likely than decay, is at $\epsilon_K = 850\,\text{GeV}$ [49]. Figure 2.8 shows the contributions to the total neutrino flux as a function of energy. The contributions are different for vertical (solid lines) and inclined showers (dashed lines), because the decay lengths are different: at larger zenith angles the mesons travel longer through thinner layers of the atmosphere, which reduces their probability to interact, and thus increases their probability to decay. With increasing energy, this effect sets in first for the pions and later also for the kaons, which at lower energies decay anyway.

[49] T. K. Gaisser. *Cosmic Rays and Particle Physics*. Cambridge University Press, 1990

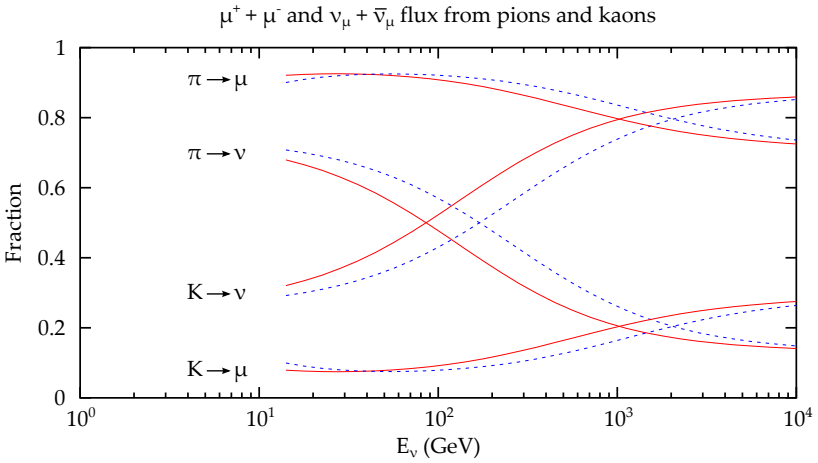

Figure 2.8: Contributions from pions and kaons to the muon neutrino flux. Also shown are their contributions to the muon flux. Solid lines are for vertical directions, dashed lines for a zenith angle of 60° [51].

From Equation 2.2, it can be seen that the competition between decay and interaction causes the neutrino energy spectrum at energies much larger than ϵ_π and ϵ_K to be steeper than the cosmic-ray spectrum by one power, i.e. $\propto E^{-3.7}$. Figure 2.10 shows the total energy spectra of ν_μ and ν_e and of the corresponding antineutrinos, as predicted by various models. For this thesis we use the model by Honda et al. (HKKM2007) [56]. The right panel shows the ratios of some of the spectra. Of particular interest here is the ν_μ/ν_e ratio. For low energies, it is ~ 2, as noted before from the pion decay chain (Equation 2.1). At higher energies the ratio increases rapidly, because – as also noted before – the muons, which are the main source of ν_e, reach the ground instead of decaying. Uncertainties in this ratio represent a systematic effect that is relevant for the analysis presented here (see Section 5.4.1).

[56] M. Honda, T. Kajita, K. Kasahara, S. Midorikawa, and T. Sanuki. Calculation of atmospheric neutrino flux using the interaction model calibrated with atmospheric muon data. *Phys. Rev. D*, 75:043 006, Feb 2007. DOI: 10.1103/PhysRevD.75.043006

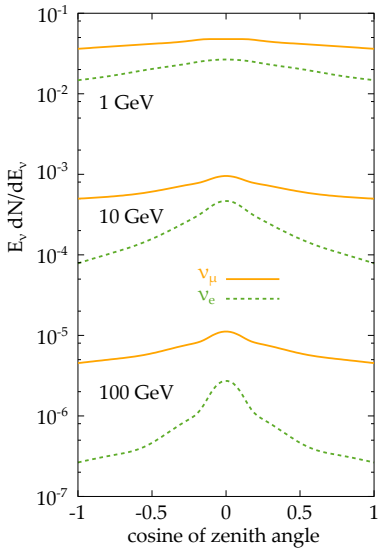

Figure 2.9: Zenith angle distributions of atmospheric neutrinos [51].

Figure 2.9 shows the zenith angle distributions of ν_μ and ν_e for three different energies. The zenith angle dependence of the decay probability is visible here, too, and causes the characteristic peak around the horizon. The magnitude of the effect increases with energy, as the main contribution to the neutrino flux shifts from pions to kaons. It is particularly pronounced for ν_e, because two decays (pion and muon) are involved in their production.

The ratio of kaons to pions as the parent particles thus influences the distributions of zenith angle and energy of the atmospheric neu-

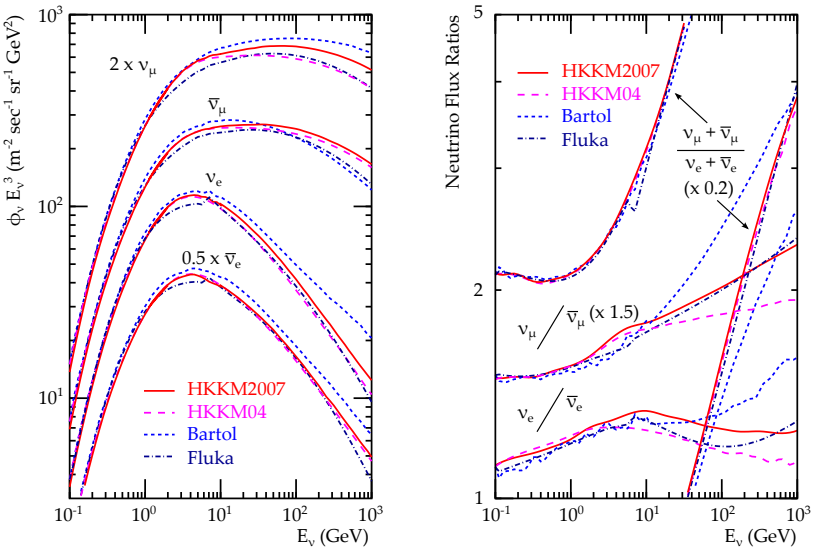

Figure 2.10: Energy spectra of atmospheric neutrinos, as predicted by various models (left), and the corresponding ν_μ/ν_e and $\nu/\bar{\nu}$ ratios (right) [56].

trinos in a non-trivial way and is thus another systematic effect that has to be considered by this analysis (see Section 5.4.1).

2.3 NEUTRINO OSCILLATIONS

A particularly interesting aspect about neutrinos – and the subject of this work – are their flavor oscillations. In the nuclear fusion reactions in the sun, electron neutrinos are produced in great numbers. In 1968 the Homestake experiment by Raymond Davis, Jr.[5] was able to detect this flux [45], but the rate was a factor 3 lower than expected. This so-called *solar neutrino problem* was solved more than 30 years later, when results from SNO[6] showed that not the ν_e flux, but the total flux of all three flavors ν_e, ν_μ, and ν_τ agrees with the rate predicted by the solar model [28]. This fact can be explained by flavor oscillations, which cause a fraction of the electron neutrinos produced in the sun to be converted to muon or tau neutrinos on Earth.

The mechanism to understand these flavor oscillations had been developed already in the 1960s by Ziro Maki, Masami Nakagawa, and Shoichi Sakata [77], after the idea of neutrino oscillations had been proposed by Bruno Pontecorvo in 1957 [84]. The basis of their theory is the difference between the neutrinos' flavor and mass eigenstates. The weak force couples to the flavor eigenstates $|\nu_\alpha\rangle$ (with $\alpha = e, \mu, \tau$), which can therefore be observed in experiments. The propagation in space, however, is given by the mass eigenstates. Figure 2.11 illustrates this principle: in a weak interaction a muon neutrino is produced, together with a muon. The muon neutrino corresponds to a certain linear combination of the mass eigenstates. Because of their different masses, the mass eigenstates propagate with a slightly different velocity. After some distance, their phase relations will thus be different from those they had at the beginning. When the neutrino is detected in another weak interaction, a different flavor eigenstate

[5] Nobel Prize 2002

[45] R. Davis, D. S. Harmer, and K. C. Hoffman. Search for Neutrinos from the Sun. *Phys. Rev. Lett.*, 20:1205–1209, May 1968. DOI: 10.1103/PhysRevLett.20.1205

[6] **S**udbury **N**eutrino **O**bservatory

[28] Q. R. Ahmad et al. Direct Evidence for Neutrino Flavor Transformation from Neutral-Current Interactions in the Sudbury Neutrino Observatory. *Phys. Rev. Lett.*, 89:011 301, Jun 2002. DOI: 10.1103/PhysRevLett.89.011301

[77] Z. Maki, M. Nakagawa, and S. Sakata. Remarks on the Unified Model of Elementary Particles. *Progress of Theoretical Physics*, 28(5):870–880, 1962. DOI: 10.1143/PTP.28.870

[84] B. Pontecorvo. Mesonium and Antimesonium. *Soviet Journal of Experimental and Theoretical Physics*, 6:429, 1958

is measured with a certain probability. In this example the muon neutrino has oscillated into a tau neutrino, producing a tau lepton in the final interaction.

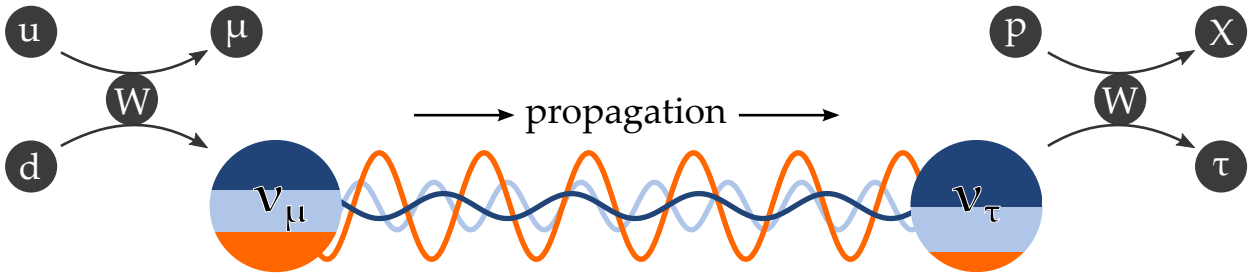

Figure 2.11: Illustration of vacuum oscillations of $\nu_\mu \to \nu_\tau$.

The mass eigenstates are denoted $|\nu_i\rangle$ (with $i = 1,2,3$) and are rotated against the flavor eigenstates. The transformation between flavor and mass eigenstates is achieved by the unitary leptonic mixing matrix U, also called Pontecorvo-Maki-Nakagawa-Sakata matrix, or PMNS matrix.

$$\begin{pmatrix} \nu_e \\ \nu_\mu \\ \nu_\tau \end{pmatrix} = U \cdot \begin{pmatrix} \nu_1 \\ \nu_2 \\ \nu_3 \end{pmatrix}$$

The matrix U itself can be written as the product of three individual rotation matrices U_{23}, U_{13}, and U_{12}:

$$U = \underbrace{\begin{pmatrix} 1 & 0 & 0 \\ 0 & c_{23} & s_{23} \\ 0 & -s_{23} & c_{23} \end{pmatrix}}_{U_{23}} \underbrace{\begin{pmatrix} c_{13} & 0 & s_{13}e^{-i\delta} \\ 0 & 1 & 0 \\ -s_{13}e^{i\delta} & 0 & c_{13} \end{pmatrix}}_{U_{13}} \underbrace{\begin{pmatrix} c_{12} & s_{12} & 0 \\ -s_{12} & c_{12} & 0 \\ 0 & 0 & 1 \end{pmatrix}}_{U_{12}}$$

with the mixing angles $c_{ij} = \cos\theta_{ij}$ and $s_{ij} = \sin\theta_{ij}$ and the CP-violating phase δ, which has not yet been measured in experiments. If neutrinos are Majorana particles, U has to be multiplied with another matrix $I = \mathrm{diag}\,(1, \exp(i\alpha_1/2), \exp(i\alpha_2/2))$, which introduces two more phases α_1 and α_2. For the following discussion of neutrino oscillations, these phases are not relevant, because the mixing matrix always occurs as the product with its complex conjugate. The phases have thus been neglected throughout this work.

Each flavor state $|\nu_\alpha\rangle$ can be written as a superposition of the mass eigenstates $|\nu_i\rangle$:

$$|\nu_\alpha\rangle = \sum_i U_{\alpha i} |\nu_i\rangle \,, \tag{2.3}$$

and vice versa the mass eigenstates as superpositions of the flavor eigenstates:

$$|\nu_i\rangle = \sum_\alpha U^*_{\alpha i} |\nu_\alpha\rangle \,.$$

The propagation of the mass eigenstates $|\nu_i\rangle$ is described by Schrödinger's equation:

$$i\frac{\mathrm{d}}{\mathrm{d}t} |\nu_i(t,\vec{x})\rangle = -\frac{1}{2m}\Delta |\nu_i(t,\vec{x})\rangle \,. \tag{2.4}$$

The solution to this equation is a plane wave, describing a freely moving relativistic particle:

$$|\nu_i\,(t,\vec{x})\rangle = e^{-i(E_i\cdot t-\vec{p}_i\cdot\vec{x})}\cdot|\nu_i(0,0)\rangle\,. \tag{2.5}$$

Since neutrino masses are small, we can calculate the equation in the relativistic limit $E \gg m$ and $v \approx c$, and thus $\vec{x} \approx L$, and Equation 2.5 becomes[7]

$$|\nu_i(L)\rangle = e^{-i\left(m_i^2\frac{L}{2E_i}\right)}\cdot|\nu_i(0)\rangle\,. \tag{2.6}$$

[7] we also reduce the dimensionality of the problem by neglecting two spatial dimensions

By substituting Equation 2.6 in Equation 2.3, the initial flavor state $|\nu_\alpha\rangle$ after having traveled a distance L can be written as

$$|\nu_\alpha(L)\rangle = \sum_i U_{\alpha i}e^{-i\left(m_i^2\frac{L}{2E}\right)}|\nu_i\rangle\,. \tag{2.7}$$

Because of the unitarity of U, pure flavor states are produced in weak interactions, i.e. a lepton of flavor α is always produced together with a neutrino of the same flavor α. Therefore the matrix elements can be interpreted as transition probabilities from one flavor into another. The probability to observe the initial state $|\nu_\alpha\rangle$ as a neutrino of flavor β after a distance L is then given by

$$\begin{aligned}
P_{\alpha\to\beta} &= \left|\langle\nu_\beta|\nu_\alpha(L)\rangle\right|^2 \\
&= \left|\sum_i U_{\alpha i}U_{\beta i}^*e^{-i\left(m_i^2\frac{L}{2E}\right)}\right|^2 \\
&= \left[\sum_i U_{\alpha i}U_{\beta i}^*e^{-i\left(m_i^2\frac{L}{2E}\right)}\right]\cdot\left[\sum_j U_{\alpha j}^*U_{\beta j}e^{-i\left(m_j^2\frac{L}{2E}\right)}\right] \\
&= \sum_{i,j} U_{\alpha i}U_{\beta i}^*U_{\alpha j}^*U_{\beta j}e^{-i\left(\left(m_i^2-m_j^2\right)\frac{L}{2E}\right)} \\
&= \sum_i\left|U_{\alpha i}U_{\beta i}^*\right|^2 + 2\sum_{i>j}U_{\alpha i}U_{\beta i}^*U_{\alpha j}^*U_{\beta j}e^{-i\left(\Delta m_{ij}^2\frac{L}{2E}\right)}\,.
\end{aligned} \tag{2.8}$$

The squared mass differences or *mass splittings* of the neutrino mass eigenstates i and j, $\Delta m_{ij}^2 = m_i^2 - m_j^2$, are – besides the mixing angles – the fundamental parameters governing neutrino oscillations.

Due to the unitarity of U, the first part of Equation 2.8 can be written as

$$\sum_i\left|U_{\alpha i}U_{\beta i}^*\right|^2 = \underbrace{\left|\sum_i U_{\alpha i}U_{\beta i}^*\right|^2}_{\delta_{\alpha\beta}} - 2\cdot\sum_{i>j}U_{\alpha i}U_{\beta i}^*U_{\alpha j}^*U_{\beta j}\,.$$

The oscillation probability (the full Equation 2.8) then becomes

$$P_{\alpha\to\beta} = \delta_{\alpha\beta} - 2\cdot\sum_{i>j}U_{\alpha i}U_{\beta i}^*U_{\alpha j}^*U_{\beta j}\left(1-e^{-i\left(\Delta m_{ij}^2\frac{L}{2E}\right)}\right).$$

Using the trigonometric identities $e^{-ix} = \cos(x) - i\sin(x)$, $\cos(x) = 1-\sin^2(x/2)$, and $\cos^2(x)+\sin^2(x) = 1$, and also translating from

natural units to SI-units, this finally becomes

$$
\begin{aligned}
P_{\alpha\to\beta} = \delta_{\alpha\beta} \\
&- 4 \cdot \sum_{i>j} \mathrm{Re}\left(U_{\alpha i} U^*_{\beta i} U^*_{\alpha j} U_{\beta j}\right) \sin^2\left(1.27 \cdot \frac{\Delta m^2_{ij}}{\mathrm{eV}^2} \cdot \frac{L/\mathrm{km}}{E/\mathrm{GeV}}\right) \\
&+ 2 \cdot \sum_{i>j} \mathrm{Im}\left(U_{\alpha i} U^*_{\beta i} U^*_{\alpha j} U_{\beta j}\right) \sin\left(2.54 \cdot \frac{\Delta m^2_{ij}}{\mathrm{eV}^2} \cdot \frac{L/\mathrm{km}}{E/\mathrm{GeV}}\right).
\end{aligned}
\tag{2.9}
$$

If the CP-violating phase δ is zero, the imaginary part vanishes. Apart from the matrix elements (the mixing angles) and the mass differences, the oscillation probability depends only on the ratio of the traveled distance, or *oscillation length*, L and the neutrino energy E. If the oscillation probability is plotted against these variables, an oscillatory pattern appears. Figure 2.12 shows this pattern using the example of the muon survival probability $P_{\mu\to\mu}$.

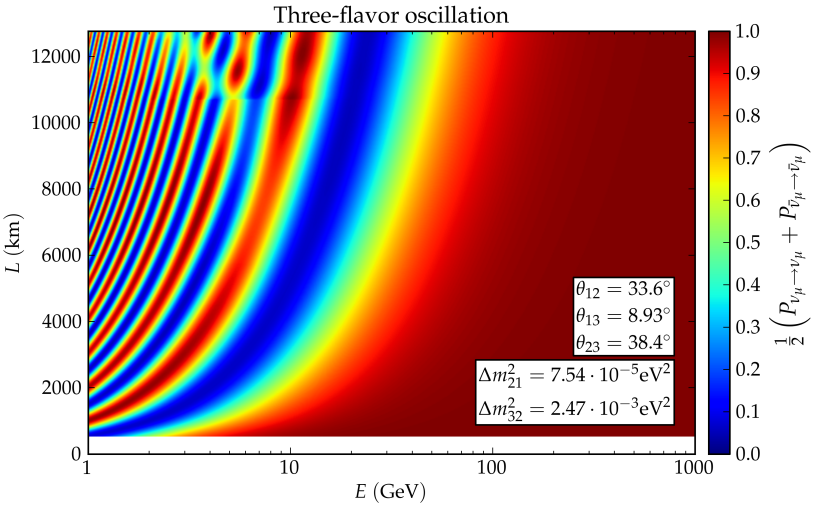

Figure 2.12: Oscillatory pattern of the muon neutrino survival probability $P_{\mu\to\mu}$ (averaged over neutrinos and antineutrinos) as a function of oscillation length L and neutrino energy E. Also included are matter effects (see Section 2.3.1)! Calculations were made with the tool *nuCraft* [98].

2.3.1 MATTER EFFECTS

On closer inspection, Figure 2.12 exhibits structures disrupting the regular oscillation pattern in the region of low energy and large oscillation length. These are caused by matter effects.

THE MSW EFFECT When neutrinos travel through matter, all flavors can interact by exchanging Z^0 bosons (NC). In contrast to the situation in vacuum, the neutrinos propagate in a non-zero potential V_{NC}. This potential alone does not introduce any change in the phase relations of the different mass eigenstates, and thus no additional oscillation effects. Electron neutrinos, however, have the additional possibility to interact with the surrounding electrons via the exchange of $W^\pm$ bosons (CC). This asymmetry introduces an additional potential V_{CC} only for electron neutrinos, which is equivalent to an effective change of the mass eigenstates. This, in turn, implies a change also in the relation between mass and flavor eigenstates and hence in the effective

oscillation parameters. This effect was first described by Lincoln Wolfenstein and later by Stanislav Mikheyev and Alexei Smirnov [80] and is therefore called *MSW effect*.

[80] S. Mikheyev and A. Y. Smirnov. Resonance Amplification of Oscillations in Matter and Spectroscopy of Solar Neutrinos. *Sov.J.Nucl.Phys.*, 42:913–917, 1985

Formally, the additional interactions with matter introduce an effective potential V_{CC}, which is experienced only by the ν_e, and which has the form

$$V_{CC} = \pm\sqrt{2} G_F N_e \,. \tag{2.10}$$

Here, G_F is the Fermi constant, and N_e the electron number density. An interesting feature of this effect is that it is different for neutrinos and antineutrinos: the upper sign in Equation 2.10 applies to neutrinos, the lower to antineutrinos. With this effective potential, the initial Hamiltonian used in Equation 2.4 has to be supplemented with

$$A = \pm \frac{2\sqrt{2} G_F N_e E_\nu}{\Delta m^2} \,,$$

with the neutrino energy E_ν. Using the same procedure as before, a modified mixing matrix U_{Mat} can be obtained. Similarly, the mass differences are adapted. In the two-flavor approximation (see Section 2.5) with only one mixing angle θ and one mass difference Δm^2, the modified oscillation parameters can be written as

$$\begin{aligned} \Delta m^2_{Mat} &= C \Delta m^2 \\ \sin 2\theta_{Mat} &= \frac{\sin 2\theta}{C} \,, \end{aligned}$$

with

$$C = \sqrt{(A - \cos 2\theta)^2 + \sin^2 2\theta} \,.$$

If $A = \cos 2\theta$, maximal mixing occurs, even if the vacuum mixing angle is small! This effect is called *MSW resonance*. It should be noted that, depending on the sign of Δm^2, the effect occurs either for neutrinos or for antineutrinos. This fact allowed to determine the sign of Δm^2_{21} and might in the future allow to fully determine the mass hierarchy (see Section 2.4.4). Most of the structures in Figure 2.12 that deviate from the regular vacuum oscillation pattern are caused by the interplay of the MSW effect with the structure of the Earth's interior [32]:

[32] E. K. Akhmedov, M. Maltoni, and A. Y. Smirnov. 1-3 leptonic mixing and the neutrino oscillograms of the earth. *Journal of High Energy Physics*, 2007(05):077, 2007. DOI: 10.1088/1126-6708/2007/05/077

- The apparent discontinuity at $L \approx 10\,500\,\text{km}$ occurs because neutrinos with longer oscillation lengths arrive from almost vertically below the detector and pass through the core which has the highest electron density, while neutrinos with shorter oscillation lengths come from closer to the horizon and pass only through the Earth's mantle, where the electron density is significantly lower.
- Neutrinos passing only through the mantle experience an MSW resonance around $5 - 7\,\text{GeV}$, causing the slight reduction of the muon survival probability in this region.
- Another MSW resonance can be found between $2 - 3\,\text{GeV}$ for neutrinos passing through the core.

PARAMETRIC RESONANCE Another matter effect, called *parametric resonance*, occurs when neutrinos travel through different layers of periodically alternating matter density. The easiest representation of such a density profile is the so-called *castle-wall profile*. In the Earth this situation is approximately realized for neutrinos crossing the Earth along its diameter and traversing mantle, core and again the mantle. If the period of the density transition is adjusted to the neutrino energy, it can lead to large enhancements of the oscillation probabilities by modifications of the phase of the oscillation [31]. In Figure 2.12 this effect is visible in the distortions of the survival probability of neutrinos passing through the core with energies above 3 GeV [32].

[31] E. K. Akhmedov. Parametric resonance of neutrino oscillations and passage of solar and atmospheric neutrinos through the earth. *Nuclear Physics B*, 538(1-2):25–51, 1999. DOI: 10.1016/S0550-3213(98)00723-8

[32] E. K. Akhmedov, M. Maltoni, and A. Y. Smirnov. 1-3 leptonic mixing and the neutrino oscillograms of the earth. *Journal of High Energy Physics*, 2007(05):077, 2007. DOI: 10.1088/1126-6708/2007/05/077

2.4 STATUS OF MEASUREMENTS OF THE OSCILLATION PARAMETERS

In the formalism described in section 2.3, neutrino oscillations in vacuum can be fully described with 6 parameters: the three mixing angles θ_{12}, θ_{13}, and θ_{23}, two mass differences, e.g. Δm^2_{21} and Δm^2_{32}, and the CP-violating phase δ.[8] Apart from the phase, all these parameters have been measured – with different precision – by various experiments. The current status of our knowledge about these parameters is presented in the next sections. Not yet resolved is the question of the mass hierarchy, i.e. the sign of Δm^2_{32}, which is presented in Section 2.4.4. Furthermore, most experiments do not measure the mixing angle θ_{23} directly, but e.g. $\sin^2(2\theta_{23})$, which is symmetrical around $\theta_{23} = \pi/4$. Thus, the question of the octant of θ_{23} (i.e. if θ_{23} is smaller or larger than $\pi/4$) is also still open.

[8] Note that the exact value of the third mass difference – here Δm^2_{31} – is fixed by the other two.

2.4.1 θ_{12} AND Δm^2_{21}

The mixing angle θ_{12} and the corresponding mass difference Δm^2_{21} can be measured by examining the flux of ν_e produced by ^{8}B decays in nuclear fusion processes in the core of the Sun. On their way out of the Sun, these ν_e undergo oscillations because of the MSW effect (see Section 2.3.1), when they cross a layer with an electron density matching the resonance condition. A wealth of experiments has observed these neutrinos and found oscillations at energies of around a couple of MeV; the leading experiment in this field is SNO [27].

Another possibility to measure θ_{12} and Δm^2_{21} arises from the observation of $\overline{\nu}_e$ from nuclear reactors. This was done by the KamLAND[9] experiment. Here, the oscillation lengths are given by the distances to nearby nuclear power plants, typically about 180 km. Again, oscillations are found at energies above 1 MeV [16].

Figure 2.13 shows the confidence regions obtained by the solar neutrino experiments (including SNO) and KamLAND, together with their combination. Of particular importance is the fact that KamLAND is especially sensitive to the mass difference, whereas the solar experiments have a better sensitivity to the mixing angle. By

[27] B. Aharmim et al. Combined analysis of all three phases of solar neutrino data from the Sudbury Neutrino Observatory. *Phys. Rev. C*, 88:025 501, Aug 2013. DOI: 10.1103/PhysRevC.88.025501

[9] **Kam**ioka **L**iquid scintillator **A**nti-**N**eutrino **D**etector

[16] S. Abe et al. Precision Measurement of Neutrino Oscillation Parameters with KamLAND. *Phys. Rev. Lett.*, 100:221 803, Jun 2008. DOI: 10.1103/PhysRevLett.100.221803

combining the results from both types of experiments, the oscillation parameters can be determined with high precision. The combined analysis – done by the SNO collaboration – finds [27]

$$\begin{aligned} \tan^2(\theta_{12}) &= 0.446^{+0.030}_{-0.029}\,, \quad \text{corresponding to} \\ \theta_{12} &= 37.1^\circ \pm 1^\circ\,, \quad \text{and} \\ \Delta m^2_{21} &= 7.41^{+0.21}_{-0.19} \cdot 10^{-5}\,\text{eV}^2\,. \end{aligned}$$

They also confirm the sign of Δm^2_{21} to be positive, i.e. $m_1 < m_2$.

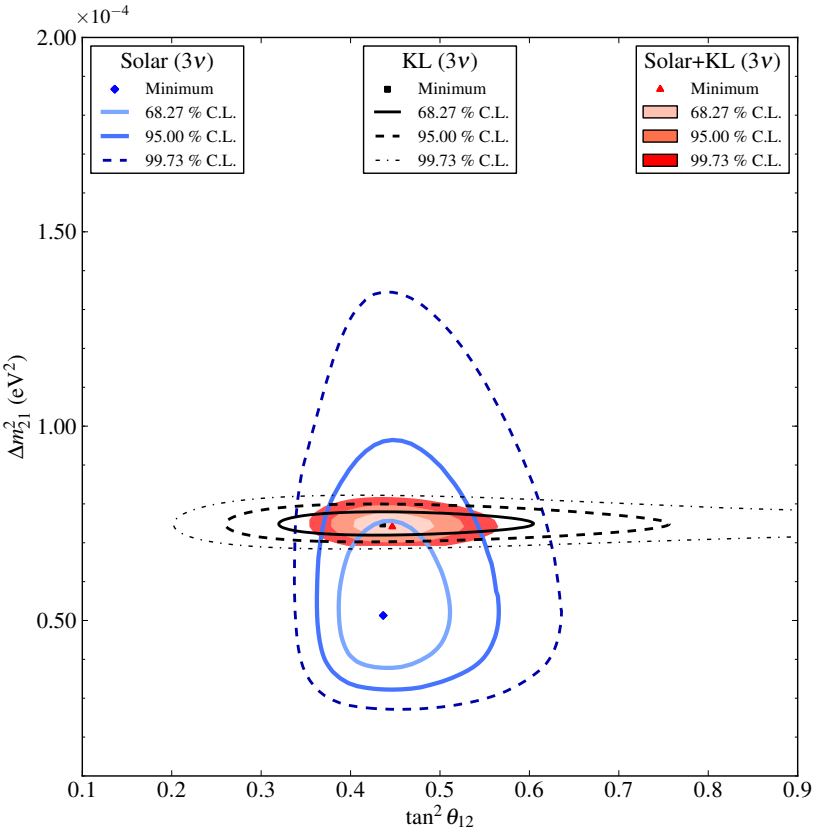

Figure 2.13: Confidence contours for $\tan^2(\theta_{12})$ and Δm^2_{21} for the solar neutrino experiments (including SNO, as well as Borexino, Super-Kamiokande, and several ^{71}Ga and ^{37}Cl experiments, such as SAGE, GALLEX, GNO, and the Homestake experiment), for KamLAND (KL), and for their combination [27].

2.4.2 θ_{23} AND Δm^2_{32}

The first experiment that measured θ_{23} and Δm^2_{32} – and with it, confirmed neutrino oscillations for the first time – was Super-Kamiokande (*Super-K*) in 1998 [48]. They searched for ν_μ produced in the atmosphere, in air showers induced by cosmic rays that interact with air molecules (see Section 2.2). Since neutrinos pass through the Earth almost unhindered, experiments sensitive to atmospheric neutrinos can utilize air showers on the other side of the globe. The oscillation length in this case can be as large as the diameter of the Earth, and the corresponding neutrino energies reach several tens of GeV (compare with Figure 2.12). Although most of the sensitivity of the Super-K detector is at energies below 1 GeV, their analysis found a zenith-angle-dependent deficit, that could not be explained by uncertainties in the atmospheric flux calculations nor by experimental effects. It

[48] Y. Fukuda et al. Evidence for oscillation of atmospheric neutrinos. *Phys. Rev. Lett.*, 81:1562–1567, Aug 1998. DOI: 10.1103/PhysRevLett.81.1562

was however consistent with the expectations from ν_μ disappearance due to neutrino oscillations.

At present, the best sensitivity to the mass difference is achieved by MINOS,[10] which uses the complementary technique of a *long-baseline* neutrino beam. A pure ν_μ beam with a peak energy of 7 GeV is produced in the NuMI[11] beamline at Fermilab near Chicago. Its properties are measured by a near detector directly after the neutrino production. A far detector deep underground in the Soudan mine in Minnesota searches for ν_μ disappearance. The oscillation length is 735 km, and full disappearance is expected at neutrino energies slightly above 1 GeV. They report a best fit of [93]

$$\begin{aligned} \sin^2(2\theta_{23}) &= 0.950^{+0.035}_{-0.036}\,, \quad \text{corresponding to} \\ \theta_{23} &= 38.5^\circ \pm 3^\circ\,, \quad \text{and} \\ \Delta m^2_{32} &= 2.41^{+0.09}_{-0.10} \cdot 10^{-3}\,\text{eV}^2\,. \end{aligned}$$

Even 15 years after their initial discovery, Super-K is still one of the leading experiments in measuring θ_{23} and Δm^2_{32}. Their sensitivity to the mixing angle is even better than MINOS', at a slightly worse resolution of the mass difference. Their best-fit point is at [95]

$$\begin{aligned} \sin^2(2\theta_{23}) &= 0.99\,, \quad \text{corresponding to} \\ \theta_{23} &= 42.1^\circ\,, \quad \text{and} \\ \Delta m^2_{32} &= 2.3 \cdot 10^{-3}\,\text{eV}^2\,, \end{aligned}$$

and in good agreement with the MINOS result.

Recently, also the neutrino telescopes ANTARES [23] and IceCube [3] have presented results on atmospheric neutrino oscillations. While the precision of their measurements is not (yet) competitive to MINOS or Super-K, the value of their observations lies in the fact that their sensitivity comes mainly from the higher energies not (or not well) covered by the other experiments. The improvement of IceCube's sensitivity towards a competitive measurement of the oscillation parameters is the main goal of this work.

The latest results on θ_{23} and Δm^2_{32} come from T2K,[12] another long-baseline experiment, using a ν_μ beam sent from the J-PARC facility in Tokai on the east coast of Japan to the Super-Kamiokande detector in western Japan. The distance between the sites and thus the oscillation length is 295 km. The energy distribution of the neutrino beam peaks at 600 MeV, exactly where maximum disappearance is expected. T2K's sensitivity to the mass difference is better than Super-K's and their sensitivity to the mixing angle is better than that of MINOS. However, the exact size of their contours depends on the choice of the octant of θ_{23} [96].

At present, no single experiment is sensitive to the octant of θ_{23}. With global fits of the results of various neutrino experiments, it is possible to obtain some initial sensitivity. The results are, however, inconclusive: while the results from Super-K and MINOS favor the first octant ($\theta_{23} < \pi/4$), the latest results from T2K slightly favor the second octant ($\theta_{23} > \pi/4$). It should be kept in mind, though, that all

[10] **M**ain **I**njector **N**eutrino **O**scillation **S**earch

[11] **Neu**trinos at the **M**ain **I**njector

[93] The MINOS Collaboration. *Proceedings of Neutrino 2012, to be published*

[95] The Super-Kamiokande Collaboration. *Proceedings of Neutrino 2012, to be published*

[23] S. Adrián-Martínez et al. Measurement of atmospheric neutrino oscillations with the ANTARES neutrino telescope. *Physics Letters B*, 714(2-5):224–230, 2012. DOI: 10.1016/j.physletb.2012.07.002

[3] M. G. Aartsen et al. Measurement of Atmospheric Neutrino Oscillations with IceCube. *Phys. Rev. Lett.*, 111:081801, Aug 2013. DOI: 10.1103/PhysRevLett.111.081801

[12] **T**okai **to** **K**amioka

[96] The T2K Collaboration. *Proceedings of EPS HEP 2013, to be published*

of these indications are up to now in the range of $1-2\,\sigma$, and thus not significant [53].

Figure 2.14 shows the most current confidence regions for θ_{23} and Δm^2_{32} from the experiments discussed above.

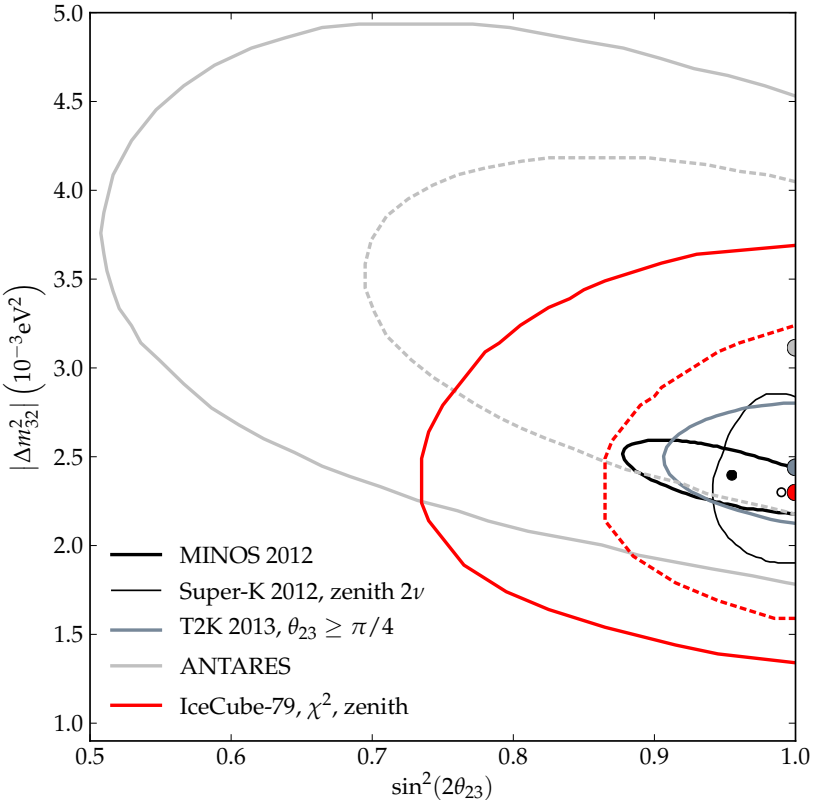

[53] M. Gonzalez-Garcia, M. Maltoni, J. Salvado, and T. Schwetz. Global fit to three neutrino mixing: critical look at present precision. *Journal of High Energy Physics*, 1212:123, 2012. DOI: 10.1007/JHEP12(2012)123

Figure 2.14: Confidence contours for $\sin^2(\theta_{23})$ and Δm^2_{32} for MINOS [93], Super-K [95], T2K, ANTARES [23] and IceCube [3]. Solid lines are 90% C.L., dashed lines are 68 % C.L. The best-fit points are shown in the corresponding color.

2.4.3 θ_{13}

The third mixing angle, θ_{13}, is small compared to the other two mixing angles (which are almost maximal), and therefore eluded a precise measurement for a long time. The first experiment to find not only an upper limit was MINOS, searching for the appearance of ν_e in a ν_μ beam, but with a significance of not much more than $1\,\sigma$ [21].

The leading experiment is again T2K. In their newest analysis they find 11 electron neutrino events at an expected background of 3.3 events, rejecting the hypothesis of $\sin^2(2\theta_{13}) = 0$ by $3.1\,\sigma$. Their best fit for the mixing angle yields [15]

$$\sin^2(2\theta_{13}) = 0.088^{+0.049}_{-0.039}\,.$$

Complementary information comes from reactor experiments. They observe the disappearance of $\overline{\nu}_e$ from the nuclear fission reactions in nearby power plants. The first experiment of this type is Double Chooz, which utilizes two reactor cores at a distance of 1050 m from the detector and finds a mixing angle of [17]

$$\sin^2(2\theta_{13}) = 0.085 \pm 0.029(\mathrm{stat.}) \pm 0.042(\mathrm{syst.})\,.$$

[21] P. Adamson et al. Search for Muon-Neutrino to Electron-Neutrino Transitions in MINOS. *Phys. Rev. Lett.*, 103:261802, Dec 2009. DOI: 10.1103/PhysRevLett.103.261802

[15] K. Abe et al. Evidence of electron neutrino appearance in a muon neutrino beam. *Phys. Rev. D*, 88:032002, Aug 2013. DOI: 10.1103/PhysRevD.88.032002

[17] Y. Abe et al. Indication of Reactor $\overline{\nu}_e$ Disappearance in the Double Chooz Experiment. *Phys. Rev. Lett.*, 108:131801, Mar 2012. DOI: 10.1103/PhysRevLett.108.131801

Within two months, this result was confirmed with higher significance by the conceptually similar experiments RENO[13] [29] and Daya Bay [33], which at the moment provides the most precise measurement with

$$\sin^2(2\theta_{13}) = 0.092 \pm 0.016(\text{stat.}) \pm 0.005(\text{syst.}) \,, \quad \text{or}$$
$$\theta_{13} = 8.8^\circ \pm 1^\circ \,.$$

[13] **R**eactor **E**xperiment for **N**eutrino **O**scillation

[29] J. K. Ahn et al. Observation of Reactor Electron Antineutrinos Disappearance in the RENO Experiment. *Phys. Rev. Lett.*, 108:191802, May 2012. DOI: 10.1103/PhysRevLett.108.191802

[33] F. P. An et al. Observation of Electron-Antineutrino Disappearance at Daya Bay. *Phys. Rev. Lett.*, 108:171803, Apr 2012. DOI: 10.1103/PhysRevLett.108.171803

2.4.4 MASS HIERARCHY

While the mass differences Δm^2_{21} and Δm^2_{32} are known with good accuracy, the absolute values of the neutrino masses (see Section 2.1), and in particular their ordering (the *mass hierarchy*), are still unknown. The sign of the smaller difference Δm^2_{21} was found to be positive by the solar neutrino experiments and KamLAND (see Section 2.4.1). Thus, there are two remaining possibilities to arrange the mass differences: the larger difference Δm^2_{32} can be between the two heavier states (*normal* hierarchy, $m_1 < m_2 \ll m_3$), or between the two lighter states (*inverted* hierarchy, $m_3 \ll m_1 < m_2$). Figure 2.15 depicts the two possible hierarchies. The lengths of the color bars indicate the "flavor content" of the mass eigenstates.

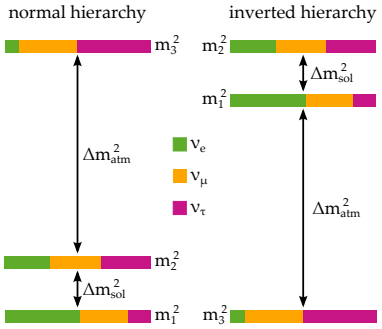

Figure 2.15: Sketch of the two possibilities for the neutrino mass hierarchy.

Besides the direct mass measurements (see Section 2.1), several types of experiments are currently being planned that would be able to address the question of the neutrino mass hierarchy. In any case, however, it will likely be another decade before conclusive results are to be expected.

- One possibility to measure the mass hierarchy arises from the proposed next generation of long-baseline neutrino experiments, such as LBNE.[14] It builds on the existing accelerator structures at Fermilab to send a high-intensity muon (anti-)neutrino beam to a detector deep underground in the Homestake mine in South Dakota. Depending on the hierarchy realized in nature, the MSW effect modifies the oscillation probability of either neutrinos or antineutrinos (see Section 2.3.1). If the funding can be secured, measurements could begin around 2021. Projected sensitivities show that LBNE could answer the question of the mass hierarchy with a significance of 3 σ or better within 10 years of operation [20].
- Due to the unexpectedly large mixing angle θ_{13}, also experiments detecting atmospheric neutrinos have a chance to measure the mass hierarchy. They would also observe the distortions in the oscillation probabilities induced by the MSW effect. If the experiment cannot discriminate neutrinos from antineutrinos directly, a measurement is still possible, because the different cross sections for neutrinos and antineutrinos determine the magnitude of the effect.

  Hyper-K, a planned successor of Super-K, would most likely be able to determine the mass hierarchy. Provided that the necessary funding2 is allocated, operations could begin around 2023, and yield a $3-5\,\sigma$ result after about 10 years [14].

  A faster route might be provided by the proposed PINGU[15]

[14] **L**ong-**B**aseline **N**eutrino **E**xperiment

[20] C. Adams et al. Scientific Opportunities with the Long-Baseline Neutrino Experiment. *arXiv:1307.7335 [hep-ex]*, 2013

[14] K. Abe, T. Abe, H. Aihara, Y. Fukuda, Y. Hayato et al. Letter of Intent: The Hyper-Kamiokande Experiment — Detector Design and Physics Potential —. *arXiv:1109.3262 [hep-ex]*, 2011

[15] **P**recision **I**ceCube **N**ext **G**eneration **U**pgrade

detector, a low-energy upgrade of the IceCube Neutrino Observatory. It could be deployed within a much shorter timescale (until 2018), and at relatively moderate costs. The performance of the detector is currently being studied. If it is found to be sufficient, PINGU could deliver a $3-5\,\sigma$ measurement of the mass hierarchy before the operations of more extensive experiments like LBNE or Hyper-K have even commenced [94].

[94] The PINGU Collaboration. PINGU Sensitivity to the Neutrino Mass Hierarchy. *Submitted to the Snowmass 2013 Proceedings, arXiv:1306.5846 [astro-ph.IM]*

- The found large value of θ_{13} has also opened up the possibility for measuring the mass hierarchy by reactor neutrino experiments. In contrast to the other approaches the sensitivity here comes not from matter effects, but from the interference of two oscillation modes driven by Δm^2_{31} and Δm^2_{32} [106]. The already funded Daya Bay-II experiment expects to start measurements around 2020 and to be able to determine the mass hierarchy with a confidence level of $4\,\sigma$ within 6 years [74].

[106] L. Zhan, Y. Wang, J. Cao, and L. Wen. Determination of the neutrino mass hierarchy at an intermediate baseline. *Phys. Rev. D*, 78:111 103, Dec 2008. DOI: 10.1103/PhysRevD.78.111103

[74] Y.-F. Li, J. Cao, Y. Wang, and L. Zhan. Unambiguous determination of the neutrino mass hierarchy using reactor neutrinos. *Phys. Rev. D*, 88:013 008, Jul 2013. DOI: 10.1103/PhysRevD.88.013008

TABLE 2.1 shows an overview of all the parameters governing neutrino oscillations. The values reported here were obtained by a global analysis of all experiments by Fogli et al. [46]. By combining the results of all experiments, they also find some emerging sensitivity to the CP-violating phase δ. For convenience, the mixing angles are also given as $\sin^2(\theta)$ and $\sin^2(2\theta)$. The values in this table are used as baseline parameters throughout the analysis presented here. Note that normal mass hierarchy is assumed, which fixes the sign of Δm^2_{32}!

[46] G. L. Fogli, E. Lisi, A. Marrone, D. Montanino, A. Palazzo, and A. M. Rotunno. Global analysis of neutrino masses, mixings, and phases: Entering the era of leptonic *CP* violation searches. *Phys. Rev. D*, 86:013 012, Jul 2012. DOI: 10.1103/PhysRevD.86.013012

Parameter	Best-fit value	Error	Unit
θ_{12}	33.6	$^{+1.1}_{-1.0}$	$^\circ$
θ_{13}	8.93	$^{+0.46}_{-0.48}$	$^\circ$
θ_{23}	38.4	$^{+1.4}_{-1.2}$	$^\circ$
$\sin^2(\theta_{12})$	3.07	± 0.18	10^{-1}
$\sin^2(\theta_{13})$	2.41	± 0.25	10^{-2}
$\sin^2(\theta_{23})$	3.86	$^{+0.24}_{-0.21}$	10^{-1}
$\sin^2(2\theta_{12})$	8.51	$^{+0.26}_{-0.29}$	10^{-1}
$\sin^2(2\theta_{13})$	9.41	$^{+0.95}_{-0.96}$	10^{-2}
$\sin^2(2\theta_{23})$	9.48	± 0.20	10^{-1}
Δm^2_{21}	+ 7.54	$^{+0.26}_{-0.22}$	$10^{-5}\,\mathrm{eV}^2$
Δm^2_{32}	+ 2.39	$^{+0.06}_{-0.10}$	$10^{-3}\,\mathrm{eV}^2$
δ	1.08	$^{+0.28}_{-0.31}$	π

Table 2.1: Overview of the current best-fit values of all oscillation parameters for normal mass hierarchy. [46]

2.5 ATMOSPHERIC NEUTRINO OSCILLATIONS

Atmospheric and solar oscillations are almost completely decoupled (i.e. they are governed by different and independent elements of the mixing matrix). Furthermore, the third mixing angle θ_{13} is small

compared to the other two. Thus, a substantial simplification in the description of atmospheric oscillations at energies above 10 GeV can be made by approximating them as two-flavor oscillations involving solely ν_μ and ν_τ. These oscillations can be described by only one mixing angle θ_{23} and one mass difference Δm^2_{32}. The PMNS matrix U simplifies considerably to a 2×2 submatrix of U_{23}:

$$U_{\text{atm}} = \begin{pmatrix} \cos\theta_{23} & \sin\theta_{23} \\ -\sin\theta_{23} & \cos\theta_{23} \end{pmatrix}.$$

Consequently, the oscillation probability (Equation 2.9) simplifies to

$$P_{\alpha\to\beta} = \delta_{\alpha\beta} - 4 \cdot \left(U_{\alpha3}U_{\beta3}U_{\alpha2}U_{\beta2}\right) \sin^2\left(1.27 \cdot \frac{\Delta m^2_{32}}{\text{eV}^2} \cdot \frac{L/\text{km}}{E/\text{GeV}}\right),$$

with $(\alpha, \beta) \in (\mu, \tau)$. For the muon survival probability $P_{\mu\to\mu}$ one obtains

$$\begin{aligned} P_{\mu\to\mu} &= 1 - 4 \cdot \left(U^2_{\mu3}U^2_{\mu2}\right) \sin^2\left(1.27 \cdot \frac{\Delta m^2_{32}}{\text{eV}^2} \cdot \frac{L/\text{km}}{E/\text{GeV}}\right) \\ &= 1 - 4 \cdot \left(\sin^2(\theta_{23})\cos^2(\theta_{23})\right) \sin^2\left(1.27 \cdot \frac{\Delta m^2_{32}}{\text{eV}^2} \cdot \frac{L/\text{km}}{E/\text{GeV}}\right) \\ &= 1 - \sin^2(2\theta_{23}) \sin^2\left(1.27 \cdot \frac{\Delta m^2_{32}}{\text{eV}^2} \cdot \frac{L/\text{km}}{E/\text{GeV}}\right). \end{aligned} \tag{2.11}$$

In the last step, the trigonometric identity $\sin(2x) = 2\sin(x)\cos(x)$ was used. The appearance probability $P_{\mu\to\tau}$ is of course

$$\begin{aligned} P_{\mu\to\tau} &= 1 - P_{\mu\to\mu} \\ &= \sin^2(2\theta_{23}) \sin^2\left(1.27 \cdot \frac{\Delta m^2_{32}}{\text{eV}^2} \cdot \frac{L/\text{km}}{E/\text{GeV}}\right). \end{aligned}$$

The 2-dimensional pattern of the muon survival probability in the two-flavor approximation is shown in Figure 2.16. The differences to Figure 2.12, obtained with the full 3-flavor treatment, are small, occur almost exclusively in the energy range below 10 GeV and are dominated by the omission of the matter effects.

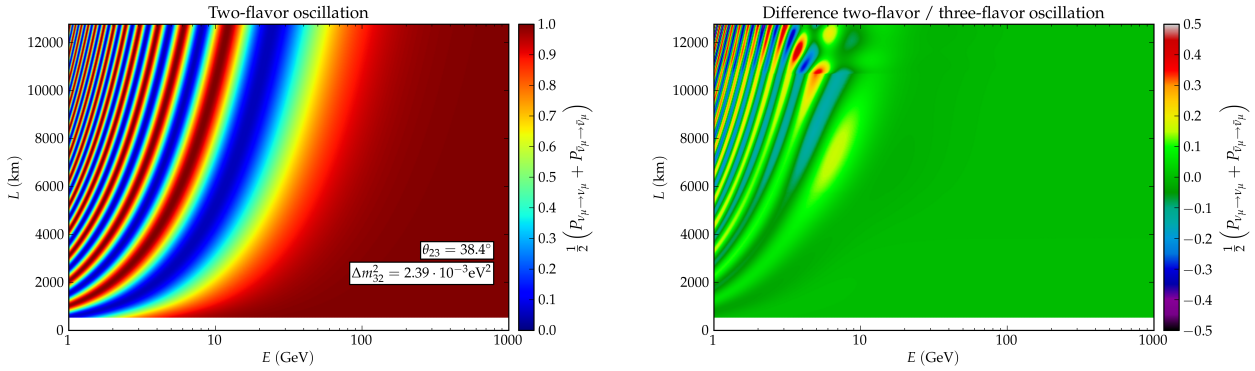

Figure 2.16: Oscillatory pattern of the muon neutrino survival probability $P_{\mu\to\mu}$ as a function of oscillation length L and neutrino energy E in two-flavor approximation (left), and the difference to the full 3-flavor treatment as in Figure 2.12 (right). Calculations were made with the tool *nuCraft* [98].

In the two-flavor approximation, the individual roles of the oscillation parameters $\sin^2(2\theta_{23})$ and Δm^2_{32} are particularly obvious: the

mixing angle determines the amplitude of the oscillation, and the mass difference its period. Figure 2.17 shows the muon survival probability $P_{\mu\to\mu}$ and the tau appearance probability $P_{\mu\to\tau}$ as a function of oscillation length L for a fixed neutrino energy of 25 GeV.

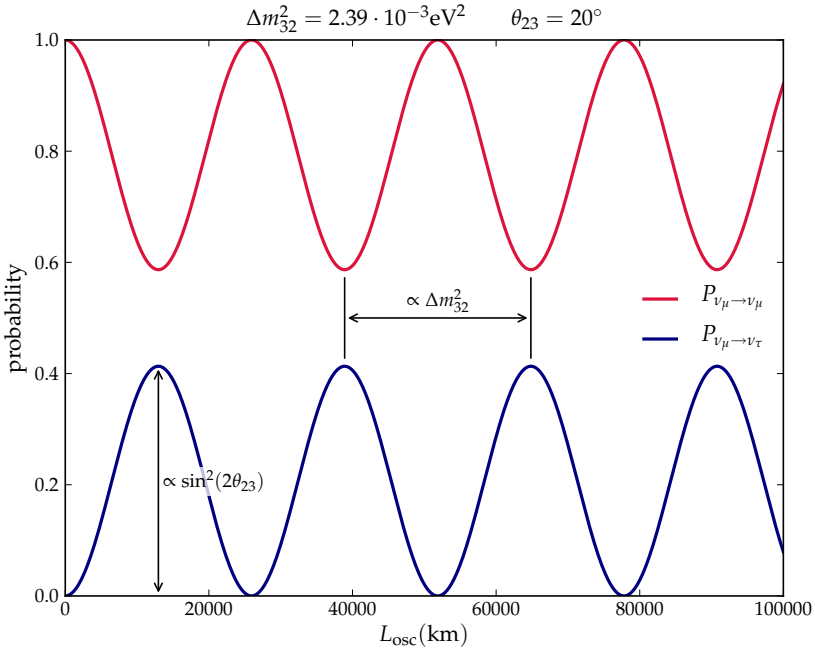

Figure 2.17: Muon neutrino survival probability $P_{\mu\to\mu}$ and tau neutrino appearance probability $P_{\mu\to\tau}$ as a function of oscillation length L for a neutrino energy of 25 GeV. The oscillation parameters are set to $\Delta m^2_{32} = 2.39 \cdot 10^{-3}\,\text{eV}^2$ and $\theta = 20°$.

2.6 STERILE NEUTRINOS

The existence of neutrino oscillations that can be described by the formalism presented in section 2.3 has been established by many experiments and their parameters have been measured with fairly good precision (see Section 2.4). However, few experimental results suggest the existence of additional neutrino flavors, which do not interact via the weak force, and are therefore called *sterile*. First, the LSND[16] experiment found an excess of $\overline{\nu}_e$ events in a $\overline{\nu}_\mu$ beam, which can not be explained by the established neutrino oscillations. A possible solution is the introduction of one or more additional neutrino flavors. If at least one additional neutrino exists with a mass larger than 0.4 eV, oscillations between the active states and this sterile state could explain the LSND result [25].

MiniBooNE,[17] built to test the LSND result, found again indications for sterile neutrinos. In addition to reproducing the LSND results with a $\overline{\nu}_\mu$ beam, they also found an excess of ν_e in a ν_μ beam [26].

Independent support for the sterile neutrino hypothesis comes from the so-called *Gallium anomaly*. The solar neutrino experiments SAGE[18] and GALLEX,[19] using Gallium as their detector material, were tested by deploying strong radioactive ^{51}Cr and ^{37}Ar sources close to the detectors. They measured a ν_e flux somewhat lower than the expectations, consistent with the disappearance of the electron neutrinos due to oscillations [18].

[16] **L**iquid **S**cintillator **N**eutrino **D**etector

[25] A. Aguilar et al. Evidence for neutrino oscillations from the observation of $\overline{\nu}_e$ appearance in a $\overline{\nu}_\mu$ beam. *Phys. Rev. D*, 64:112 007, Nov 2001. DOI: 10.1103/PhysRevD.64.112007

[17] **Mini Boo**ster **N**eutrino **E**xperiment

[26] A. Aguilar-Arevalo et al. A Combined $\nu_\mu \to \nu_e$ and $\overline{\nu}_\mu \to \overline{\nu}_e$ Oscillation Analysis of the MiniBooNE Excesses. *arXiv:1207.4809 [hep-ex]*, 2012

[18] **S**oviet-**A**merican **G**allium **E**xperiment

[19] **GALL**ium **EX**periment

[18] M. A. Acero, C. Giunti, and M. Laveder. Limits on ν_e and $\overline{\nu}_e$ disappearance from Gallium and reactor experiments. *Phys. Rev. D*, 78:073 009, Oct 2008. DOI: 10.1103/PhysRevD.78.073009

Recently, a global re-analysis of reactor neutrino data found a similar deficit in almost all measured reactor $\overline{\nu}_e$ fluxes. This *reactor antineutrino anomaly* could again be explained by oscillations into additional sterile neutrinos [79].

It should, however, be noted that there is no confirming evidence for the LSND and MiniBooNE results from other experiments. Moreover, a sterile neutrino that could explain these results would be in slight conflict with results obtained from cosmology, which prefer three neutrino flavors over four by more than 2 σ [22].

[79] G. Mention et al. Reactor antineutrino anomaly. *Phys. Rev. D*, 83:073 006, Apr 2011. DOI: 10.1103/PhysRevD.83.073006

[22] P. A. R. Ade et al. Planck 2013 results. XVI. Cosmological parameters. *Submitted to A&A*

The existence of sterile neutrinos would also influence the oscillation signature this analysis searches for. Figure 2.18 shows the muon survival probability $P_{\mu\to\mu}$ as a function of oscillation length L and neutrino energy E, as in Figure 2.12, but with one additional sterile neutrino with a squared mass difference of $\Delta m^2_{41} = 0.5\,\mathrm{eV}^2$ and an additional mixing angle $\theta_{24} = 7.1°$. The largest differences to three-flavor oscillations are found at higher energies, but smaller deviations occur also in the energy range essential for this analysis: the peaks in the muon survival probability below 10 GeV are not as pronounced, and the large minimum at about 25 GeV is slightly broadened. Note, however, that the exact shape and magnitude of the effects depend on the mass of the additional sterile neutrino and on the additional mixing angles.

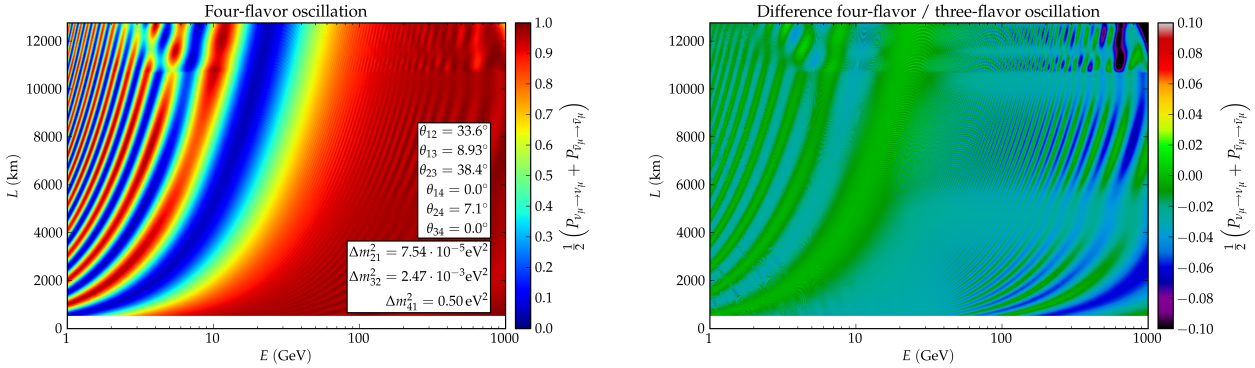

Figure 2.18: Oscillatory pattern of the muon neutrino survival probability $P_{\mu\to\mu}$ as a function of oscillation length L and neutrino energy E, for one additional sterile neutrino with a squared mass difference of $\Delta m^2_{41} = 0.5\,\mathrm{eV}^2$ and an additional mixing angle $\theta_{24} = 7.1°$ (left), and the difference to 3-flavor oscillations as in Figure 2.12 (right). Calculations were made with the tool *nuCraft* [98].

3 The IceCube Neutrino Observatory

The detection of neutrinos is always challenging because of their tiny interaction cross section. Typically, huge volumes have to be instrumented. For the study of atmospheric neutrinos, detectors in the kiloton range are needed [49]; the detection of the much lower fluxes of astrophysical neutrinos requires even larger detectors. The IceCube Neutrino Observatory is the first gigaton neutrino detector and uses about 1 km^3 of the glacial ice sheet at the Geographic South Pole as its detection medium.

[49] T. K. Gaisser. *Cosmic Rays and Particle Physics*. Cambridge University Press, 1990

This chapter explains the underlying detection principles (Section 3.1), presents the event signatures that can be expected for the different neutrino flavors (Section 3.2), and gives an overview of the IceCube detector and its components (Section 3.3).

3.1 Detection Principle

A particularly successful type of neutrino detectors are *water Cherenkov detectors*. They equip large volumes of water with photosensitive devices (typically photomultipliers) to detect Cherenkov light emitted by charged leptons produced in the interaction of a neutrino with a nucleus of the target material. IceCube is a variation of such a detector, in that it uses not liquid water but ice as its detection material, but the underlying detection principle is the same as for conventional water Cherenkov detectors.

3.1.1 Neutrino Interactions

In water Cherenkov detectors, the primary neutrino itself is not detected, but instead the Cherenkov light emitted by secondary particles. Therefore, the basis for the neutrino detection is always a charged- or neutral-current interaction. As described in Section 2.1, the most important processes are the interactions with nucleons by exchange of a $W^{\pm}$ or Z^0 boson:

$$\nu_l + N \to l + X \qquad \text{(CC)} \qquad (3.1)$$

$$\nu_l + N \to \nu_l + X \qquad \text{(NC)} \qquad (3.2)$$

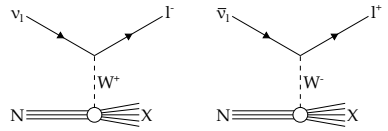

Figure 3.1: Feynman diagrams for a charged-current interaction with a nucleon.

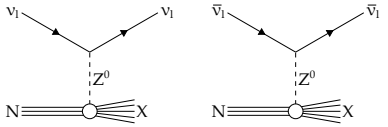

Figure 3.2: Feynman diagrams for a neutral-current interaction with a nucleon.

[36] J. Beringer et al. Review of particle physics. *Phys. Rev. D*, 86:010 001, Jul 2012. DOI: 10.1103/PhysRevD.86.010001

Figure 3.3: Measurements of the total ν_μ CC neutrino-nucleon scattering cross sections for neutrinos and antineutrinos by various accelerator experiments. Note the transition between logarithmic and linear energy scale at 100 GeV! [36]

[78] K. McFarland. Neutrino Interactions (Published in *Neutrinos in Particle Physics, Astrophysics and Cosmology*, CRC Press, 2009). *arXiv:0804.3899 [hep-ex]*, 2008

N denotes a nucleon of the target material, which is destroyed in both cases, and a hadronic cascade X is induced. Figures 3.1 and 3.2 show Feynman diagrams of these interactions (compare also with Figure 2.1).

Figure 3.3 shows the total interaction cross sections for CC interactions of neutrinos and antineutrinos. NC cross sections (not shown) are smaller, but the same considerations apply there. At high energies the cross sections are dominated by deep inelastic scattering, and approximately linear in E_ν. At energies below 100 GeV, targeted by the analysis presented here, other processes like resonant pion production and quasi-elastic scattering come into play and cause the deviation from linearity seen in Figure 3.3 [36]. Also the errors become large, representing a systematic uncertainty that has to be considered (see Section 5.4.1).

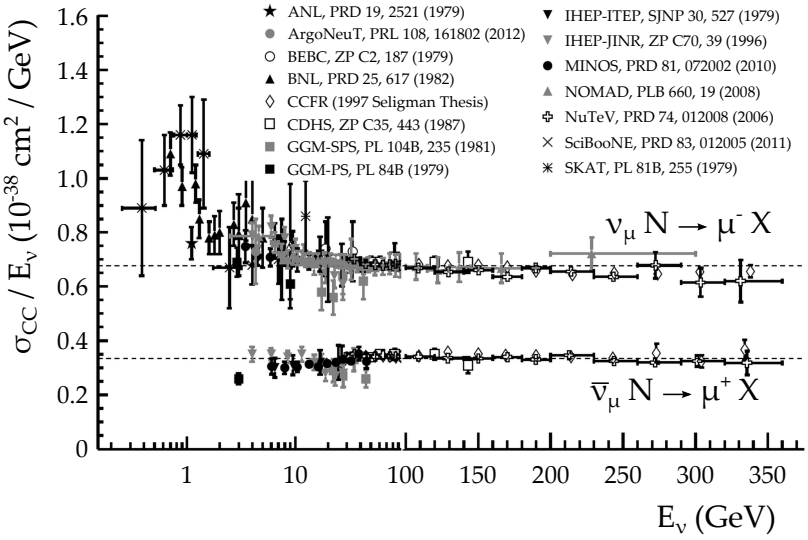

An additional systematic effect is introduced by the fact, that in the nucleon, the momentum carried by quarks is greater than that carried by antiquarks. This causes the differential cross sections for neutrinos and anti-neutrinos to depend differently on the inelasticity y, defined by the scattering angle θ in the center-of-mass system:

$$y = \frac{1}{2}(1 - \cos\theta)\,.$$

Figure 3.4 shows the ν_μ CC cross sections as a function of the inelasticity. For small y, the neutrino and antineutrino cross sections are equal. For larger values of y (larger scattering angles), helicity suppression causes the neutrinos to see only quarks, while the antineutrinos see only antiquarks, which leads to the observed difference in the cross sections [78].

In the laboratory reference frame, the inelasticity is also the fraction of the neutrino energy going into the hadron system:

$$y = \frac{E_{\text{had}}}{E_\nu} = \frac{E_\nu - E_\mu}{E_\nu}\,.$$

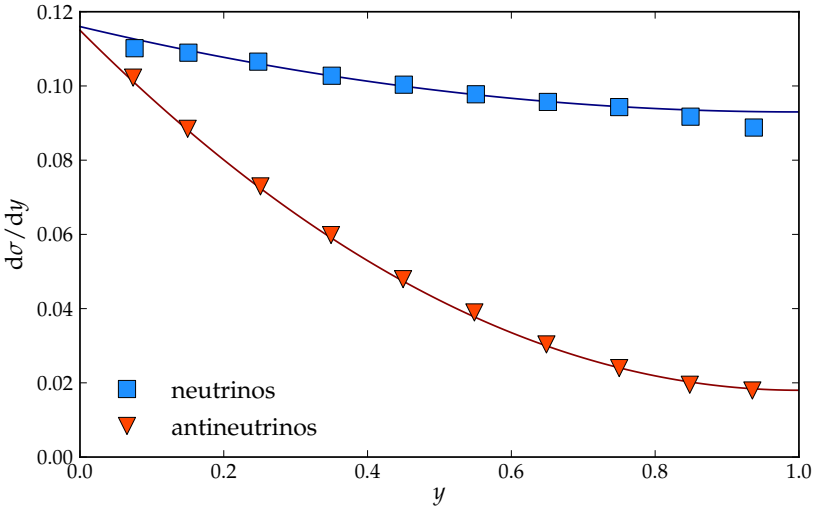

Figure 3.4: Differential ν_μ CC cross sections as a function of the inelasticity [78].

Events with low inelasticity, where most of the energy goes into the muon, appear track-like, whereas events with large y, where most of the energy is transferred to the hadronic cascade, appear more cascade-like. This, in turn, means that an analysis rejecting cascade-like events enriches the contribution from antineutrinos at the same time.

An essential feature of water Cherenkov detectors is their ability to reconstruct the neutrino direction. Although the neutrino itself is not detected, its direction can be inferred from the direction of the lepton, which is correlated to the direction of the neutrino and which can be reconstructed from the detected pattern of Cherenkov light. For muon neutrinos, the angle between the initial neutrino and the muon can be parametrized as [91]

$$\Delta\Psi \approx 0.7^\circ \cdot \left(\frac{E_\nu}{\mathrm{TeV}}\right)^{-0.6} . \tag{3.3}$$

This yields an angular difference of about 2.5° at 100 GeV, increasing to about 10° at 10 GeV.

[91] The ANTARES Collaboration. A Deep Sea Telescope for High-Energy Neutrinos. *arXiv:astro-ph/9907432*, 1999

The charged leptons from CC interactions are not the only particles emitting Cherenkov light. The particles forming the hadronic cascade in both NC and CC interactions do so, as well, which means that also NC interactions of every flavor can be detected. Of particular importance is the Cherenkov light from secondary particles, which are created in energy loss processes of the charged leptons while they propagate through the detection medium. These secondary particles form a halo which encompasses the track of the lepton. Their Cherenkov light yield is of comparable magnitude to that from the initial lepton and is therefore essential for the detection [86]. The energy loss processes in which these secondary particles are created are described in the following section.

[86] L. Rädel and C. Wiebusch. Calculation of the Cherenkov light yield from low energetic secondary particles accompanying high-energy muons in ice and water with Geant4 simulations. *Astroparticle Physics*, 38:53–67, 2012. DOI: 10.1016/j.astropartphys.2012.09.008

3.1.2 ENERGY LOSS OF CHARGED LEPTONS

The dominant energy loss processes differ between the lepton flavors.

MUONS Muons lose their energy gradually and can travel large distances (up to several km in ice) through matter. In a simplified picture, their energy loss can be described by

$$-\frac{1}{\rho}\frac{\mathrm{d}E}{\mathrm{d}x} = a(E) + b(E)\cdot E\,. \tag{3.4}$$

The parameters a and b depend only weakly on the muon energy and can be approximated as constant over a large energy range. They also do not vary strongly between different materials. Typical values are [83]

$$a \approx 2.0\,\frac{\mathrm{MeV\,cm^2}}{\mathrm{g}} \quad \text{and}$$
$$b \approx 3.3\cdot 10^{-6}\,\frac{\mathrm{cm^2}}{\mathrm{g}}\,.$$

[83] PDG. Atomic and nuclear properties of materials: Water. http://pdg.lbl.gov/2013/AtomicNuclearProperties/HTML_PAGES/276.html, accessed 27-September-2013

The parameter a describes the energy loss by ionization, which is a quasi-continuous process and dominates at lower energies. With increasing energy, radiative processes, occurring stochastically along the track, become more and more important. The energy loss caused by these processes is described by b, which itself can be written as [83]

$$b = b_{\mathrm{pair}} + b_{\mathrm{nucl}} + b_{\mathrm{brems}}\,,$$

with the individual contributions from pair production, bremsstrahlung, and photo-nuclear interactions

$$b_{\mathrm{pair}} \approx 1.6\cdot 10^{-6}\,\frac{\mathrm{cm^2}}{\mathrm{g}}\,,$$
$$b_{\mathrm{brems}} \approx 1.2\cdot 10^{-6}\,\frac{\mathrm{cm^2}}{\mathrm{g}}\,, \quad \text{and}$$
$$b_{\mathrm{nucl}} \approx 0.5\cdot 10^{-6}\,\frac{\mathrm{cm^2}}{\mathrm{g}}\,.$$

Figure 3.5 shows the total energy loss for muons according to the parametrization from Equation 3.4, and using the values given above.

The contributions from ionization and radiative processes to the total energy loss are equal at the critical energy $\epsilon = a/b \approx 600\,\mathrm{GeV}$. In the energy range below 100 GeV, where oscillation effects are expected, the muon energy loss is thus dominated by ionization, $-\mathrm{d}E/\rho\mathrm{d}x \approx a$, and the muon track length is proportional to the energy. Solving Equation 3.4 for the mean range of a muon R_μ with energy E_0 yields

$$\begin{aligned} R_\mu(E_0) &= \frac{1}{\rho\cdot b}\cdot \ln\left(\frac{E_0}{\epsilon}+1\right) \\ &\approx \frac{1}{\rho}\frac{E_0}{a} \qquad \text{for small } E_0\,. \end{aligned}$$

A 100 GeV muon leaves a track of roughly 500 m.

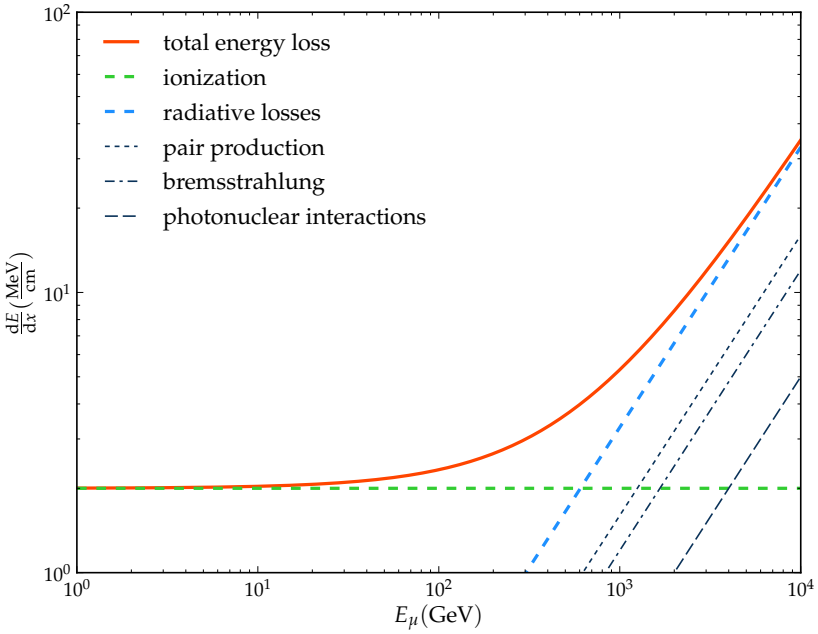

Figure 3.5: Total muon energy loss according to the parametrization from Equation 3.4.

ELECTRONS Electrons lose energy predominantly by bremsstrahlung. The energy loss can be described by

$$-\frac{1}{\rho}\frac{dE}{dx} = \frac{E}{X_0},$$

with the radiation length $X_0 \approx 36.08\,g/cm^2$ for water or ice [36]. In contrast to muons, the complete energy is lost on small distances, resulting in an electromagnetic cascade with a typical extent of a few meters.

[36] J. Beringer et al. Review of particle physics. *Phys. Rev. D*, 86:010 001, Jul 2012. DOI: 10.1103/PhysRevD.86.010001

TAUS Taus could be treated similar to muons if they would not decay almost immediately: The τ lifetime is only $2.91 \cdot 10^{-13}$ s at rest [36]. Only at extremely high energies – far above those of interest for this thesis – the τ is boosted enough to travel a measurable distance, about 50 m at 1 PeV. At lower energies, if the tau lepton decays leptonically into a muon ($BR = 17.4\%$), the muon track might be observed in addition to the hadronic cascade from the CC interaction. In most cases, however, only the overlapping cascades from the initial CC interaction and from the τ decay are observed.

3.1.3 CHERENKOV LIGHT

In addition to the energy loss processes described in the previous sections, all charged particles loose energy continuously by the emission of Cherenkov light. While the actual energy loss (about $850\,eV/cm$) is small compared to the processes described above, the Cherenkov light is the key to the detection and reconstruction of the charged leptons.

The process was first observed by Pavel Cherenkov in 1934 [39]. A theoretical description [47] was worked out by Ilya Frank and Igor Tamm until 1937[1]. According to their theory, the effect occurs when a

[39] P. A. Cherenkov. Visible Radiation Produced by Electrons Moving in a Medium with Velocities Exceeding that of Light. *Phys. Rev.*, 52:378–379, Aug 1937. DOI: 10.1103/PhysRev.52.378

[47] I. Frank and I. Tamm. Coherent visible radiation from fast electrons passing through matter. *C. R. Acad. Sci. USSR*, 14:109–114, 1937

[1] Cherenkov, Frank, and Tamm shared the Nobel Prize 1958 for their discovery.

charged particle moves through a transparent medium with a velocity v greater than the speed of light c/n (with the refractive index n) in that same medium:

$$v \geq \frac{c}{n}, \quad \text{or} \quad \beta = \frac{v}{c} \geq \frac{1}{n}.$$

The atoms of the medium are polarized by the charged particle, and emit light during relaxation. Because of the superluminal speed of the charged particle, this radiation interferes constructively and forms a wavefront of light moving outwards on a cone. Figure 3.6 illustrates the process.

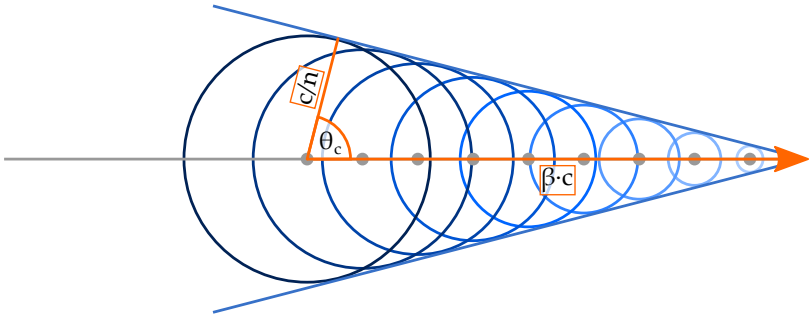

Figure 3.6: Illustration of the emission of Cherenkov light.

The opening angle of the cone depends on the ratio of the speed of the particle and the speed of light in the medium. As can also be seen from Figure 3.6, the *Cherenkov angle* θ_c is given by

$$\cos(\theta_c) = \frac{c/n}{\beta \cdot c} \quad \Leftrightarrow \quad \theta_c = \arccos \frac{1}{n\beta}. \tag{3.5}$$

For highly relativistic particles with $\beta \approx 1$ in water or ice ($n \approx 1.3$), the Cherenkov angle is $\theta_c \approx 41°$. Equation 3.5 also allows to derive the threshold for the production of Cherenkov light:

$$\theta_c \geq 0 \quad \Leftrightarrow \quad \beta \geq \frac{1}{n}.$$

For a particle of mass m this converts to a minimum total energy of

$$E_{\text{min}} = \frac{m}{\sqrt{1 - \frac{1}{n^2}}}.$$

In water or ice, this corresponds to a threshold energy of $E_{\text{min},\mu} \approx 160\,\text{MeV}$ for muons, $E_{\text{min},e} \approx 775\,\text{keV}$ for electrons, and $E_{\text{min},\tau} \approx 2.7\,\text{GeV}$ for tau leptons.

The number of photons produced per length and wavelength interval can be calculated by the Frank-Tamm formula [47]:

$$\frac{\mathrm{d}^2 N}{\mathrm{d}x \mathrm{d}\lambda} = \frac{2\pi\alpha}{\lambda^2} \cdot \left(1 - \frac{1}{n^2\beta^2}\right),$$

where $\alpha \approx 1/137$ is the Sommerfeld fine-structure constant. The intensity of the Cherenkov light grows with decreasing wavelength; most photons are produced in the ultraviolet region. The sensitivity

[47] I. Frank and I. Tamm. Coherent visible radiation from fast electrons passing through matter. *C. R. Acad. Sci. USSR*, 14:109–114, 1937

of PMTs (and the human eye) is typically largest in the blue-to-green wavelength range, which is therefore most important for the detection. In the relevant wavelength range between 300 nm and 500 nm, a muon in ice produces about 250 photons per cm [86].

[86] L. Rädel and C. Wiebusch. Calculation of the Cherenkov light yield from low energetic secondary particles accompanying high-energy muons in ice and water with Geant4 simulations. *Astroparticle Physics*, 38:53–67, 2012. DOI: 10.1016/j.astropartphys.2012.09.008

3.2 EVENT SIGNATURES IN A DETECTOR

For neutrino telescopes in ice or water that are based on a regular grid of photo sensors, different event signatures are observed for different event types (see also Section 3.1.2).

3.2.1 MUON TRACKS

The muons from ν_μ CC interactions leave long tracks in a detector. Figure 3.7 shows an illustration of a muon traveling through a regular lattice of photo sensors and an IceCube event view of a high-energy muon track. Because of the known opening angle of the Cherenkov cone, the direction of the muon can be reconstructed with high precision from the photon arrival times of the hit sensors. The reconstruction of the muon energy is more difficult and the techniques depend on the targeted energy range. As described in Section 3.1.2, the muon energies in the oscillation regime are in the minimum ionizing energy range, where the length of the muon track is proportional to its energy. Consequently, the analysis presented in this thesis uses the reconstructed track length as energy proxy (see Section 5.1). At higher energies the tracks are typically longer than the size of the detector. This means that a significant part of the muon track and therefore of the lost energy is outside the instrumented volume. Since $\langle \mathrm{d}E/\mathrm{d}x \rangle \propto E$, however, the energy can be estimated from measuring $\langle \mathrm{d}E/\mathrm{d}x \rangle$, i.e. the "brightness" of the muon track.

Figure 3.7: Illustration of a muon traveling through a regular lattice of photo sensors (left) and a corresponding IceCube event view (right). The event was found in an IceCube search for a diffuse flux of extragalactic neutrinos [9, 88].

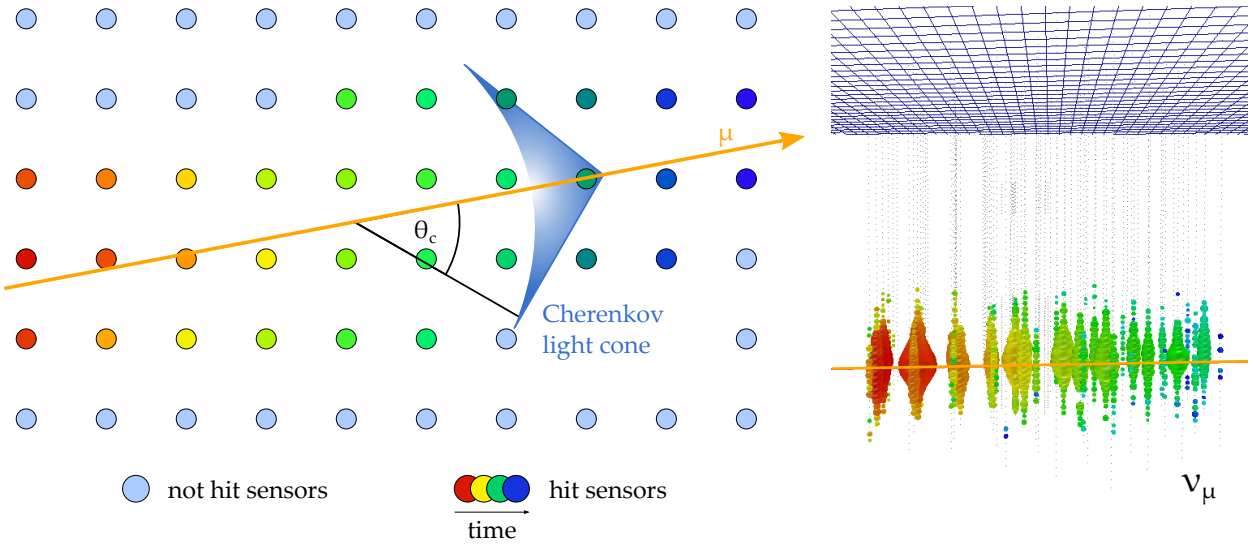

3.2.2 CASCADES

Electrons lose their energy almost instantaneously in an electromagnetic cascade with a size of a few meters. Similarly, neutral-current events of all flavors produce only a hadronic cascade in the initial neutrino interaction. In detectors like IceCube, where the spacing of photo sensors is large compared to the cascade, this results in a light pattern spreading out almost spherically. Figure 3.8 shows an illustration of a cascade in a regular lattice of photo sensors and an IceCube event view of a high-energy cascade.

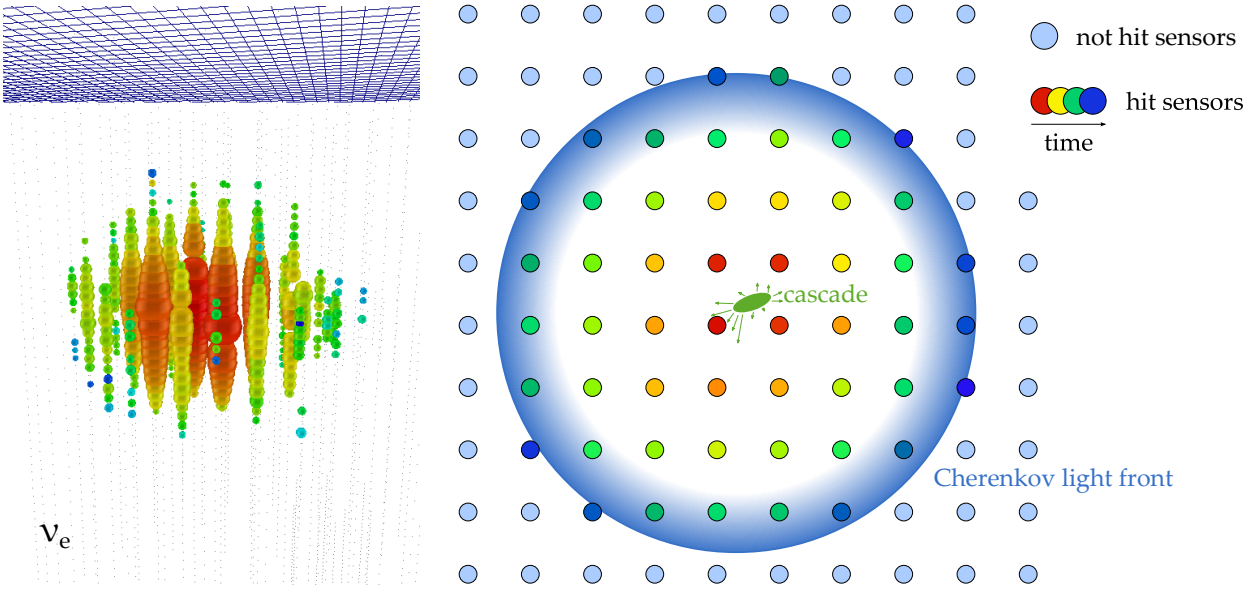

Figure 3.8: Illustration of a cascade in a regular lattice of photo sensors (right) and a corresponding IceCube event view (left). The event was found in an IceCube analysis searching for high-energy neutrino events [2].

The intensity of the Cherenkov light is slightly larger in forward direction. These small deviations from a perfectly spherical light distribution can be used to extract some directional information. For very high energies, resolutions on the order of $\sim 10^\circ$ can be achieved [2]. The energy reconstruction, on the other hand, is more accurate for cascades, which are – unlike muons – often completely contained in the detector.

3.2.3 TAUS

At PeV energies, τ events can exhibit a unique event signature: a hadronic cascade at the initial neutrino interaction, a track from the τ lepton, and another cascade from the decay of the τ. Because of their distinctive shape, these events are called *double bangs*. Figure 3.9 shows an illustration of such an event in a regular lattice of photo sensors and an IceCube event view of a simulated double-bang event. Up to now, no such event has been observed.

However, as already mentioned in Section 3.1.2, the second cascade can not be separated from the first at the energies of the analysis presented here. The two cascades completely overlap, and tau leptons

[2] M. G. Aartsen et al. Evidence for High-Energy Extraterrestrial Neutrinos at the IceCube Detector. *Science*, 342(6161):1242856, 2013. DOI: 10.1126/science.1242856

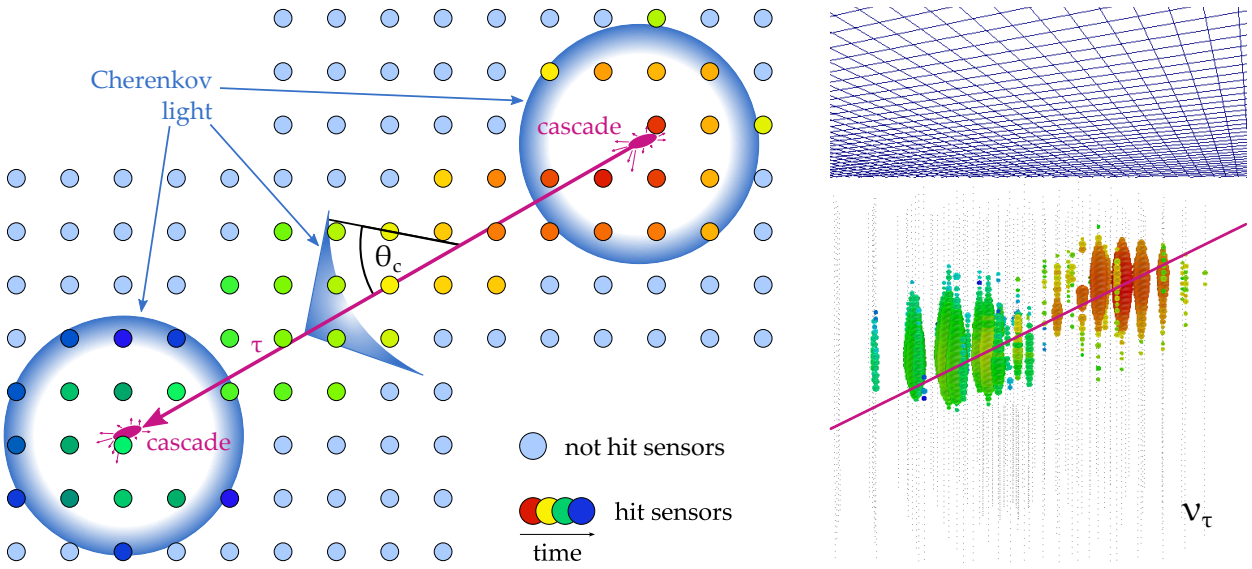

Figure 3.9: Illustration of a high-energy tau event in a regular lattice of photo sensors (left) and a corresponding IceCube event view of a simulated event (right).

appear as single cascades, indistinguishable from electrons or neutral-current events.

It should be noted that the event signatures presented above in Figures 3.7 to 3.9 are ideal cases for high energies. The analysis presented in this thesis operates at the lower energy threshold of IceCube. This introduces an additional challenge, since short muon tracks can appear very similar to cascade events in many respects. Figure 3.10 shows typical event views of a ν_μ, a ν_e, and a ν_τ event with neutrino energies around 50 GeV.

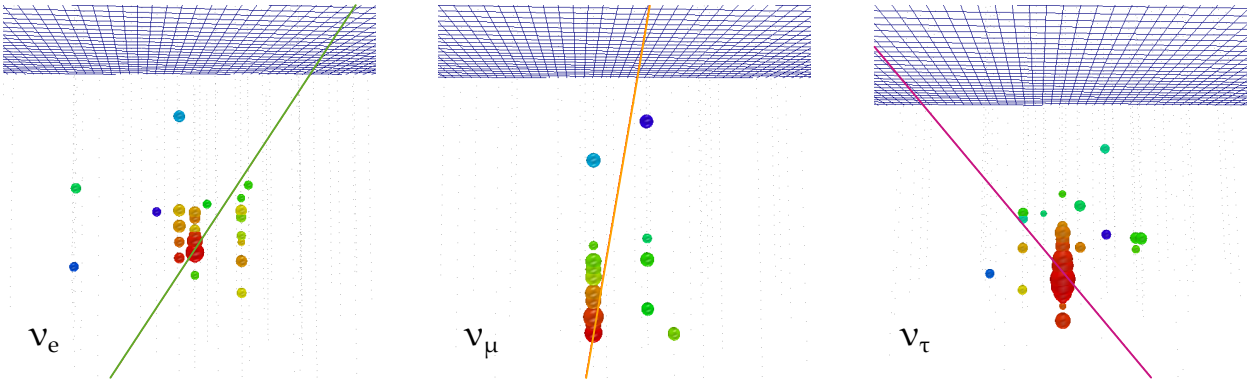

Figure 3.10: Event views of ν_e, ν_μ, and ν_τ events with energies around 50 GeV. Events like this are typical for the analysis presented here.

3.3 ICECUBE

IceCube is currently the world's largest neutrino detector, located at the Amundsen-Scott South Pole station in Antarctica. Figure 3.12 shows a sketch of IceCube and its components. In contrast to traditional water Cherenkov detectors, it utilizes 1 km^3 of the Antarctic ice sheet as its detection medium. All the instrumentation is installed

in depths between 1450 m and 2450 m to shield the detector from atmospheric background as much as possible. The regular grid of photo sensors is established by 5160 so-called *DOMs*[2] on 86 *strings*, forming a 3-dimensional lattice deep in the ice. During construction, the strings were deployed into holes melted in the ice with a hot-water drill. The construction started in 2004 and continued every austral summer until the deployment of the final string on 18 December 2010. The strings, basically km-long cables holding 60 DOMs each, are arranged in a hexagonal pattern with an inter-string distance of 125 m. In the largest part of the detector, the vertical DOM spacing is about 17 m. The very center of the array is instrumented more densely, to allow the detection of lower-energy events. This *DeepCore* sub-array is described in detail in Section 3.3.1.

Because the individual strings function completely independent from the others, IceCube was able to take data already during the years of construction. Figure 3.13 shows the progress of the construction over the years. The data used for this analysis was taken with the 79-string configuration (*IceCube-79*), the last configuration before completion. With IceCube-79, six of eight DeepCore strings were deployed, so DeepCore was largely finished and fully operational for the first time.

Besides the in-ice component, IceCube also includes *IceTop*, an air shower detector on the ice surface. It consists of 81 stations, approximately at the top of each string. A station consists of two tanks at a distance of 10 m from each other, filled with clear ice and equipped with two DOMs each. IceTop serves as a veto and calibration instrument for the in-ice component, but is a full-fledged cosmic-ray detector on its own. The unique combination of IceCube and IceTop – a deep-underground detector measuring the muonic air shower component, and a surface array measuring predominantly the electromagnetic component – allows precision measurements of the cosmic-ray energy spectrum and composition [13].

3.3.1 DEEPCORE

Of particular importance for the analysis presented here is the DeepCore sub-array. The standard string and DOM spacing as described in Section 3.3 provide IceCube with an energy threshold of about 100 GeV. This would prohibit the investigation of atmospheric neutrino oscillations, where all effects are expected below 100 GeV (see Figure 2.12). To lower IceCube's energy threshold, DeepCore was designed and installed. Eight strings with a denser DOM spacing were deployed in between the central regular strings, deviating from the hexagonal grid of the main detector (see Figure 3.13). These strings again hold 60 DOMs, 50 of which are installed with a vertical spacing of only 7 m at depths below 2100 m. The remaining 10 DOMs are placed at shallower depths between 1760 m and 1850 m and have a vertical spacing of 10 m. These DOMs improve the veto against atmospheric muons coming from above. The range in between the

[2] **D**igital **O**ptical **M**odules

[13] R. Abbasi et al. Cosmic ray composition and energy spectrum from 1-30 PeV using the 40-string configuration of IceTop and IceCube. *Astroparticle Physics*, 42:15–32, 2013. DOI: 10.1016/j.astropartphys.2012.11.003

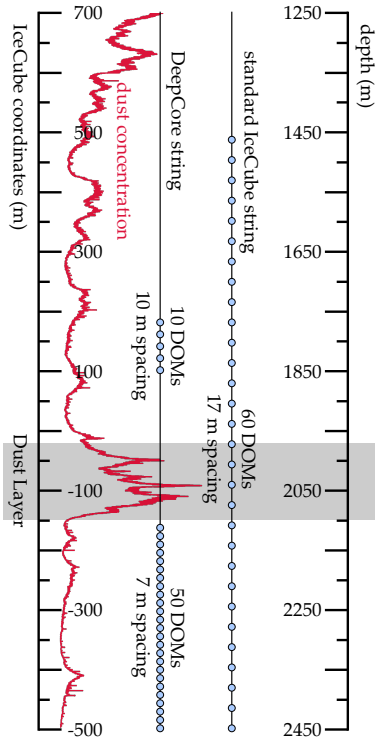

Figure 3.11: Comparison of the standard IceCube and DeepCore string geometries. The red line traces the dust concentration, which strongly influences scattering and absorption of light in the ice (see Section 3.3.2).

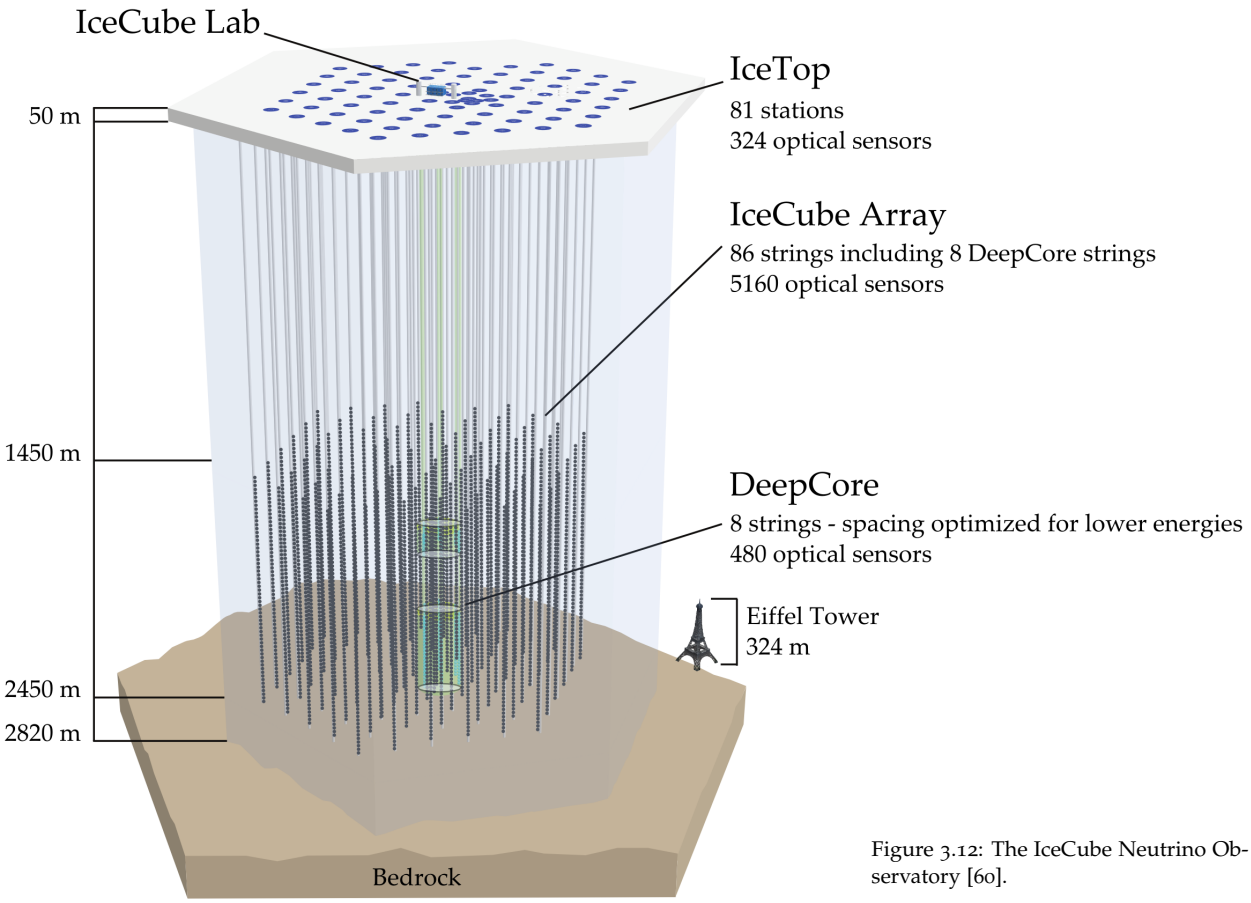

Figure 3.12: The IceCube Neutrino Observatory [60].

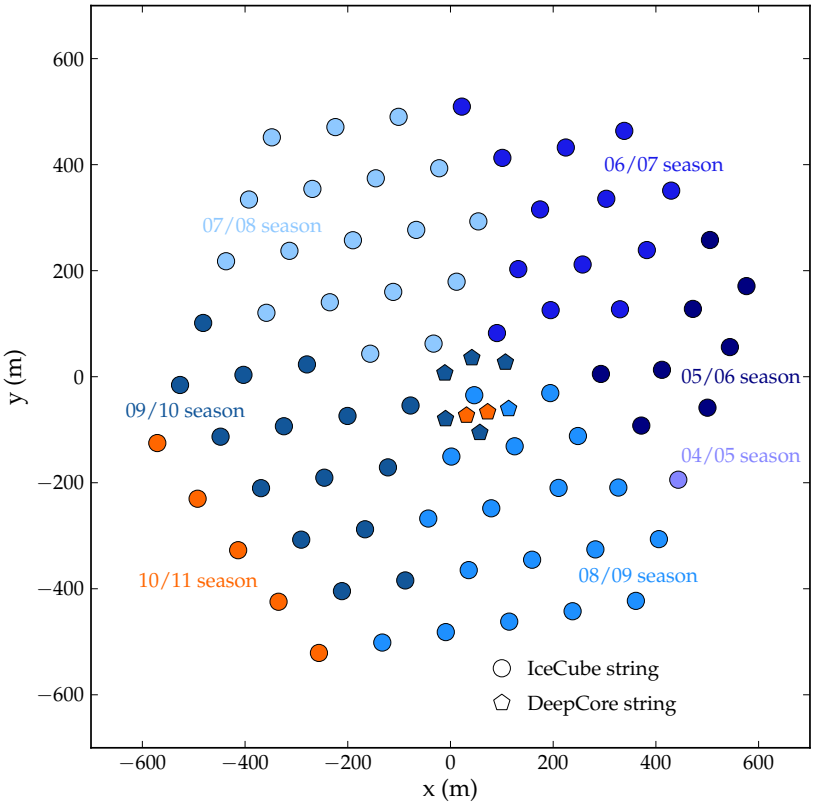

Figure 3.13: IceCube surface geometry, x and y in IceCube coordinates (i.e. centered around a point close to the geometrical center of IceCube). The colors show the progress of construction. The strings marked in shades of blue form IceCube-79, the configuration used in this thesis. The strings marked in orange were deployed in December 2010, after the data used here was taken. The circles denote strings with the standard IceCube string geometry, while the pentagons denote DeepCore strings with their smaller DOM spacing (see also Figure 3.11).

two instrumented areas was left out, because the ice in this region is not as clear as below (see Section 3.3.2). Figure 3.11 visualizes the differences between the DeepCore and standard IceCube strings. The red curve shows the dust concentration, measured in the hole of string 86 in the center of IceCube [8]. In addition to the denser spacing, the DOMs on the DeepCore strings are equipped with photomultiplier tubes (PMTs) with a quantum efficiency about 35% higher [12] than the standard IceCube PMTs [11], to capture as much light as possible from the darker low-energy events.

Altogether, these modifications lower IceCube's energy threshold by an order of magnitude to energies as low as 10 GeV, which permits to study atmospheric neutrino oscillations as in the analysis presented here.

[8] M. G. Aartsen et al. South Pole glacial climate reconstruction from multi-borehole laser particulate stratigraphy. *Journal of Glaciology*, 59:1117–1128, 2013

[12] R. Abbasi et al. The design and performance of IceCube DeepCore. *Astroparticle Physics*, 35(10):615–624, 2012. DOI: 10.1016/j.astropartphys.2012.01.004

[11] R. Abbasi et al. Calibration and characterization of the IceCube photomultiplier tube. *Nucl.Instrum.Meth. A*, 618(1-3):139–152, 2010. DOI: 10.1016/j.nima.2010.03.102

Besides oscillations, DeepCore also provides access to various other physics topics:

- *Dark matter*: To improve IceCube's sensitivity to neutrinos from annihilations of dark matter particles was one of the main considerations that lead to the construction of DeepCore. In particular in the case of a spin-dependent WIMP-proton scattering cross section, IceCube is able to set the most stringent limits (shown in Figure 3.14) in a WIMP mass range down to 35 GeV [7].

[7] M. G. Aartsen et al. Search for Dark Matter Annihilations in the Sun with the 79-String IceCube Detector. *Phys. Rev. Lett.*, 110:131 302, Mar 2013. DOI: 10.1103/PhysRevLett.110.131302

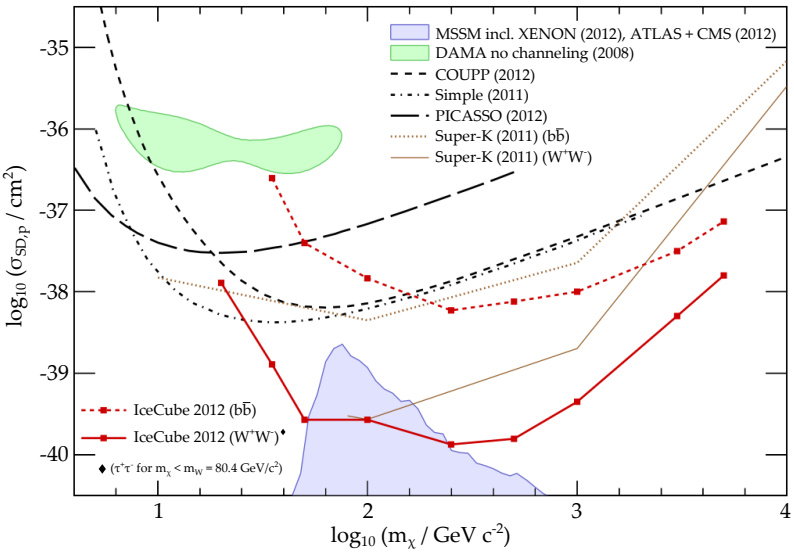

Figure 3.14: Limits on the spin-dependent WIMP-proton scattering cross section [7].

- *Atmospheric neutrinos*: Even besides oscillations, atmospheric neutrinos are an interesting field of research. With DeepCore, IceCube for the first time was able to observe cascades (i.e. ν_e and ν_τ CC interactions and all-flavor NC interactions) induced by atmospheric neutrinos and measure the atmospheric ν_e flux [5], as shown in Figure 3.15.
- *Galactic neutrino sources*: Supernova remnants and pulsar wind nebulae are among the prime candidates for Galactic neutrino

[5] M. G. Aartsen et al. Measurement of the Atmospheric ν_e Flux in IceCube. *Phys. Rev. Lett.*, 110:151 105, Apr 2013. DOI: 10.1103/PhysRevLett.110.151105

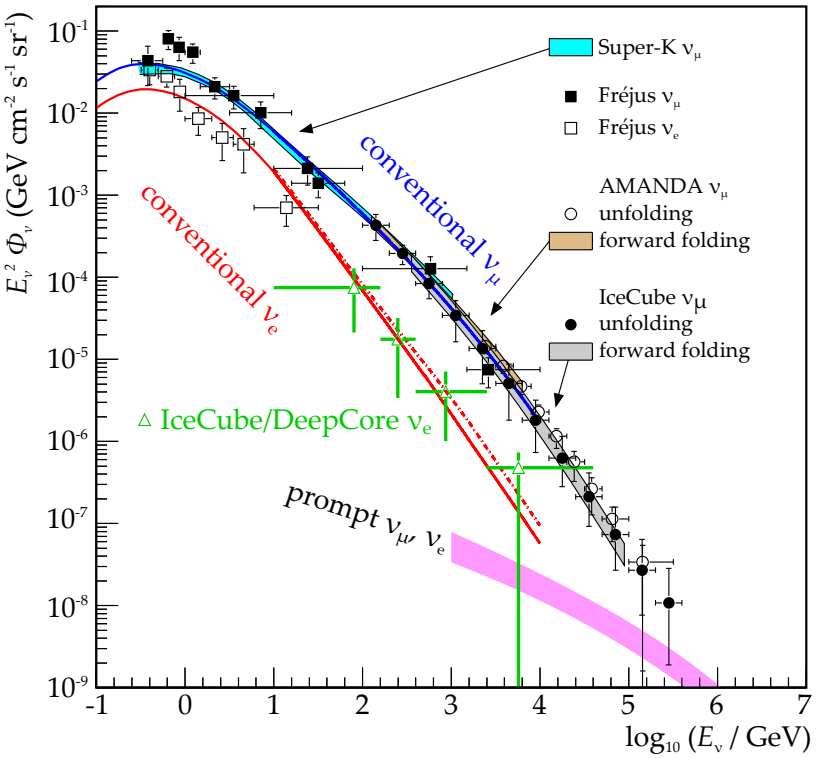

Figure 3.15: Atmospheric neutrino fluxes [5].

sources. Most of them are strong gamma ray sources, and evidence for hadronic acceleration was found at least for the supernova remnants IC 443 [90] and SN 1572 ("Tycho's Supernova") [82]. However, gamma ray measurements of many sources also show a cutoff in the energy spectrum in the TeV range. For neutrinos, this translates to a cutoff at energies even lower by about a factor 2, and therefore possibly in the range around 1 TeV [66]. The sensitivity to these sources is therefore significantly enhanced by a lower energy threshold.

[90] M. Tavani et al. Direct Evidence for Hadronic Cosmic-Ray Acceleration in the Supernova Remnant IC 443. *The Astrophysical Journal Letters*, 710(2):L151, 2010. DOI: 10.1088/2041-8205/710/2/L151

[82] G. Morlino and D. Caprioli. Strong evidence for hadron acceleration in Tycho´s supernova remnant. *A&A*, 538:A81, 2012. DOI: 10.1051/0004-6361/201117855

[66] A. Kappes, J. Hinton, C. Stegmann, and F. A. Aharonian. Potential Neutrino Signals from Galactic Gamma-Ray Sources. *Astrophys.J.*, 656:870–896, 2007. DOI: 10.1086/508936, 10.1086/518161

3.3.2 THE ICE

A unique feature of IceCube is the detection medium: the ice was not produced in a laboratory under controlled conditions, but has naturally grown over tens of thousands of years. As in every glacier, the ice at the South Pole is formed at the surface from compressed snow. Every year, a new layer forms and buries the older layers; the ice at the bottom of IceCube is estimated to be 165 000 years old [85]. In this process, the atmospheric conditions (e. g. temperature or atmospheric dust concentration) at production time are imprinted in properties like crystal structure, isotope composition, or dust concentration of the particular layer. These properties have a large impact on the light propagation through the ice. To know the ice properties throughout the detection volume is therefore a key factor in the understanding of the detector.

[85] P. B. Price, K. Woschnagg, and D. Chirkin. Age vs depth of glacial ice at South Pole. *Geophysical Research Letters*, 27(14):2129–2132, 2000. DOI: 10.1029/2000GL011351

The ice properties are probed by IceCube with the help of *flashers*,

LED light sources installed on each DOM (see Section 3.3.3). These can be flashed with varying brightness and duration. From the response of the surrounding DOMs, the ice properties in between can be deduced. The results are compiled in an *ice model*, describing scattering and absorption in dependence of wavelength and depth.

Figure 3.16 shows the scattering coefficient b_e and the absorptivity a – the reciprocals of effective scattering length λ_e and absorption length λ_a – of the South Pole ice, as determined by the WHAM![3] ice model [19]. The absorption length is defined as the distance after which the survival probability of a photon has dropped to $1/e$; the effective scattering length is given by

$$\lambda_e = \frac{\lambda_s}{1 - \langle \cos\theta \rangle}, \tag{3.6}$$

with θ the scattering angle and λ_s the mean distance between two scattering processes.

[3] **W**ater-**H**ardened **A**bsorption **M**odel

[19] M. Ackermann et al. Optical properties of deep glacial ice at the South Pole. *Journal of Geophysical Research: Atmospheres*, 111(D13), 2006. DOI: 10.1029/2005JD006687

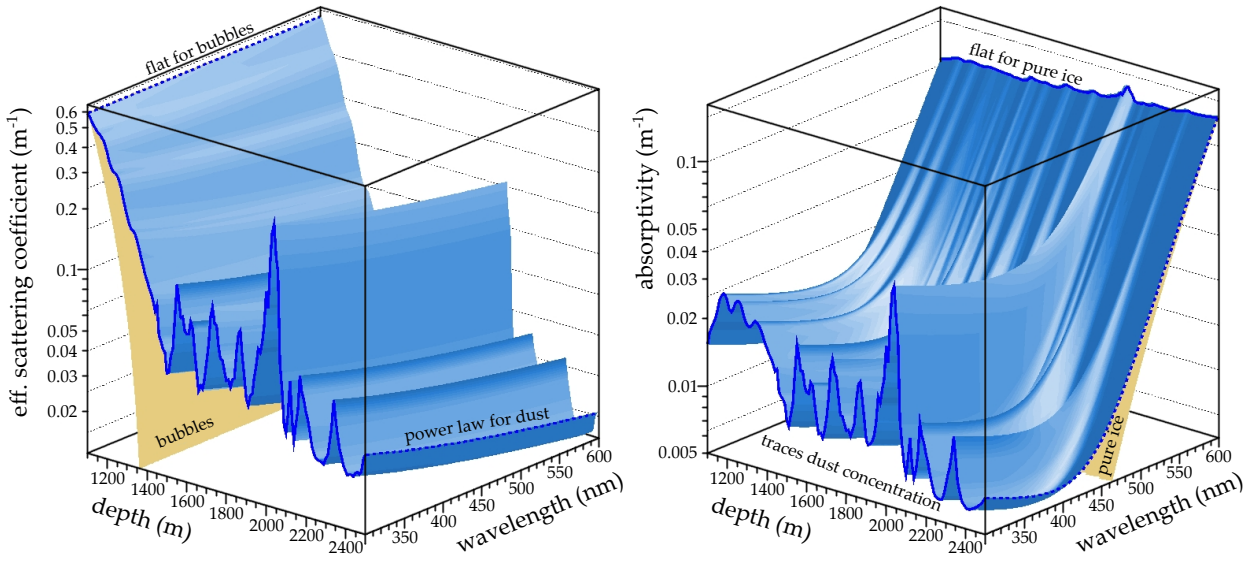

Figure 3.16: Depth and wavelength dependence of scattering and absorption in the ice at the South Pole, as determined by the WHAM! ice model [19].

From Figure 3.16, it is immediately clear that the ice is most transparent for shorter wavelength and at greater depths. Longer wavelengths are more efficiently absorbed by the ice, and at shallower depths, air bubbles in the ice lead to stronger scattering. With increasing depth below $\sim 1300\,\mathrm{m}$, these air bubbles are compressed by the rising pressure until the air molecules are embedded in the ice structure, forming a clathrate compound [19]. In the depth and wavelength range most important for IceCube, scattering and absorption are dominated by the dust concentration. Of particular importance – also for the design of DeepCore (see Section 3.3.1) – is the most prominent dust peak at a depth of about 2050 m, known as "Peak D" or simply "the Dust Layer". Here, scattering and absorption length rise by a factor of $\sim$4 compared to the ice above. The clearest ice in

the detector is found below the Dust Layer – a fact that contributed to the decision to build DeepCore in that region. Typical values for λ_e and λ_a throughout most of the IceCube depth range are

$$\lambda_e \approx 15\,\text{m} - 25\,\text{m}\,, \quad \text{and} \quad \lambda_a \approx 90\,\text{m} - 110\,\text{m}\,,$$

but below the Dust Layer, scattering and absorption length can be as large as $\lambda_e \approx 50\,\text{m}$ and $\lambda_a \approx 200\,\text{m}$.

The baseline ice model for the analysis presented here is not WHAM!, but the SPICEMie[4] model [4]. It fits the ice properties to data obtained with flasher events with a wide range of brightness settings and over all distances in the detector. WHAM!, in contrast, relies only on single-photon data from the DOMs in the same ice layer as the emitter. As a consequence, WHAM! describes the ice as horizontal layers. SPICEMie, on the other hand, allows the layers to be tilted and indeed finds a tilt of up to 100 m in depth over a horizontal distance of 500 m [4].

[4] **S**outh **P**ole **Ice**, "Mie" stands for Mie scattering, which occurs in the ice.

[4] M. G. Aartsen et al. Measurement of South Pole ice transparency with the IceCube LED calibration system. *Nucl.Instrum.Meth. A*, 711:73–89, 2013. DOI: 10.1016/j.nima.2013.01.054

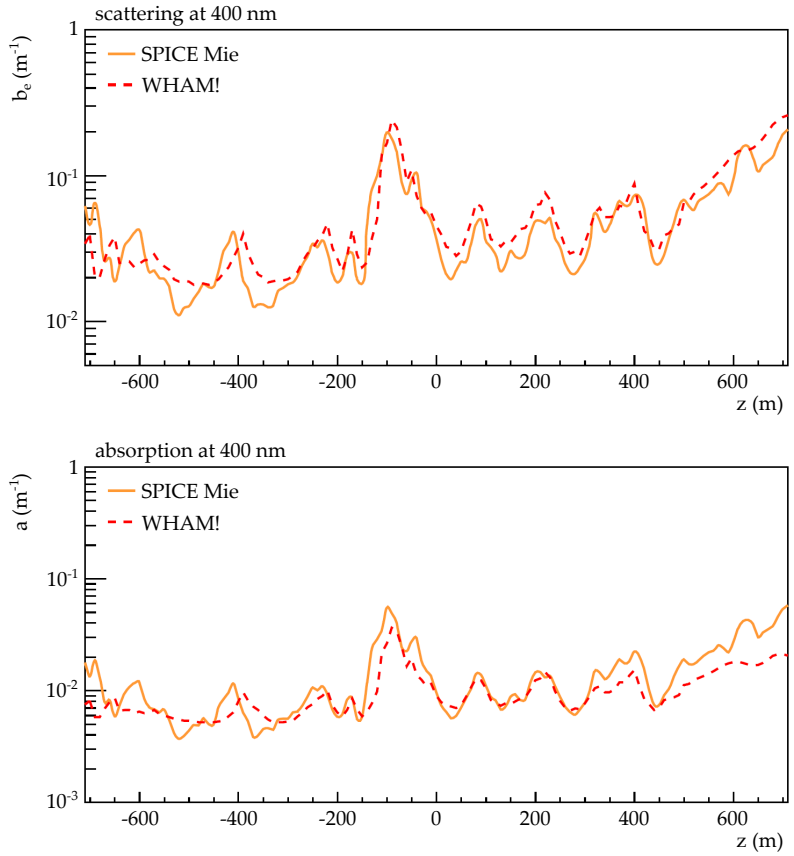

Figure 3.17: Scattering and absorption as a function of depth for the WHAM! and SPICEMie ice models. The depth is shown in detector coordinates, i. e. the center of IceCube is at $z = 0$. The SPICEMie curve is shown for the string in the center of the detector [88].

Figure 3.17 compares the depth profiles of scattering and absorption obtained by the WHAM! and SPICEMie ice models, for a fixed wavelength of 400 nm and at the string in the center of the detector. The overall structure is similar in both models, but appears more pronounced in the SPICEMie model, which also finds a slightly larger scattering coefficient over all depths. Also, the whole structure appears to be vertically stretched in the SPICEMie model. Simulation

produced with SPICEMie has shown better agreement to data in many high-level variables and was therefore chosen as the baseline model by the IceCube collaboration. In the analysis presented here, WHAM! is used to study systematic effects, together with SPICEMie datasets with varied scattering and absorption coefficients.

3.3.3 THE ICECUBE DOM

The Digital Optical Module is the basic building block of IceCube. Each DOM is a fully autonomous module for detection and digitization of light signals [54]. A schematic view is shown in Figure 3.18.

[54] K. Hanson and O. Tarasova. Design and production of the IceCube digital optical module. *Nucl.Instrum.Meth. A*, 567(1):214–217, 2006. DOI: 10.1016/j.nima.2006.05.091

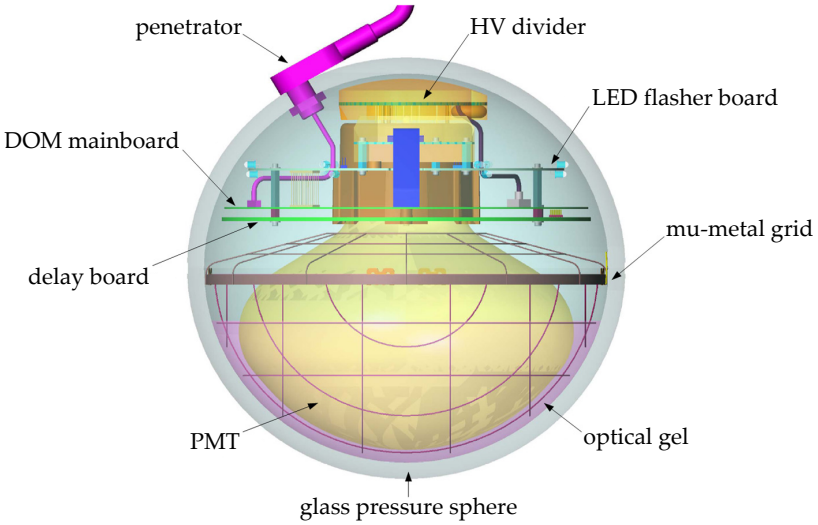

Figure 3.18: Schematic view of the IceCube DOM [10].

Enclosed in a glass pressure sphere, its main component is a large (10 inch) hemispherical 10-stage photomultiplier tube (Hamamatsu R7081-02), with a good time resolution of about 2 ns. The DOMs are sensitive to wavelengths between 350 and 650 nm, with the lower cut-off given by the glass of the pressure sphere [11]. The peak sensitivity is reached at $\sim$ 390 nm, with a quantum efficiency of about 25% for the standard DOMs and 35% for the DeepCore DOMs. The PMT is coupled to the glass sphere by means of an optical gel, in which a mu-metal grid for shielding against magnetic fields is embedded.

[11] R. Abbasi et al. Calibration and characterization of the IceCube photomultiplier tube. *Nucl.Instrum.Meth. A*, 618(1-3):139–152, 2010. DOI: 10.1016/j.nima.2010.03.102

Although all DOMs are installed looking downwards, the acceptance is omnidirectional and increases roughly linearly with the cosine of the zenith angle of the incoming photon, see Figure 3.19. The acceptance is further modified by the *hole ice*, the refrozen ice around the strings. It is expected to have a much shorter scattering length than the surrounding bulk ice, on the order of 50 cm [67]. More scattering would bring more photons from above onto the sensitive area of the PMT and thus increase the sensitivity of the DOM for small $\cos\theta$. The situation, however, is complicated by a newer analysis using a camera system lowered into one of the holes. It found hole ice even clearer than the surrounding bulk ice, but with a possible column of bubbles with very high scattering in the very center of the hole [59].

[67] A. Karle and K. Woschnagg. Hole Ice Studies with YAG data/MC. `http://icecube.berkeley.edu/kurt/interstring/hole-ice/yak.html`

[59] P. O. Hulth. Results from the IceCube video camera system at 2455 meters ice depth. *Proceedings of VLVνT 2013, to be published*

Besides the PMT, each DOM contains a stack of electronics boards:

- The *DOM mainboard* provides readout and digitization of the PMT signals [10]. The main component are two Analog Transient Waveform Digitizer (ATWD) chips, operated in an alternating mode to reduce dead time. They sample the PMT signal in 128 bins of 3.3 ns. To capture PMT signals lasting longer than these 422 ns, an additional Flash Analog-to-Digital Converter (FADC) records the PMT signal over 6.4 µs, albeit with a coarser binning of only 25 ns. The digitized PMT signal is called a *waveform*.
- The *flasher board* contains 12 LEDs, which are used for measuring the ice properties (see Section 3.3.2). Moreover, they are used for precise calibration of the position and timing of the individual DOMs.
- The *HV board* supplies the PMT with the high voltage needed.

The design of the optical modules has proven to be extremely reliable. Of the 5160 modules deployed, 49 – less than 1% – have failed unrecoverably. Most of these failures can be attributed to mechanical stress to the connectors and subsequent breakdown during the freeze-back process. Another 36 DOMs are partly functioning, but have major issues preventing them from normal data taking. In total, more than 98% of the DOMs are working within the specifications and contribute to the data taking [63].

[10] R. Abbasi et al. The IceCube data acquisition system: Signal capture, digitization, and timestamping. *Nucl.Instrum.Meth. A*, 601(3):294–316, 2009. DOI: 10.1016/j.nima.2009.01.001

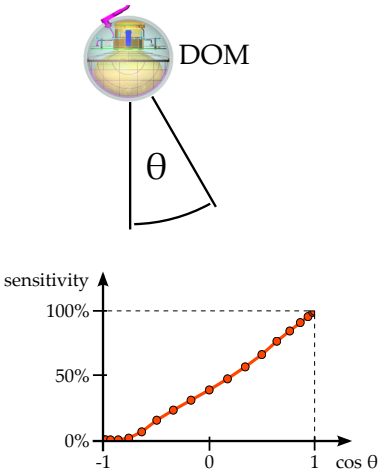

Figure 3.19: Angular acceptance of the IceCube DOM [61].

[63] IceCube wiki. Problem DOMs. https://wiki.icecube.wisc.edu/index.php?title=Problem_DOMs&oldid=204056, accessed 28-September-2013

3.3.4 LOCAL COINCIDENCES

A DOM with a signal is called a *hit DOM*, or simply a *hit*. To reduce the data volume, not every hit is provided with the full amount of information. The complete waveform from ATWD and FADC is stored only for hits with at least one other hit within 1 µs in the two adjacent DOMs below or the two DOMs above [10]. These hits are called *Hard Local Coincidences* (HLC).

The low-temperature environment of IceCube efficiently reduces thermal PMT noise; after the freeze-back the DOMs have a relatively low noise rate of about 650 Hz. In IceCube, the dominant source of noise is the decay of radioactive isotopes producing light in the glass of the pressure sphere of the DOMs. Isolated hits without neighbors are much more likely caused by PMT noise than by a light-emitting particle passing by. These isolated hits are called *Soft Local Coincidences* (SLC). Only a time stamp and three bins (the bin with the highest amplitude and its neighbors) out of the FADC waveform are stored for these [10].

For IceCube events with a typical length of 10 µs, HLC hits contain essentially no noise hits. Contrary to those, the vast majority (typically more than 90%) of the SLC hits are due to noise. Nonetheless, SLC hits are of supreme importance for low-energy analyses:

- Low-energy events produce few hits anyway. Often the amount of information in the HLC hits is not sufficient for a precise reconstruction – or not for any reconstruction at all. Those SLC

[10] R. Abbasi et al. The IceCube data acquisition system: Signal capture, digitization, and timestamping. *Nucl.Instrum.Meth. A*, 601(3):294–316, 2009. DOI: 10.1016/j.nima.2009.01.001

hits that are not caused by noise can be vital for identifying and reconstructing these events.

- Low-energy analyses often rely on veto techniques to reject atmospheric background (see Section 4.5). Dim muons can penetrate deep into the fiducial volume without producing HLC hits on the outer layers of IceCube. They often leave SLC hits, though, which are therefore crucial to identify those events as atmospheric muons and reject them.

To discern the SLC hits caused by a light-emitting particle from those caused by noise is a major challenge of low-energy analyses. Section 4.6 revisits this topic in more detail.

3.3.5 EVENT BUILDING

The signals of all DOMs are collected and processed in the *IceCube Lab*, a building on the ice surface. Since the detector cannot be read out continuously, a recorded event has to fulfill one out of several trigger conditions. IceCube's main trigger condition is a *Simple Multiplicity Trigger* with a threshold of 8 (SMT8), which requires 8 hits within a time interval of 5 µs. Additionally, all of these have to be HLC hits [12]. For the detection of low-energy neutrinos, a low trigger threshold is needed. For DeepCore, an additional SMT3 trigger was put into operation, a variant of the SMT8 trigger which requires only 3 HLC hits within 2.5 µs and is run only on the lower 50 DOMs of the DeepCore strings and the lower 22 DOMs of the 7 adjacent standard IceCube strings [12]. There are other triggers dedicated to low-energy events, for example the *string trigger*, which requires at least 5 DOMs out of a series of 7 on one string to be hit within a time window of 1.5 µs [87]. For the analysis presented here, however, only the SMT3 trigger is relevant.

[12] R. Abbasi et al. The design and performance of IceCube DeepCore. *Astroparticle Physics*, 35(10):615–624, 2012. DOI: 10.1016/j.astropartphys.2012.01.004

[87] C. Rott, P. Toale, D. Grant, and V. Viscomi. String Trigger Proposal. *IceCube internal document*, 2008

If any trigger condition is fulfilled, the complete detector is read out. The length of the read-out window depends on the trigger; for the DeepCore SMT3 trigger it is $[-4\,\mu s, +6\,\mu s]$ around the initial trigger time, which is identical to the time of the hit that activated the trigger (i.e. the third HLC hit in DeepCore). If the trigger condition is fulfilled again within the read-out window, it is prolonged until 6 µs after the last trigger. The so obtained time slice is stored as one *event*.

A significant fraction of these time slices contains hits from two or more unrelated particles, which happen to pass through the detector at the same time; these events are called *coincident events*. Later in the data processing, algorithms are applied to identify them (e.g. *topological trigger* [40], see also Section 4.11). These algorithms can split the events into sub-events, which allows to treat them individually from there on.

[40] D. Chirkin. Neutrino search with IceCube. *IceCube internal report*, icecube/200807006, 2008

A BOTTLENECK in the processing of IceCube data is the transmission from the South Pole to the North: all data has to be transferred via satellite. The bandwidth is limited to roughly 100 GB per day

(80 GB/d for the time the data used in this thesis was recorded), which makes a rigorous preselection of the triggered events necessary. This is done by several filter algorithms, each dedicated to a particular physics topic [65]. For this analysis, only the *DeepCore filter* is used, which applies a simple veto algorithm to reject the largest part of the atmospheric muon background while keeping almost all neutrino events. A detailed description of the DeepCore filter is given in Section 4.8.

[65] IceCube wiki. TFT 2010 Season Planning. https://wiki.icecube.wisc.edu/index.php?title=TFT_2010_Season_Planning%&oldid=122189, accessed 02-October-2013

4 Data selection

At the beginning of every IceCube analysis stands the data selection. Since IceCube is a multi-purpose detector, the bulk of events recorded is not of interest for any particular analysis. The signal of one analysis can be the background for another one. The data selection faces the challenge to reject the background well enough to get a sufficiently pure signal sample, while keeping as much of the desired signal as possible.

Section 4.1 defines signal and backgrounds for this analysis. The following section explains the way in which the required simulated datasets are generated. Section 4.4 and 4.3 presents the simulated atmospheric muon dataset used here and the experimental data sample. Section 4.5 describes the general strategy of the data selection, while Sections 4.8 to 4.14 take a tour through its individual steps. In Sections 4.6 and 4.7 crucial techniques used in the data selection are explained.

4.1 Signal and background

signal This analysis searches for the disappearance of atmospheric muon neutrinos. Consequently, the data selection is designed to keep low-energy muon tracks from charged-current ν_μ interactions. In the energy range between 10 GeV and 100 GeV, the oscillation length for maximum disappearance must be several thousand km (see Figure 2.12). Only events moving upwards through the detector (*up-going* events) have been traveling through a large part of the Earth and are therefore of interest for this analysis.

background The primary background for this analysis (as for most IceCube analyses) are muons from cosmic-ray air showers. They make up by far the most abundant signal recorded in IceCube. The overall IceCube trigger rate (for IceCube-79) is about 1900 Hz [12], about 6 orders of magnitude above the neutrino interaction rate in the detector.

The other source of background are cascade events produced by ν_e, ν_τ, and all-flavor neutral-current interactions.

[12] R. Abbasi et al. The design and performance of IceCube DeepCore. *Astroparticle Physics*, 35(10):615–624, 2012. DOI: 10.1016/j.astropartphys.2012.01.004

4.2 SIMULATION

This analysis relies on a comparison of experimental to simulated data (see Chapter 5). Moreover, the complete data selection has been developed mostly with simulated data. Therefore, an accurate simulation of the whole detection process, from the neutrino generation in the atmosphere to its interaction to the trigger logic, is of high importance.

4.2.1 PARTICLE GENERATION

The simulation chain starts with the generation of the initial particle, either a neutrino or a muon from a cosmic-ray air shower. Different software programs are used, depending on the particle type.

ν_μ AND ν_e SIMULATION The ν_μ and ν_e are generated and propagated through the Earth by the program *Neutrino Generator* (NuGen), developed within the IceCube collaboration [52]. Because of the small interaction cross sections, most neutrinos pass through the detector without interacting. To allow the generation of sufficient amount of simulated data within a reasonable time, all simulated neutrinos are forced to interact within a volume somewhat larger than the actual detector. The probability of the interaction is stored as a weight for that particular event. The energy range of the NuGen datasets used in this analysis is 10 GeV to 1 EeV. The lower threshold is determined by the cross sections implemented in NuGen: because the program was originally developed for higher neutrino energies, the implemented cross sections stop at 10 GeV. Figure 4.1 shows the ν_μ cross section for the interaction with an oxygen target as implemented in NuGen (ANIS[1]) and GENIE[2], another neutrino generator software [34], together with measurements by various experiments. ANIS includes only deep inelastic scattering cross sections, which introduces an error at lower energies (see Section 3.1.1). GENIE, on the other hand, uses a mixture of theoretical predictions and tuning to match the measured data. At the lowest energies, the discrepancy between the ANIS cross sections used in NuGen and the GENIE cross sections adds up to almost 15%. For the NuGen ν_μ datasets used in this analysis, a correction is applied that matches the NuGen cross sections below 100 GeV to the ones of GENIE, also for NC interactions. The same problem exists also for the ν_e datasets, but a similar correction is not available, introducing a systematic uncertainty.

The simulated energy spectrum of the neutrino datasets used in this analysis is $\propto E^{-2}$, but since the interaction probability is stored as a weight, the datasets can be reweighted to any desired spectrum. For this analysis, all neutrino datasets are reweighted to an atmospheric spectrum according to the model by Honda et al. [56] (see Section 2.2).

ν_τ SIMULATION While the accuracy of the ν_μ and ν_e cross sections implemented in NuGen only gradually degrades below 100 GeV, its

[52] A. Gazizov and M. P. Kowalski. ANIS: High energy neutrino generator for neutrino telescopes. *Comput.Phys.Commun.*, 172:203–213, 2005. DOI: 10.1016/j.cpc.2005.03.113

[1] **A**ll **N**eutrino **I**nteraction **S**imulation
[2] **G**enerates **E**vents for **N**eutrino **I**nteraction **E**xperiments

[34] C. Andreopoulos, A. Bell, D. Bhattacharya, F. Cavanna, J. Dobson et al. The GENIE Neutrino Monte Carlo Generator. *Nucl.Instrum.Meth. A*, 614:87–104, 2010. DOI: 10.1016/j.nima.2009.12.009

[56] M. Honda, T. Kajita, K. Kasahara, S. Midorikawa, and T. Sanuki. Calculation of atmospheric neutrino flux using the interaction model calibrated with atmospheric muon data. *Phys. Rev. D*, 75:043 006, Feb 2007. DOI: 10.1103/PhysRevD.75.043006

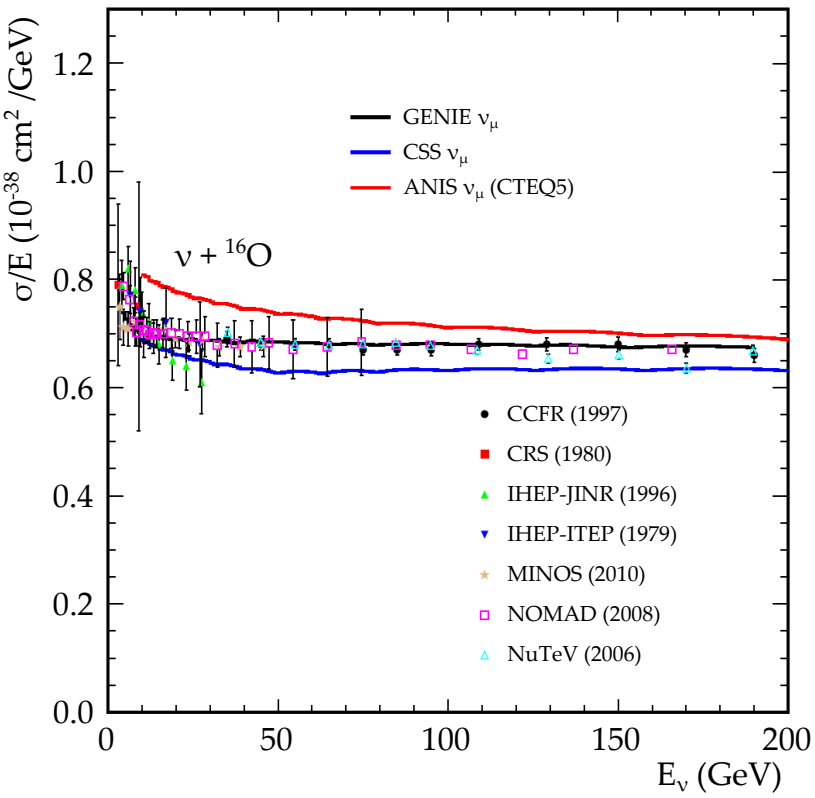

Figure 4.1: Total ν_μ cross section for a CC interaction with a ^{16}O target, as implemented in ANIS (red) and GENIE (black) and the prediction by the CSS model (blue), together with measurements by various experiments.

ν_τ cross sections are valid only above several hundred GeV. For this analysis, where ν_τ events are expected only at the lowest energies up to $\sim 100\,\text{GeV}$, the existing NuGen ν_τ datasets are thus not usable. Instead, the ν_τ datasets are simulated using the already mentioned software GENIE. The energy range of the ν_τ datasets used is $1 - 190\,\text{GeV}$. GENIE, too, produces an E^{-2} spectrum, but the same reweighting procedure as in the NuGen case is applied. The ν_τ datasets are weighted to the expectation from appearance due to oscillations, assuming the Honda model.

ATMOSPHERIC MUON SIMULATION For the simulation of muons from cosmic-ray air showers, the CORSIKA[3] program [55] is used. It simulates the full air shower, beginning with the primary cosmic-ray particle and its interaction with an air molecule. The simulated chemical composition and energy spectrum of the primary particles are based on the model by Hörandel [57].

[3] **Co**smic **R**ay **Si**mulations for **Ka**scade

[55] D. Heck, G. Schatz, T. Thouw, J. Knapp, and J. Capdevielle. CORSIKA: A Monte Carlo code to simulate extensive air showers. *FZKA Report*, 6019, 1998

[57] J. R. Hörandel. On the knee in the energy spectrum of cosmic rays. *Astroparticle Physics*, 19(2):193–220, 2003. DOI: 10.1016/S0927-6505(02)00198-6

4.2.2 PROPAGATION

From this step on, the simulation chain is the same for all types of simulation.

LEPTON PROPAGATION The output of the generators described above is always a hadronic cascade and (in case of a CC interaction) one or more charged leptons. These are then propagated through

the ice by the program *MMC*[4] [42]. It simulates stochastic energy losses along the lepton path according to the energy loss processes described in Section 3.1.2 and generates secondary particles.

PHOTON GENERATION AND PROPAGATION The particles generated by MMC (the primary lepton and its secondary particles) all produce photons along their trajectories, and so does the hadronic cascade from the neutrino interaction. The program *PPC*[5] [4] generates these photons and propagates them individually through the ice until they are absorbed or detected by one of the DOMs. In this process, the depth-dependent scattering and absorption properties of the ice are taken into account (see Section 3.3.2).

4.2.3 DETECTOR SIMULATION

The last step is the simulation of the detector hardware. For all photons that hit a DOM, the PMT response is simulated, as well as the digitization. Random noise is added. Finally, the full trigger logic is applied.

FROM HERE ON, simulated and experimental data can be treated consistently and by the same software.

4.3 THE EXPERIMENTAL DATA SAMPLE

The experimental dataset at the basis of this analysis was recorded by IceCube-79 between May 31, 2010 and May 13, 2011. IceCube's data taking is subdivided in *runs* with a duration of up to 8 hours. Not all runs are dedicated to normal data taking; they can for example be used to test new software in the filtering chain, or to probe the ice properties with flashers (see Section 3.3.3). These runs are removed from the analysis. Also standard runs can have issues which makes it necessary to remove them, e.g. when parts of the detector malfunction and individual strings or DOMs no longer take data. For a small fraction of the runs, the DeepCore filter (which was mentioned briefly in Section 3.3.5 and will be explained in detail in Section 4.8) shows a strongly deviating rate. If the reason cannot be determined, these runs are also removed. After removal of all these runs, the remaining data sample has a livetime of 312.3 days. Figure 4.2 shows the event rate after the DeepCore filter for all runs which survived the cleaning. The annual variation, caused by seasonal changes of the atmospheric conditions, is clearly visible, but no run deviates strongly in rate.

4.4 THE SIMULATED ATMOSPHERIC MUON DATASET

The generation of the simulated datasets is done centrally in the IceCube collaboration, since it is computationally expensive in terms of both CPU time and storage space needed. Above all, this is true for the atmospheric muon datasets. Because of the high rate of atmospheric

[4] **M**uon **M**onte **C**arlo

[42] D. Chirkin and W. Rhode. Propagating leptons through matter with Muon Monte Carlo (MMC). *arXiv:hep-ph/0407075*, 2004

[5] **p**hoton **p**ropagation **c**ode

[4] M. G. Aartsen et al. Measurement of South Pole ice transparency with the IceCube LED calibration system. *Nucl.Instrum.Meth. A*, 711:73–89, 2013. DOI: 10.1016/j.nima.2013.01.054

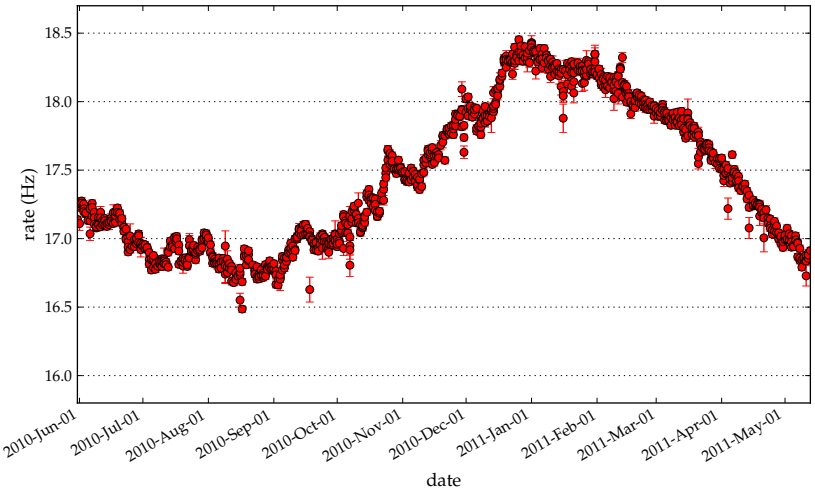

Figure 4.2: Event rate per run as a function of date. Shown is the rate after the DeepCore filter (see Section 4.8).

muons in IceCube (the overall trigger rate is about 1.9 kHz [12]), huge amounts of events need to be generated to describe the detector for a reasonable amount of time. The statistics of the dataset used in this analysis correspond to a livetime of about 11 days, far less than the experimental livetime of 312 days. On the final cut level, only 69 events are left.

[12] R. Abbasi et al. The design and performance of IceCube DeepCore. *Astroparticle Physics*, 35(10):615–624, 2012. DOI: 10.1016/j.astropartphys.2012.01.004

An important parameter in the simulation is the optical efficiency, which describes the amount of light recorded from an event of a certain energy (see Section 5.4.2). During the course of this thesis, the IceCube collaboration decided to switch the default value of the optical efficiency from 100% (in arbitrary units) to 110%. For the computational reasons explained above, replacing high-statistics datasets is a major effort. While the neutrino datasets were replaced with new datasets of equal statistics, the atmospheric muon dataset was not. A dataset with statistics lower by an order of magnitude is available for testing purposes, but it cannot be used for the actual oscillation parameter fit.

Because the optical efficiency strongly impacts the veto efficiency, this probably leads to an overestimation of the atmospheric muon rate on the final cut level (see Section 5.4.2). In fact, the problem of low statistics of the atmospheric muon simulation concerns all the discrete systematics datasets described in Section 5.4.2. Test datasets with low statistics are generally available, but the only dataset with sufficient statistics to be used in the fitting procedure is the one simulated with default parameters (apart from the optical efficiency). Thus, only this single atmospheric muon dataset is used throughout this analysis.

4.5 THE VETO APPROACH

The rejection of the muon background is a prime challenge of this analysis. Although all of these events come from above the detector (*down-going* events), and are therefore fundamentally different from the up-going signal events as defined in Section 4.1, the reconstructed

direction is not a sufficient criterion to reject them: the finite reconstruction accuracy causes a small fraction of these down-going events to be reconstructed as up-going, but because of the high muon rate, this fraction still dwarfs any neutrino signal. This is true especially for analyses working at the detection threshold: low-energy events, which produce only a small number of hits, relatively often provide too sparse information to the reconstruction algorithms to allow an unambiguous reconstruction.

Usually in IceCube this challenge is met by selecting only events reconstructed as up-going and then cutting on track reconstruction quality parameters. Atmospheric muons with an up-going reconstruction are misreconstructed by definition, and usually have a low reconstruction quality. Figure 4.3 shows an example of such a quality parameter, *rLogL*, the reduced log-likelihood of the track fit, for ν_μ events and atmospheric muons. A cut on the reconstructed direction has been applied before, i.e. the histograms contain only events reconstructed as up-going. A cut at rLogL = 7.5 removes essentially the complete muon background, and still keeps about 10% of the ν_μ events.

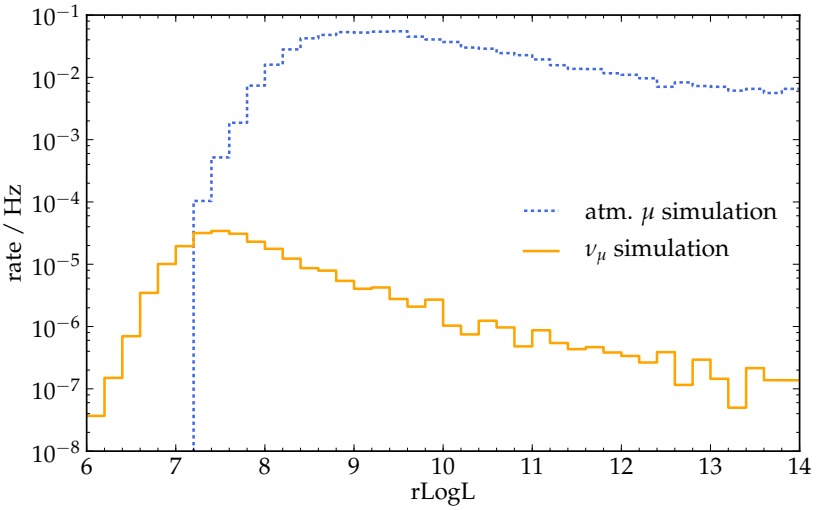

Figure 4.3: Distribution of reconstruction quality parameter rLogL, for ν_μ events (yellow, solid) and atmospheric muons (blue, dashed). The histograms contain only events reconstructed as up-going.

The problem with this approach is that most of these quality parameters are strongly correlated with the neutrino energy and/or zenith direction. Figure 4.4 shows the correlation of rLogL with the neutrino energy. This correlation can be understood, since – as mentioned earlier – higher-energy events are easier to reconstruct, leading to "better" values in the reconstruction quality parameters. Cuts on these parameters therefore introduce (in the best case) selection biases on the zenith angle and energy distributions of the retained event sample. The analysis presented here is based on a comparison of the experimental and simulated zenith angle and energy distributions (see Chapter 5), and the biases in the experimental data have thus to be modeled very accurately by the simulation. Differences between experimental and simulated data can easily distort the results.

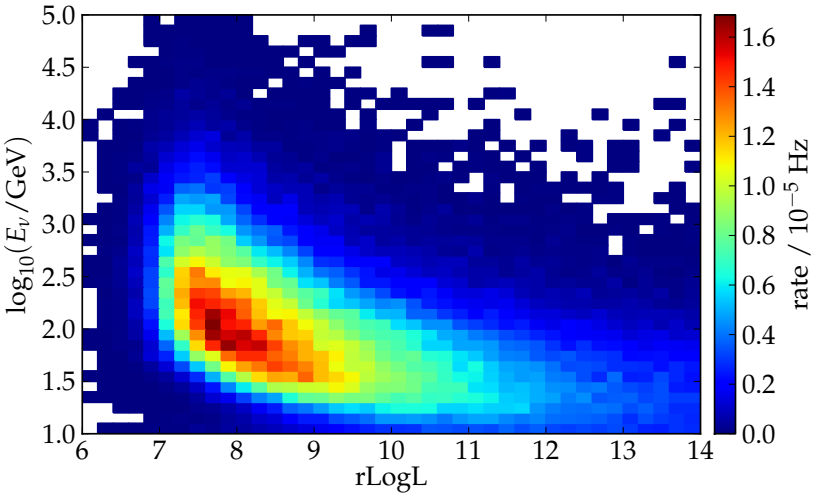

Figure 4.4: Correlation of rLogL with neutrino energy.

In the worst case, cuts on track reconstruction quality parameters simply cut away the largest part of the desired signal. In the example given above, a cut on rLogL $= 7.5$ reduces the muon background by 5 orders of magnitude. It keeps 10% of the ν_μ events, but exclusively at higher energies. Below 100 GeV, where oscillation effects are expected, 6 orders of magnitude of the neutrino signal are removed.

For this analysis, a different approach has been developed. It uses the outer layers of IceCube as a veto to search for *starting events*. Atmospheric muons always enter the fiducial volume from the outside, which implicates the possibility to produce hits in the outer layers they pass through. An event clearly starting inside the fiducial volume, on the other hand, is an unambiguous signature for a neutrino interaction. Figure 4.5 illustrates this principle.

At the same time, the probability of a neutrino interaction to happen inside or outside the fiducial volume does not depend on the neutrino energy or zenith angle at all. Because the fiducial volume features a higher instrumentation density (see Section 3.3.1) and a lower trigger threshold (see Section 3.3.5) than the rest of the detector, however, the probability to *detect* a neutrino interaction is the highest here. Figure 4.6 shows the spatial distribution of the neutrino vertices for the ν_μ events passing the DeepCore filter. The plot shows approximately the entire detector, its center is at (0,0). The accumulation of events within DeepCore is obvious. By definition, the vertices of atmospheric muon events are located far outside the detector. A veto-based data selection makes it possible to exploit this information and can potentially achieve more unbiased distributions of energy and zenith angle while maximizing the fraction of kept low-energy events.

Cascade events – the other type of background – are not as numerous as the CC ν_μ signal events, but they cannot be rejected by veto methods, since they constitute starting neutrino events themselves.

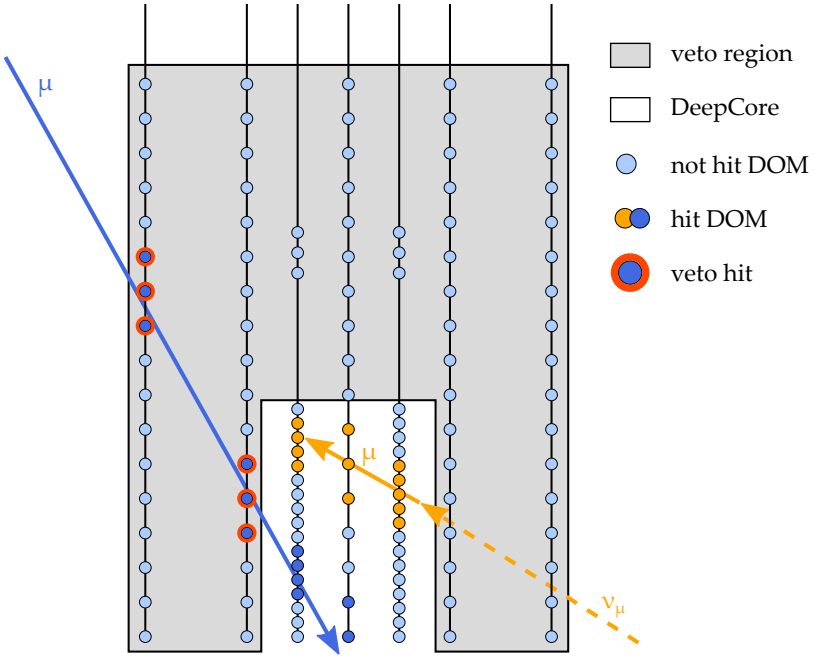

Figure 4.5: The veto idea: atmospheric muons always enter the detection volume from the outside and are therefore prone to produce hits on the outer strings of IceCube. Neutrino events, on the contrary, can start deep inside the detection volume.

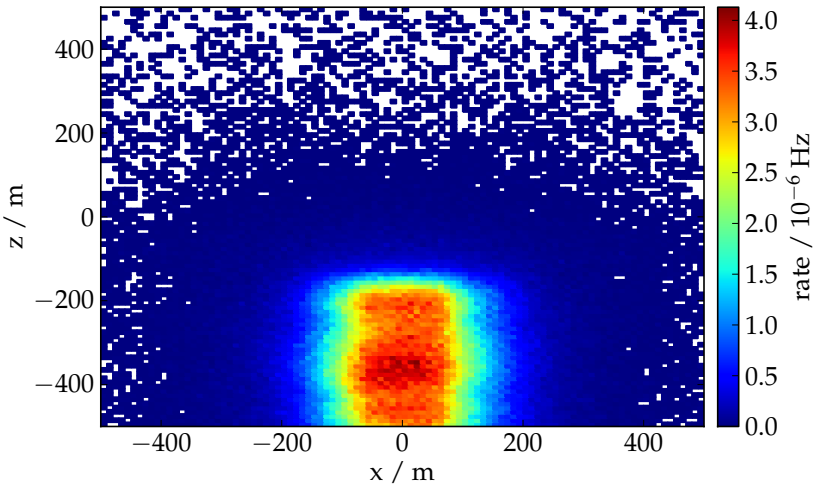

Figure 4.6: Spatial distribution of the neutrino vertices in the detector, for all events passing the DeepCore filter. Shown is the projection onto the xz-plane. The plotting range is adjusted to the approximate size of the detector. Its center is at (0,0).

Because of their similarity to the low-energy muon events, they are difficult to reject at all: Cuts that would remove cascade-like events, would also remove many low-energy muon events. Cascade events thus form an irreducible background for this analysis.

4.6 HIT CLEANING

In triggered events, a large number of the SLC hits are caused by noise instead of light from a particle (see Section 3.3.4). If the number of noise hits is comparable to the number of physics hits, or even larger (which is often the case for low-energy events), a *hit cleaning* is needed, an algorithm that tries to identify the physics hits and remove the noise hits. The performance of this algorithm has to be carefully balanced between a too strict cleaning, which removes too many physics hits, and a too soft cleaning, which keeps too many noise hits. It is easy to see that different cleanings are required for different applications: directional reconstructions can be severely compromised by a small number of noise hits and therefore require a rather strict cleaning. The loss of some physics hits is not as severe as intuitively expected, because the first hits to be removed by the hit cleaning are often low-quality, isolated hits, produced by heavily scattered light. These isolated physics hits, on the other hand, can be crucial for vetoing atmospheric muons, which often leave only such isolated hits in the outer layers of IceCube. In this case, the presence of some additional noise hits can be tolerated easily. Therefore, veto algorithms in general require a softer hit cleaning. Two algorithms, developed within the IceCube collaboration, are used in this analysis:

- *classicRT cleaning*: For veto purposes a very robust hit cleaning is used. It leaves the HLC hits untouched. For every SLC hit is checked if a second hit (SLC or HLC) can be found within a radius $R = 150\,\mathrm{m}$ and a time difference $T = 1000\,\mathrm{ns}$. If so, the hit is kept. If there is no hit nearby, the isolated hit is discarded. This cleaning keeps about 96% of the physics hits, and about 18% of the noise hits [64].
- *seededRT cleaning*: This algorithm iteratively checks for nearby hits. Instead of removing hits that do not fulfill the RT-criterion, it starts with a configurable "seed" of hits which are already believed to be physics hits, and then adds nearby hits fulfilling the RT-criterion. The so obtained subset of hits is kept and can be used as seed for another iteration. When no more hits can be added, or after the chosen number of iterations, all other hits are discarded. For this analysis, the radius and time difference are set to $R = 150\,\mathrm{m}$ and $T = 1000\,\mathrm{ns}$, similar as for the classicRT cleaning. The initial seed are those HLC hits that fulfill the RT-condition themselves.[6] Three iterations are performed. This approach is more strict than the classicRT cleaning: it discards all but 3% of the noise hits, and keeps almost 92% of the physics hits [64]. The seededRT-cleaned subset of hits is used for the initial directional reconstructions.

[64] IceCube wiki. SLC hit cleaning. `https://wiki.icecube.wisc.edu/index.php?title=SLC_hit_cleaning&oldid=126846`, accessed 02-October-2013

[6] Since HLC hits always come in pairs, this means that another HLC pair must be within the specified R- and T-range. This setting was conceived to remove noise HLC pairs from the initial seed [64].

4.7 LENGTH RECONSTRUCTION

A central part of this analysis is the reconstruction of the muon track length by the algorithm *FiniteReco* [58]. Its output is used in the final steps of the event selection (see Section 4.14), but more important, the reconstructed length is used as the energy observable in the fit of the oscillation parameters (see Chapter 5).

The output tracks of the directional reconstruction algorithms are defined by a position, a time and a direction. Their length is infinite. The FiniteReco algorithm starts with such a reconstructed track geometry as input, and then estimates the starting and stopping point of the muon on this track. The first step is a simple approximation. All hit DOMs within a certain radius (200 m in this analysis) around the track are selected. Under the assumption that the reconstruction is accurate, hits further away from the track are not related to the muon that generated the track. The selected DOMs are projected onto the track under the Cherenkov angle. The outermost projected points define the reconstructed starting point (or *reconstructed vertex*) and stopping point. This procedure is illustrated in Figure 4.7.

[58] J.-P. Hülß. P_{Hit}-P_{noHit} likelihood identification of starting muons. Talk at the IceCube Collaboration Meeting, Brussels, 2007. https://events.icecube.wisc.edu/contributionDisplay.py?contribId=98&sessionId=42&confId=1

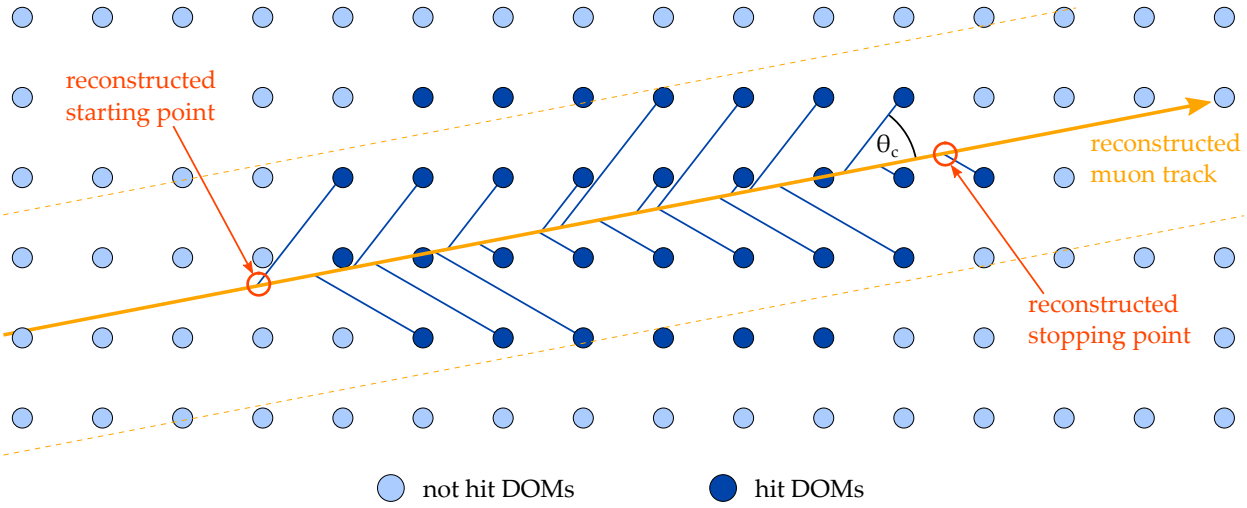

Figure 4.7: Illustration of the first-guess step of the FiniteReco algorithm. From all hits within a cylinder around the track, it projects back onto the track under the Cherenkov angle. The outermost projected points define the reconstructed vertex and stopping point.

In a second step, the reconstructed starting and stopping points are further refined by a likelihood maximization procedure, using a no-hit likelihood. All DOMs upstream of the reconstructed vertex (and analogously, downstream of the reconstructed stopping point) are selected. As these DOMs did not detect anything, for each of them, the probability to have seen no hit is calculated under two assumptions:

- $p(\text{noHit}|\text{track})$: the probability to have seen no hit under the assumption of an infinite track, and
- $p(\text{noHit}|\text{noTrack})$: the probability to have seen no hit under the assumption of a track starting at the reconstructed vertex (or stopping at the reconstructed stopping point, respectively).

The DOM selection is illustrated in Figure 4.8.

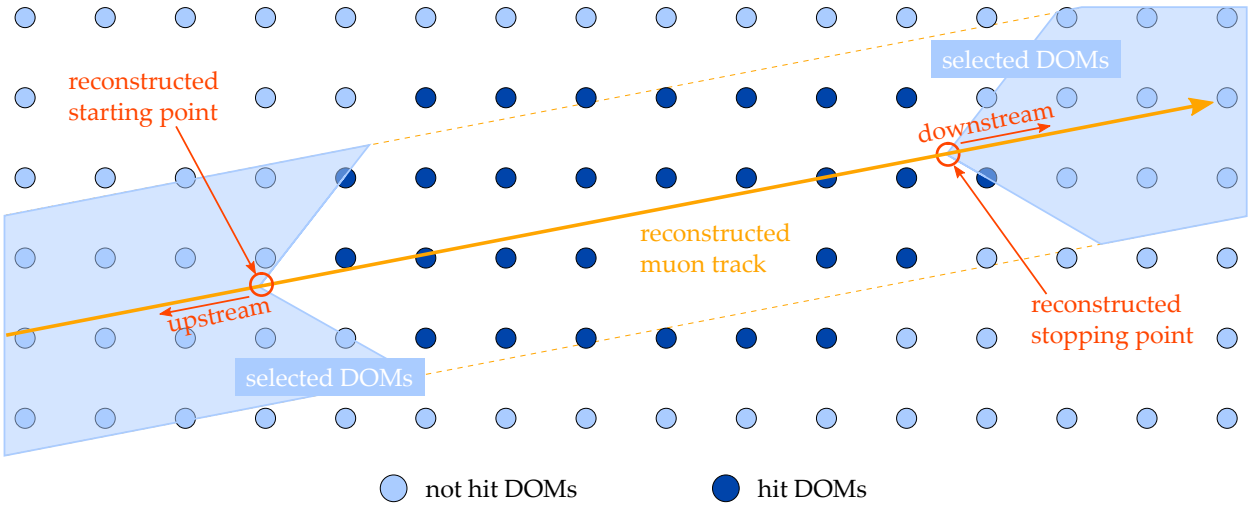

Figure 4.8: Illustration of the selection of DOMs for the calculation of the no-hit probability by the FiniteReco algorithm.

The no-hit probabilities depends on the distance between the DOM and the track, and on the optical properties of the ice in between. They are calculated using the *Photorec* tables of the *Photonics* project [76]. From these tables, the expected number of photoelectrons in a DOM at a given depth, as well as at a given distance and orientation relative to a muon track can be obtained. From the expected number of photoelectrons, the no-hit probability can be calculated, assuming Poisson statistics:

$$p_\lambda(\text{noHit}) = p_\lambda(0) = \frac{\lambda^0}{0!} e^{-\lambda} = e^{-\lambda} ,$$

with λ the expected number of photoelectrons. To construct the likelihood, the no-hit probabilities of all DOMs are multiplied:

$$P(\text{noHit}|\text{track}) = \prod_i p_i(\text{noHit}|\text{track}) ,$$
$$P(\text{noHit}|\text{noTrack}) = \prod_i p_i(\text{noHit}|\text{noTrack}) .$$

The ratio of these two likelihoods is then maximized with respect to the position of the reconstructed vertex (or stopping point, respectively). The algorithm returns the positions of reconstructed vertex and stopping point, as well as the distance in between, the *reconstructed length*. Furthermore, the obtained likelihood ratio can be used to estimate statistical confidence of the reconstructed vertices, and thus to reject events which are not unambiguously starting.

4.8 DEEPCORE FILTER (L2)

Although the DeepCore online filter, already mentioned briefly in Section 3.3.5, is run *online* (during data taking) at the South Pole, it can be regarded as the first stage of the event selection. In contrast to the later steps, which were developed after the data was recorded,

[76] J. Lundberg et al. Light tracking through ice and water—Scattering and absorption in heterogeneous media with PHOTONICS. *Nucl.Instrum.Meth. A*, 581(3):619–631, 2007. DOI: 10.1016/j.nima.2007.07.143

the settings of the filter had to be decided on before the start of the IceCube-79 physics run and could not be changed afterwards. Its output provides the basis of almost all low-energy neutrino analyses in IceCube: only events passing one of the filters are transmitted to the North and are available for analyses, see Section 3.3.5. Therefore it was designed to reduce the data rate by about a factor 10, while being optimized for a high efficiency for triggered neutrino events.

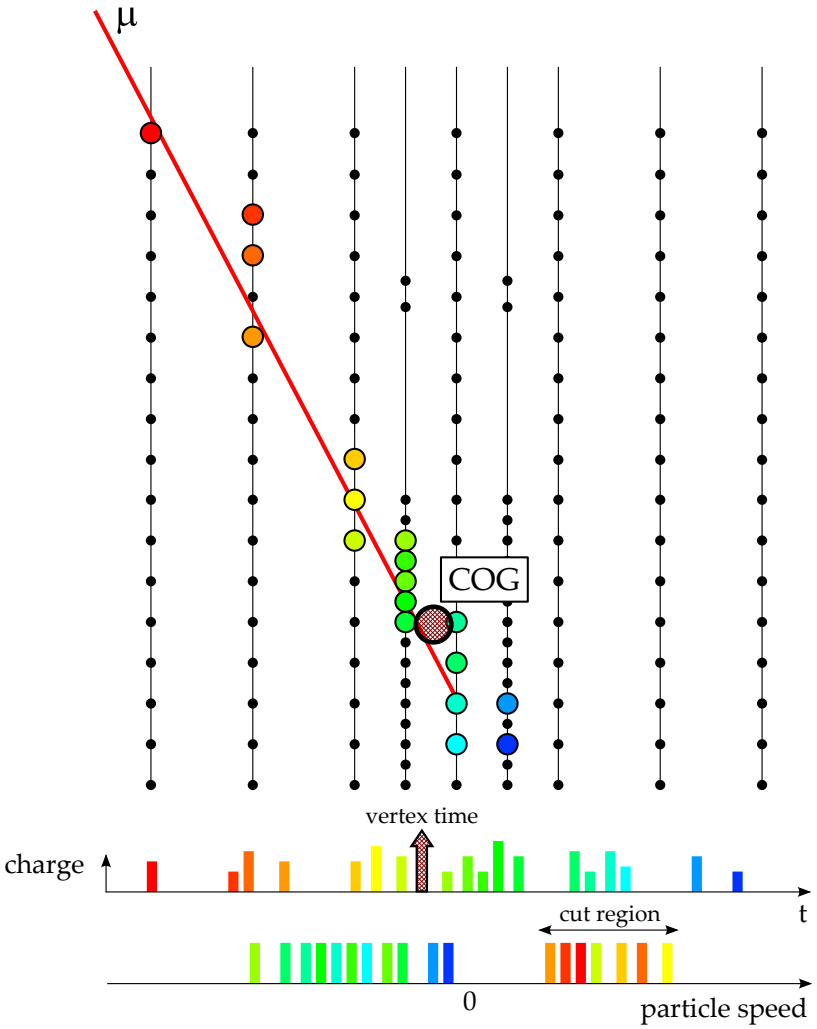

Figure 4.9: Illustration of the functional principle of the DeepCore filter [12].

It accomplishes this goal by means of a simple veto algorithm [12]. For each event, the algorithm estimates the center of gravity (COG) of the hits inside DeepCore. It first calculates the average position $\langle \vec{r} \rangle$ and time $\langle t \rangle$ of all hits in DeepCore. In a second step, this first estimate is further refined:

- Considering only those hits in the average that are within one standard deviation of the previously estimated average time $\langle t \rangle$ yields the estimated position of the center of gravity, $\vec{r}_{\mathrm{COG}}$.

- The refined time of the estimated center of gravity, t_{COG}, is obtained by calculating the average of "corrected hit times", which

[12] R. Abbasi et al. The design and performance of IceCube DeepCore. *Astroparticle Physics*, 35(10):615–624, 2012. DOI: 10.1016/j.astropartphys.2012.01.004

are obtained by subtracting from the time of each hit the time unscattered light would require to travel from $\vec{r}_{\mathrm{COG}}$.

Relative to the COG, a *particle speed* v is calculated for all hits outside DeepCore. It is given by the temporal and spatial difference between the hits and the COG:

$$v = \frac{|\vec{r}_{\mathrm{COG}} - \vec{r}_{\mathrm{hit}}|}{t_{\mathrm{COG}} - t_{\mathrm{hit}}}$$

Following this definition, positive particle speeds are associated with hits before the COG. Hits produced by an incoming muon, moving with the speed of light, will thus have positive particle speeds consistent with the speed of light: $v \approx +0.3\,\mathrm{m/ns}$. Figure 4.9 illustrates the principle of the DeepCore filter, and Figure 4.10 shows the resulting particle speed distributions for atmospheric and neutrino-induced muons, normalized to the probability per event to have at least one hit with the corresponding particle speed.

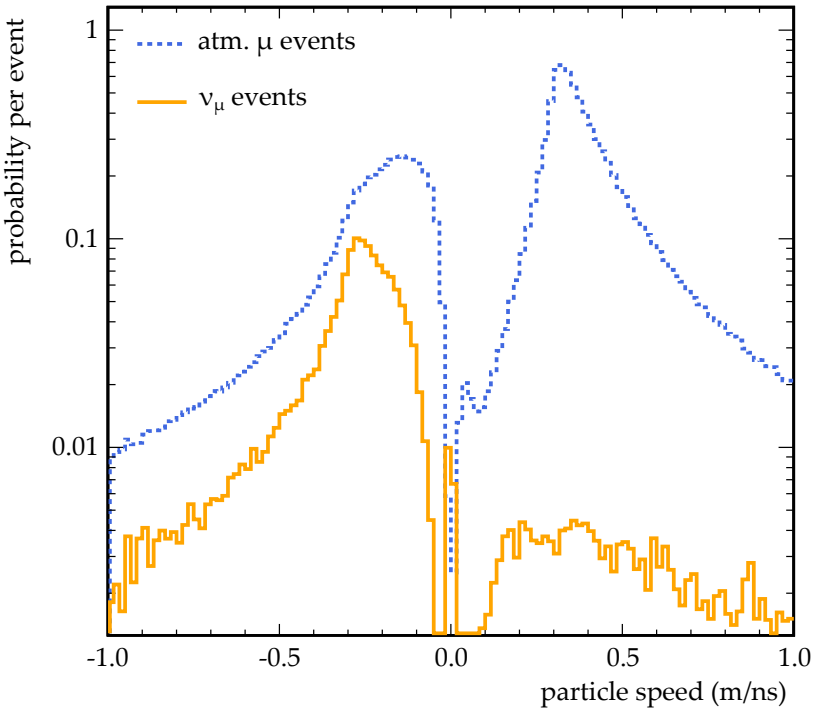

Figure 4.10: Particle speed distributions given by the DeepCore filter, for atmospheric muons (blue, dashed) and for neutrino-induced muons (yellow, solid) [12].

To remove atmospheric muons, all events with at least one hit with a particle speed v between $0.25\,\mathrm{m/ns}$ and $0.4\,\mathrm{m/ns}$ are rejected. This cut reduces the data rate from 185 Hz (SMT3 trigger rate) to 17.5 Hz, and thus achieves a background rejection of about one order of magnitude, while keeping about 99.4% of the neutrino-induced events [12].

4.9 REMOVING OBVIOUS BACKGROUND EVENTS (L3)

The event selection progresses in steps, or *cut levels*, grouping together cuts with a similar objective. The cut levels are incremental, i.e. the

cuts of a particular level are applied on the events passing the previous cut level. Within one cut level, the cuts are applied simultaneously.

The first step after the DeepCore filter removes events caused by different backgrounds.

NOISE TRIGGERS A large fraction of the events triggered by the SMT3 is not caused by a particle moving through the detector, but by pure noise. Unsimulated noise triggers explain the large difference in rate between experimental data (17.4 Hz) and simulation (12.3 Hz) at filter level (see Table 4.1, and in particular Figure 4.12). The *NoiseEngine* is an algorithm which was developed to remove these noise-triggered events [70]. It takes all the hits of an event, builds all possible pairs, and then searches for correlations in the zenith and azimuth directions of the vectors connecting the two hits of each pair. For noise-triggered events, these directions will be orientated randomly in space. For a muon track, on the other hand, most hit pairs will be orientated along the same direction – that of the muon track. A histogram of the directions will therefore show a peak around the direction of the muon. As an example, Figure 4.11 shows the distribution of the zenith angle of the connecting vectors of all hit pairs for a muon event (left) and a noise-triggered event (right).

[70] D. Koskinen. Removing Pure Noise Events With TrackEngine. Talk at the IceCube Collaboration Meeting, Uppsala, 2011. https://events.icecube.wisc.edu/getFile.py/access?contribId=58&sessionId=20&resId=0&materialId=slides&confId=36

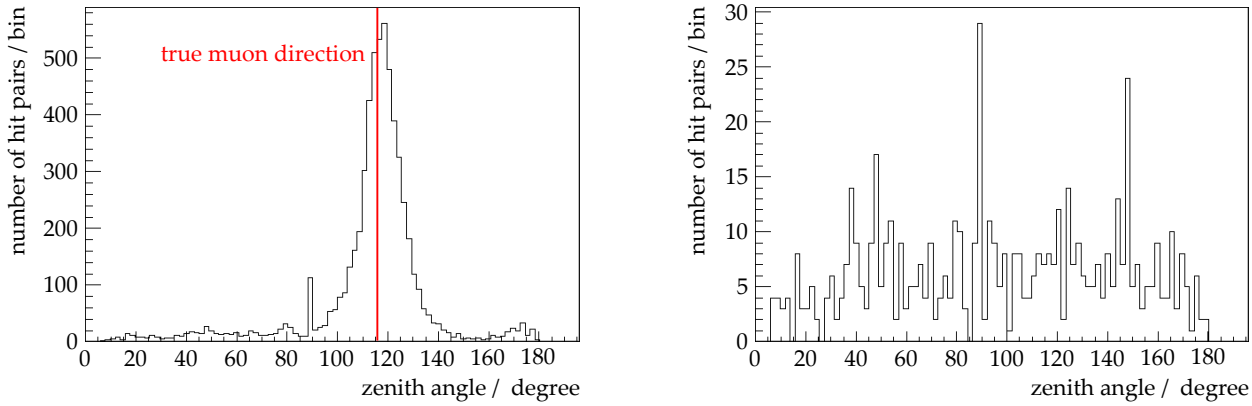

Figure 4.11: Distribution of the zenith angle of the connecting vectors of all pairs of hits of a muon event (left) and a noise-triggered event (right). The red line shows the true muon direction. For illustration purposes, this example uses a binning different from the settings used in the analysis.

[7] **H**ierarchical **E**qual **A**rea iso**L**atitude **Pix**elisation

With the settings used in this analysis, the NoiseEngine uses 48 HEALPix[7] bins (different from the example in Figure 4.11). An event passes if more than three hit pairs fall into the same bin. With these settings, more than 99% of the noise triggers are removed, and about 90% of the neutrino events are kept [70].

RECONSTRUCTED AS DOWN-GOING The events which are reconstructed as down-going are dominated by atmospheric muons. A cut on the reconstructed zenith angle is a big step forward in eliminating the atmospheric muon background. It also reduces the amount of data to a volume that can be handled much easier through the following steps. To allow slightly misreconstructed events around the horizon to pass, the cut is not set directly at the horizon, but $\sim 12^\circ$

above, at $\cos(\theta) < 0.2$. To reject as much background as possible, this cut is applied to the output of two reconstruction algorithms:

- the *LineFit* is a fast first-guess algorithm [1]. It ignores the ice properties and the geometry of the Cherenkov cone. Instead it assumes the light traveling with velocity $\vec{v}$ along a line (with the reference point $\vec{r_0}$) connecting the positions $\vec{r_i}$ of the DOMs hit at the times t_i. It then performs an analytical minimization of

$$\chi^2 = \sum_{i=1}^{N_{\text{hit}}} (\vec{r_i} - \vec{r_0} - \vec{v} \cdot t_i)^2$$

  with the free parameters $\vec{r_0}$ and $\vec{v}$. The reconstructed direction is given by $\vec{v}/|\vec{v}|$.

- The LineFit serves as the seed for a more complex iterative likelihood reconstruction [30]. The likelihood $\mathcal{L}$ to be maximized describes the probability density distribution of the arrival times of the photons at the DOMs in terms of *time residuals* $t_{\text{res}} = t_{\text{hit}} - t_{\text{geo}}$, i.e. the difference between the measured time t_{hit} and the geometrically expected time t_{geo}. The likelihood also incorporates the geometry of the Cherenkov cone and scattering of the photons in the ice. Two formulations can be used: the *single-photoelectron* likelihood (SPE) considers only the first photon in every DOM and describes the probability to observe this photon at time t_{hit}. This approach is computationally fast, but mathematically incorrect if more than one photon has been observed in a DOM. The *multi-photoelectron* likelihood (MPE) addresses this by providing the probability to observe the first of N photons detected in a DOM at the time t_{hit}. The likelihood reconstruction can be performed iteratively. This means that after the maximum likelihood $\mathcal{L}_{\text{max}}$ of the first iteration has been found, the maximization is repeated with randomly chosen start values for the direction. If one of these iterations finds a better likelihood than the initial $\mathcal{L}_{\text{max}}$, it is stored as the new $\mathcal{L}_{\text{max}}$. This procedure prevents the fit from returning local maxima. For this data selection, an SPE fit with 4 iterations (SPE4) is performed.

[1] M. Aartsen et al. Improvement in Fast Particle Track Reconstruction with Robust Statistics. *Nucl.Instrum.Meth. A*, 736:143–149, 2014. DOI: 10.1016/j.nima.2013.10.074

[30] J. Ahrens et al. Muon track reconstruction and data selection techniques in AMANDA. *Nucl.Instrum.Meth. A*, 524(1-3):169–194, 2004. DOI: 10.1016/j.nima.2004.01.065

TOO FEW HITS The standard likelihood reconstruction algorithms in IceCube run on the seededRT-cleaned (sRT) subset of hits (see Section 4.6). Events with less than 6 hits in this subset cannot be reconstructed by those algorithms. These events are removed.

EVENTS ARE REMOVED in this step that cannot be used in the further analysis for various reasons. In summary, the cuts are:

$$\begin{aligned} &\text{NoiseEngine: at least one bin with} > 3 \text{ hit pairs}\,, \\ &\cos(\theta_{\text{LineFit}}) < 0.2\,, \\ &\cos(\theta_{\text{SPE4}}) < 0.2\,, \\ &N_{\text{hit}}(\text{sRT}) \geq 6\,. \end{aligned}$$

Figure 4.12 shows the distribution of the cut parameter $N_{\text{hit}}(\text{sRT})$ for experimental data and the individual simulations. Immediately visible is the excess at low N_{hit}, which is caused by unsimulated noise triggers, and which is removed largely – but not completely – by the cut on $N_{\text{hit}}(\text{sRT}) \geq 6$. The distributions of the other cut parameters can be found in appendix A.1.

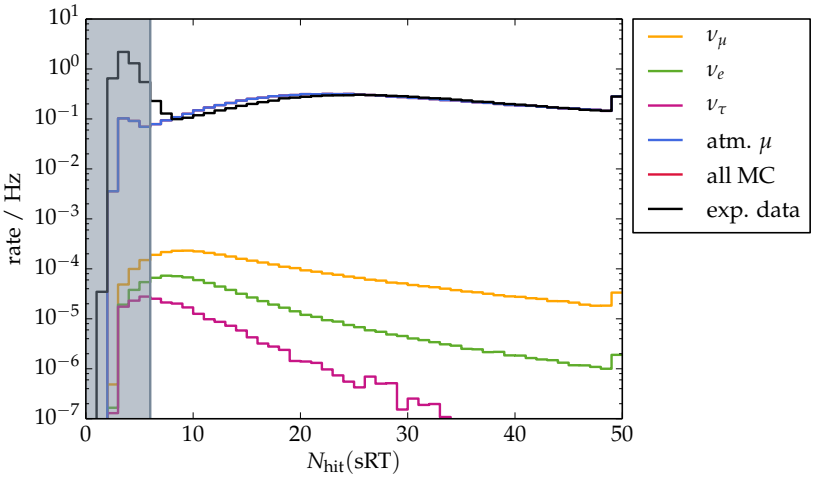

Figure 4.12: Distribution of the cut parameter $N_{\text{hit}}(\text{sRT})$. The excess at low N_{hit} is caused by unsimulated noise triggers. Events with less than 6 hits (the gray shaded area) are removed. The simulation is completely dominated by atmospheric muons, which causes the "all MC" curve to be hidden behind the "atm. μ" curve.

	event rate (Hz) before L3	after L3
ν_μ	$4.40 \cdot 10^{-3}$	$2.23 \cdot 10^{-3}$
ν_e	$8.54 \cdot 10^{-4}$	$3.95 \cdot 10^{-4}$
ν_τ	$2.19 \cdot 10^{-4}$	$9.39 \cdot 10^{-5}$
atm. μ	12.4	0.307
all MC	12.4	0.310
exp. data	17.4	0.334

Table 4.1: Experimental data and simulation event rates in Hz before and after the L3 cuts.

Table 4.1 shows the event rates for experimental data and simulation before and after the cuts, which reduce the rate of the atmospheric muon background by almost two orders of magnitude. Figure 4.13 shows the ν_μ energy and zenith angle distributions before and after the cuts, and in the bottom panels the fraction of events kept. As intended, the cuts on the reconstructed direction primarily remove down-going events ($\cos(\theta_\nu) > 0$). The effect of the cut on $N_{\text{hit}}(\text{sRT})$ can be seen in the energy distribution: it primarily removes low-energy events in the oscillation region. This loss is unavoidable, however, since these events cannot be reconstructed with the current algorithms.

4.10 HIT VETO (L4)

The next step in the data selection employs a simple veto by dividing the detector into a veto and a fiducial region, and then counting hits in these two separate regions.

- The *fiducial region* comprises DeepCore as defined for the SMT3 trigger (see Section 3.3.5), i.e. all DOMs below the dust layer on the 6 special DeepCore strings and the 7 adjacent standard IceCube strings.
- The remainder of the detector (all outer strings and the DOMs above DeepCore) forms the *veto region*.

Of particular importance at this point is the choice of the hit cleaning: for the reasons described in Section 4.6, the best separation between atmospheric muon background and neutrino signal is achieved with

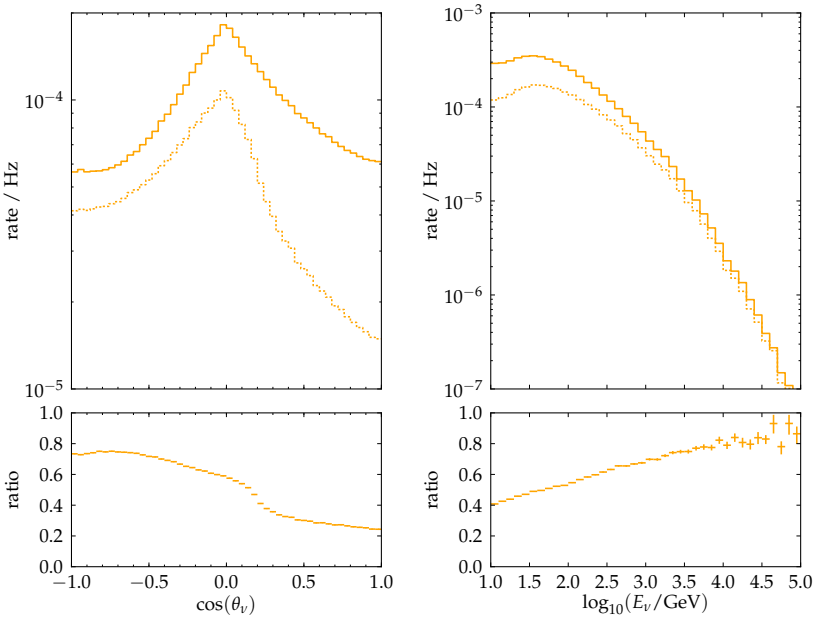

Figure 4.13: Distributions of ν_μ zenith angle (left) and energy (right), before (solid) and after the L3 cuts (dashed). The bottom panels show the fraction of events kept, i.e. the ratio of the distributions after and before the cuts.

the classicRT-cleaned subset of hits, which is therefore used here. Furthermore, to reject incoming muons but keep events starting in DeepCore and moving outwards, only hits earlier than the SMT3 trigger time (i.e. the time of the third HLC hit in DeepCore, see Section 3.3.5) are counted in the veto region. Figure 4.14 shows the distributions of the number of hits in DeepCore and the veto region, for simulated ν_μ and atmospheric muons. The first row shows the distributions for the seededRT cleaning used in the previous step, the second row shows the classicRT cleaning used here, and the last row shows the distributions obtained when no cleaning at all is applied. It is obvious that the best separation is achieved with the classicRT cleaning. With the seededRT cleaning, most atmospheric muon events have zero veto hits, because the cleaning discards too many isolated hits in the veto region (as discussed in Section 4.6). If no cleaning is applied, the ν_μ events are flooded by noise hits, and again cannot be distinguished from atmospheric muon events.

Events are kept if they have not more than one hit in the veto region and if they have at least 6 hits in DeepCore, all counted in the classicRT-cleaned subset of hits:

$$N_{\mathrm{hit}}(\mathrm{cRT}, \mathrm{DC}) \geq 6\,,$$
$$N_{\mathrm{hit}}(\mathrm{cRT}, \mathrm{veto}) \leq 1\,.$$

The distributions of the cut parameters can be found in appendix A.2.

Table 4.2 shows the event rates for experimental data and simulation before and after the cuts. This cut level achieves another order of magnitude in rejection of the atmospheric muon background.

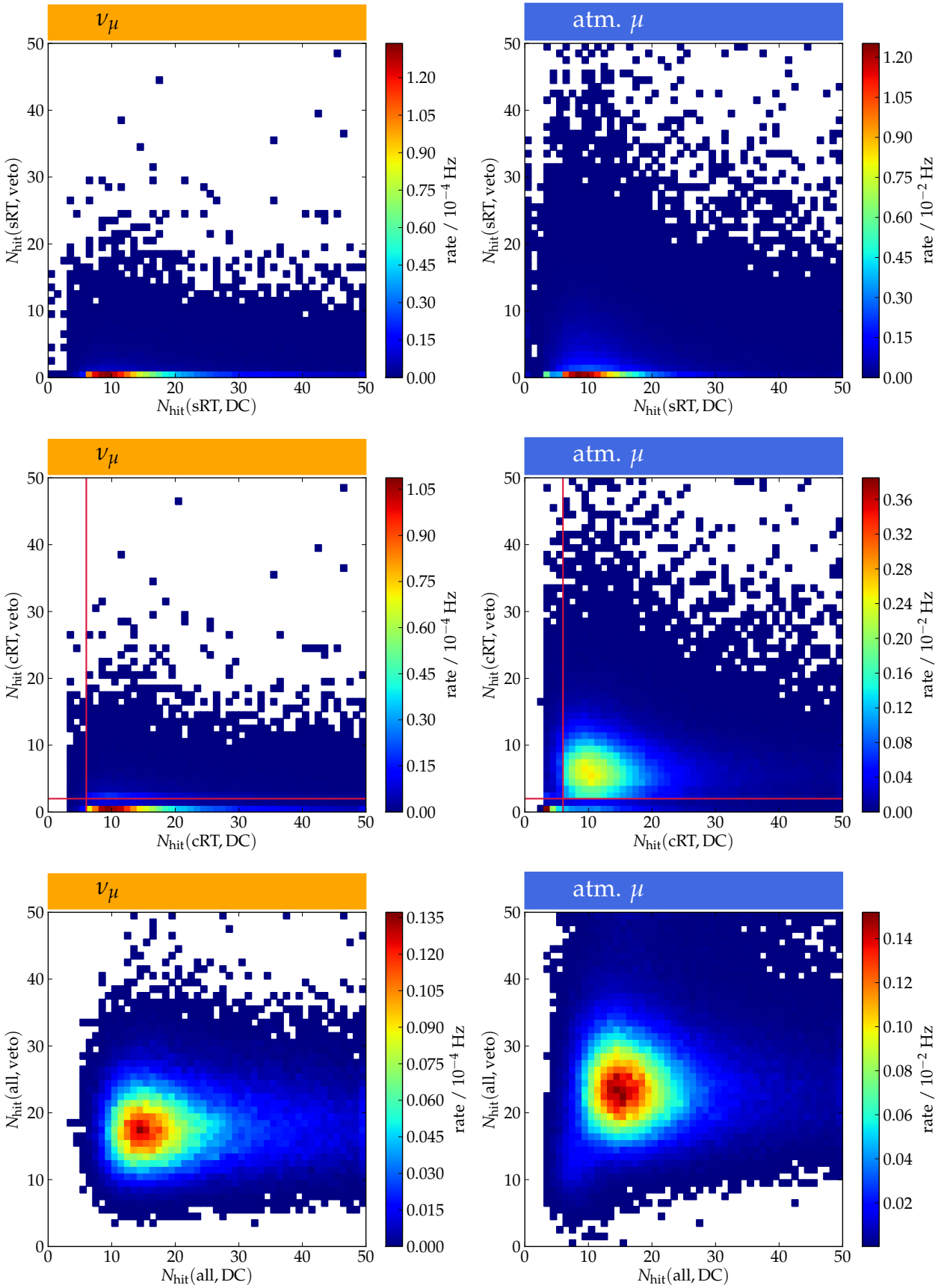

Figure 4.14: Two-dimensional distribution of the cut parameters $N_{\mathrm{hit}}(\mathrm{DC})$ and $N_{\mathrm{hit}}(\mathrm{veto})$, for ν_μ (left) and atmospheric muon simulation (right), and for different hit cleanings: seededRT (top), classicRT (middle) and no cleaning (bottom). The best separation is achieved with the classicRT cleaning, which is therefore used here. The red lines mark the positions of the cuts.

Figure 4.15 shows the ν_μ energy and zenith angle distributions before and after the cuts, and in the bottom panels the fraction of events kept. In zenith angle, the cut efficiency is approximately constant at 80%. However, the fraction of events that is rejected increases with energy. While low-energy events are typically confined within a small geometrical volume, high-energy events more often extend into the veto region, and have thus a higher probability for veto hits as defined here.

	event rate (Hz) before L4	after L4
ν_μ	$2.23 \cdot 10^{-3}$	$1.67 \cdot 10^{-3}$
ν_e	$3.95 \cdot 10^{-4}$	$3.30 \cdot 10^{-4}$
ν_τ	$9.39 \cdot 10^{-5}$	$7.73 \cdot 10^{-5}$
atm. μ	0.307	$2.06 \cdot 10^{-2}$
all MC	0.310	$2.27 \cdot 10^{-2}$
exp. data	0.334	$3.18 \cdot 10^{-2}$

Table 4.2: Experimental data and simulation event rates in Hz before and after the L4 cuts.

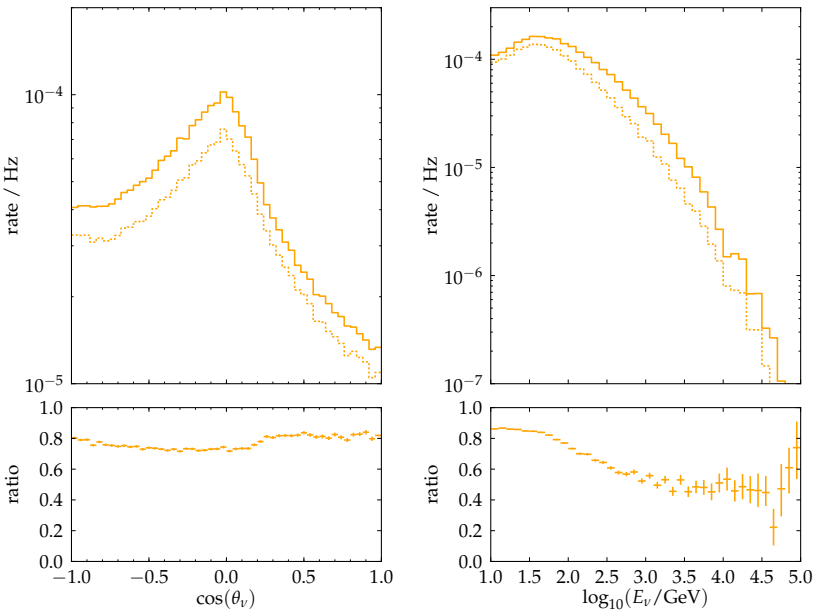

Figure 4.15: Distributions of ν_μ zenith angle (left) and energy (right), before (solid) and after the L4 cuts (dashed). The bottom panels show the fraction of events kept, i.e. the ratio of the distributions after and before the cuts.

4.11 CLUSTER VETO (L5)

In this step, the *topological trigger* algorithm [40] is used. It was designed to identify coincident events, i.e. events with two or more separate and unrelated particles (see also Section 3.3.5). These events can severely disturb the reconstruction algorithms expecting only one particle per event. For example, depending on their relative arrival time and geometry, two consecutive down-going muons are often interpreted as one up-going particle by the reconstruction algorithms. Figure 4.16 shows an example of such an event. Topological trigger tries to identify the subsets of hits (*clusters*) that are caused by the same particle. With the settings used here, it checks for all pairs of hits

- if they are separated by not more than 15 DOMs (for hits on the same string), or
- if their strings are less than 150 m away from each other (for hits on different strings), and
- if the two hits are causally connected with $\Delta t - \Delta r/c < 450\,\mathrm{ns}$.

[40] D. Chirkin. Neutrino search with IceCube. *IceCube internal report*, icecube/200807006, 2008

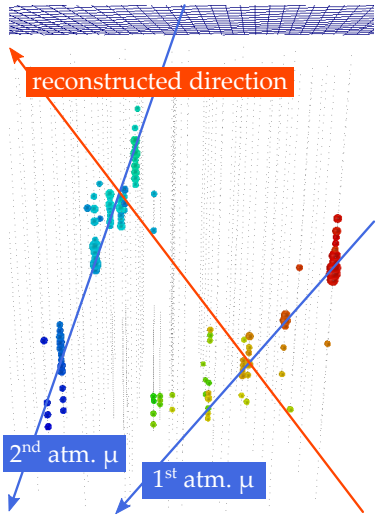

Figure 4.16: Event display of a coincident muon event. Two atmospheric muons pass through the detector at about the same time. The reconstruction algorithm cannot separate their hits and reconstructs the whole event as up-going.

If two hits comply with all these conditions, they likely stem from the same particle, and are sorted into the same cluster. In this analysis, the number of clusters is limited to 2, which are called *TT0* and *TT1*. A cluster is required to contain at least 5 hits. If less than 5 causally connected hits are found, the event is treated as if no cluster was found, i.e. the number of hits in the cluster is set to 0. Figure 4.17 shows the two-dimensional distribution of the number of hits in the clusters TT0 and TT1, for signal and background simulation and experimental data. The gaps in the distributions between $N_{\text{hit}} = 1$ and $N_{\text{hit}} = 5$ are a result of the requirement for a cluster to contain at least 5 hits. Striking is the large number of events with no cluster found at all (the bin at 0, 0) in experimental data, caused by remaining noise triggers. Apart from this bin, which completely dominates the distribution, experimental data and simulation agree well in rate (see also Figure A.5). Note the different statistics between the atmospheric muon simulation and the experimental data (see also Section 4.4)!

EVENTS ARE REMOVED if more than one cluster is found, and also if the primary cluster TT0 is empty:[8]

$$N_{\text{hit}}(\text{TT1}) = 0\,,$$
$$N_{\text{hit}}(\text{TT0}) > 0\,.$$

While the first cut removes coincident events, the second cut is particularly effective in removing the remaining noise triggers: if no causally connected hits can be found in an event, it was most likely triggered on noise. The distributions of the cut parameters can be found in appendix A.3.

[8] It should be noted that the cut $N_{\text{hit}}(\text{TT0}) > 0$ is equivalent to $N_{\text{hit}}(\text{TT0}) \geq 5$ due to the gap in the distribution.

Figure 4.17: Two-dimensional distribution of the number of hits in the clusters found by topological trigger, $N_{\text{hit}}(\text{TT0})$ and $N_{\text{hit}}(\text{TT1})$. The distribution for experimental data (right) is dominated by the large amount of events where no cluster could be found at all, caused by noise triggers. The large gaps in the distributions are caused by the requirement for a cluster to contain at least 5 hits.

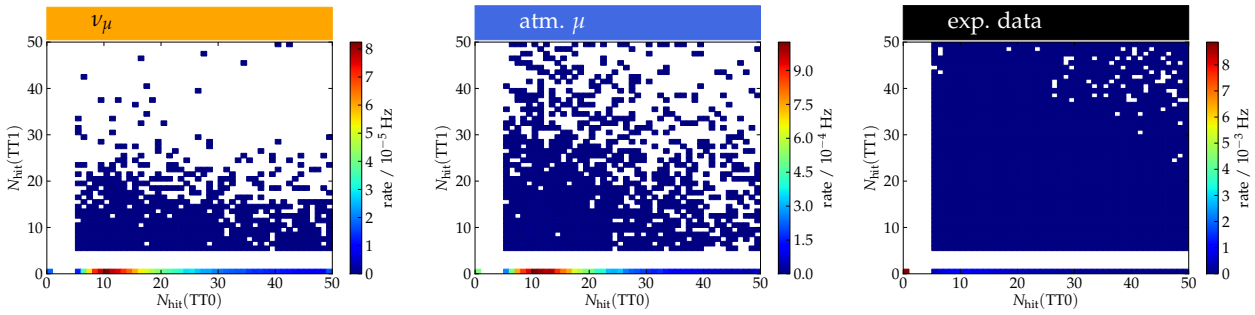

	event rate (Hz) before L5	after L5
ν_μ	$1.67 \cdot 10^{-3}$	$1.58 \cdot 10^{-3}$
ν_e	$3.30 \cdot 10^{-4}$	$3.24 \cdot 10^{-4}$
ν_τ	$7.73 \cdot 10^{-5}$	$7.56 \cdot 10^{-5}$
atm. μ	$2.06 \cdot 10^{-2}$	$1.73 \cdot 10^{-2}$
all MC	$2.27 \cdot 10^{-2}$	$1.93 \cdot 10^{-2}$
exp. data	$3.18 \cdot 10^{-2}$	$1.86 \cdot 10^{-2}$

Table 4.3: Experimental data and simulation event rates in Hz before and after the L5 cuts.

Table 4.3 shows the event rates for experimental data and simulation before and after the cuts. This cut level has the largest effect on the experimental data by removing (unsimulated) noise-triggered events. After their removal, the rates of simulation and experimental data agree well. The data is still dominated by atmospheric muons. Figure 4.18 shows the ν_μ energy and zenith angle distributions before and after the cuts, and in the bottom panels the fraction of events kept. Only ∼5% of the ν_μ events are removed. The loss occurs almost exclusively at energies above the oscillation region, where the events

have more hits than at low energies. Topological trigger has thus a higher chance of misidentifying a second cluster of causally connected hits.

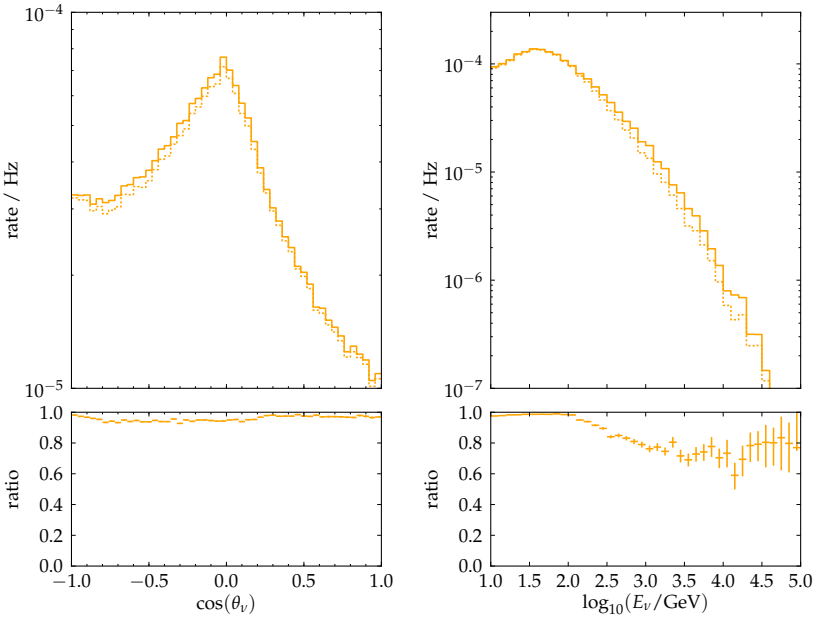

Figure 4.18: Distributions of ν_μ zenith angle (left) and energy (right), before (solid) and after the L5 cuts (dashed). The bottom panels show the ratio of before and after the cuts.

4.12 MORE SOPHISTICATED RECONSTRUCTIONS (L6)

At this point, the total amount of data has been reduced sufficiently for more sophisticated (and computationally more intensive) reconstructions to be performed.

- The first new reconstruction is the *improved LineFit* [1]. It is based on the standard LineFit (see Section 4.9), but utilizes a special hit cleaning before the actual fit, which aims to remove hits caused by light which was scattered multiple times, and thus arrives later at a DOM than geometrically expected. The improved LineFit (iLF) is performed only on the subset of hits forming the primary cluster returned by Topological Trigger, TT0 (see Section 4.11).
- The improved LineFit (iLF) again serves as a seed for an SPE reconstruction (see Section 4.9), this time with 32 iterations (SPE32). It not only uses the improved LineFit as seed, but also the subset of hits obtained by its hit cleaning process.

[1] M. Aartsen et al. Improvement in Fast Particle Track Reconstruction with Robust Statistics. *Nucl.Instrum.Meth. A*, 736:143–149, 2014. DOI: 10.1016/j.nima.2013.10.074

Cuts are again applied to the reconstructed zenith angle, but now directly at the horizon:

$$\cos(\theta_{\mathrm{iLF}}) < 0.0\,,$$
$$\cos(\theta_{\mathrm{SPE32}}) < 0.0\,.$$

The distributions of the cut parameters can be found in appendix A.4.

Table 4.4 shows the event rates for experimental data and simulation before and after the cuts. Figure 4.19 shows the ν_μ energy and

	event rate (Hz) before L6	after L6
ν_μ	$1.58 \cdot 10^{-3}$	$1.01 \cdot 10^{-3}$
ν_e	$3.24 \cdot 10^{-4}$	$1.96 \cdot 10^{-4}$
ν_τ	$7.56 \cdot 10^{-5}$	$4.62 \cdot 10^{-5}$
atm. μ	$1.73 \cdot 10^{-2}$	$3.90 \cdot 10^{-3}$
all MC	$1.93 \cdot 10^{-2}$	$5.15 \cdot 10^{-3}$
exp. data	$1.86 \cdot 10^{-2}$	$4.33 \cdot 10^{-3}$

Table 4.4: Experimental data and simulation event rates in Hz before and after the L6 cuts.

zenith angle distributions before and after the cuts, and in the bottom panels the fraction of events kept. The distributions are very similar to those of the L3 cuts (Figure 4.13). For the zenith angle distribution this is intuitively expected, since this cut level again applies cuts on the reconstructed zenith angle. In the energy distribution, the larger loss of low-energy events reveals an implicit cut on the number of hits: If the hit cleaning that comes with the improved LineFit reduces the number of hits to less than 6, the subsequent SPE fit cannot reconstruct the event, and it is discarded. This loss of low-energy events is tolerated here for the gain of the new reconstructions, which allow a significantly improved background rejection.

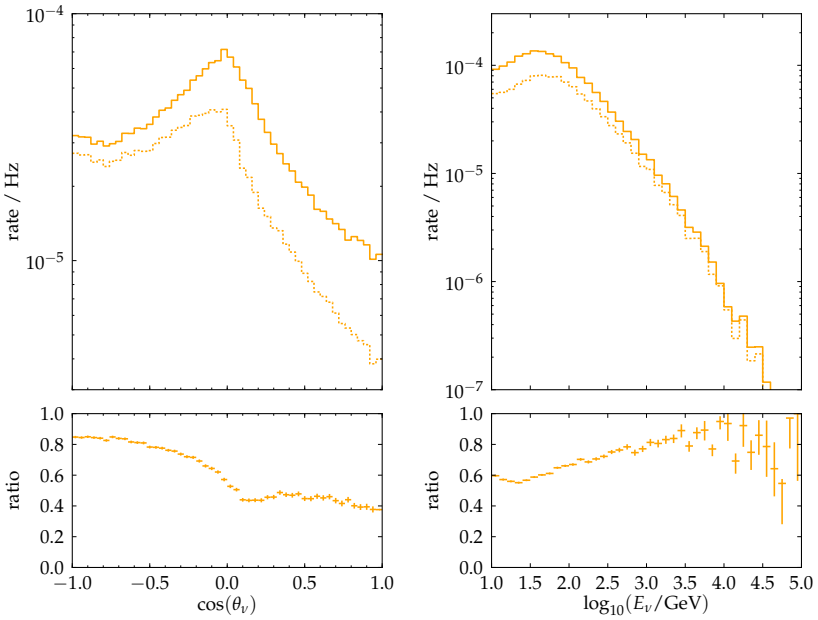

Figure 4.19: Distributions of ν_μ zenith angle (left) and energy (right), before (solid) and after the L6 cuts (dashed). The bottom panels show the ratio of before and after the cuts.

4.13 CAUSALITY VETO (L7)

The next step is constituted by another, more sophisticated veto algorithm. Its principle is illustrated by Figure 4.20. First, a reference hit is defined by the hit that activated the SMT3 trigger (i.e. the third HLC hit in DeepCore, see Section 3.3.5). For all other hits i we calculate the geometrical distance $\Delta r = |\vec{r}_{\mathrm{ref}} - \vec{r}_i|$ and the time difference $\Delta t = t_{\mathrm{ref}} - t_i$ with respect to that reference hit. In the definition used, positive time differences are given by hits which occur before the trigger, negative time differences stem from later hits. In this projection, a particle entering the detector from the outside, triggering the detector, and then leaving the detector would move from top to bottom of the figure, approximately along the lines defined by the speed of light c (the dashed lines in the left panel of Figure 4.20). Thus, hits found along the line in the upper half are an indication for an incoming muon, whereas hits along the line in the lower half indicate a track leaving the detector. In this ideal picture, hits from unscattered light detected close to the track are expected

approximately *on* the speed-of-light lines, whereas hits from scattered light or farther away from the track are found *below*. The space *above* the lines would correspond to hits detected earlier than geometrically expected, if the reference hit itself was from unscattered light.

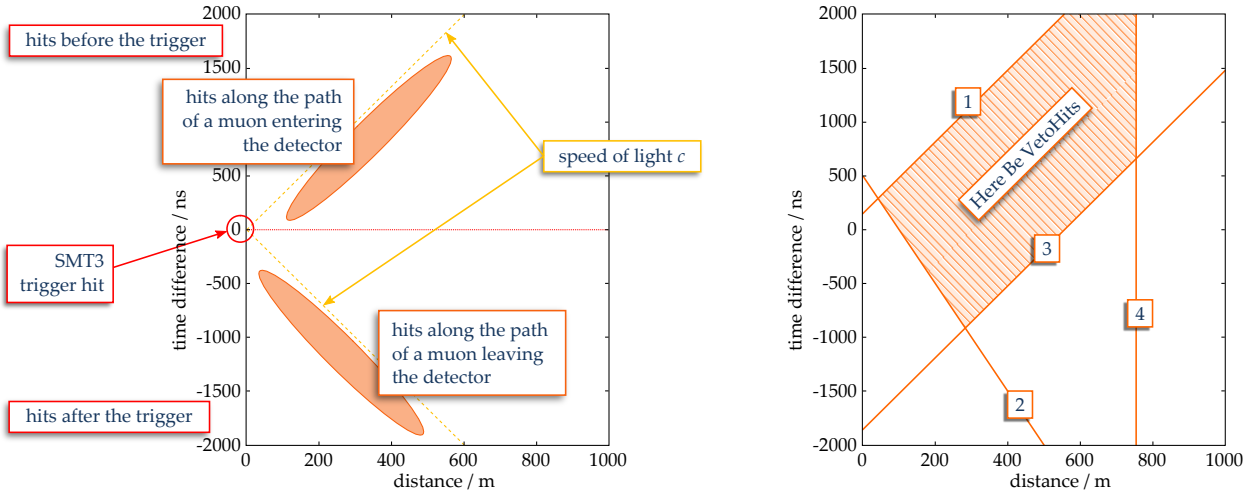

Figure 4.20: Principle of the causality veto (left) and definition of the "veto hit region" (right).

A simple way to identify background in this scheme is to count the number of "veto hits" within an area along the "incoming muon" line. The right panel of Figure 4.20 shows such an area, as it is defined in this analysis:

- *Line 1* is defined by $\Delta t = \frac{\Delta r}{0.3\,\mathrm{m/ns}} + 150\,\mathrm{ns}$. It is approximately parallel to the line given by the speed of light. Hits from incoming muons are expected below this line.
- *Line 2* is defined by $\Delta t = -\frac{\Delta r}{0.2\,\mathrm{m/ns}} + 500\,\mathrm{ns}$. Hits below this line are potentially from muons leaving the detector. Since this includes muons starting in DeepCore, veto hits have to be above this line.
- *Line 3* is parallel to line 1, but shifted by 2 µs to smaller values: $\Delta t = \frac{\Delta r}{0.3\,\mathrm{m/ns}} + 1850\,\mathrm{ns}$. If hits below this line still stem from incoming muons, they are delayed by more than 2 µs. Veto hits have to be above this line.
- *Line 4* marks a distance of 750 m from the trigger hit: $\Delta r = 750\,\mathrm{m}$. Hits even further out are ignored; veto hits have to be to the left of this line.

Note that while the approximate positions of the defining lines can be motivated by physical arguments (as done above), their exact positions have been optimized in terms of background rejection power. Figure 4.21 shows the distributions of distance and time difference for signal and background simulation and experimental data.

At first glance, the distributions (upper row) do not exhibit large differences, because the largest fraction of atmospheric muon events has already been rejected by earlier cuts. The distributions are dominated by hits close to the reference hit: a first population in its

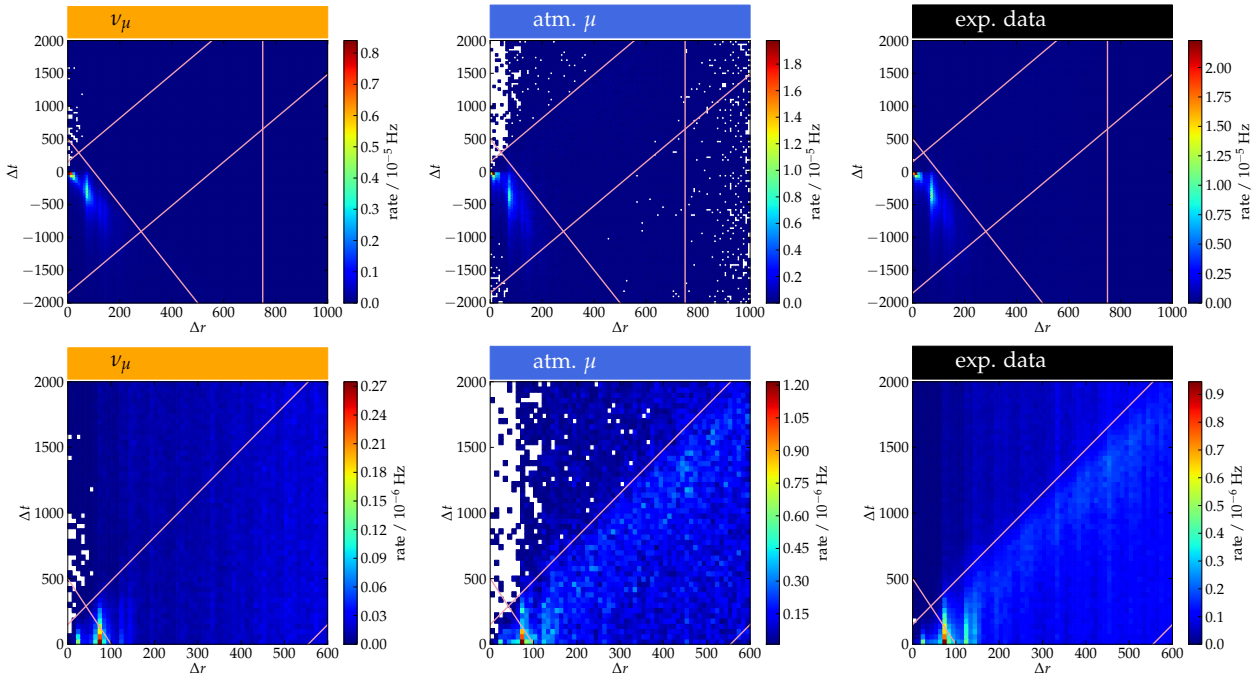

Figure 4.21: Two-dimensional distributions of distance Δr and time difference Δt of all hits to the reference hit which fulfilled the SMT3 trigger condition (upper row) and detail of the positive time difference range (lower row). The lines correspond to Figure 4.20.

	event rate (Hz) before L7	after L7
ν_μ	$1.01 \cdot 10^{-3}$	$4.39 \cdot 10^{-4}$
ν_e	$1.96 \cdot 10^{-4}$	$9.27 \cdot 10^{-5}$
ν_τ	$4.62 \cdot 10^{-5}$	$2.41 \cdot 10^{-5}$
atm. μ	$3.90 \cdot 10^{-3}$	$2.22 \cdot 10^{-4}$
all MC	$5.15 \cdot 10^{-3}$	$7.78 \cdot 10^{-4}$
exp. data	$4.33 \cdot 10^{-3}$	$6.67 \cdot 10^{-4}$

Table 4.5: Experimental data and simulation event rates in Hz before and after the L7 cuts.

immediate vicinity and a second one at small negative Δt and at a distance of about 70 m, corresponding to the inter-string distance in DeepCore. A closer look to positive time differences (lower row) reveals the structure expected from incoming muons in the distributions of atmospheric muon simulation and experimental data. Only events with less than 3 hits in the "veto hit region" are accepted:

$$N_{\text{veto}} < 3\,.$$

Figure 4.22 shows the distribution of N_{veto} for experimental data and the individual simulations and the location of the cut. Table 4.5 shows the event rates for experimental data and simulation before and after the cut. This step of the event selection achieves to push the background rate below the ν_μ rate. The data is now dominated by muon neutrino events, albeit with a still low purity. Figure 4.23 shows the ν_μ energy and zenith angle distributions before and after the cut, and in the bottom panels the fraction of events kept. The cut removes more than 50% of the ν_μ, but, as expected from a true veto cut, its efficiency does not depend on the neutrino zenith or energy (see also Section 4.5): the ratios in the bottom plots of Figure 4.23 are almost flat.

4.14 QUALITY CUTS (L8)

The causality veto discussed in the last section succeeds in reducing the atmospheric muon background to below the neutrino signal. To further enhance the signal purity of the sample, soft cuts on the reconstruction quality are applied.

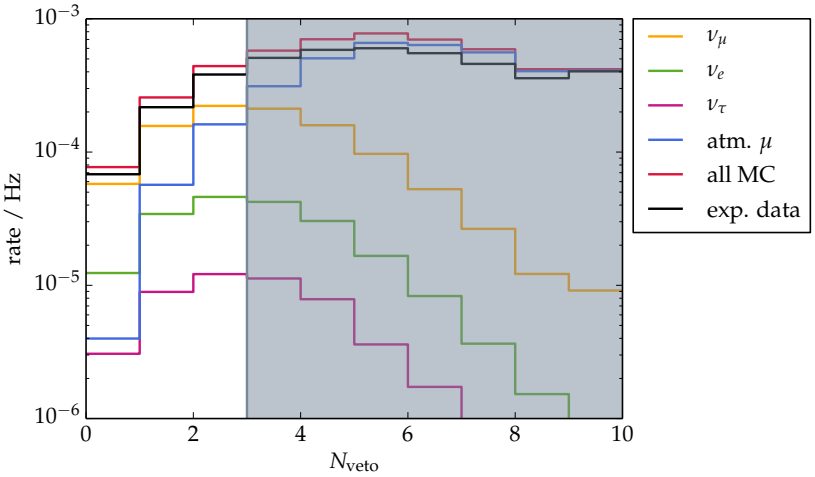

Figure 4.22: Distribution of the cut parameter N_{veto}. Events with more than 2 veto hits (the gray shaded area) are removed.

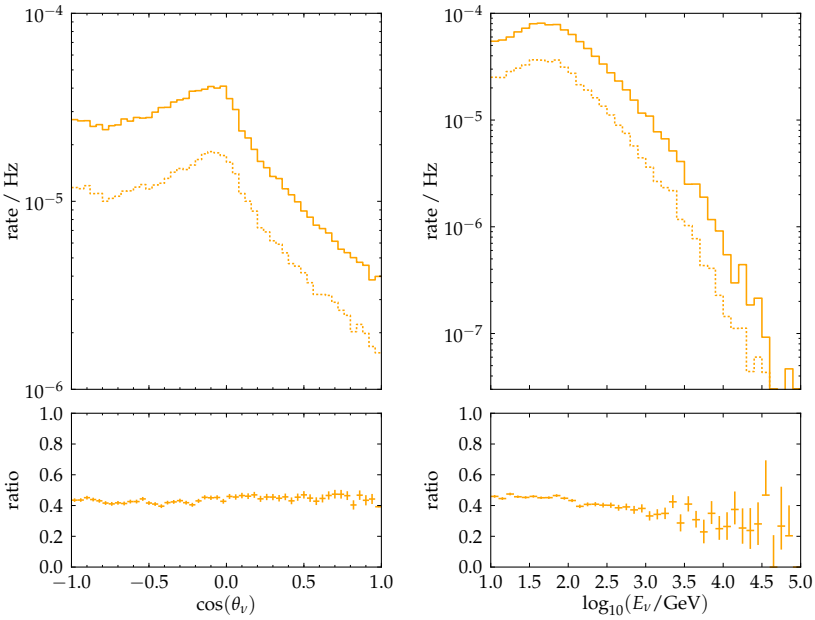

Figure 4.23: Distributions of ν_μ zenith angle (left) and energy (right), before (solid) and after the L7 cuts (dashed). The bottom panels show the ratio of before and after the cuts.

DIRECT HITS Hits with small time residuals (see Section 4.9) are called *direct hits* [30]. In the definition used here, hits have to arrive within a time window of $[-15, +75]$ ns around the geometrically expected time. A large number of direct hits is an indication for an accurate reconstruction. It should be noted that the "direct" subset of hits depends on the chosen reconstruction! For this step of the data selection, an MPE reconstruction (see Section 4.9) is used, which is seeded with the SPE32 fit (see Section 4.12) and performed on the same cleaned subset of hits. Events with less than 3 direct hits are discarded.

In addition to the number of direct hits, their spatial distribution is used as a cut parameter: the *direct length* is defined as the distance between the outermost direct hits, projected orthogonally on the reconstructed track [30]. For a well-reconstructed muon, the reconstructed track should follow the cloud of hits and produce a rather large direct length. Looking at it the other way around, for an event with a large direct length, the directional estimate is more reliable, because of the larger lever arm of the fit. Here, events with a direct length shorter than 20 m are discarded.

RECONSTRUCTION LIKELIHOOD Another important quality parameter is the value of the likelihood maximum found by the reconstruction. Often, the *reduced log-likelihood (rLogL)* (see Figure 4.3) is used [30], defined as the negative logarithm of the maximum likelihood $\mathcal{L}$, divided by the number of degrees of freedom, which is $N_{\text{hit}} - 5$:

$$\text{rLogL} = \frac{-\log(\mathcal{L})}{N_{\text{hit}} - 5}\,.$$

In this analysis, we use the variant *pLogL* [62], which is defined as

$$\text{pLogL} = \frac{-\log(\mathcal{L})}{N_{\text{hit}} - 3.5}\,.$$

A particular effective method to reject the atmospheric muon background is the use of a zenith weighted (Bayesian) likelihood [30]: another likelihood fit of the direction is performed, but the likelihood is replaced by a combination of the MPE likelihood and a Bayesian prior incorporating the known shape of the zenith angle distribution of atmospheric muons. The likelihood ratio *bayesLLHdiff* of the standard MPE fit and this modified reconstruction is used as a cut parameter.

FINITERECO Although not track quality parameters as such, the results of the length reconstruction algorithm FiniteReco (see Section 4.7) are used as cut parameters. The input objects for FiniteReco are the MPE reconstruction and the classicRT-cleaned subset of hits.

A first cut is applied to the position of the reconstructed vertex. Its radial component

$$r_{\text{vertex}} = \sqrt{x_{\text{vertex}}^2 + y_{\text{vertex}}^2}$$

[30] J. Ahrens et al. Muon track reconstruction and data selection techniques in AMANDA. *Nucl.Instrum.Meth. A*, 524(1-3):169–194, 2004. DOI: 10.1016/j.nima.2004.01.065

[62] IceCube wiki. Plogl. `https://wiki.icecube.wisc.edu/index.php?title=Plogl&oldid=113008`, accessed 05-October-2013

is required to be within 180 m around the string in the center of DeepCore. This cut is actually another variant of a veto condition, since it implicitly requires that the first hit along the reconstructed track is somewhere close to the center of the detector. Figure 4.24 shows the location of the reconstructed vertices in terms of their radial and z-components, r_{vertex} and z_{vertex}, for signal and background simulation and experimental data.

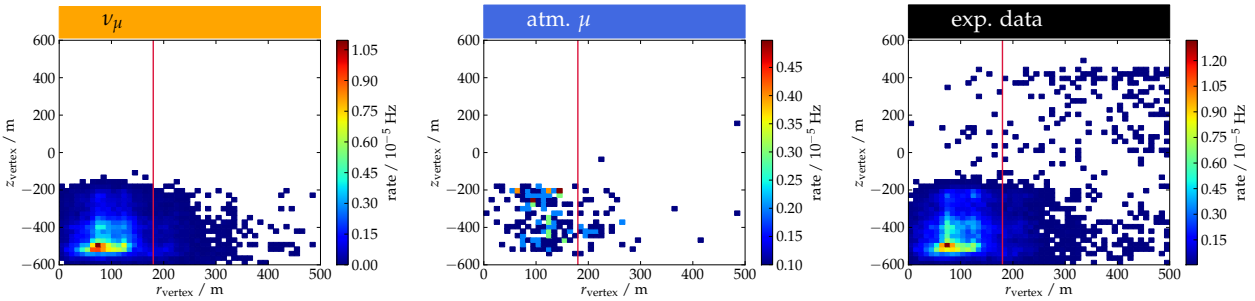

Figure 4.24: Position of the reconstructed vertex, radial distance from the center of DeepCore and depth in IceCube coordinates. From left to right: ν_μ simulation, atmospheric muon simulation and experimental data.

It is obvious that the data is dominated by neutrino events, which have their vertices at the bottom of the detector. The experimental data shows a small population of events in the upper right part of the plot ($r_{\text{vertex}} \approx z_{\text{vertex}} \approx 400$ m, i.e. at the top edge of the detector). This population might indicate a component of inclined atmospheric muon events, which would leave single hits at the top of the detector, but would then enter the dust layer, "disappear" from view and thus escape the veto conditions applied in the previous cut levels. They would reappear in the DeepCore volume and mimic starting neutrino events. These events appear to be missing from the atmospheric muon distribution. The insufficient statistics of the simulated atmospheric muon dataset (see also Section 4.4) make it impossible to decide if this is because of shortcomings in the simulation or because the statistics are too low. The cut on the radial component of the reconstructed vertex removes these events.

Another cut is applied to the reconstructed track length, which must be larger than 40 m. This cut deserves special attention, since it significantly impairs the power of this analysis. During the course of this thesis it was discovered that the light yield of low-energy hadronic cascades is not simulated correctly by the IceCube software. Hadronic cascades, which occur at each neutrino interaction vertex (see Section 2.1), emit in general less light than electromagnetic cascades of the same energy, for several reasons:

- A fraction of the energy is transferred to neutrons produced in the cascade, which do not emit Cherenkov light.
- The visible energy is reduced by large binding energies of the participating nuclei.
- The Cherenkov threshold is higher for hadrons than for electrons.

Hadronic cascades always have an electromagnetic part: pions produced in the shower decay almost exclusively into leptons and thus

initiate an electromagnetic cascade. If this occurs early in the shower development, the cascade can be strongly biased towards an electromagnetic particle content. The event-to-event fluctuations are therefore larger than for electromagnetic cascades. The light yield also differs significantly between different types of hadrons [71]. Nonetheless, the IceCube simulation chain does not distinguish between different hadrons, but uses an average value for the light yield. Moreover, the program PPC, which is responsible for generation and propagation of the photons (see Section 4.2.2), parametrizes the hadronic light yield L_{had} in terms of the electromagnetic light yield L_{em} by applying a scaling factor F:

[71] M. Kowalski. Search for Neutrino-Induced Cascades with the AMANDA-II Detector. Ph.D. thesis, Humboldt-Universität Berlin, 2004

$$L_{\text{had}} = F \cdot L_{\text{em}}$$

The scaling factor F depends on the cascade energy. With decreasing energy, F decreases as well, because hadronic cascades become less and less similar to electromagnetic cascades. The implementation in PPC takes the energy dependence of the scaling factor from Ref. [71], which is, however, valid only above 10 GeV. For lower energies, the implementation returns the value at 10 GeV:

$$F(E < 10\,\text{GeV}) = F(10\,\text{GeV}) \approx 0.65\,.$$

Figure 4.25 shows the parametrization used in PPC. Also shown are a newer parametrization, which reaches down to 2 GeV, but which was not available when the simulation datasets used in this analysis were generated, and their ratio.

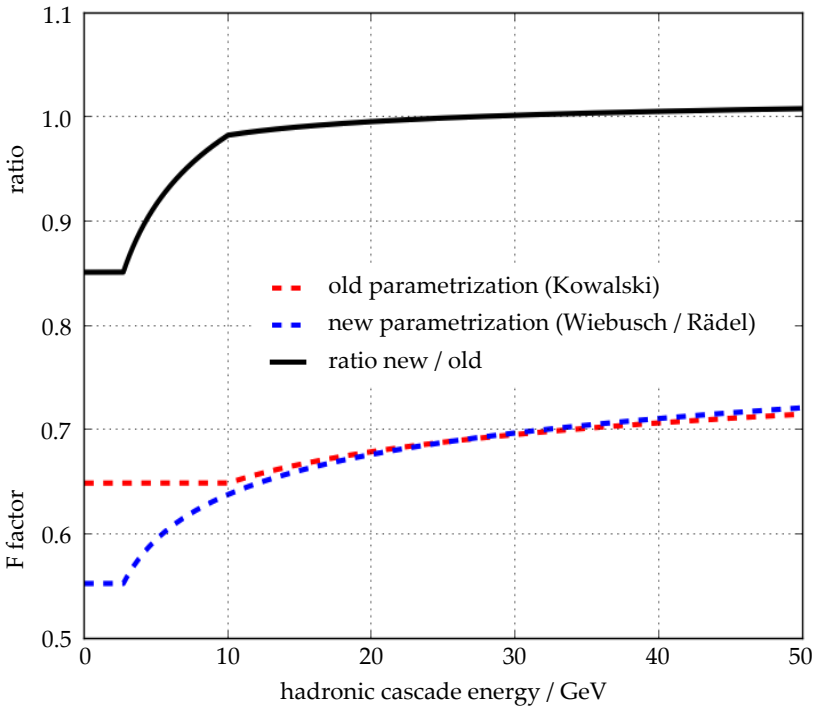

Figure 4.25: Parametrization of the light yield of hadronic cascades. The red curve shows the implementation that was used for the simulation datasets for this analysis. The blue curve shows a newer parametrization extending to lower energies. The black curve shows the ratio of new and old parametrization [104].

The assumption of a constant factor F leads to a significant overestimation of the light yield below 10 GeV. For most IceCube analyses

at higher energies this does not pose a problem. For oscillation analyses, operating at the lower energy threshold of IceCube, hadronic cascades with energies below 10 GeV are a common occurrence. An overestimation of the hadronic light yield increases the number of low-energy events in the simulation. When such a faulty simulation is compared to experimental data, the experimental data will thus show an apparent deficit of low-energy events, which is also the signature expected from oscillations!

To prevent a possible bias in the oscillation parameter fit, it is therefore necessary to remove the lowest-energy events. On the other hand, a large loss of events in the main region of interest around $\sim 25\,\mathrm{GeV}$ must be avoided. Both goals are achieved by the cut on the reconstructed length, as can be seen from the energy distribution in Figure 4.26.

In summary, the final quality cuts are:

$$\begin{aligned} N_{\mathrm{Dir}} &\geq 3\,, \\ L_{\mathrm{Dir}} &\geq 20\,\mathrm{m}\,, \\ \mathrm{pLogL} &\leq 11\,, \\ \mathrm{bayesLLHdiff} &\leq -17\,, \\ r_{\mathrm{vertex}} &< 180\,\mathrm{m}\,, \\ l_{\mathrm{reco}} &> 40\,\mathrm{m}\,. \end{aligned}$$

The distributions of the cut parameters can be found in appendix A.5.

Table 4.6 shows the event rates for experimental data and simulation before and after the cuts. The final sample is dominated by ν_μ events, with a purity of about 70%. Figure 4.26 shows the ν_μ energy and zenith angle distributions before and after the cuts, and in the bottom panels the fraction of events kept. The cuts cause a significant loss of events at the lowest energies. This is the result in particular of the cut on the reconstructed length.

	event rate (Hz) before L8	after L8
ν_μ	$4.39 \cdot 10^{-4}$	$2.78 \cdot 10^{-4}$
ν_e	$9.27 \cdot 10^{-5}$	$4.63 \cdot 10^{-5}$
ν_τ	$2.41 \cdot 10^{-5}$	$9.85 \cdot 10^{-6}$
atm. μ	$2.22 \cdot 10^{-4}$	$6.88 \cdot 10^{-5}$
all MC	$7.78 \cdot 10^{-4}$	$4.03 \cdot 10^{-4}$
exp. data	$6.67 \cdot 10^{-4}$	$3.01 \cdot 10^{-4}$

Table 4.6: Experimental data and simulation event rates in Hz before and after the L8 cuts.

4.15 SUMMARY

Altogether, the event selection succeeds in rejecting more than 6 orders of magnitude of atmospheric muon background, while keeping about 10% of the desired neutrino signal. Figure 4.27 shows the rates of the simulations and the experimental data as a function of the cut level. Table 4.7 lists the final event rates, assuming standard oscillation parameters (see Table 2.1). The final experimental data sample consists of 8117 events. It should be noted that this dataset has much higher statistics than those of typical neutrino oscillation experiments, simply because of the sheer size of IceCube. The difference to the number of events expected from simulations (10874) is quite large, but it should be kept in mind that the number of atmospheric muon events is probably largely overestimated (see Section 4.4). Furthermore, the uncertainty on the absolute normalization of the atmospheric neutrino flux is about 25% (see Section 5.4.1). About 70% of the events in

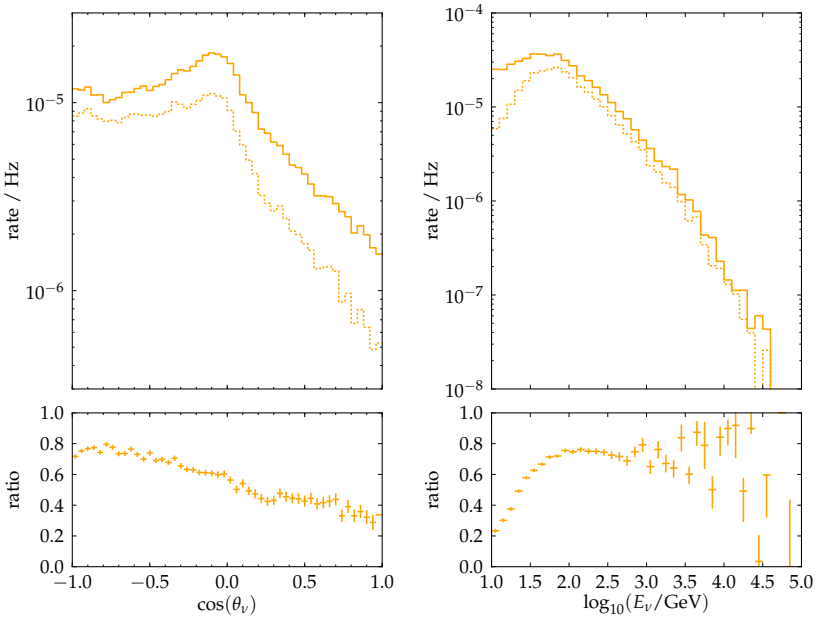

Figure 4.26: Distributions of ν_μ zenith angle (left) and energy (right), before (solid) and after the L8 cuts (dashed). The bottom panels show the ratio of before and after the cuts.

the final sample are expected to be muon neutrinos. Their energy spectrum is shown in Figure 4.28, together with the corresponding spectrum on filter level (L2). It peaks at about 70 GeV and retains high statistics throughout the energy range where oscillation effects are expected. It drops towards the simulation threshold of 10 GeV – less than 3% of the sample are estimated to be below that threshold.

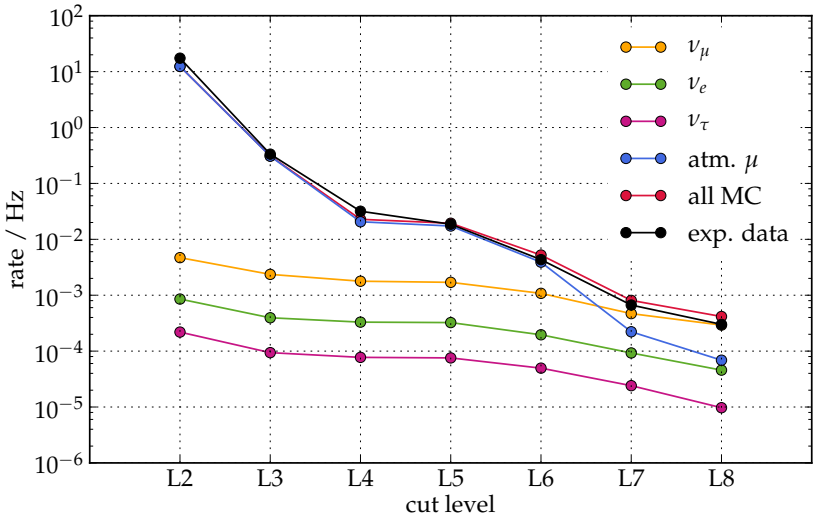

Figure 4.27: Rates of experimental data and simulation as a function of the cut level.

	event rate (Hz)	events in 312.3 d	fraction
ν_μ	$2.78 \cdot 10^{-4}$	7502	69.0%
ν_e	$4.63 \cdot 10^{-5}$	1249	11.5%
ν_τ	$9.72 \cdot 10^{-6}$	266	2.4%
atm. μ	$6.88 \cdot 10^{-5}$	1857	17.1%
all MC	$4.03 \cdot 10^{-4}$	10874	100%
exp. data	$3.01 \cdot 10^{-4}$	8117	–

Table 4.7: Final event rates and numbers for experimental data and simulation. The last column gives the fraction of the total sample of the respective contribution

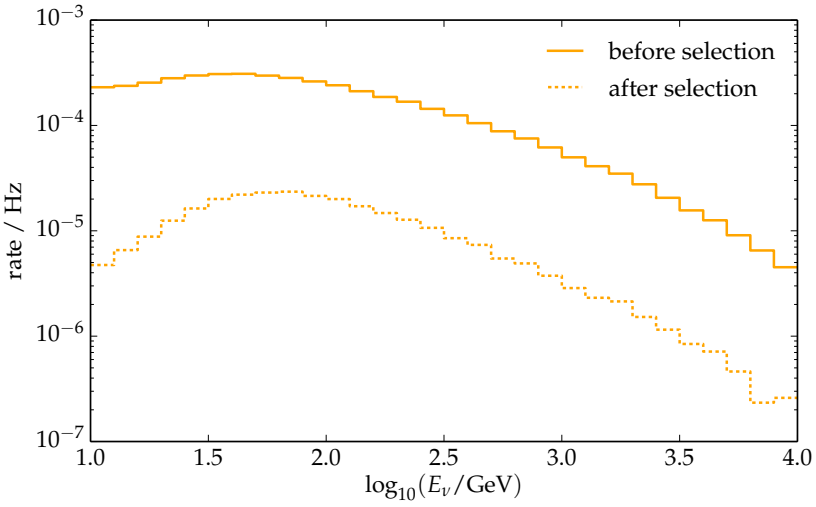

Figure 4.28: Muon neutrino energy spectrum before (solid) and after selection (dashed).

5 Analysis method

In this analysis the oscillation parameters are derived from a comparison of the experimental data to the expectation from the simulation. Basis of this comparison is the two-dimensional distribution of oscillation length and neutrino energy (see for example Figure 2.12). Both oscillation length and energy are not directly observable in the detector. Suitable detector observables, which are correlated with these quantities, are the reconstructed zenith angle and geometrical event length, as described in Section 5.1. The performance of the algorithms reconstructing these observables is evaluated in Section 5.2, before the actual analysis method is introduced in Section 5.3. Systematic uncertainties are considered in Section 5.4, and a validation of the method is presented in Section 5.5.

5.1 Detector observables

Oscillation length The oscillation length L_{osc} is directly connected to the neutrino zenith angle θ_ν measured in IceCube, as illustrated by Figure 5.1. It can be calculated as

$$L_{\text{osc}} = \left[r_{\text{atm}}^2 + r_{\text{det}}^2 - 2 r_{\text{atm}} r_{\text{det}} \cdot \cos\left(\theta_\nu - \arcsin\left(\frac{\sin(\pi - \theta_\nu) \cdot r_{\text{det}}}{r_{\text{atm}}} \right) \right) \right]^{\frac{1}{2}}.$$

Here, $r_{\text{atm}} = 6391\,\text{km}$ is the distance from the center of the Earth to the edge of the atmosphere, $r_{\text{det}} = 6369\,\text{km}$ is the distance from the center of the Earth to the detector, and θ_ν is the zenith angle of the neutrino.

In this analysis, however, the comparison of experimental data and simulation uses directly the (reconstructed) zenith angle; a conversion to oscillation length is never performed. Only when calculating the oscillation probabilities for the simulated neutrino events, the software performs a conversion from the (simulated) zenith angle to oscillation length.

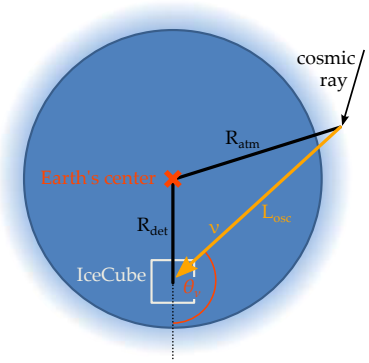

Figure 5.1: Connection between oscillation length and neutrino zenith angle.

Neutrino energy The muons in the energy range of interest for this analysis are mostly minimum ionizing, which means that the length of the muon track is proportional to its energy (see Section 3.1.2). The relation between muon energy and neutrino energy depends on the inelasticity of the interaction (see Section 3.1.1). On average, however, the muon energy is proportional to the neutrino energy, $\langle E_\mu \rangle \propto E_\nu$, and therefore the reconstructed muon track length

is used as a measure for the neutrino energy. Figure 5.2 shows the correlation of the muon track length and the neutrino energy for the ν_μ selected in this analysis. The neutrino energy sets an upper limit for the muon track length. There is no lower limit, though. Even a high-energy neutrino can yield a muon with a vanishing track length if the largest fraction of the energy goes into the hadronic cascade.

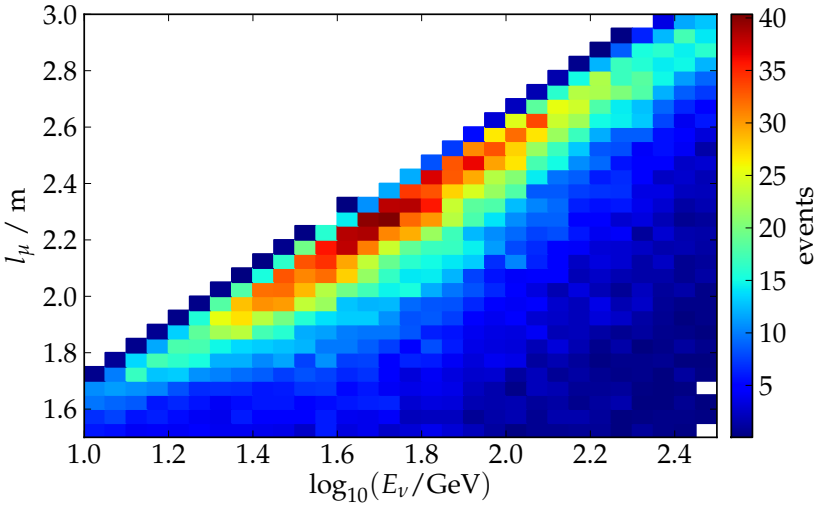

Figure 5.2: Correlation of simulated muon track length l_μ and neutrino energy E_ν for the selected muon neutrinos.

OSCILLATION SIGNATURE IN DETECTOR OBSERVABLES The expected oscillation signature in these detector observables is shown in Figure 5.3. Both plots show the distribution of simulated muon track length l_μ and neutrino zenith angle θ_ν for the selected ν_μ. While the left plot shows the expectation without oscillations, the right plot assumes the standard oscillation parameters given in Table 2.1. The minimum at short track lengths and large zenith angles is obvious.

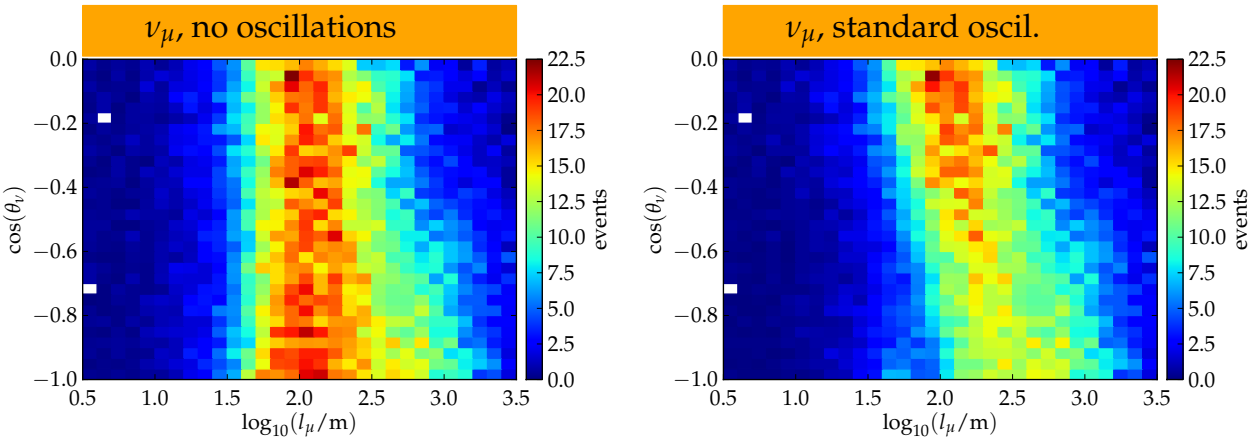

Figure 5.3: Distribution of simulated muon track length and neutrino zenith angle for the selected ν_μ, assuming no oscillations (left) and oscillations with the standard parameters from Table 2.1 (right). The oscillations cause a large minimum at short track lengths and large zenith angles.

5.2 RECONSTRUCTION PERFORMANCE

The previous section showed the effect of oscillations on the simulated distributions of zenith angle and muon track length. In the actual analysis, these two parameters have to be reconstructed from detector data. The performance of the reconstruction algorithms is thus critical.

ZENITH ANGLE The MPE likelihood fit (see Section 4.9) that was also used in the last step of the event selection (see Section 4.14) is used for the reconstruction of the zenith angle. The MPE fit is a standard IceCube tool, used by many analyses, and with a well-understood behavior and performance. Typically, it achieves a median resolution of better than 1° [9]. Since it was not developed for the low-energy range of this analysis, however, such a performance cannot be expected here. Figure 5.4 shows the cumulative distribution of the difference between reconstructed and simulated neutrino zenith angle for the ν_μ selected in this analysis. The distribution extends to large values and a median resolution of slightly less than 10° is achieved here.

[9] M. G. Aartsen et al. Search for a diffuse flux of astrophysical muon neutrinos with the IceCube 59-string configuration. *Phys. Rev. D*, in press

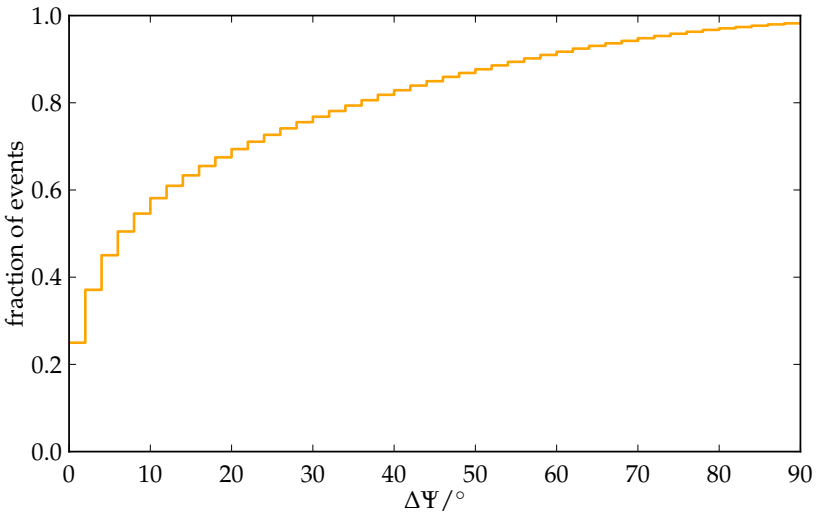

Figure 5.4: Zenith angle resolution for the selected muon neutrinos. Shown is the difference between reconstructed and simulated neutrino zenith angle.

The angular resolution depends strongly on the neutrino energy and zenith angle: Figure 5.5 shows the median zenith angle resolution for various zenith angle and energy bands. For most of the zenith range, the reconstruction achieves a median resolution of less than 5°. Towards the horizon, the resolution degrades. The reason lies in IceCube's geometry: the DOM spacing (7 m) is a factor 10 smaller than the string spacing 70 m). Therefore, horizontal events need higher energies to produce the same number hits – and thus deposit the same amount of information – than vertical events, which move along the strings. Similarly, the resolution is worst at low neutrino energies. In the energy range of the first oscillation maximum, the median resolution reaches about 20°. At the highest neutrino energies, the resolution becomes comparable to that of other high-energy analyses.

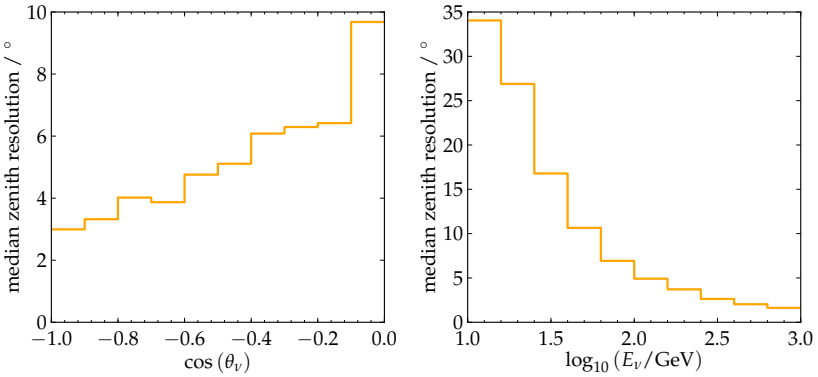

Figure 5.5: Median zenith angle resolution for various zenith angle (left) and energy bands (right). For each zenith band the resolution is calculated from all energies, and for each energy band from all zenith angles.

Figure 5.6 shows the correlation of reconstructed and simulated neutrino zenith angle. The distribution is not exactly symmetrical, as can be seen from the profile histograms: the distribution is flat in θ_ν, but not in θ_{reco}, where it rises towards small $\cos(\theta_{\text{reco}})$. This means that the algorithm tends to reconstruct events as vertically up-going, independent of their true zenith angle. This behavior transforms the true zenith angle distribution, which is almost flat with a slight increase towards the horizon, into a distribution peaked at the vertical direction (compare for example Figures 5.3 and 5.10). Since the oscillation signature is a depletion of vertically-up-going events, simulation and experimental data have to be in good agreement describing this bias, to prevent possible repercussions on the measured oscillation parameters.

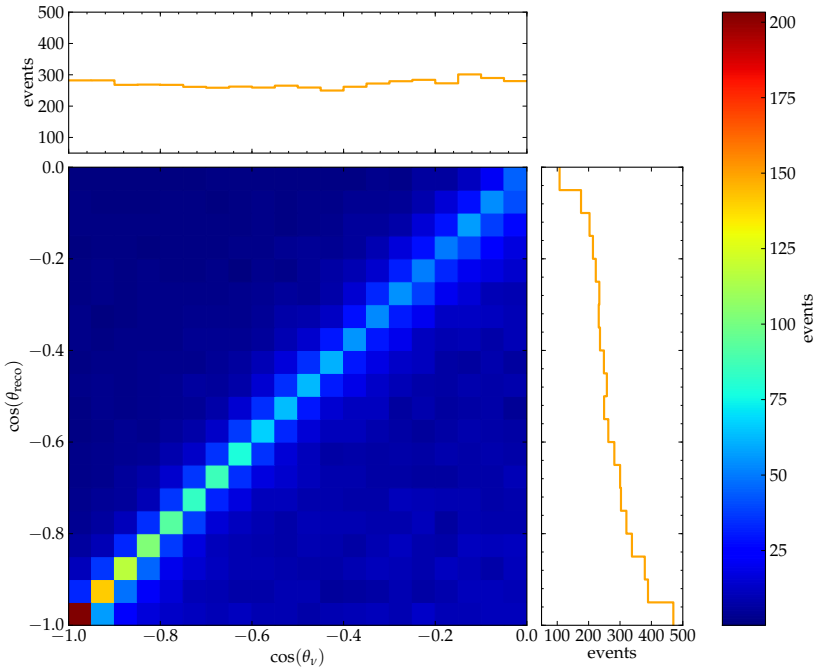

Figure 5.6: Correlation of reconstructed zenith angle θ_{reco} and simulated neutrino zenith angle θ_ν for the selected ν_μ. Also shown are the profile histograms along the x- and y-axis.

TRACK LENGTH The muon track length is reconstructed by FiniteReco (see Section 4.7), and was – as the zenith angle reconstruction – al-

ready used in the last step of the event selection (see Section 4.14). Since the reconstructed track length is to be used as an energy proxy in this analysis, it must be ensured that FiniteReco delivers an unbiased and reasonably precise estimate of the true muon track length, in order to preserve the correlation between track length and neutrino energy seen in Figure 5.2.

Figure 5.7 shows the difference of the reconstructed and the simulated track length for the selected ν_μ. The distribution is peaked at 0, but exhibits a longer tail towards the left, caused by muon tracks only partially contained within the detector. For these tracks the reconstructed length is always shorter than the true length, since only the part within the detector can be observed and reconstructed. This is necessarily the case for both experimental and simulated data, and thus no problem for the further analysis. The width of the distribution is about 60 m. As this corresponds to an energy resolution of roughly ~ 12 GeV, it is considered to be sufficient for the purpose of this analysis.

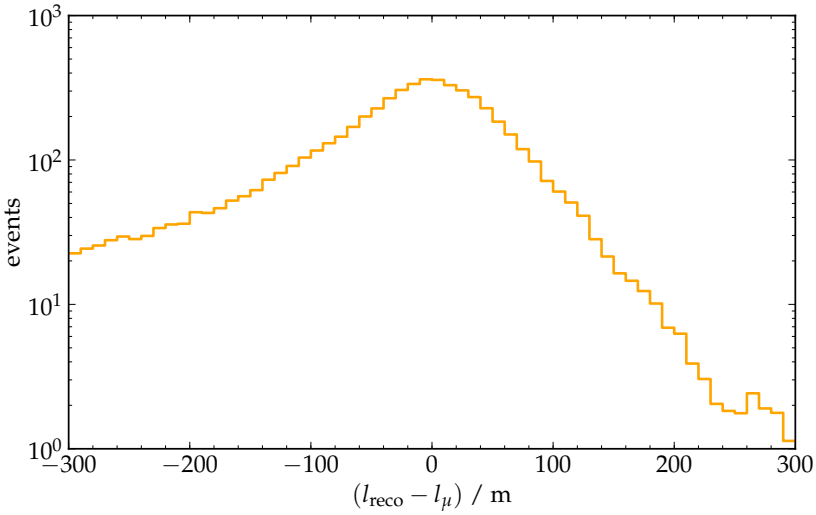

Figure 5.7: Difference between reconstructed muon track length l_{reco} and simulated track length l_μ for the selected muon neutrinos.

To check for a length-dependent bias, Figure 5.8 shows the difference of reconstructed and simulated track length as a function of the simulated track length. The black points show mean and standard deviation of the distribution. The distribution for all selected ν_μ events in the upper panel exhibits an apparent length-dependent bias: For short tracks the length is overestimated, whereas the length of longer tracks is systematically underestimated. The lower panel, however, proves that this bias is merely an artifact of the chosen quantities and caused by the hard lower edge of the distribution: when only events away from this edge are selected, the apparent bias completely vanishes. It is also interesting to note that, through the whole range, the length resolution stays approximately constant at about 60 m.

Finally, Figure 5.9 shows the correlation of reconstructed track length and neutrino energy, which is fundamental for the success of the analysis. The correlation is not nearly as strong as for the

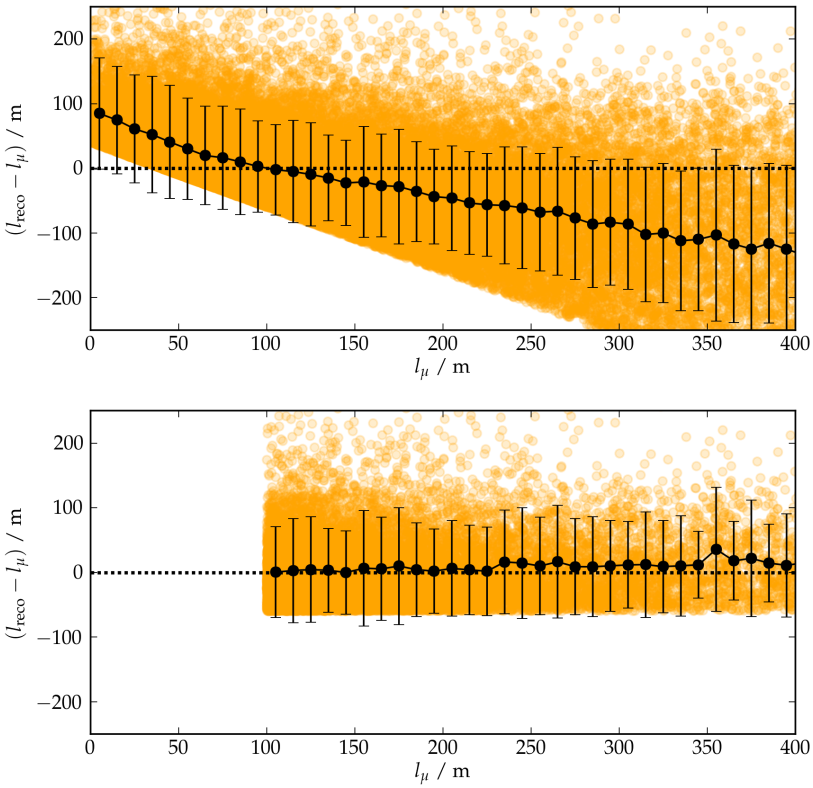

Figure 5.8: Difference between reconstructed muon track length l_{reco} and simulated track length l_μ for the selected muon neutrinos (top) and the same quantity for only those events with $l_\mu > 60\,\text{m}$ and $l_{\text{reco}} - l_\mu > -60\,\text{m}$ (bottom). The black points show mean and standard deviation of the distribution.

simulated track length, but still well visible. The distribution shows some structure at $l_{\text{reco}} = 100\,\text{m}$, which was found to stem from the Photorec tables used by FiniteReco (see Section 4.7), but does not impact the overall performance.

OSCILLATION SIGNATURE IN RECONSTRUCTED OBSERVABLES In comparison to Figure 5.3, Figure 5.10 shows the expected oscillation signature in the reconstructed detector observables, i.e. the reconstructed muon track length and zenith angle. As mentioned before, the behavior of the reconstruction algorithms causes the peak towards the vertical direction. Again, the left plot shows the expectation without any oscillations, and the right plot assumes standard oscillation parameters. The binning was adapted to the binning which is used in the analysis procedure (compare with Figure 5.11). The diagonal structure of the oscillation minimum from Figure 5.3 is no longer visible, but the overall difference in shape is still immediately noticed.

5.3 THE LIKELIHOOD FIT

The fundamental technique for the determination of the oscillation parameters is a likelihood analysis, comparing the two-dimensional distribution of reconstructed zenith angle and track length to the expectation from the simulation. This expectation changes under variation of the oscillation parameters and is fitted to the data by maximizing a global likelihood. Those oscillation parameters which

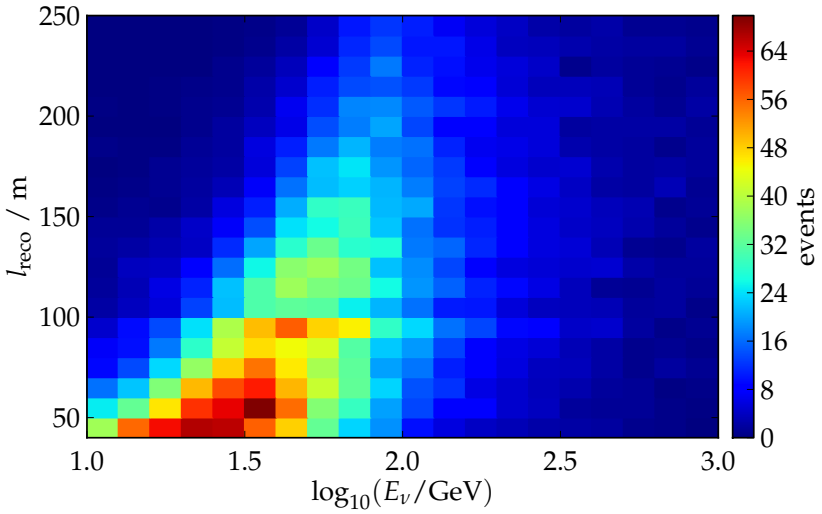

Figure 5.9: Correlation of reconstructed track length l_{reco} and simulated neutrino energy E_ν for the selected muon neutrinos.

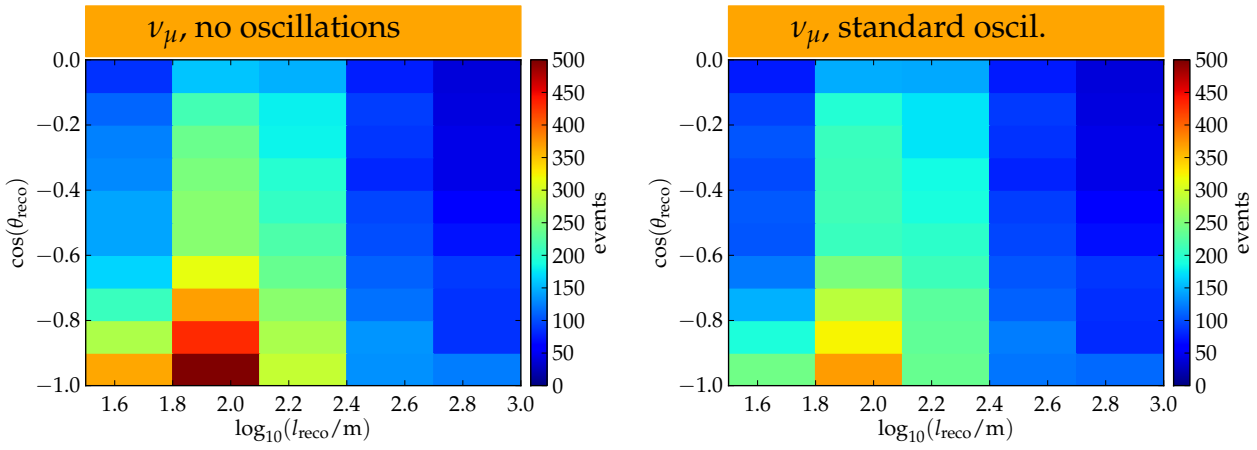

Figure 5.10: Distribution of reconstructed muon track length and zenith angle for the selected ν_μ, assuming no oscillations (left) and oscillations with standard parameters (right).

yield the maximum likelihood – and thus the best agreement with the experimental data – provide the result of this analysis.

5.3.1 PREPARATION OF THE 2D-HISTOGRAMS

In the first step the histograms used in the likelihood fit are prepared. Experimental data and the individual simulation components are filled into two-dimensional histograms of reconstructed zenith angle and track length. The cosine of the zenith angle is binned in 10 bins between $\cos(\theta_\nu) = -1.0$ (vertically up-going) and $\cos(\theta_\nu) = 0.0$ (horizontal), the reconstructed length in 5 logarithmic bins between $\log_{10}(l_{\text{reco}} = 1.5)$ and $\log_{10}(l_{\text{reco}} = 3.0)$. A finer binning would push the statistics per bin below an acceptable limit (at least in the atmospheric muon and the ν_τ histograms, see Figure 5.11), and an even coarser binning would risk to destroy the oscillation signature. For the comparison to experimental data, the individual simulation components have to be added. In this process, the relative normalizations can be chosen individually for each component, to account for certain systematic effects (see Section 5.4). For the neutrino simulations, two further parameters are taken into account, as well: the variations of the primary cosmic ray spectral index and of the contribution of kaons relative to pions to the neutrino flux (only for ν_μ and ν_τ). All these parameters are described in detail in Section 5.4.1. Finally, the histograms depends on the choice of the oscillation parameters. All these parameters are realized by weights, which are multiplied to the already existing weights for each event. The total weights are composed by the following constituents:

- For the neutrino simulations, the basic weight is given by the atmospheric neutrino spectrum according to Honda et al. [56] (see Section 4.2). $w_{\text{atm},i}$ denotes this atmospheric weight, without oscillations, for $i = (e, \mu)$. Note that there is no generic ν_τ weight $w_{\text{atm},\tau}$, since the only source of ν_τ is from oscillations of disappearing ν_μ events! Thus the ν_τ events have to be provided with the atmospheric ν_μ weight instead.

- For the atmospheric muon simulation the basic weight of each event is simply 1.

- $P_{\mu\to\mu}$ and $P_{\mu\to\tau}$ are the muon survival and tau appearance probability, respectively. Note that no oscillation probability is applied to the ν_e in the two-flavor approximation used here!

- c_i denotes the normalization for each component $i = (e, \mu, \tau)$.

- $E^{\Delta\gamma}$ describes the variation of the primary cosmic ray spectral index, which is the same for all neutrino flavors.

- $\Delta r_{K/\pi}$ describes the variation of the kaon/pion contribution to the neutrino flux.

[56] M. Honda, T. Kajita, K. Kasahara, S. Midorikawa, and T. Sanuki. Calculation of atmospheric neutrino flux using the interaction model calibrated with atmospheric muon data. *Phys. Rev. D*, 75:043 006, Feb 2007. DOI: 10.1103/PhysRevD.75.043006

To summarize, the weights are given by:

$$\begin{aligned} w_\mu &= w_{\text{atm},\mu} \cdot c_\mu \cdot P_{\mu\to\mu} \cdot E^{\Delta\gamma} \cdot \Delta r_{K/\pi} && \text{(for } \nu_\mu\text{)} \\ w_e &= w_{\text{atm},e} \cdot c_e \cdot E^{\Delta\gamma} && \text{(for } \nu_e\text{)} \\ w_\tau &= w_{\text{atm},\mu} \cdot c_\tau \cdot P_{\mu\to\tau} \cdot E^{\Delta\gamma} \cdot \Delta r_{K/\pi} && \text{(for } \nu_\tau\text{)} \\ w_c &= c_c && \text{(for atm. } \mu\text{)} \end{aligned} \tag{5.1}$$

It should be noted that $E^{\Delta\gamma}$ and $\Delta r_{K/\pi}$ (and of course the oscillation probabilities) are functions of the neutrino energy and zenith angle and have thus to be calculated for every event individually! The normalizations c_i, on the other hand, are global factors and equal for all events.

Figure 5.11 shows the 2D-histograms for the individual simulation components, for their sum, and for experimental data, with all parameters are set to their default values.

5.3.2 COMPARISON OF THE HISTOGRAMS

The comparison of the combined simulation and experimental data histograms is realized by means of a Poisson likelihood: For each bin (i, j) of the histograms of zenith angle and track length, the probability to observe d_{ij} events in the experimental data is calculated, given s_{ij} in the combined simulation prediction:

$$L_{\text{Poisson}} = \frac{s_{ij}^{d_{ij}}}{d_{ij}!} \cdot \exp(-s_{ij}) \,.$$

The logarithm of this expression is summed over all bins to obtain the negative log-likelihood that is minimized (constant terms are omitted):

$$-LLH = \sum_{i,j} \left(s_{ij} - d_{ij} \ln\left(s_{ij}\right) \right) \,.$$

Strictly speaking, the Poissonian approach described above is valid only in the limit of infinite simulation statistics, because it assumes s_{ij} to be perfectly well known and to be free from statistical fluctuations. There exists a modification of the standard Poisson likelihood to take into account finite simulation statistics [41]. The statistics of the ν_μ and ν_e simulations used in this analysis cover more than a year of detector livetime, but the statistics of the ν_τ simulations are much lower, and the statistics of the atmospheric muon simulations are low on all accounts (see Figure 5.11). Therefore, the modified likelihood was tested in the course of this thesis. In data challenges (see Section 5.5), however, it was not found to be noticeably superior to the classical Poisson likelihood. Because this modified approach is computationally more expensive, the standard Poisson formulation is used throughout this analysis.

[41] D. Chirkin. Likelihood description for comparing data with simulation of limited statistics. *arXiv:1304.0735 [astro-ph.IM]*, 2013

5.3.3 NUISANCE PARAMETERS

Besides the oscillation parameters Δm^2_{32} and $\sin^2(2\theta_{23})$, the additional parameters described in Section 5.3.1 are implemented in the fitting

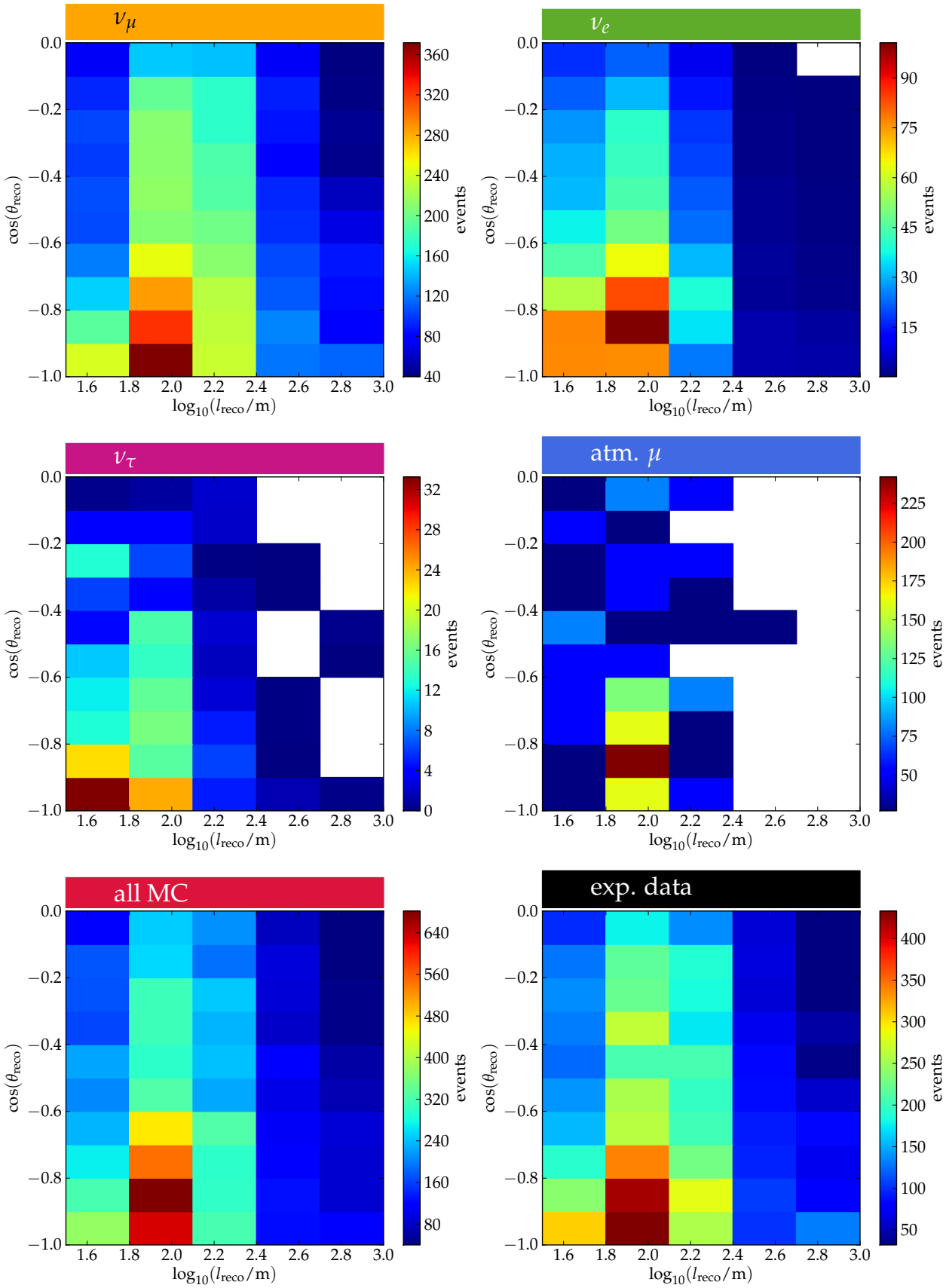

Figure 5.11: Two-dimensional histograms of reconstructed track length and zenith angle, for the individual simulation components, their sum and experimental data. For the simulated data, standard oscillation parameters are assumed, all relative normalizations are set arbitrarily to 1.0, as well as the changes in spectral index and the relative kaon/pion contributions.

procedure as nuisance parameters k, to absorb certain systematic uncertainties. Prior knowledge about their values (if available) is incorporated in the form of Gaussian priors, which are added to the likelihood, yielding the final expression

$$-LLH = \sum_{i,j} \left(s_{ij} - d_{ij} \ln\left(s_{ij}\right)\right) + \frac{1}{2} \sum_{k} \left(\frac{q_k - \langle q_k \rangle}{\sigma_k} \right)^2 . \qquad (5.2)$$

The Gaussian priors penalize the likelihood for nuisance parameter values too far from the expected value and thus prevent the fit from wandering into unphysical regions. Section 5.4 describes in more detail the systematic effects covered by this approach and gives in Table 5.1 the values of $\langle q_k \rangle$ and σ_k.

5.3.4 OSCILLATION PARAMETER FIT

The negative log-likelihood (Equation 5.2) is minimized with respect to the oscillation parameters Δm^2_{32} and $\sin^2(2\theta_{23})$. In each minimization step, the minimizer chooses a new set of oscillation and nuisance parameters and creates a new combined simulation histogram by recalculating the weights accordingly, as explained in Section 5.3.1. The minimum of the likelihood space yields the best-fit oscillation parameters. It should be noted that the fitted parameter is $\sin^2(2\theta_{23})$, and not the mixing angle θ_{23}. This requires the parameter to be bounded above, because values of $\sin^2(2\theta_{23}) > 1$ are unphysical.

5.3.5 REJECTION OF THE NON-OSCILLATION HYPOTHESIS

Besides the best-fit values of the oscillation parameters, the primary result of this analysis is the rejection of the non-oscillation hypothesis with a certain significance. A commonly used method to estimate a significance in a likelihood analysis relies on Wilks' theorem [102], which says that for two different hypotheses H and H_0 (under certain conditions) the test statistic $2\Delta LLH = 2\left(LLH(H_0) - LLH(H)\right)$ will be χ^2-distributed with degrees of freedom equal to the difference in dimensionality of H and H_0. In that case, the significance can be calculated from the likelihood ratio using a χ^2 distribution with the corresponding number of degrees of freedom.

[102] S. Wilks. The Large-Sample Distribution of the Likelihood Ratio for Testing Composite Hypotheses. *Annals Math.Statist.*, 9(1):60–62, 1938. DOI: 10.1214/aoms/1177732360

For this analysis, the non-oscillation hypothesis is H_0, and the likelihood value for the best-fit point (H) has to be compared to the likelihood value of H_0. The null hypothesis H_0 is realized by performing another fit with the oscillation parameters set to $\Delta m^2_{32} = 0$ and $\sin^2(2\theta_{23}) = 0$, and only the nuisance parameters are left free to float. The difference in dimensionality of H and H_0 is thus 2 (the two oscillation parameters), and the test statistic $2\Delta LLH$ would be expected to follow a χ^2 distribution with 2 degrees of freedom.

However, Wilks' theorem is not fully applicable under certain conditions, for example:

- if the parameters are bounded in the fitting process. This condition is certainly realized in this analysis, where the mixing angle is

bounded above at 1. For technical reasons (to prevent the minimizer from testing unphysical values), also some other parameters are bounded, even if the allowed range is large, and extreme values are never reached in the minimization process.

- if the null hypothesis H_0 is not well-defined. In this analysis, the null hypothesis can be obtained by setting either one of the oscillation parameters to 0, the value of the other parameter is then no longer relevant.

It has been shown that the likelihood ratio test can be modified to yield again a χ^2 distribution [38], but the extent to which the distribution of $2\Delta LLH$ differs from the χ^2 distribution is not obvious a priori. The χ^2-like behavior of the likelihood ratio can be tested in data challenges (see Section 5.5). In principle, the agreement has to be verified over the whole parameter space. For this analysis, we have found for a few test points that the deviation from a χ^2 distribution is not too large, and Wilks' theorem can be used as an approximation (see Section 5.5). For the final result, however, we will perform full ensemble tests which will deliver a correct confidence result.

[38] H. Chen, J. Chen, and J. D. Kalbfleisch. A modified likelihood ratio test for homogeneity in finite mixture models. *Journal of the Royal Statistical Society. Series B (Statistical Methodology)*, 63(1):19–29, 2001

5.3.6 PARAMETER SCAN

To obtain confidence contours as in Figure 2.14, a scan of the oscillation parameter space is performed. In every point of a regular grid over the chosen region of the parameter space, a minimization of the likelihood with respect to only the nuisance parameters is done, while the oscillation parameters are fixed to the values determined by the grid point. The ratio of the likelihood value at each point to the fitted global maximum is used to calculate confidence regions in the oscillation parameter space. The significance levels are approximated on the basis of Wilks' theorem.

5.4 SYSTEMATICS

While the size of IceCube provides much higher statistics than "classical" oscillation experiments, the insight into systematic influences is more indirect than under laboratory conditions. It should be noted that the event selection was designed to keep a large range in energy and zenith angle including also regions where no oscillation effects are expected. The reason is that, in the global fit, these regions constrain the systematics – in particular the normalizations.

In this analysis, systematic effects are taken into account by varying the simulated prediction and thus changing the level of agreement with the experimental data. Depending on the particular systematic influence, two different approaches are being followed:

- *Continuous parameters*: systematic effects which can be modeled by continuously reweighting the simulated events.
- *Discrete parameters*: systematic effects which can be modeled only by discrete simulation datasets.

5.4.1 CONTINUOUS PARAMETERS

Certain systematic effects are absorbed by the nuisance parameters described in Section 5.3.3. For this approach, the systematic effects are modeled by weights which are applied to the individual events as described in Section 5.3.1, and in particular in Equations 5.1.

NORMALIZATIONS The absolute normalizations c_i of the individual simulation components i absorb the uncertainty of the absolute cosmic ray flux, but also uncertainties in the neutrino cross sections and the overall optical efficiency of the detector. The normalizations of the ν_μ and ν_τ subsamples have been condensed to one common normalization $c_{\mu\tau} := c_\mu = c_\tau$, since ν_τ can only stem from oscillations of ν_μ. This approach somehow ignores uncertainties in the ν_τ cross sections, but this is a small effect, since the number of ν_τ events in the data sample is small. It also improves the stability and execution speed of the minimization process. The ν_e normalization c_e is kept independent to be able to absorb uncertainties in the atmospheric ν_μ/ν_e production ratio (see Section 2.2). The effect of a normalization shift on the expected distributions of reconstructed length and zenith angle is illustrated by Figure 5.12. It shows for the selected ν_μ the length and zenith angle distributions obtained with the default normalization, and with the normalization increased and decreased by 25%.

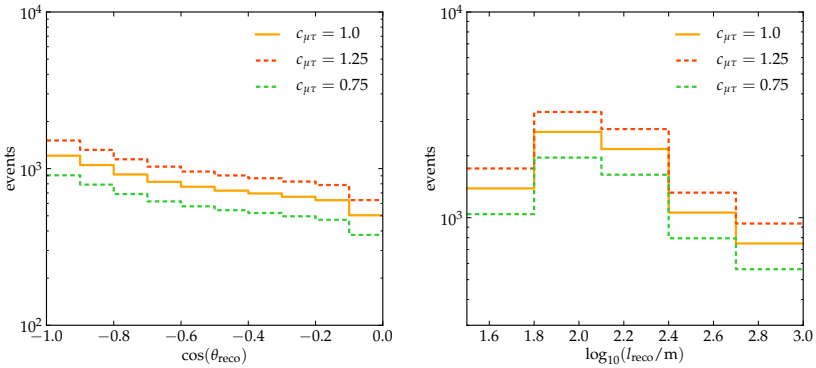

Figure 5.12: Distribution of reconstructed zenith angle (left) and length (right), for the default normalization $c_{\mu\tau}$, and for the normalization varied by 25% in both directions.

SPECTRAL INDEX A change in the spectral index γ of the primary cosmic ray spectrum manifests itself almost exclusively in the reconstructed length distribution: A harder spectral index yields relative more events at higher energy, and thus more tracks with greater length. Figure 5.13 shows the length and zenith angle distributions obtained with the default spectral index $\gamma = 2.65$, and with modified values of $\gamma = 2.40$ and $\gamma = 2.90$. Note that a variation this large was chosen only to make the effect more visible and is overestimating the actual uncertainty, which is about $\Delta\gamma = \pm 0.05$.

In principle, a variation of the spectral index as described by Equation 5.1 is highly correlated to the absolute normalization: Since neutrino energies are given in GeV, a positive value of $\Delta\gamma$ increases

the weights of all events above 1 GeV, i.e. of all simulated events, since the lower energy threshold for the simulation is 10 GeV. To decouple the spectral index from the normalizations, the weights are always renormalized after the spectral index has been varied.

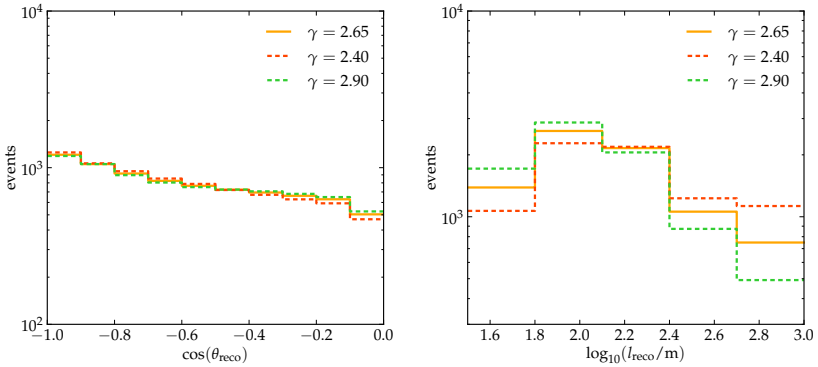

Figure 5.13: Distribution of reconstructed zenith angle (left) and length (right), for the default cosmic ray spectral index, and for the spectral index varied by 0.25 in both directions.

KAON/PION RATIO Even less pronounced is the effect of a different relative contribution of kaons and pions to the atmospheric muon neutrino flux (see Section 2.2). The parameter $r_{K/\pi}$ implemented in the fit describes a scaling of the kaon contribution: a value of $r_{K/\pi} = 1$ corresponds to the default prediction by Honda et al. [56], larger values of $r_{K/\pi}$ imply a larger contribution from kaons. This is realized by multiplying the kaon part of Equation 2.2 for ν_μ by $r_{K/\pi}$ [100]:

$$\Phi_\nu = \frac{0.018 \cdot E^{-\gamma}}{1 + 0.367 \cdot r_{K/\pi}} \left(\frac{1}{1 + 2.77 \cdot E_\nu \cos\theta_\nu / 115\,\text{GeV}} + \frac{0.367 \cdot r_{K/\pi}}{1 + 1.18 \cdot E_\nu \cos\theta_\nu / 850\,\text{GeV}} \right) .$$

The factor $\Delta r_{K/\pi}$, that is multiplied to the event weights (see Equation 5.1), is then given by the ratio of the modified to the default neutrino flux:

$$\Delta r_{K/\pi} = \frac{\Phi_\nu(r_{K/\pi})}{\Phi_\nu(r_{K/\pi} = 1.0)} .$$

Again, the weights are renormalized after changing the kaon/pion ratio parameter to decouple its effects from the absolute normalization.

Figure 5.14 shows the length and zenith angle distributions obtained with the default value of $r_{K/\pi}$, and with the kaon contribution increased and decreased by 75%. Again, such a large variation is grossly overestimating the actual uncertainty, which is on the order of 10%, and was chosen only for illustration purposes. A larger kaon contribution leads to an increased flux at high energies and vertical directions. It thus counteracts the energy dependent zenith angle structures seen in Figure 2.9, and evens out the zenith angle spectrum.

THE NUISANCE PARAMETERS are constrained by Gaussian priors, as described in Section 5.3.3. Table 5.1 lists the central values $\langle q_k \rangle$ and uncertainties σ_k for the Gaussian priors as defined in Equation 5.2.

[56] M. Honda, T. Kajita, K. Kasahara, S. Midorikawa, and T. Sanuki. Calculation of atmospheric neutrino flux using the interaction model calibrated with atmospheric muon data. *Phys. Rev. D*, 75:043 006, Feb 2007. DOI: 10.1103/PhysRevD.75.043006

[100] C. Wiebusch and S. Euler. IC79 ν_μ Disappearance Analysis: Results. Talk at the IceCube Collaboration Meeting, Madison (WI), 2013. `https://docushare.icecube.wisc.edu/dsweb/Get/Document-65382/Christopher_Wiebusch_IC79OscillationResults_Parallel_Madison2013.pptx`

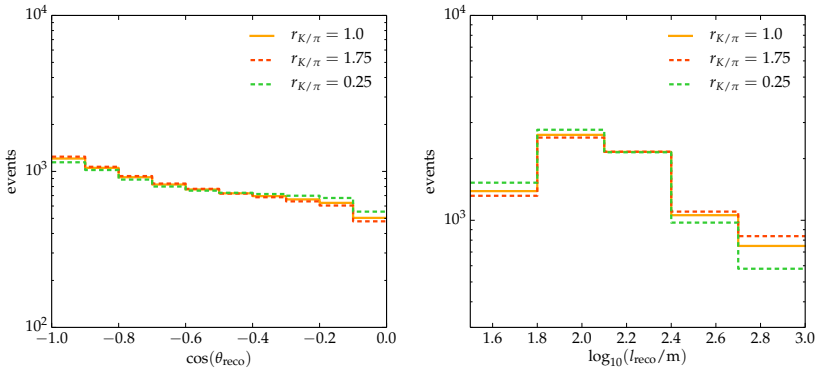

Figure 5.14: Distribution of reconstructed zenith angle (left) and length (right), for the default kaon/pion ratio parameter $r_{K/\pi}$, and for the parameter varied by 75% in both directions.

Note that the prior of the ν_e normalization c_e is centered around the ν_μ & ν_τ normalization and is given an uncertainty of 20% of that value. Large differences between the ν_e normalization and the ν_μ & ν_τ normalization are thus disfavored in the fit. The atmospheric muon normalization is given no constraint at all, because the simulation is believed to overestimate this contribution by an unknown factor (see Section 5.4.2).

nuisance parameter k		$\langle q_k \rangle$	σ_k
$c_{\mu\tau}$	ν_μ & ν_τ norm.	1.0	25%
c_e	ν_e norm.	$c_{\mu\tau}$	20%
c_c	atm. μ norm.	— no constraint —	
γ	spectral index	2.65	0.05
$r_{K/\pi}$	K/π ratio	1.0	10%

Table 5.1: Central values and uncertainties of the Gaussian priors for the nuisance parameters.

5.4.2 DISCRETE PARAMETERS

Systematic effects, which can not be modeled by reweighting the simulated events, are evaluated in separate fits: the whole fitting procedure is repeated with modified simulation datasets, generated with e.g. a different ice model. It should be noted, however, that the parameters are varied only in the neutrino simulation; the atmospheric muon simulation is always the same (see Section 4.4). The global best fit is defined by the dataset that gives the best likelihood at the best-fit point (i.e. globally the deepest minimum). To be able to produce combined confidence regions, also the parameter scan is repeated for each of the modified simulation datasets. Then the infimum of all resulting likelihood maps (i.e. in each bin the minimum likelihood value of all maps) is taken to produce a new, combined likelihood map. This method is in fact a minimization "by hand" and thus fully consistent with the treatment of the continuous nuisance parameters: for every given set of oscillation parameters, the nuisance parameters are chosen to maximize the likelihood. In case of the nuisance parameters, a minimizer scans a continuous parameter space, whereas here simply the lowest one of two or three values is chosen. The confidence contours are then calculated on the basis of this combined

likelihood map.

The inclusion of additional systematic datasets introduces another problem: The likelihood values are comparable only if the datasets have the same statistics. If the simulation statistics become small, the statistical errors become large and the agreement with the experimental data becomes better by definition, resulting in a better likelihood value. For this analysis it was made sure that the statistics of the discrete datasets differ by not more than 10%. Additionally, it was checked with the baseline dataset by how much the likelihood value changes if only half of the available simulations were used. It was found that the effect is small – even with only 50% of the simulation statistics the likelihood value improves by only $\sim 0.1\,\sigma$.

ICE MODEL VARIATIONS Variations in the description of the optical properties of the ice are systematic effects which cannot be modeled by reweighting simulated events. Exemplary, Figure 5.15 shows the length and zenith angle distributions obtained with the baseline ice model SPICE Mie, with SPICE Mie, but absorption and scattering reduced by 7%, and with the alternative model WHAM! (see Section 3.3.2).

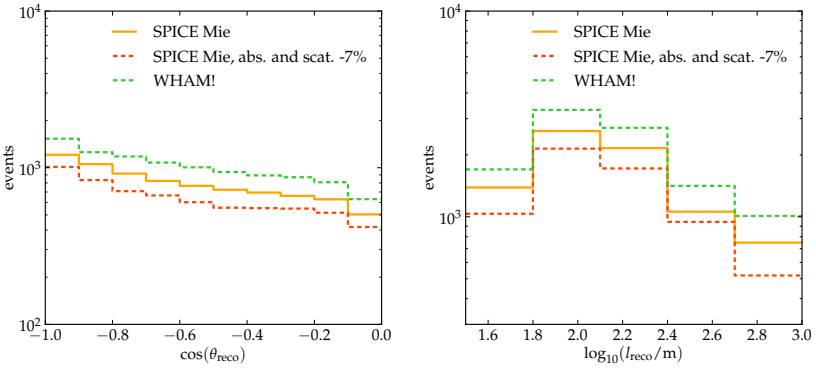

Figure 5.15: Distribution of reconstructed zenith angle (left) and length (right), for the baseline ice model SPICE Mie, for SPICE Mie with scattering and absorption reduced by 7%, and for WHAM!, an alternative ice model.

Other ice model variations considered in this analysis are:

- SPICE Mie with scattering increased by 10%
- SPICE Mie with absorption increased by 10%
- The hole ice, the refrozen ice around the strings, is known to have scattering and absorption properties very different from the bulk ice, modifying the angular acceptance of the DOMs (see Section 3.3.3). The baseline simulation assumes a scattering length of only 50 cm. For this analysis, additionally the (unrealistic) case of no hole ice – or hole ice with the same properties as the bulk ice – was considered.

OPTICAL EFFICIENCY The optical efficiency is a simulation parameter combining several systematic effects that are related to the apparent "brightness" of an event of a certain energy, i.e. to the *energy scale*. These effects are all highly correlated:

- the amount of Cherenkov photons produced by the charged particles traveling through the ice
- the optical transparency of the ice
- the optical transparency of the refrozen hole ice around the strings
- the quantum efficiency of the PMT
- the overall photon detection efficiency of the assembled DOM
- shadowing of photons by detector components, e.g. cables

All these effects are primarily correlated with the total normalization and can thus be combined into one single parameter. In the simulation this is realized by scaling the photon detection efficiency of the DOM. The baseline simulation uses a value of 110% (in arbitrary units), the estimated uncertainty is on the order of 10%. Figure 5.16 shows the length and zenith angle distributions obtained with the baseline value of 110%, and with two alternative values of 100% and 120%.

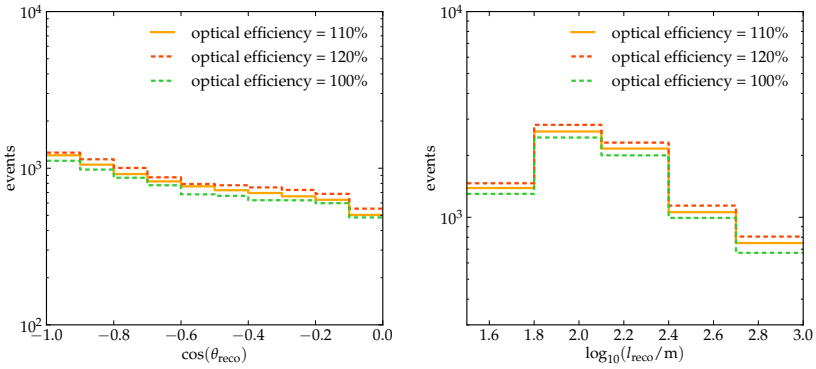

Figure 5.16: Distribution of reconstructed zenith angle (left) and length (right), for the default optical efficiency of 110%, and for the parameter varied by 10% in both directions.

The optical efficiency has particular influence on the efficiency of the veto. A higher optical efficiency makes hits from relatively dark muons more likely and thus the veto more efficient. In the final event sample, it thus yields a higher neutrino fraction, but a lower fraction of atmospheric muons. While the baseline efficiency is 110%, the atmospheric muon simulation used for this analysis was generated with the older default value of 100% (see Section 4.4). This likely leads to an overestimation of the atmospheric muon rates at final level. Studies with low-statistics datasets, simulated with higher optical efficiencies, have indicated that the atmospheric muon rate might be lower by a factor of $\sim$3.

RELATIVE HQE DOM EFFICIENCY Another systematic effect is the relative efficiency of the newer DOMs with higher quantum efficiency, which were deployed mainly on the DeepCore strings (see Section 3.3.3). In laboratory measurements, an efficiency of 1.35 ± 0.03 relative to the standard DOMs was determined. A higher efficiency of these DOMs would effectively lower the trigger threshold and increase

the number of events with very low energies. Because the necessary datasets are not available, this effect is currently not included.

TABLE 5.2 lists all discrete systematics considered in this analysis, the default values and all tested alternatives.

Table 5.2: Default and alternative values of the discrete systematics considered in this analysis.

systematic effect	default value	alternative values
ice model variations	SPICE Mie	SPICE Mie, abs. & scat. -7% SPICE Mie, scattering $+10\%$ SPICE Mie, absorption $+10\%$ SPICE Mie, no hole ice WHAM!
optical efficiency	110%	100% 120%

5.5 DATA CHALLENGES

Before the analysis chain is employed on the experimental data, it is tested in *data challenges*. Here, the complete analysis is tested on simulated data, with known input parameters. The fitted nuisance and oscillation parameters can thus be checked against the input values, which allows to verify that the analysis returns the unbiased input parameters and gives an estimate of its sensitivity. Two approaches have been used here:

- In the *frequentist approach*, many random variations of the combined simulation histogram are created. To produce such a variation, the number of events in each bin is replaced by a random number drawn from a Poissonian distribution with a mean of the number of events in the original combined simulation histogram. All the histograms in the ensemble are then processed through the complete analysis procedure. The fitted oscillation and nuisance parameters are expected to be distributed around the input parameters. The spread of these distributions allows to estimate the sensitivity of the analysis and the correlation of the parameters.

- In the *Asimov approach* [44], only the initial combined simulation histogram itself is put through the analysis procedure. The method relies on the assumption, that this histogram already represents the average of the Poissonian variations created for the frequentist approach[1]. Since it involves the fitting of only this single histogram, it is computationally much less intensive than the frequentist approach. Therefore, with this approach it is possible to perform not only the fitting of the oscillation parameters, but the whole scan of the parameter space. The resulting likelihood map can be translated to Gaussian significances, giving a direct estimation of the size of the confidence contours which can be expected eventually.

[44] G. Cowan, K. Cranmer, E. Gross, and O. Vitells. Asymptotic formulae for likelihood-based tests of new physics. *Eur. Phys. J.*, C71(2):1–19, 2011. DOI: 10.1140/epjc/s10052-011-1554-0

[1] The approach is named after the author Isaac Asimov, in whose science fiction short story *Franchise* [35] elections are replaced by interviewing a single "average" person and predicting the outcome of the potential election from its answers.

5.5.1 DATA CHALLENGE WITH DEFAULT PARAMETERS

In a first data challenge, all parameters are set to their default values, listed in Table 5.3 (compare also with Table 5.1).

parameter	default value	data challenge input value
$\sin^2(2\theta_{23})$	$0.948^{+0.19}_{-0.20}$	0.948
Δm^2_{32}	$2.39^{+0.06}_{-0.10}$	2.39
$c_{\mu\tau}$	1.0 ± 0.25	1.0
c_e	1.0 ± 0.2	1.0
c_c	1.0	1.0
γ	2.65 ± 0.05	2.65
$r_{K/\pi}$	1.0 ± 0.1	1.0

Table 5.3: Input values for the data challenge with default parameters.

Figure 5.17 shows the confidence contours obtained by the Asimov approach, as well as the results of 500 fits with the frequentist approach. The large blue circle denotes the best-fit point of the Asimov approach, the red star marks the input values. The two additional histograms show the projected distributions of the frequentist best fits in mixing angle and mass difference.

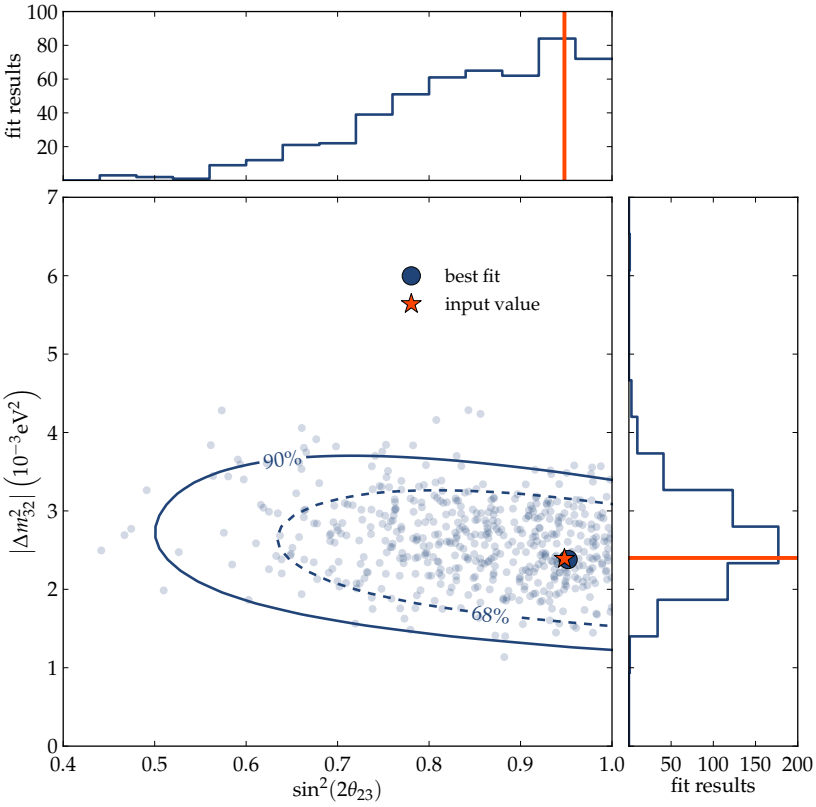

Figure 5.17: Results of the data challenge with default parameters. The confidence regions and the best-fit point are obtained by the Asimov approach. The blue dots denote the best-fit results of 500 frequentist fits. The red star marks the input oscillation parameters.

Both the Asimov approach and the frequentist fits precisely reproduce the input values. The non-oscillation hypothesis can be rejected with a likelihood difference corresponding to about 4.5 σ. The contours were calculated from the likelihood ratios on the basis of Wilks'

theorem. They exhibit a slight overcoverage: the 68% contour contains ∼80%, the 90% contour ∼94% of all frequentist fit results. The likelihood ratios follow reasonably closely a χ^2 distribution, though, as shown by Figure 5.18.

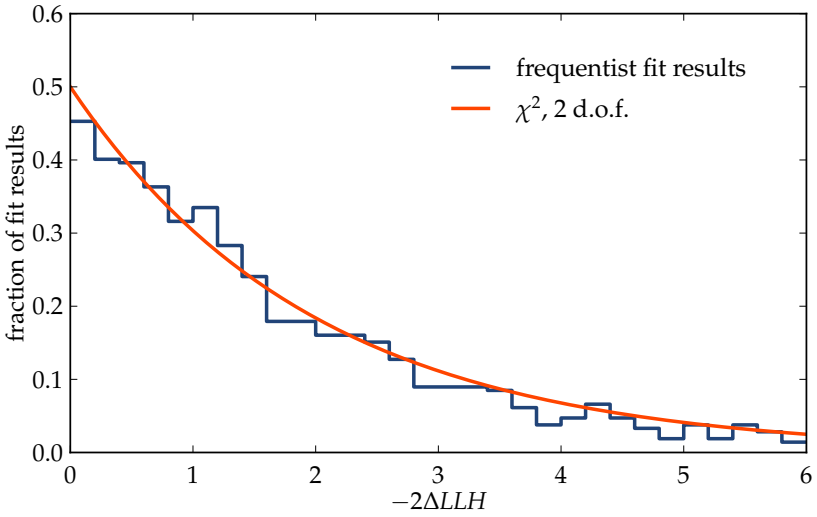

Figure 5.18: Likelihood ratios of the data challenge with default parameters, in comparison with a χ^2 distribution with 2 degrees of freedom.

Finally, Figure 5.19 shows the fitted values of the nuisance parameters. Histogrammed are the results of the frequentist fits, the solid lines mark the result at the Asimov best-fit point, and the dashed red lines always indicate the input value. The vast majority of the fit results are within the assumed uncertainties around their input values. Furthermore, the results at the Asimov best-fit point always agree with the input values.

5.5.2 MAXIMALLY SHIFTED NUISANCE PARAMETERS

In the second data challenge, the values of the nuisance parameters are shifted to the edge of their expected uncertainties. Table 5.4 lists the values of the nuisance parameters. The oscillation parameters are left at their standard values. Figure 5.20 shows the resulting confidence contours and the fit results, as in Figure 5.17. The significance of the rejection of the non-oscillation hypothesis slightly drops to 4.4 σ, and the shape of the contours does not change significantly. It is interesting to note, however, that the contours, together with the best-fit point from the Asimov approach, and also with the distribution of the frequentist fit results, are all shifted towards larger mixing angles and into the unphysical region. The reason for this shift is the small value of the ν_e normalization $c_e = 0.75$, which causes an apparent deficit of low-energy events, requiring stronger oscillations and thus a larger value of $\sin^2(2\theta_{23})$.

5.5.3 DATA CHALLENGE WITH ALL PARAMETERS MODIFIED

A further data challenge sets all parameters to modified values – the oscillation parameters as well as the nuisance parameters. The

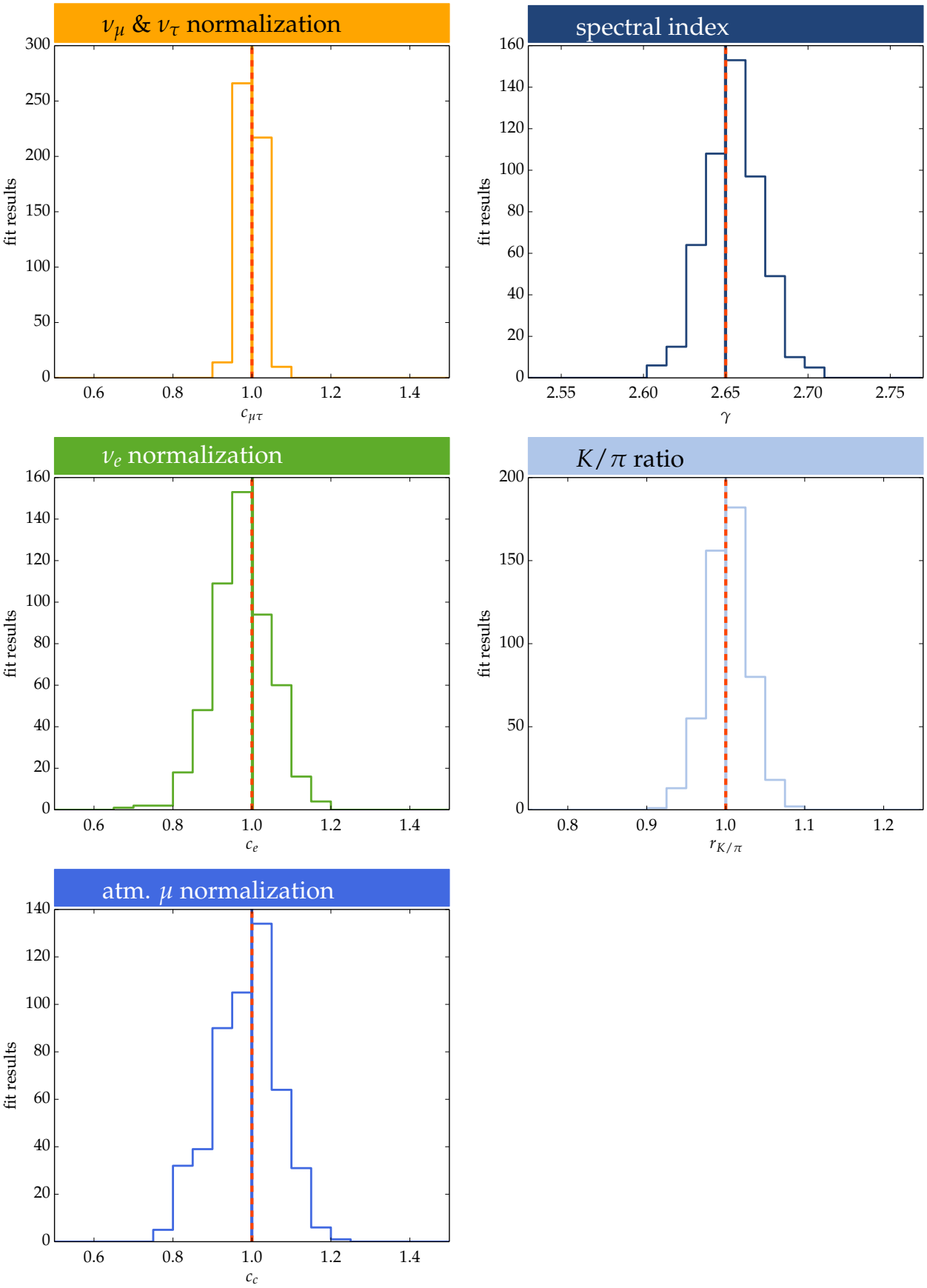

Figure 5.19: Nuisance parameter values fitted in the data challenge with default parameters. The histograms show the results of the frequentist fits, the solid lines mark the result at the Asimov best-fit point, and the dashed red lines indicate the input values.

Table 5.4: Input values for the data challenge with maximally shifted nuisance parameters. For comparison, also the default values are shown.

parameter	default value	data challenge input value
$c_{\mu\tau}$	1.0 ± 0.25	0.9
c_e	1.0 ± 0.2	0.75
c_c	1.0	0.5
γ	2.65 ± 0.05	2.7
$r_{K/\pi}$	1.0 ± 0.1	0.9

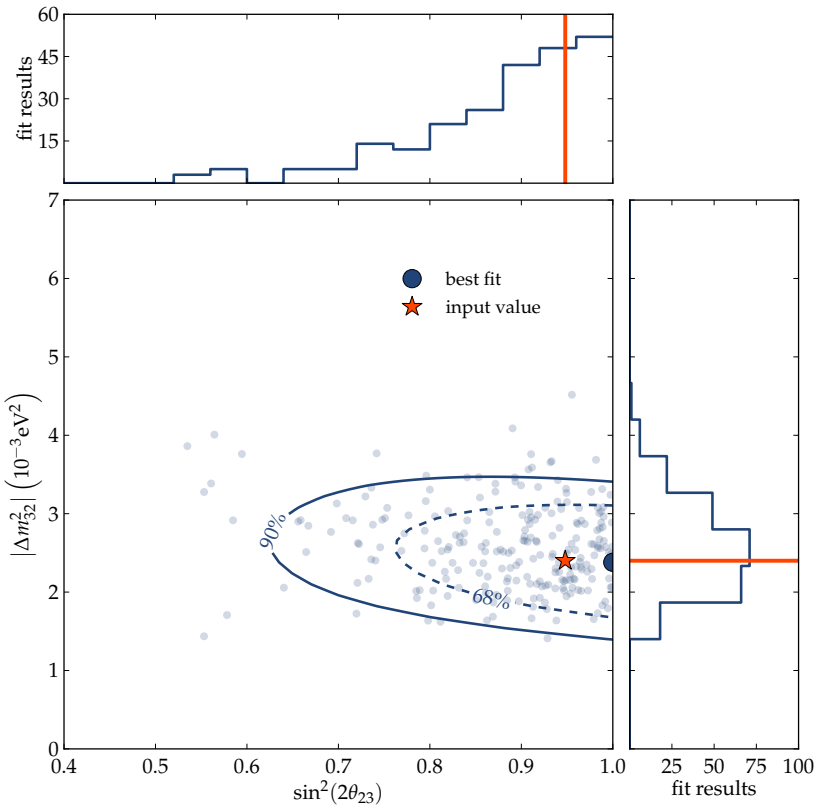

Figure 5.20: Results of the data challenge with maximally shifted nuisance parameters. The confidence regions and the best-fit point are obtained by the Asimov approach. The blue dots denote the best-fit results of 300 frequentist fits. The red star marks the input oscillation parameters.

modified values are listed in Table 5.5, together with the defaults. Partly, they are shifted well out of their expected uncertainties.

parameter	default value	data challenge input value
$\sin^2(2\theta_{23})$	$0.948^{+0.19}_{-0.20}$	0.7
Δm^2_{32}	$2.39^{+0.06}_{-0.10}$	3.5
$c_{\mu\tau}$	1.0 ± 0.25	0.75
c_e	1.0 ± 0.2	0.75
c_c	1.0	1.25
γ	2.65 ± 0.05	2.45
$r_{K/\pi}$	1.0 ± 0.1	1.2

Table 5.5: Input values for the data challenge with all parameters modified. For comparison, also the default values are shown.

Figure 5.21 shows the confidence contours obtained with the Asimov approach, as well as the results of 1000 fits with the frequentist approach. The best fit of the Asimov approach is again slightly shifted from the input values, but well within the 68% contour. The contours again exhibit a slight overcoverage: the 68% contour contains ~74%, the 90% contour ~92% of all frequentist fit results. The likelihood ratios still follow a χ^2 distribution, shown in Figure 5.23.

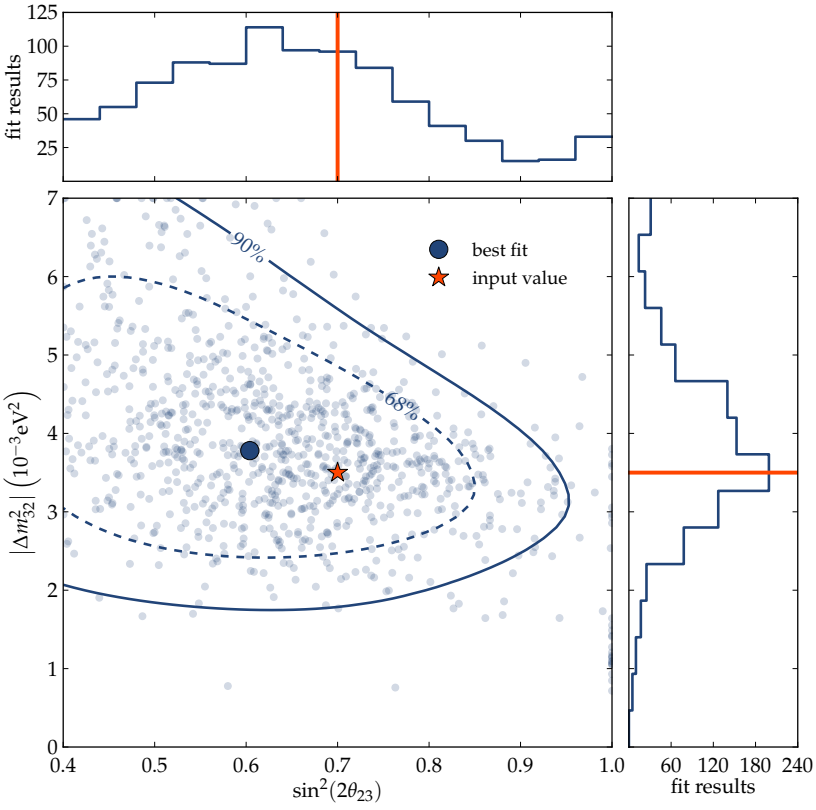

Figure 5.21: Results of the data challenge with all parameters modified. The confidence regions and the best-fit point are obtained by the Asimov approach. The blue dots denote the best-fit results of 1000 frequentist fits. The red star marks the input oscillation parameters.

Figure 5.22 shows the fitted values of the nuisance parameters. As before, the majority of the fit results are within the assumed uncertainties. The width of the distributions is almost the same as before, but the differences between the results at the Asimov best-fit point and the input values are slightly larger.

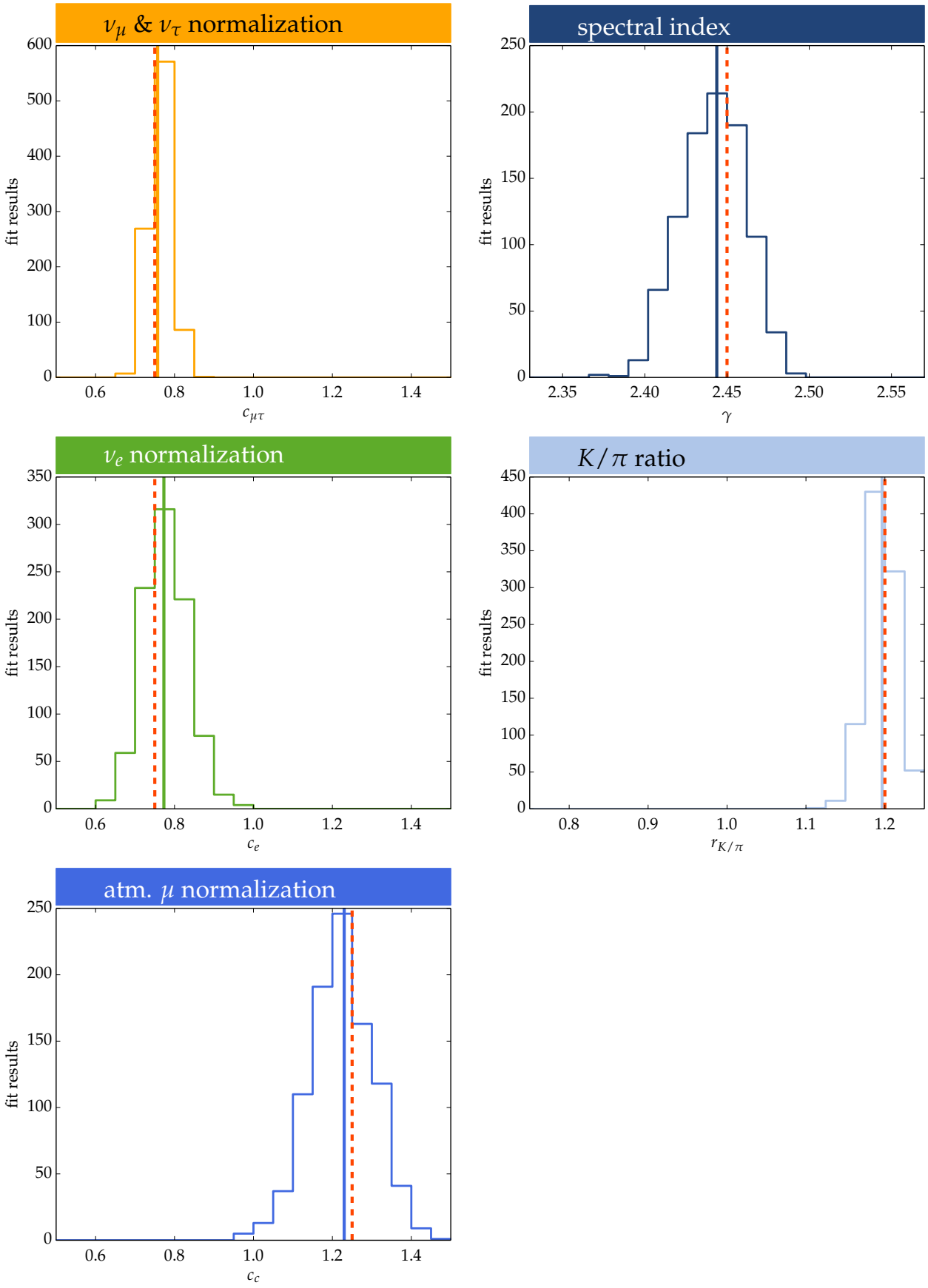

Figure 5.22: Nuisance parameter values fitted in the data challenge with all parameters modified. The histograms show the results of the frequentist fits, the solid lines mark the result at the Asimov best-fit point, and the dashed red lines indicate the input values.

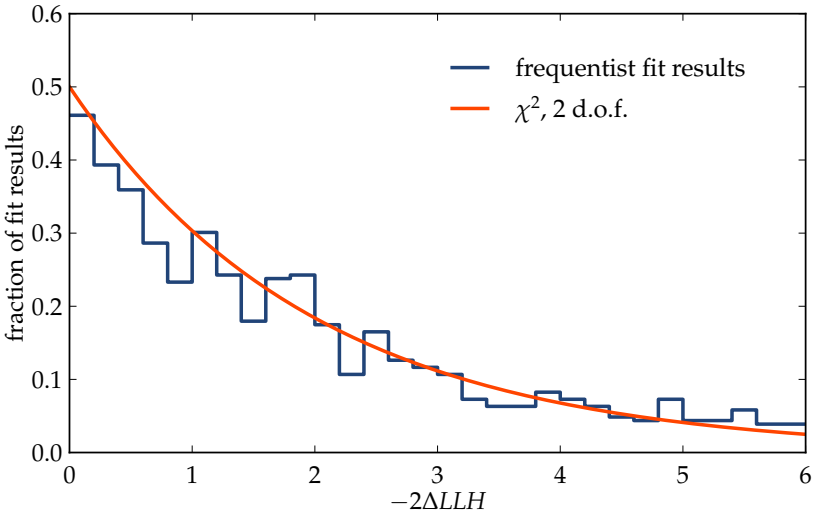

Figure 5.23: Likelihood ratios of the data challenge with all parameters modified, in comparison with a χ^2 distribution with 2 degrees of freedom.

5.5.4 SYSTEMATICS PERFECTLY KNOWN

A last data challenge explores the influence of systematics to this analysis. All nuisance parameters are fixed at their default values, and not varied in the fit, as if the corresponding systematics were perfectly known. Figure 5.24 shows the confidence contours obtained with the Asimov approach, as well as the results of 600 fits with the frequentist approach. The contours shrink significantly and the non-oscillation hypothesis can be rejected with more than 11 σ. They also still show some overcoverage, with 72% and 92%, respectively.

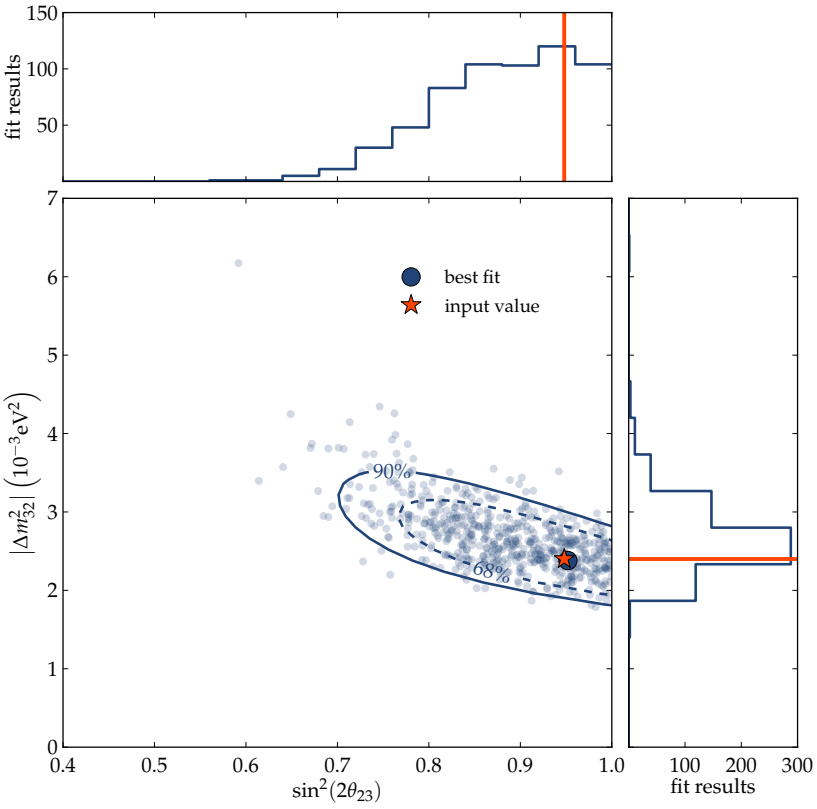

Figure 5.24: Results of the data challenge with fixed nuisance parameters. The confidence regions and the best-fit point are obtained by the Asimov approach. The blue dots denote the best-fit results of 600 frequentist fits. The red star marks the input oscillation parameters.

6 Results

6.1 Best-fit results

The fit is conducted as described in Section 5.3.4. It yields the best-fit oscillation parameters:

$$\left|\Delta m^2_{32}\right| = 2.74 \cdot 10^{-3}\,\mathrm{eV}^2$$
$$\sin^2(2\theta_{23}) = 1.0$$

To estimate the rejection of the non-oscillation hypothesis, the fit is repeated with only the nuisance parameters left free to float, and the oscillation parameters set to 0, as described in Section 5.3.5. The likelihood difference between both best-fit points is 17.1, which corresponds to 5.5 σ, when converted into standard deviations. The best fit is achieved not for the baseline dataset, but the systematics dataset where the ice is modeled with 7% less scattering and absorption. For the non-oscillation hypothesis, the best fit is achieved by the dataset with 100% optical efficiency. Table 6.1 shows the fitted values of the nuisance parameters, at the two best-fit points.

nuisance parameter	best-fit value w/ osc.	best-fit value w/o osc.
$c_{\mu\tau}$	0.85	0.82
c_e	0.65	0.60
c_c	0.04	0.06
γ	2.61	2.68
$r_{K/\pi}$	1.01	0.97

Table 6.1: Fitted values of the nuisance parameters, for the fits with and without oscillations.

All fitted values are within their expected uncertainties, with the possible exception of the atmospheric muon normalization, c_c, where no uncertainty has been assumed. Because the atmospheric muon simulation was generated with the old (and probably too low) default value for the optical efficiency, it is expected to overestimate the background contribution (see Sections 4.4 and 5.4.2). It is not clear, however, if the overestimation is really of the order of a factor ∼20, as indicated by the fitted value of the nuisance parameter c_c. Problems with the low statistics might also play a role here, since the used dataset has only 69 events left at the final cut level. These questions could only be addressed by new simulation datasets with higher statistics. The low values for the normalizations of the neutrino datasets, $c_{\mu\tau}$ and c_e, are a consequence of the simulations overpredicting the data by about 30% at the final cut level (see also Section 4.15). This deviation is within the range of the uncertainty on the atmospheric neutrino flux.

Figure 6.1 shows the resulting combined simulation histogram (obtained with the best-fit oscillation and nuisance parameters given here), together with the histogram for experimental data. For the initial histograms before the fit see Figure 5.11.

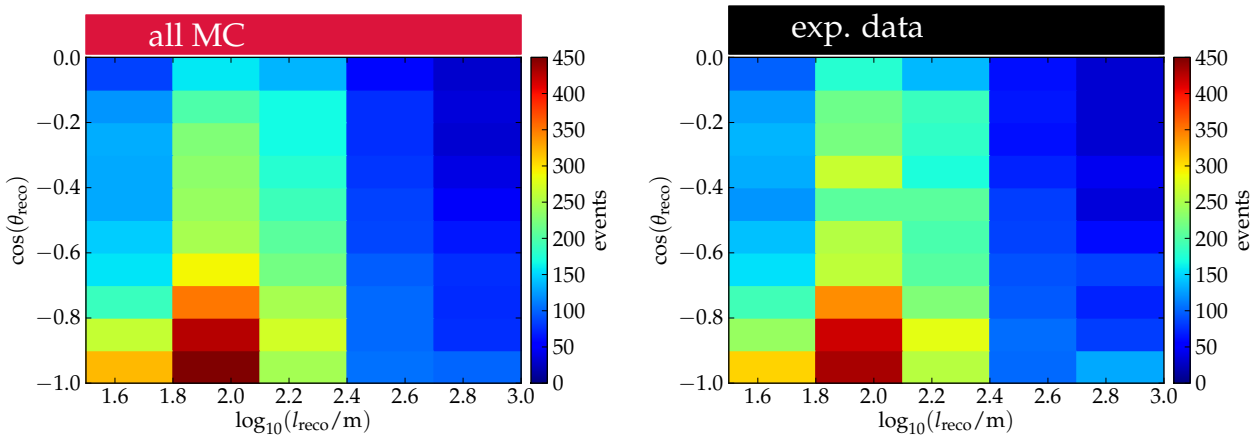

Figure 6.1: Two-dimensional histograms of reconstructed track length and zenith angle, for the best-fit simulation and for experimental data.

6.1.1 L/E RATIO

Since the oscillation probability (Equation 2.11) depends on the ratio of oscillation length and neutrino energy, a convenient way to visualize the observed oscillation effects is to plot the number of events against this quantity, L/E. In the analysis presented here, oscillation effects are expected only for the lowest energies and for the largest oscillation lengths, and thus for large L/E. The analysis does not measure the neutrino energy directly, but uses the reconstructed muon track length as a proxy. Therefore, the ratio L/E in this case becomes the ratio of oscillation length and reconstructed track length, $L_{\text{osc}}/l_{\text{reco}}$. The left panel of Figure 6.2 shows the resulting distribution, together with the best-fit oscillation and non-oscillation curves. The maximum oscillation length is the diameter of the Earth, and the shortest reconstructed length is 40 m, because shorter tracks have been removed in the event selection (see Section 4.14). Therefore, the distribution cuts off at

$$\log_{10}\left(\frac{L_{\text{osc}}}{l_{\text{reco}}}\right) = \log_{10}\frac{12\,760\,\text{km}}{40\,\text{m}} \approx 2.5\,.$$

Even with an oscillation length of the diameter of the Earth, no oscillations can occur for neutrinos with energies higher than roughly 100 GeV (see Figure 2.12), corresponding to a muon track length of about 500 m (see Section 3.1.2). This means that below

$$\log_{10}\frac{12\,760\,\text{km}}{500\,\text{m}} \approx 1.4\,,$$

no oscillation effects should be visible in the $L_{\text{osc}}/l_{\text{reco}}$ plot. This fact justifies to normalize the non-oscillation histogram to the best-fit oscillation histogram in the first three bins, where no oscillation effects can occur. In the fitting process of the non-oscillation hypothesis, the nuisance parameters are tuned to values that yield the best agreement over the whole range, even if the shape of the distribution does not match the experimental data. The normalization procedure applied here preserves the shape of the non-oscillation distribution imprinted

by the fitted values of the nuisance parameters, but ensures that the histograms agree where no oscillations are expected, but disagree in the oscillation region, and thus enhances the visibility of the effect.

The lower panel of Figure 6.2 shows the distributions for experimental data and the best-fit oscillations as a ratio to the non-oscillation histogram. In this representation the oscillation effect is even more obvious. For low $L_{\text{osc}}/l_{\text{reco}}$, the data is in agreement with both hypotheses, but for larger $L_{\text{osc}}/l_{\text{reco}}$, the data deviates significantly from the non-oscillation curve. It should be noted that the experimental data seems to deviate even more strongly from the non-oscillation histogram than the best-fit oscillation histogram, which already features maximal mixing ($\sin^2(2\theta_{23}) = 1$). This fact is more closely studied in Section 6.3.1.

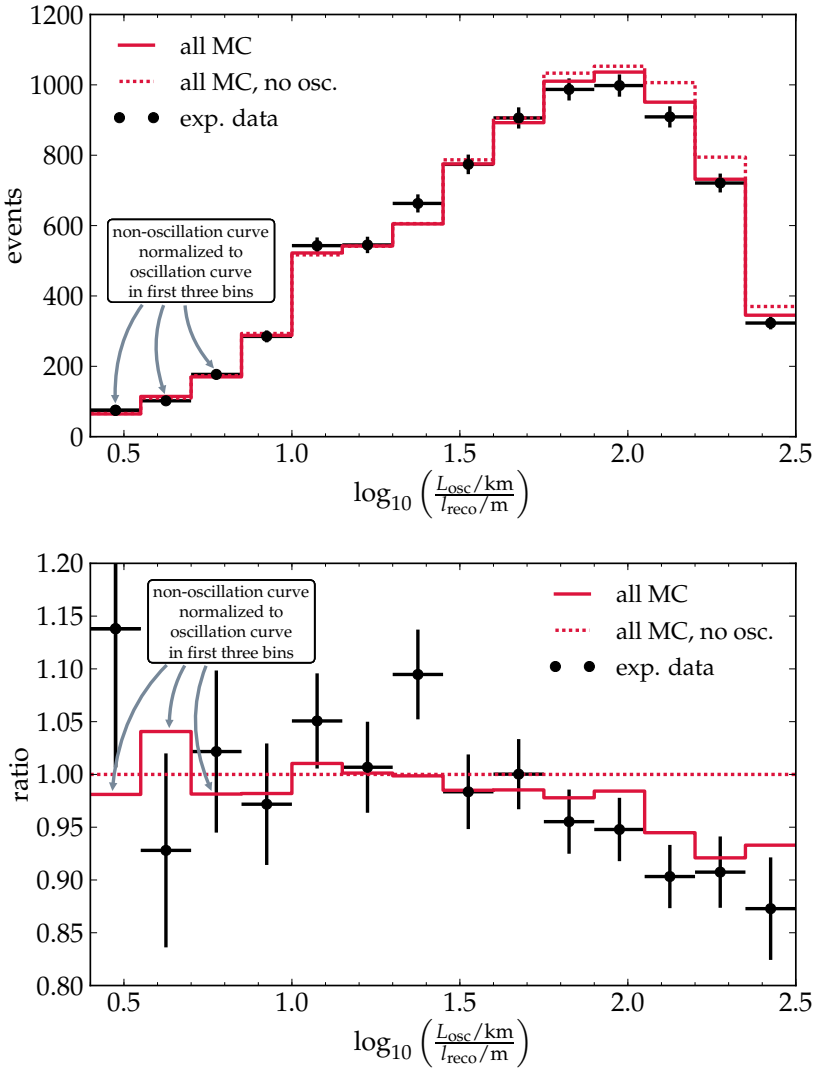

Figure 6.2: Number of events against the ratio of L_{osc} and l_{reco} (top) and ratio of data and best-fit oscillations to the best-fit non-oscillation hypothesis (bottom). In both plots, the non-oscillation curve has been normalized to the oscillation curve in the first three bins.

6.2 PARAMETER SCAN

To obtain confidence contours for the oscillation parameters, a 50×50 grid in the oscillation parameter space is constructed, ranging from 0.4 to 1.0 in $\sin^2(2\theta_{23})$ and from $0\,\mathrm{eV}^2$ to $7.0 \cdot 10^{-3}\,\mathrm{eV}^2$ in Δm^2_{32}. For each point on this grid, the minimization of the likelihood with respect to only the nuisance parameters is performed, as described in Section 5.3.6. The resulting likelihood landscape in units of standard deviations is shown in Figure 6.3. The conversion into standard deviations and thus the determination of the location of the contours were done using Wilks' theorem (see Section 5.3.5).

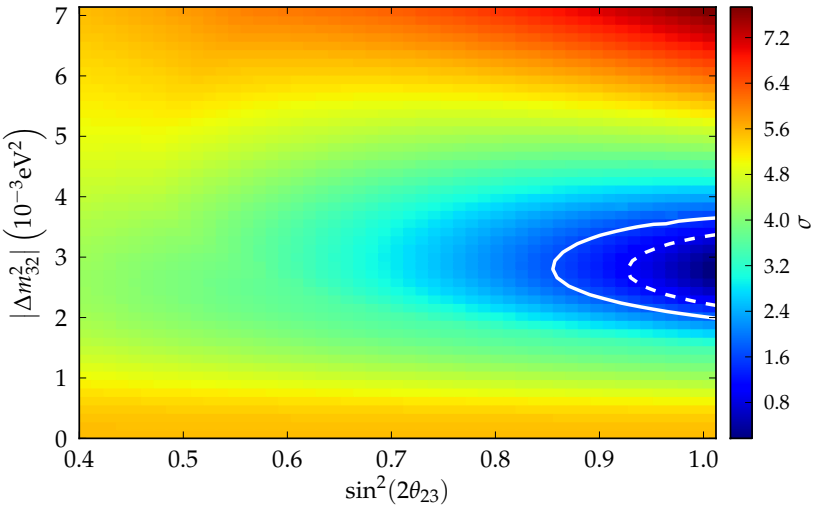

Figure 6.3: Likelihood landscape and 68% and 90% confidence contours resulting from the oscillation parameter scan. The likelihood values were converted into standard deviations using Wilks' theorem.

Figure 6.4 shows which discrete dataset produces the maximum likelihood at which grid point. The dataset with 7% less scattering and absorption, which yields also the global best fit, dominates the parameter space at large mixing angles and mass differences. At smaller Δm^2_{32} and $\sin^2(2\theta_{23})$ the best results come from the dataset with reduced optical efficiency. No other dataset of discrete systematics delivers the best likelihood anywhere in the considered section of the parameter space. The results of the parameter scans of all individual systematics datasets can be found in appendix B.

Figure 6.5 shows the fitted values of the five continuous nuisance parameters throughout the probed parameter space. The position of the best-fit oscillation parameters is marked by the star. The z-axis is scaled such that it corresponds to the 1 σ-range of the corresponding uncertainties given in Table 5.1. The obvious structure is an artifact introduced by the two datasets which contribute to the combined likelihood map (see Figure 6.4): All nuisance parameter maps exhibit a step at the boundary between the regions where the maximum likelihood comes from either dataset. Throughout the whole parameter space, however, no large differences in the fitted values are observed. They are virtually everywhere within the assumed 1σ-range. The only exception is the ν_e normalization c_e, which is at the lower edge of the 1σ-range already at the best-fit point, and becomes smaller in

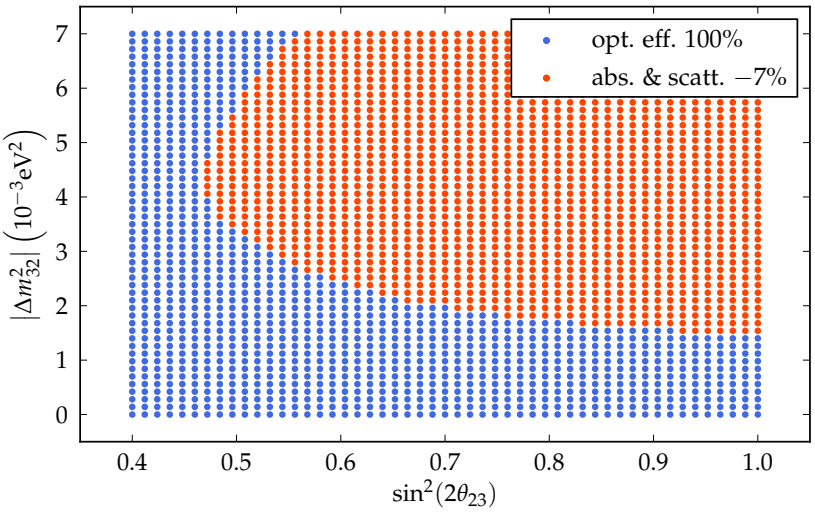

Figure 6.4: Map of which dataset yields the maximum likelihood at a certain grid point.

a large range of the parameter space. The atmospheric muon normalization c_c is small throughout the parameter space. The nuisance parameter maps for all individual systematics datasets can be found in appendix B, together with the likelihood maps.

6.3 QUALITY OF THE FIT

The quality of the fit can be evaluated from the fit residuals, which relate the contents of the experimental data histogram to the fitted histogram. The normalized residual (or *pull*) R_{ij} of the bin (i, j) is defined as:

$$R_{ij} = \frac{N_{ij}^{\mathrm{exp}} - N_{ij}^{\mathrm{fit}}}{\sqrt{N_{ij}^{\mathrm{exp}}}} .$$

For a perfect match between experimental and simulated data, these pulls would be 0 everywhere.

Figure 6.6 shows the pulls for both the best-fit oscillation hypothesis (with all parameters free in the fit) and the best-fit non-oscillation hypothesis (with only the nuisance parameters left free, and the oscillation parameters set to 0). It is obvious that the non-oscillation hypothesis delivers a worse fit. The largest pulls are found in the left half, at smaller track lengths, where the strongest oscillation effects are expected. With the oscillation parameters fixed at 0, the fit is not able to deliver agreement between the simulation and the experimental data, with deviations of typically 3 σ in many bins. At larger track lengths the differences between the two fits are small. Figure 6.6 shows also the χ^2 values, the sum of the squared pulls. Both histograms have 50 bins. For the best-fit oscillation hypothesis, 7 parameters are fitted at the same time, which leads a number of degrees of freedom of 43. For the non-oscillation hypothesis, the two oscillation parameters are fixed, so the number of degrees of freedom is 45 in this case. The resulting χ^2/ndf are 1.30 and 1.94, respectively, confirming the visual impression of a significantly better

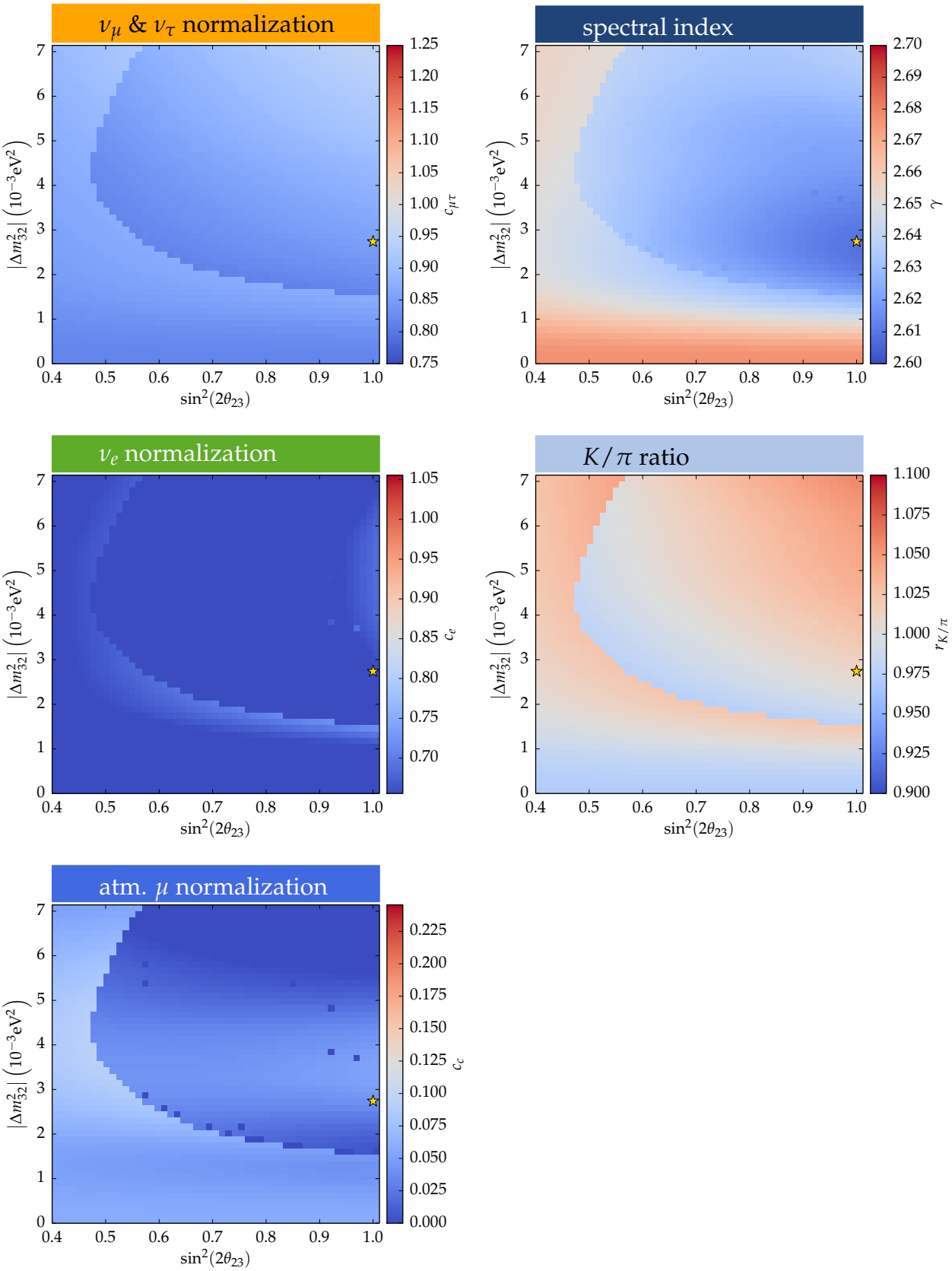

Figure 6.5: Fitted values of the nuisance parameters. The z-axis is aligned to the Gaussian priors (if applicable), and covers the 1σ-range around the central value. The star marks the position of the best-fit oscillation parameters.

fit for the oscillation hypothesis. It should not be overlooked, though, that also the pulls of the best-fit oscillation hypothesis show some remaining structure: there are still too many vertical events in the fitted simulation, and correspondingly too few events at the horizon. It appears that the fit could be further improved if it were allowed to consider even stronger oscillations. This is consistent with the observation in Figure 6.2.

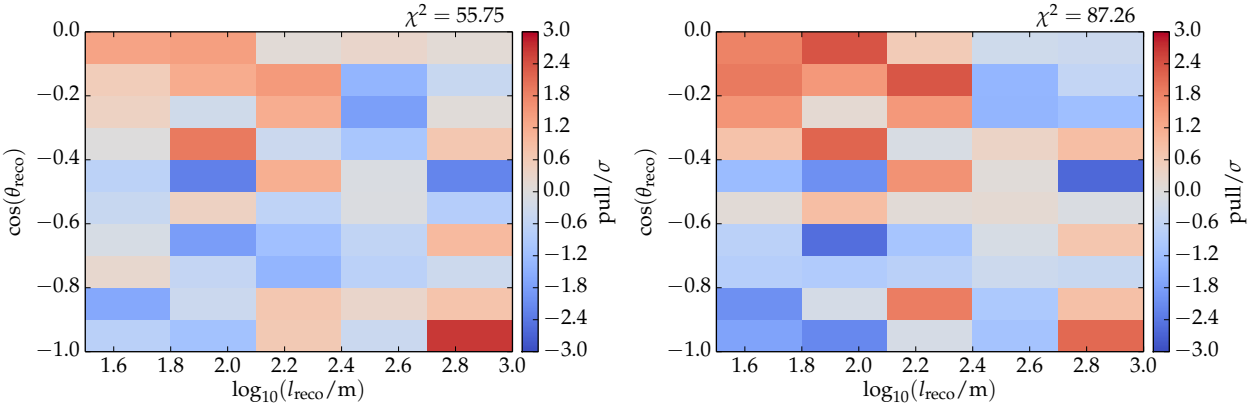

Figure 6.6: Pulls of the fit, for the best-fit oscillation (left) and non-oscillation hypothesis (right).

Another visualization of the quality of the fit is given by Figure 6.7, which shows the one-dimensional projections of the two-dimensional histogram to zenith angle and track length. These projections offer the advantage that simulation and data can be shown on the same plot. The deviation of the fit results from the experimental data is quantified by the χ^2 values given.

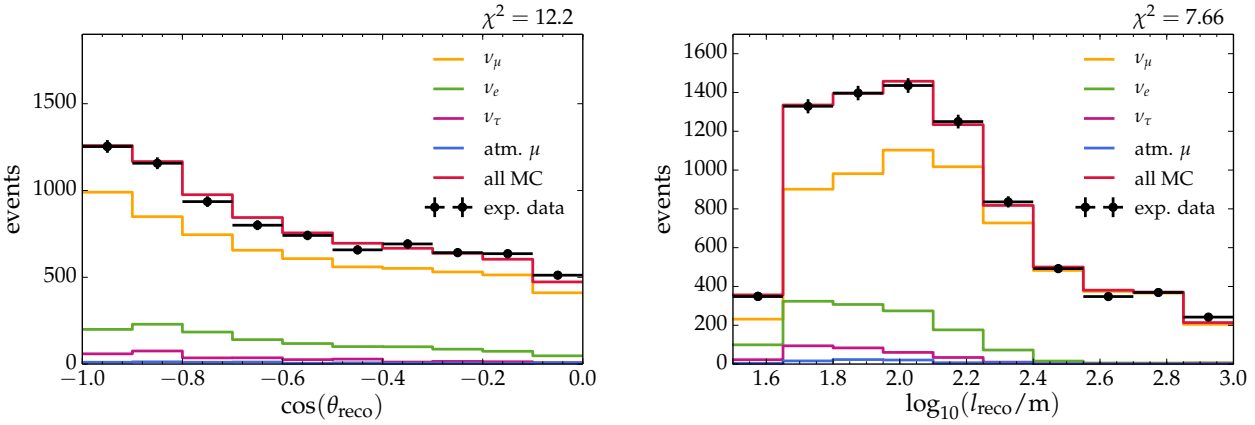

Figure 6.7: Projections of the two-dimensional histograms to zenith angle (left) and track length (right).

6.3.1 FIT WITH THE MIXING ANGLE LEFT FREE

As mentioned in the previous sections, there are hints that the fit could be improved by allowing stronger oscillations. The origin of this effect is not obvious at this point in time. Presumably, an important systematic effect has not yet been considered appropriately (e.g. three-flavor oscillations, matter effects, or the relative HQE DOM

efficiency). It should be noted, however, that the observed deviations are also consistent with a statistical fluctuation. Since the fitted mixing angle is already maximal, $\sin^2(2\theta_{23}) = 1$, stronger oscillations would push the fitted mixing angle into unphysical regions. It is, however, possible to leave the mixing angle free in the fit, since the minimizer does not "know" that the parameter is not supposed to be larger than 1. In the following, the fit is thus repeated, with the mixing angle left free to float. Also the parameter scan is repeated, but with the 50×50 grid extended to a range from 0.4 to 2.0 in $\sin^2(2\theta_{23})$, at the expense of a coarser binning.

The best-fit oscillation parameters, found with this new fit, are:

$$\left|\Delta m^2_{32}\right| = 2.53 \cdot 10^{-3}\,\mathrm{eV}^2$$
$$\sin^2(2\theta_{23}) = 1.35$$

Figure 6.8 shows the likelihood landscape and confidence contours, which are obtained using Wilks' theorem, as before. The previous best-fit point, with the mixing angle constrained to $\sin^2(2\theta_{23}) \leq 1$ is marked by the white star. It falls at the edge of the 90% confidence region (at $1.5\,\sigma$ from the minimum), not unambiguously ruling out a statistical fluctuation as the cause of the shift of the best-fit point to unphysical mixing angle values.

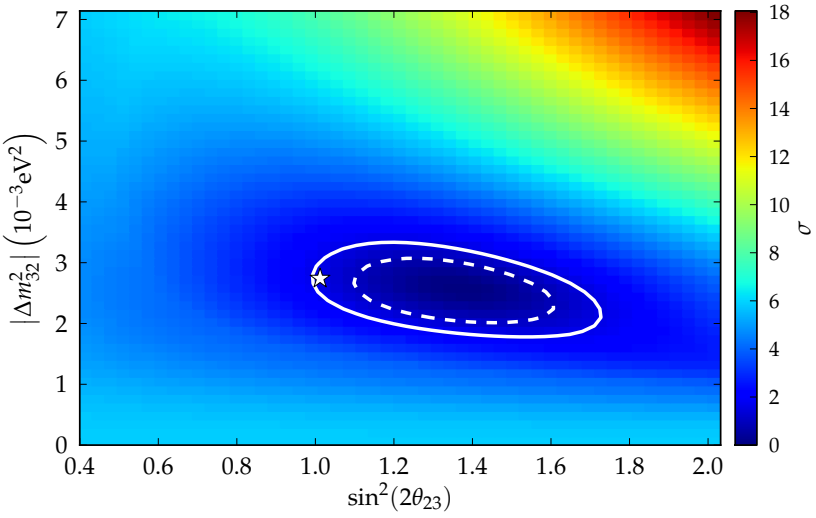

Figure 6.8: Likelihood landscape and 68% and 90% confidence contours resulting from the oscillation parameter scan with the mixing angle left free to float. The star marks the previous best-fit point, with the mixing angle constrained to $\sin^2(2\theta_{23}) \leq 1$. The likelihood values were converted into standard deviations using Wilks' theorem.

Figure 6.9 shows the pulls of the fit, as in Figure 6.6. As the non-oscillation hypothesis has not changed, its pulls are the same as before and not shown here again. For the new best fit, a slight improvement in the fit quality can be noticed. The χ^2/ndf improves from 1.30 to 1.24. There still seems to be a remaining structure in the pulls. This might be explained by the fact that the extension to $\sin^2(2\theta_{23}) > 1$ is unphysical; and an unphysical fit cannot – by definition – be a good description of experimental data.

Figure 6.10, finally, shows the new L/E distribution. Also here, the agreement of the experimental data to the best-fit simulation is improved, but the tension does not seem to be completely relieved. The cause of this remaining tension remains unclear.

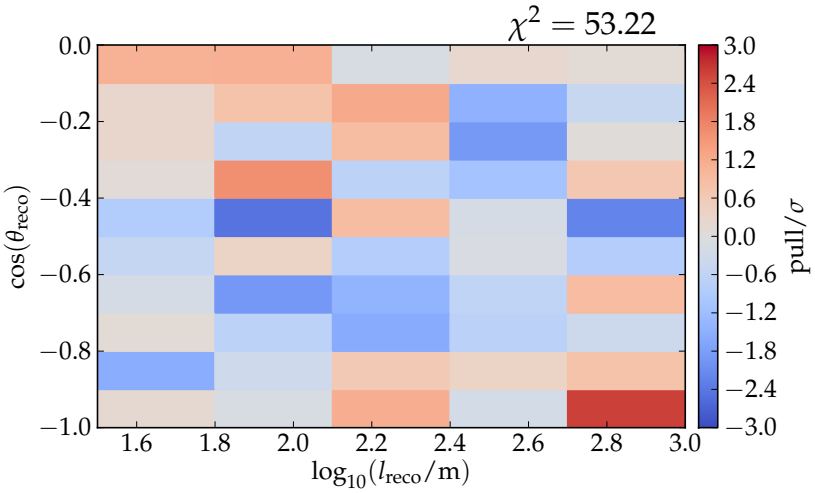

Figure 6.9: Pulls of the fit with the mixing angle left free to float. The pulls for the non-oscillation hypothesis are the same as in Figure 6.6 and not shown here.

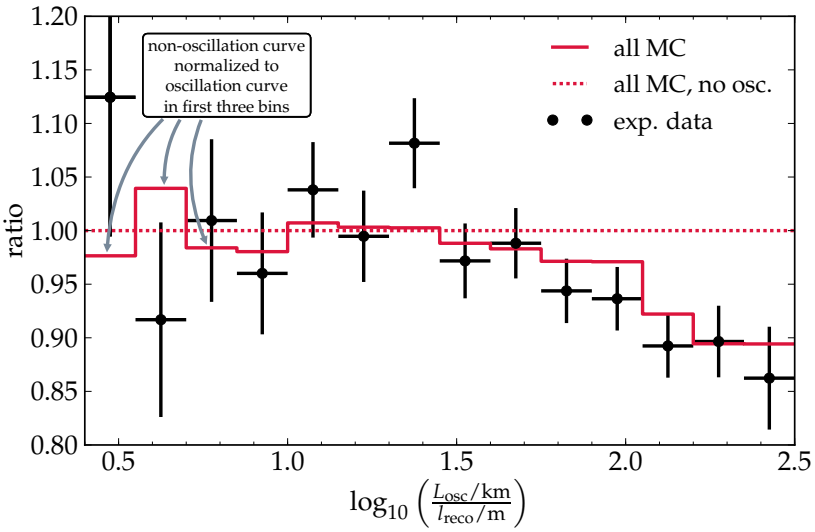

Figure 6.10: Number of events against the ratio of L_{osc} and l_{reco} for the fit with the mixing angle left free to float (top) and ratio of data and best-fit oscillations to the best-fit non-oscillation hypothesis (bottom). In both plots, the non-oscillation curve has been normalized to the oscillation curve in the first three bins.

7 Summary & Outlook

This thesis presents an analysis searching for oscillations of atmospheric muon neutrinos. Atmospheric neutrinos are produced all over the Earth's atmosphere in cosmic-ray-induced air showers. They are able to propagate through the whole Earth and reach a detector from all directions. In the two-flavor approximation used here, their oscillation probability depends on the oscillation parameters Δm^2_{32} and $\sin^2(2\theta_{23})$, as well as on the ratio of the propagated distance and their energy. Vertically upward going neutrinos have propagated a distance of the diameter of the Earth. For this distance, maximum disappearance is expected at about 25 GeV.

The analysis is performed with the IceCube Neutrino Observatory, a km^3-size Cherenkov detector at the Geographic South Pole that uses the Antarctic ice sheet as its detection medium. The detection threshold for neutrinos is about 100 GeV, and measuring the oscillation parameters would be impossible without DeepCore, a low-energy extension of IceCube, which lowers IceCube's energy threshold by roughly an order of magnitude to about 10 GeV. The analysis uses an experimental data sample that was recorded in the first year of DeepCore operations, between May 2010 and May 2011, when IceCube was almost completed in its 79-string configuration. The selected neutrino sample for this analysis contains 8117 up-going events with energies above 10 GeV, and has thus higher statistics than any previous neutrino oscillation experiment. Most of these events are muon neutrinos. However, the sample also contains a background from electron neutrinos, a small contamination from misreconstructed atmospheric muons and potentially tau neutrinos from oscillated muon neutrinos.

An important aspect of this data selection is also that background from cosmic-ray-induced atmospheric muons is highly efficiently rejected by using the outer layers of IceCube as an active veto. It achieves a background rejection of more than 6 orders of magnitude while keeping about 10% of the desired signal.

The oscillation parameters are determined by a global likelihood fit using energy and zenith angle information. The reconstructed muon track length is taken as a proxy for the neutrino energy. The zenith angle of the arrival direction is directly related to the propagated distance of the neutrino as the neutrino was produced in the atmosphere on the other side of the Earth in the direction of arrival. Reconstructed zenith angle and track length are binned into a two-dimensional his-

togram. This histogram is compared to the expectation, which is the sum of all components (ν_e, ν_μ, ν_τ, and atmospheric muons) assuming Poisson statistics. Based on the assumed oscillation parameters, the expectation for ν_μ and ν_τ changes. The likelihood that the experimental data is described by the expectation is maximized with respect to the oscillation parameters.

The oscillation parameters that yield the best agreement, and thus the maximum likelihood, determine the best-fit results. Systematic effects also affect the expectation. These are: the absolute normalization of the atmospheric neutrino flux, uncertainties in the neutrino interaction cross sections, the primary cosmic-ray spectral index, and the ratio of kaons to pions as the source of atmospheric neutrinos, as well as uncertainties in the description of light propagation in the ice and the optical efficiency of the detector. They are taken into account by fitting them as free nuisance parameters along with the oscillation parameters. Some of these uncertainties are not varied continuously as they are related to discrete models, e. g. variations of scattering and absorption of light in the ice. For these, separate fits with discrete simulation datasets are done and the global maximum likelihood is used. In addition to the fit, a scan of the oscillation parameter space is performed. Confidence regions are calculated from the likelihood differences on the basis of Wilks' theorem.

The analysis finds the best-fit oscillation parameters

$$\left|\Delta m^2_{32}\right| = 2.74 \cdot 10^{-3}\,\mathrm{eV}^2 \text{ and}$$
$$\sin^2(2\theta_{23}) = 1.0\ .$$

The non-oscillation hypothesis can be rejected with a significance of $5.5\,\sigma$. The fitted values of the nuisance parameters are all within the $1\,\sigma$-range of their expected uncertainties. Figure 7.1 shows the final confidence contours, in comparison with other results. The analysis achieves a significant improvement with respect to previous IceCube results [3]. However, after a more detailed analysis of the result, the question remains if the result is fully unbiased. The mixing angle, when left free in the fit, is pushed into the unphysical region to $\sin^2(2\theta_{23}) = 1.35$. With a likelihood ratio of the best fit in the physical region and the global best fit corresponding to 1.5 standard deviations, this is marginally consistent with a statistical fluctuation. The best-fit expectation seem to not perfectly match the measured data. In particular the residuals in the oscillation region of the experimental observables seem to deviate on the level of $1-2$ standard deviations. The best fit, however, describes the data substantially better than the non-oscillation hypothesis and the inspection of the resulting L/E distribution reveals clear evidence of a pattern as expected from oscillations.

[3] M. G. Aartsen et al. Measurement of Atmospheric Neutrino Oscillations with IceCube. *Phys. Rev. Lett.*, 111:081801, Aug 2013. DOI: 10.1103/PhysRevLett.111.081801

This analysis, as a first attempt to explore oscillation physics with the initial data of DeepCore, has revealed a clear observation of oscillations, demonstrating the potential of DeepCore to probe fundamental

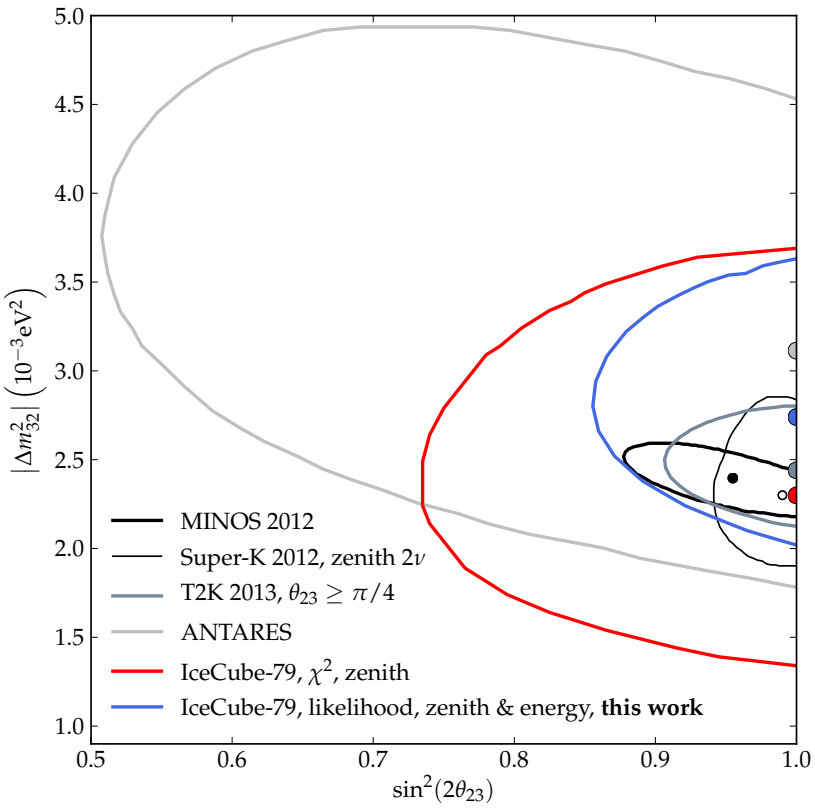

Figure 7.1: 90% confidence regions obtained by the analysis presented here, together with results from MINOS [93], Super-K [95], T2K [96], ANTARES [23], and older IceCube results [3].

particle physics. Furthermore, this measurement is probing a parameter region of higher neutrino energies than previously probed by underground experiments like Super-K. The ability to describe the here measured disappearance of muon neutrinos by oscillations to tau neutrinos with parameters consistent with the best-known oscillation parameters is adding evidence to the standard 3-flavor oscillation formalism. However, despite of the huge statistics of muon neutrinos, the analysis is limited by systematic uncertainties and corresponding deficits in the accuracy of the simulated description of the expectation. This is reflected by the marginally acceptable goodness-of-fit of the final result. Also limiting is a still large contamination with background, mostly electron neutrinos, which had to be included in the final fit on a statistical basis. These systematic uncertainties and deficits in the simulated description of the data need to be better understood in order to make full use of the unprecedented statistical power of the data delivered by IceCube-DeepCore.

7.1 FUTURE ICECUBE ANALYSES

In addition to the aforementioned better understanding of systematic uncertainties, the analysis can be improved by adding more data from the completed IceCube detector with 86 strings. This detector configuration also includes two additional DeepCore strings, which further increase the sensitivity to low-energy neutrinos (see Figure 3.13). While this analysis was finalized, improved simulation tools have

become available, in particular the GENIE neutrino simulation software. In addition to the deep inelastic cross sections used here, it includes also elastic and quasi-elastic neutrino-nucleon cross sections, as well as single pion production. It also models the cross sections below 10GeV, whose absence is another limitation in this analysis. New reconstruction algorithms dedicated to low-energy events have been developed recently. All these measures help to gain access to neutrino energies around and below 10 GeV. A first analysis using the full detector (IceCube-86) and these new techniques and methods has been finalized shortly after this analysis [92]. Its experimental data sample has only 20% of the statistics of the analysis presented here, but its sensitivity is comparable. The lower neutrino energy threshold and the more precise reconstructions compensate for the lower statistics.

[92] The IceCube Collaboration. Measurement of neutrino oscillations with the full IceCube detector. *Proceedings of the 33rd International Cosmic Ray Conference 2013, Rio de Janeiro, arXiv:1309.7008 [astro-ph.HE]*

Several studies are already in work to improve this analysis. The full data selection chain has been reviewed and optimized [97] and it was shown that the selection efficiency can still be significantly increased by the use of a *Boosted Decision Tree* [89]. At the same background level it achieves a 60% higher signal efficiency. Another planned improvement is to extend the global fit in this analysis to the full three-flavor formalism [69]. Within another study it is attempted to determine the background from atmospheric muons from the experimental data itself [72]. The highly insufficient statistics of atmospheric muon simulations on the final selection level substantially contribute to the uncertainties of this analysis. These simulations are computationally expensive. Therefore the statistics cannot easily be increased and systematic uncertainties of these expectations are difficult to quantify.

[97] M. Vehring. Ph.D. thesis, RWTH Aachen University, in preparation

[89] M. Stahlberg. Optimization of the data selection for the neutrino oscillation analysis with IceCube. Bachelor's thesis, RWTH Aachen University, 2013

[69] A. Koob. Master's thesis, RWTH Aachen University, in preparation

[72] A. Kriesten. Master's thesis, RWTH Aachen University, in preparation

7.2 PINGU

The analysis presented here has also served as basis for a sensitivity study for the planned PINGU detector [94]. If it was built, its main purpose would be to measure the neutrino mass hierarchy, but it would also be able to significantly improve the measurement of the oscillation parameters. With the event selection of this analysis, only slightly modified and adapted to the PINGU geometry, a data sample with 22 000 events and at the same time higher muon neutrino purity could be obtained [73]. A design study, based on the methods of this thesis, finds confidence contours that are after one year of data competitive with the measurements of all other experiments, and in terms of the mass difference even superior. Figure 7.2 shows these confidence contours, together with the results from MINOS and T2K. With several years of data, PINGU might be able to set the World's best constraints on the oscillation parameters Δm^2_{32} and $\sin^2(2\theta_{23})$.

[94] The PINGU Collaboration. PINGU Sensitivity to the Neutrino Mass Hierarchy. *Submitted to the Snowmass 2013 Proceedings, arXiv:1306.5846 [astro-ph.IM]*

[73] K. Krings. Studies on the Measurement of Atmospheric Neutrino Oscillations with the PINGU Detector. Master's thesis, RWTH Aachen University, 2013

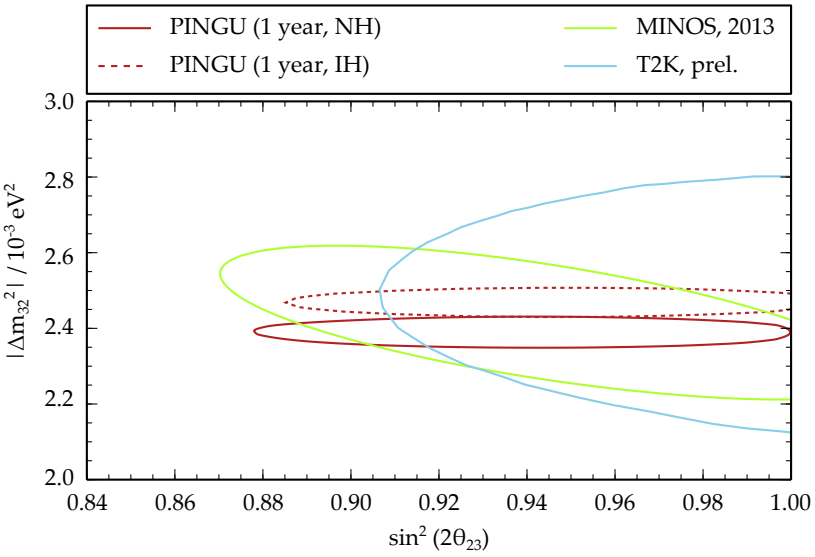

Figure 7.2: 90% confidence contours for one year of PINGU data, for normal and inverse mass hierarchy, and in comparison with results from MINOS and T2K [73].

Appendix A: Distributions of cut parameters

This section presents the remaining cut parameter distributions that were not shown in Chapter 4.

A.1 Removing obvious background events (L3)

Cuts are applied to the reconstructed zenith angle of all events. Two reconstruction algorithms are used: the first-guess algorithm *LineFit* and the more sophisticated *SPE4*. For both reconstructions, events reconstructed as down-going are removed. The cut is placed slightly above the horizon, at $\cos(\theta) < 0.2$. For a more detailed description, see Section 4.9. Figures A.1 and A.2 show the distributions of the reconstructed zenith angle and the cut value.

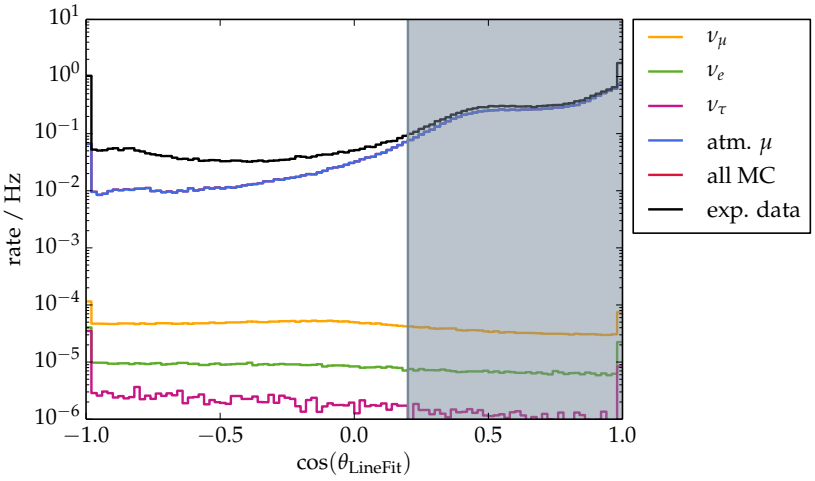

Figure A.1: Distribution of the zenith angle reconstructed by the *LineFit* algorithm. The large mismatch between the simulation (which is completely dominated by atmospheric muons) is caused by unsimulated noise triggers. Events with a zenith angle $\cos(\theta_{\text{LineFit}}) > 0.2$ (the gray shaded area) are removed.

A.2 Hit veto (L4)

To pass the next step, events are required to have not more than one hit in the veto region and at least 6 hits in DeepCore. For a more detailed description and the definition of these two regions, see Section 4.10. Figures A.3 and A.4 show the distributions of these

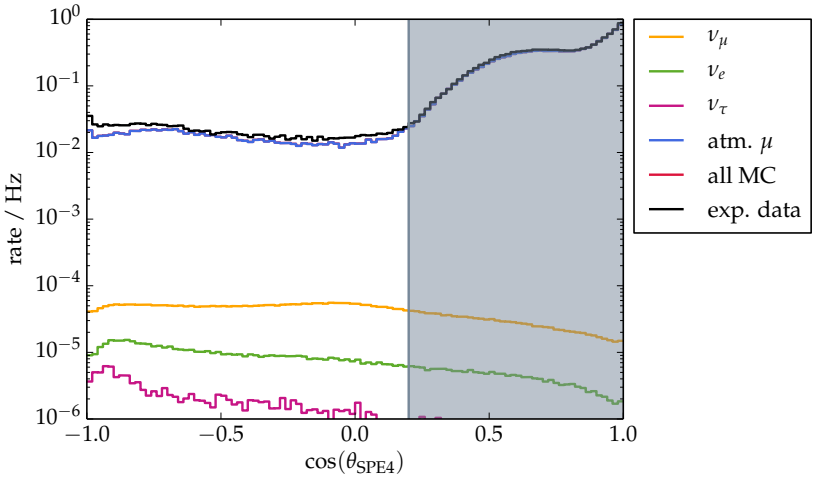

Figure A.2: Distribution of the zenith angle reconstructed by the *SPE4* algorithm. Events with a zenith angle $\cos(\theta_{\mathrm{SPE4}}) > 0.2$ (the gray shaded area) are removed.

parameters and the positions of the cuts.

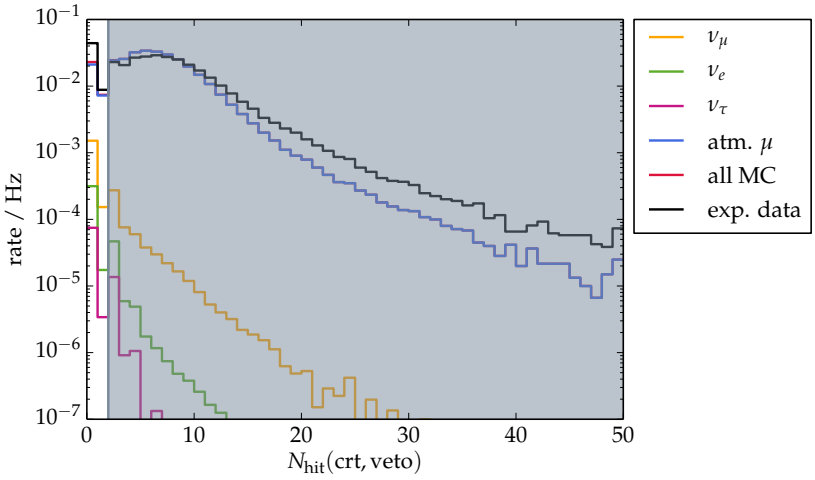

Figure A.3: Distribution of the number of hits in the veto region. Events with more than one hit (the gray shaded area) are removed.

A.3 CLUSTER VETO (L5)

Events are removed, if more than one cluster of causally connected hits is found by the algorithm *topological trigger*, and also if no cluster of causally connected hits at all is found. For a more detailed description, see Section 4.11. Figures A.5 and A.6 show the cut parameter distributions and the position of the cut. The large gaps in the distributions are caused by the requirement for a cluster to contain at least 5 hits. If less than 5 causally connected hits are found, the event is treated as if no cluster had been found.

A.4 MORE SOPHISTICATED RECONSTRUCTIONS (L6)

Again, cuts are applied to the zenith angle, as reconstructed by two reconstruction algorithms: the *improved LineFit* and the more sophisticated *SPE32*. For both reconstructions, events reconstructed as

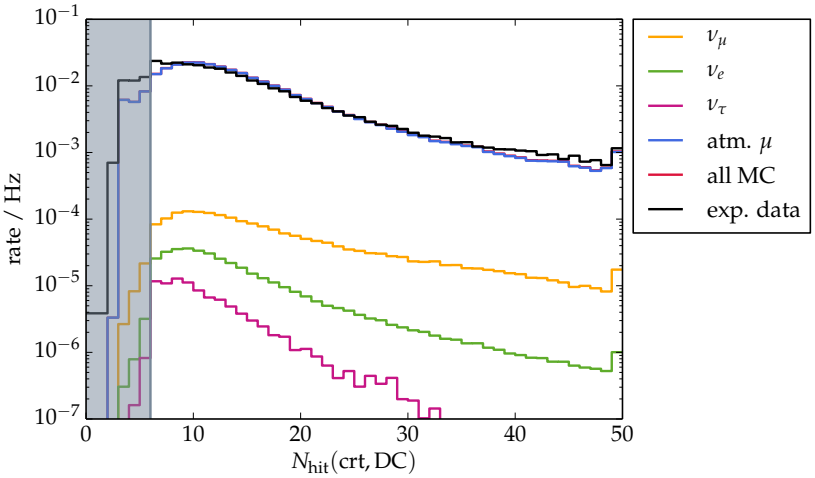

Figure A.4: Distribution of the number of hits in the DeepCore region. Events with less than 6 hits (the gray shaded area) are removed.

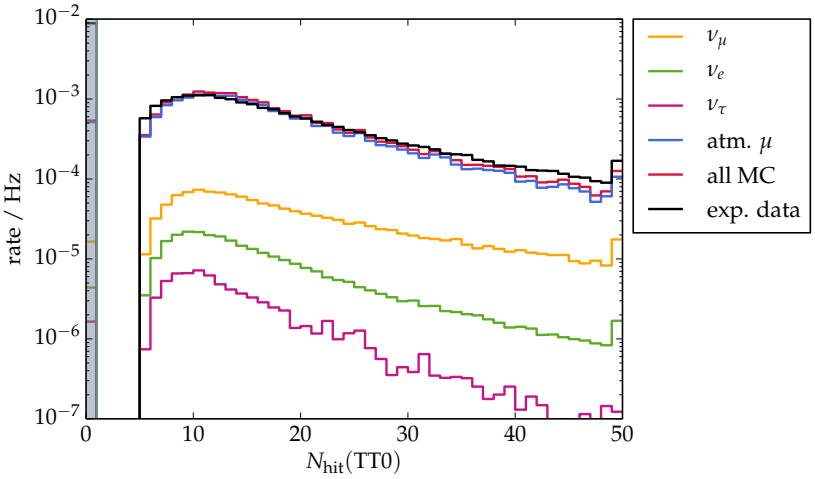

Figure A.5: Distribution of the number of hits in the primary cluster found by topological trigger. Events, where no causally connected cluster could be found (the gray shaded area), are removed. The large gap in the distribution is caused by the requirement for a cluster to contain at least 5 hits.

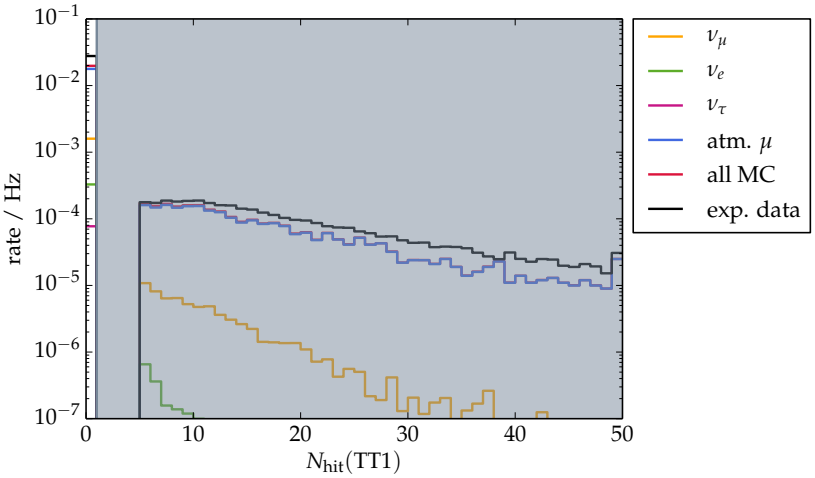

Figure A.6: Distribution of the number of hits in the secondary cluster found by topological trigger. Events, where such a secondary cluster is found (the gray shaded area), are removed. The large gap in the distribution is caused by the requirement for a cluster to contain at least 5 hits.

down-going are removed. This time, however, the cut is placed directly at the horizon. For a more detailed description, see Section 4.12. Figures A.7 and A.8 show the distributions of the reconstructed zenith angle and the cut value.

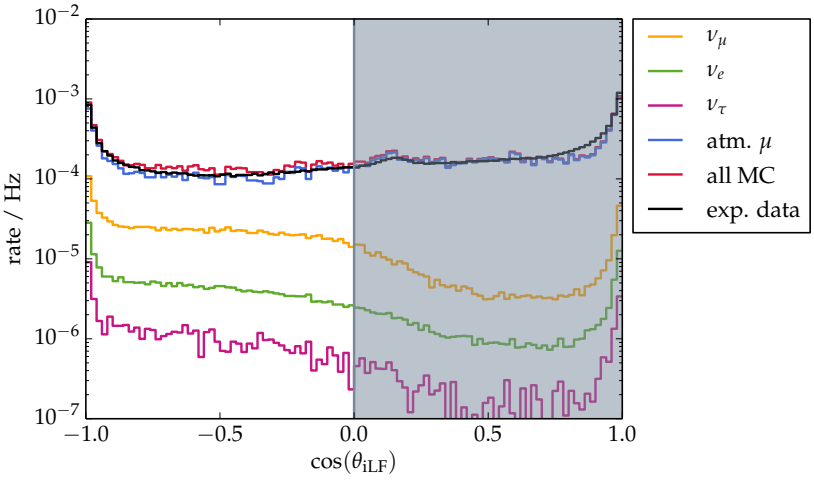

Figure A.7: Distribution of the zenith angle reconstructed by the *improved LineFit* algorithm. Events with a zenith angle $\cos(\theta_{\mathrm{iLF}}) > 0.0$ (the gray shaded area) are removed.

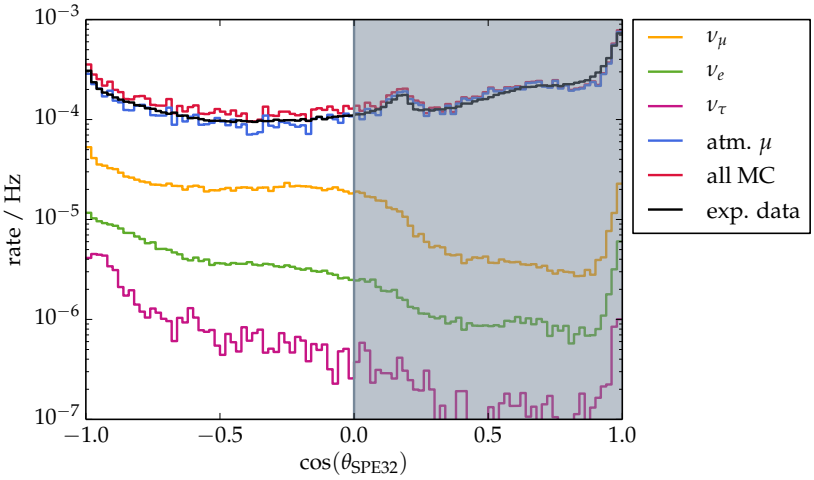

Figure A.8: Distribution of the zenith angle reconstructed by the *SPE32* algorithm. Events with a zenith angle $\cos(\theta_{\mathrm{SPE32}}) > 0.0$ (the gray shaded area) are removed.

A.5 QUALITY CUTS (L8)

In the last step of the data selection, cuts on various parameters are applied: the number of *direct hits*, their spatial distribution (*direct length*), the likelihood value of the reconstruction *pLogL*, and the difference between the standard likelihood and a zenith-weighted likelihood (*Bayesian likelihood difference*).

Two more cut parameters are given by the algorithm for reconstructing the track length, *FiniteReco*: the radial position of the reconstructed vertex must be within 180 m of the string in the center of DeepCore, and the reconstructed track length must be larger than 40 m. For a more detailed description of these parameters, see Section 4.14. Figures A.9 through A.13 show the corresponding distributions.

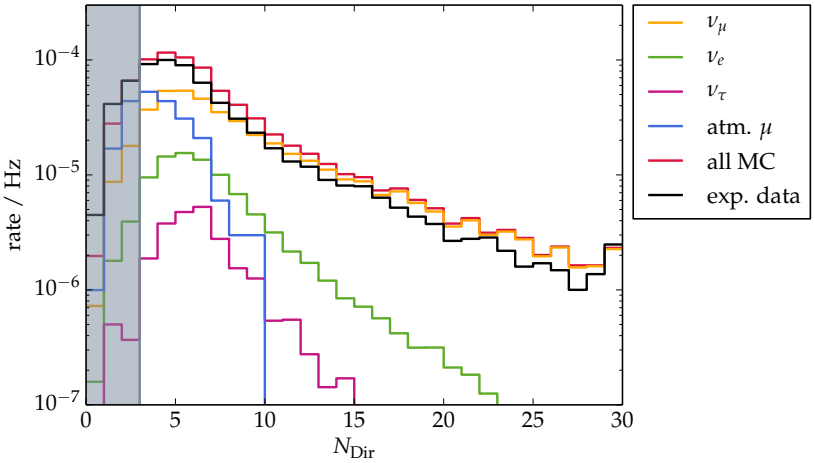

Figure A.9: Distribution of the number of direct hits, N_{Dir}. Events with less than 3 direct hits (the gray shaded area) are removed.

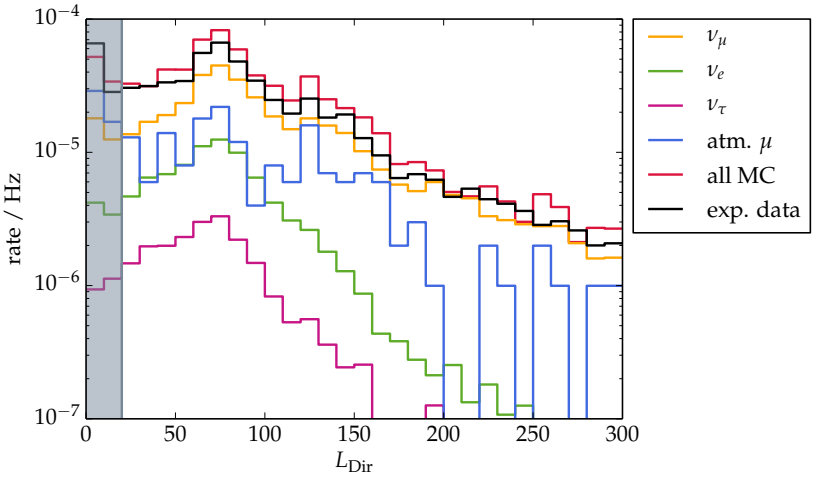

Figure A.10: Distribution of the direct length, L_{Dir}. Events with a direct length of less than 20 m (the gray shaded area) are removed.

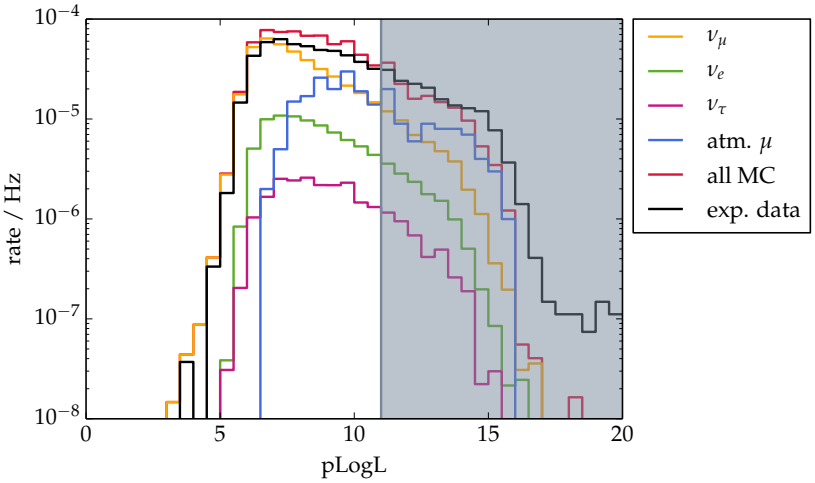

Figure A.11: Distribution of the cut parameter pLogL. Events with pLogL $>$ 11 (the gray shaded area) are removed.

Figure A.12: Distribution of the Bayesian likelihood difference, bayesLLHDiff. Events with bayesLLHDiff > -17 (the gray shaded area) are removed.

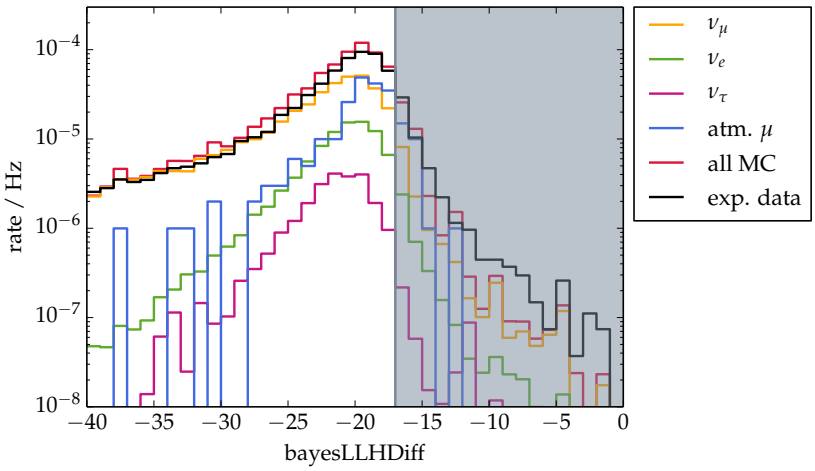

Figure A.13: Distribution of the radial position of the reconstructed vertex, $r_{\text{vertex}} = \sqrt{x^2_{\text{vertex}} + y^2_{\text{vertex}}}$. Events further than 180 m from the center of DeepCore (the gray shaded area) are removed.

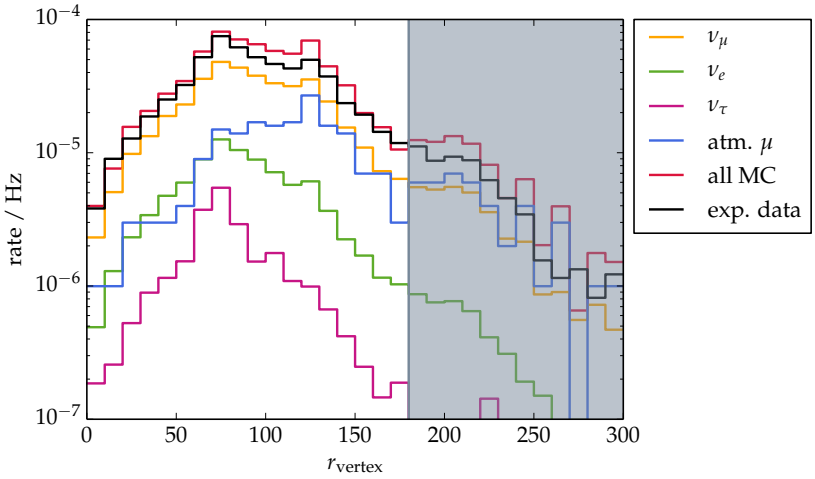

Figure A.14: Distribution of the reconstructed length, l_{reco}. Events with a reconstructed length of less than 40 m (the gray shaded area) are removed.

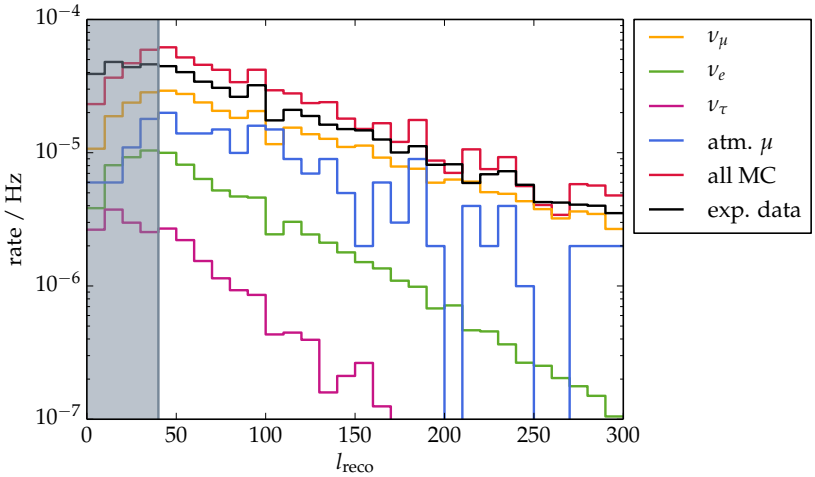

Appendix B:
Fit results for individual datasets

This section shows the results of the oscillation parameter scans of the discrete systematics datasets, i.e. for the datasets with varied ice models and optical efficiencies. For details, see Section 5.4.2. For each dataset the likelihood landscape is shown together with the 68% and 90% confidence contours, calculated on the basis of Wilks' theorem (see Section 5.3.5). The shape of the likelihood landscape is similar for all considered datasets. In addition, the maps of the fitted values of the nuisance parameters are shown.

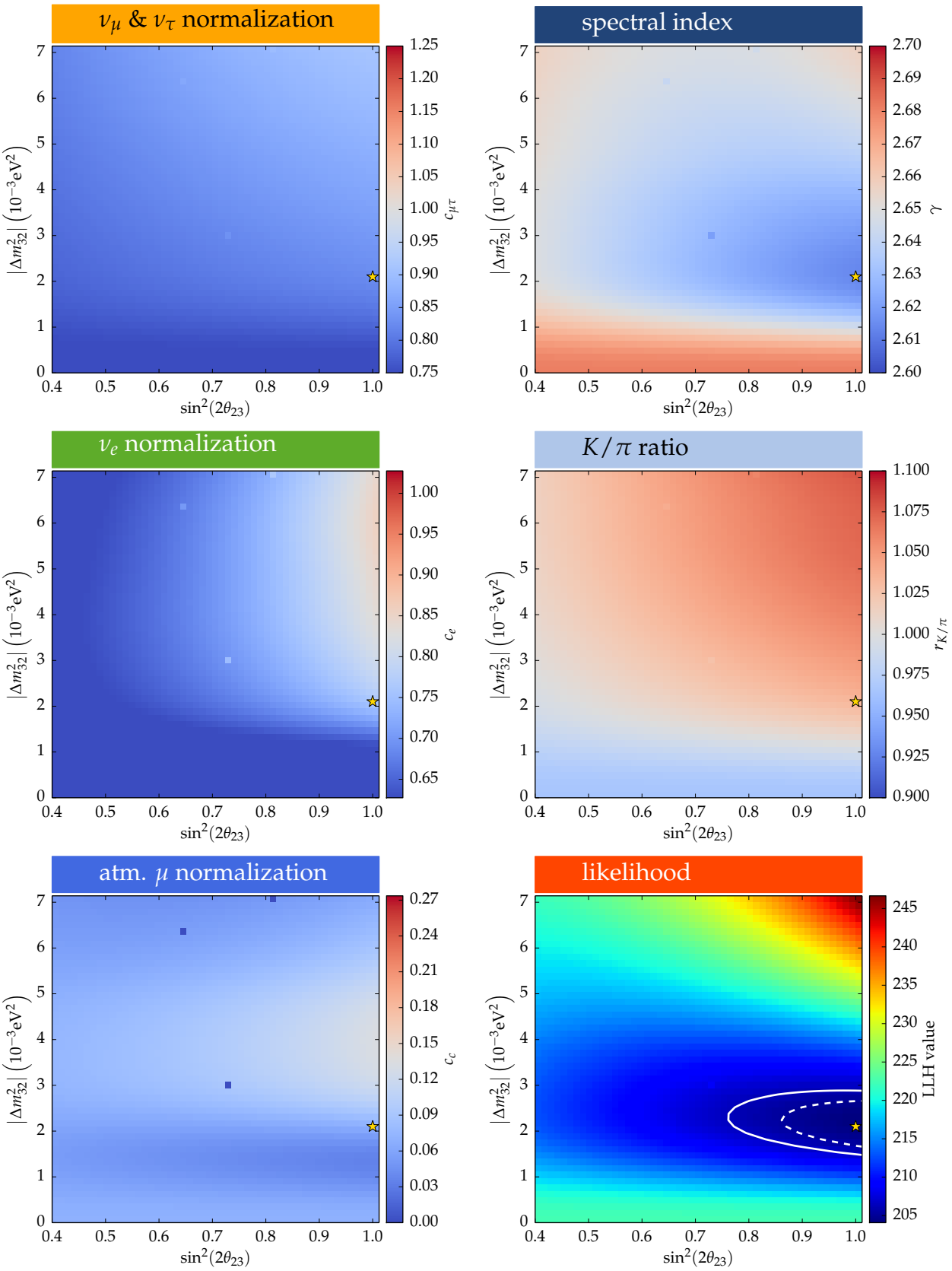

Figure B.1: Fit results for the baseline simulation. Bottom right panel: likelihood landscape with 68% and 90% contours. The star marks the position of the best-fit point. Other panels: Fitted values of the nuisance parameters. The z-axis is aligned to the Gaussian priors (if applicable), and covers the 1σ-range around the central value.

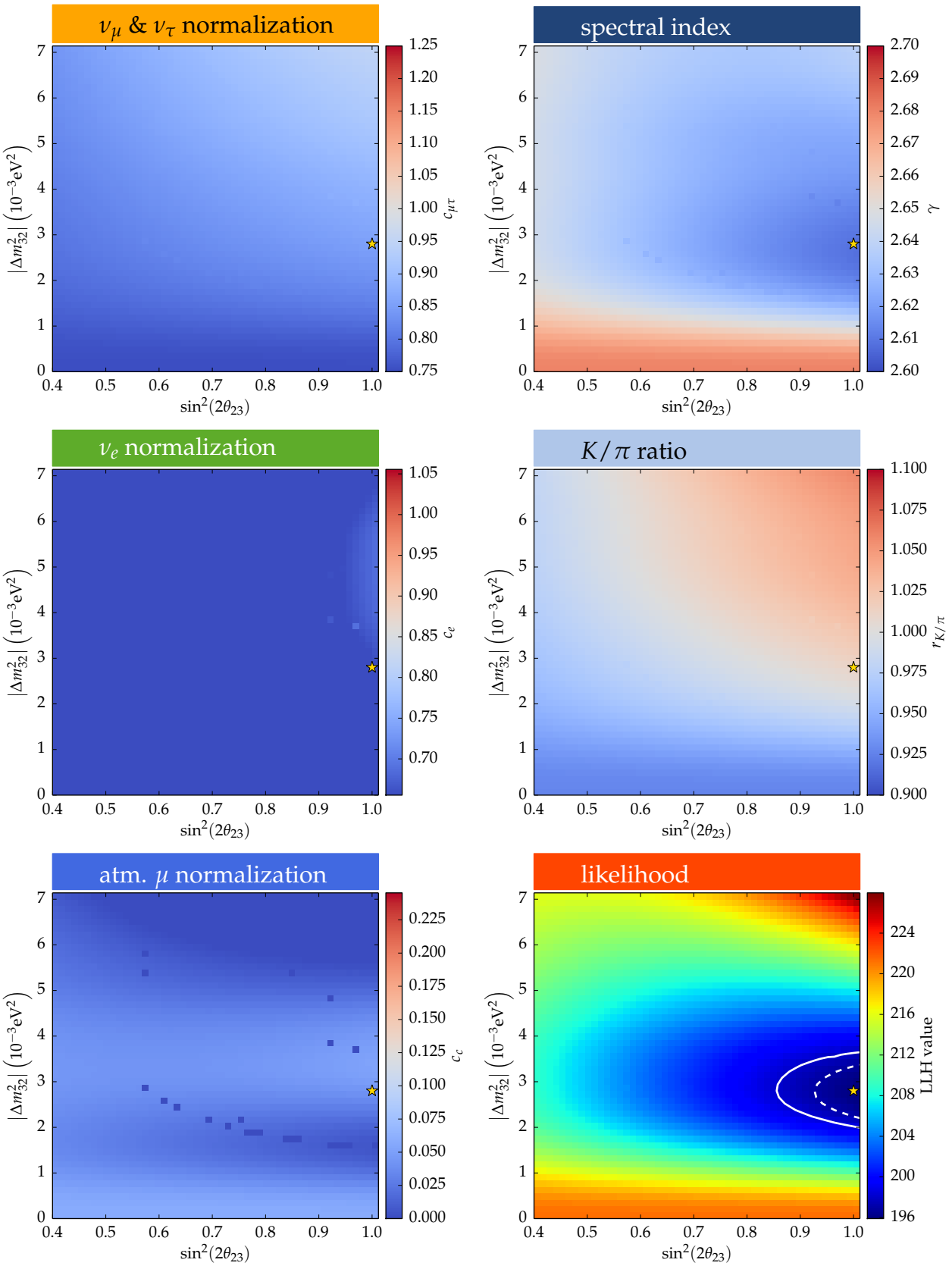

Figure B.2: Fit results for the simulation with scattering and absorption in the ice reduced by 7%. Bottom right panel: likelihood landscape with 68% and 90% contours. The star marks the position of the best-fit point. Other panels: Fitted values of the nuisance parameters. The z-axis is aligned to the Gaussian priors (if applicable), and covers the 1σ-range around the central value.

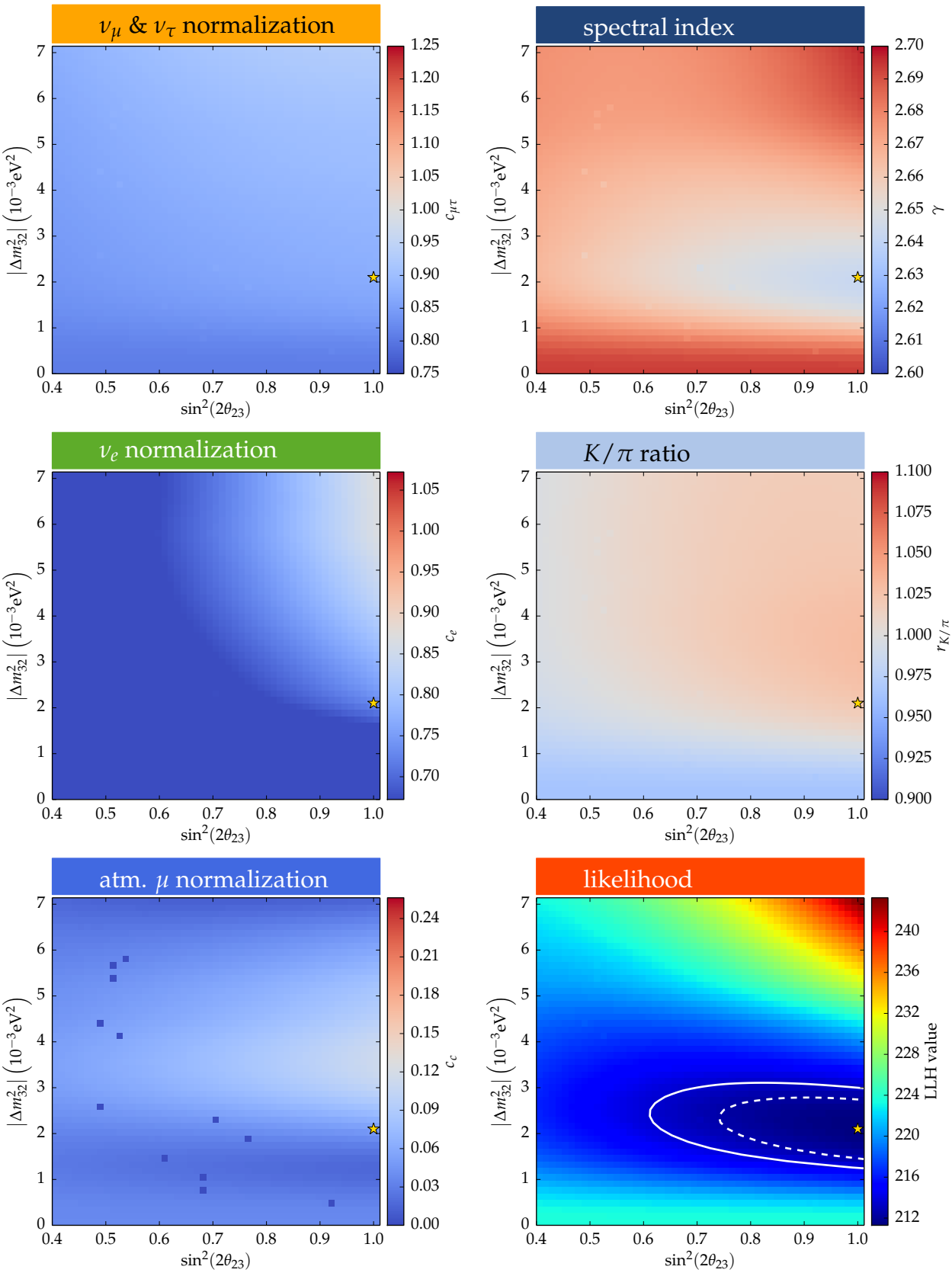

Figure B.3: Fit results for the simulation with scattering in the ice increased by 10%. Bottom right panel: likelihood landscape with 68% and 90% contours. The star marks the position of the best-fit point. Other panels: Fitted values of the nuisance parameters. The z-axis is aligned to the Gaussian priors (if applicable), and covers the 1σ-range around the central value.

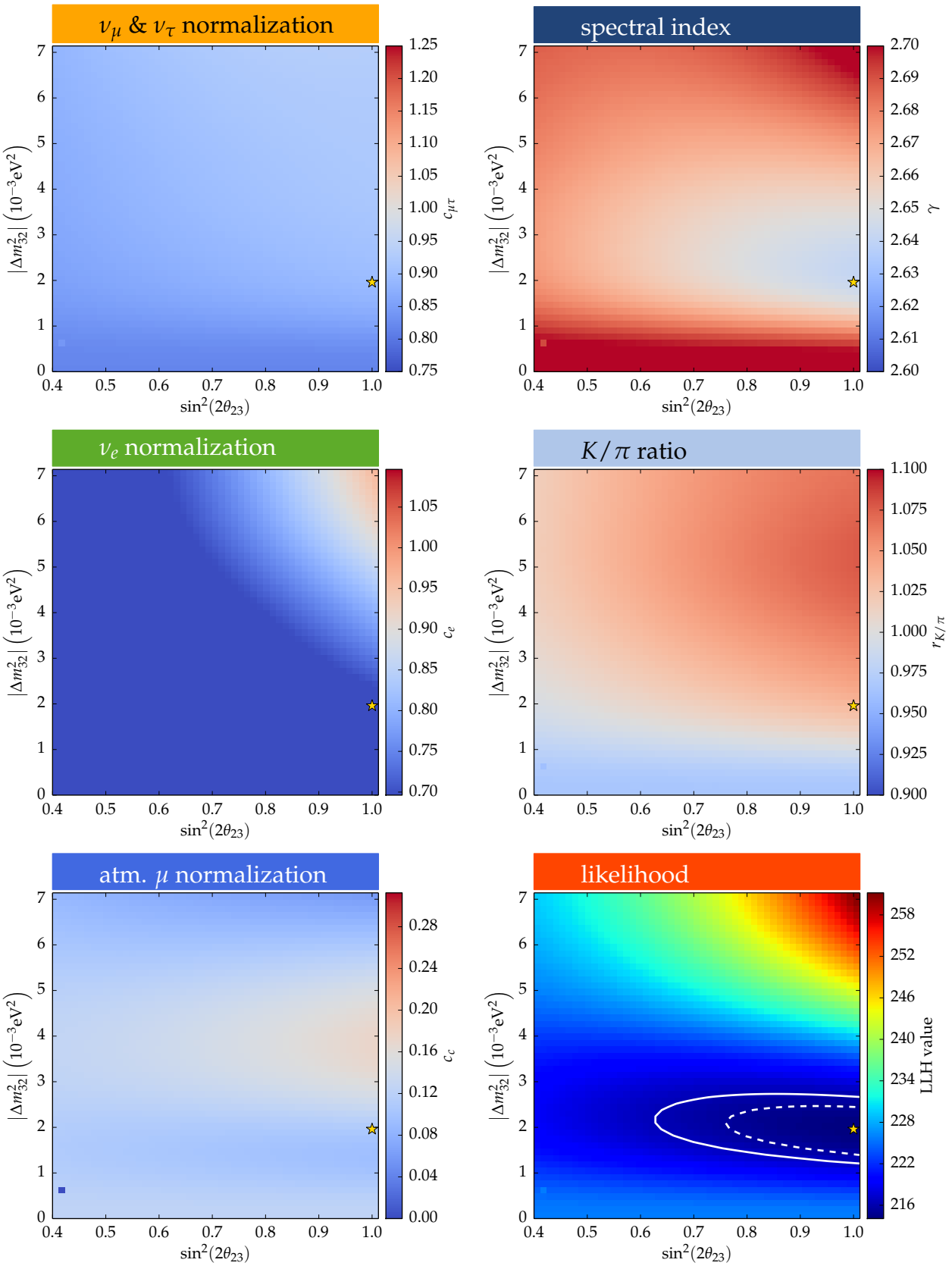

Figure B.4: Fit results for the simulation with absorption in the ice increased by 10%. Bottom right panel: likelihood landscape with 68% and 90% contours. The star marks the position of the best-fit point. Other panels: Fitted values of the nuisance parameters. The z-axis is aligned to the Gaussian priors (if applicable), and covers the 1σ-range around the central value.

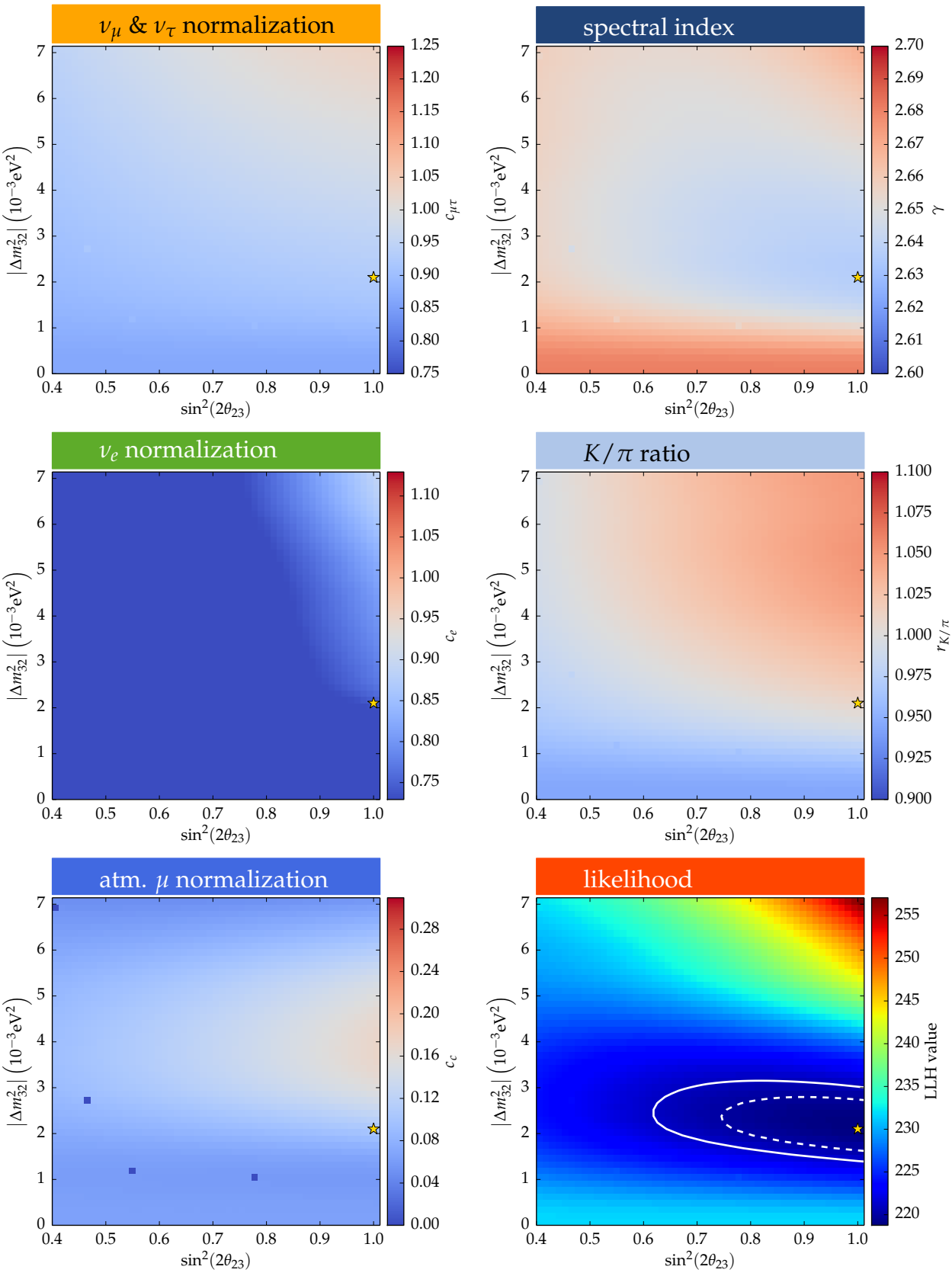

Figure B.5: Fit results for the simulation with the alternative WHAM! ice model. Bottom right panel: likelihood landscape with 68% and 90% contours. The star marks the position of the best-fit point. Other panels: Fitted values of the nuisance parameters. The z-axis is aligned to the Gaussian priors (if applicable), and covers the 1σ-range around the central value.

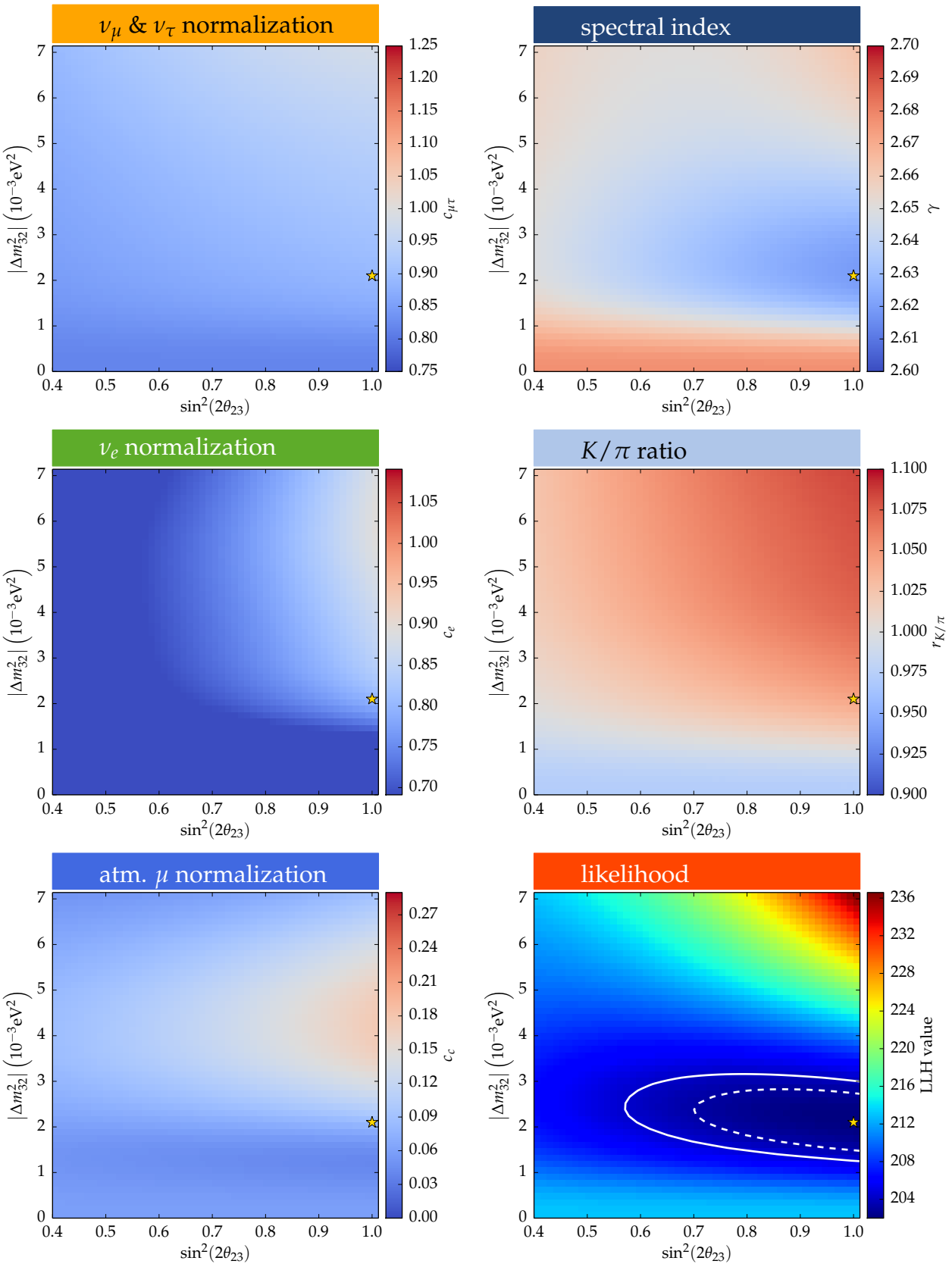

Figure B.6: Fit results for the simulation with a reduced optical efficiency of 100%. Bottom right panel: likelihood landscape with 68% and 90% contours. The star marks the position of the best-fit point. Other panels: Fitted values of the nuisance parameters. The z-axis is aligned to the Gaussian priors (if applicable), and covers the 1σ-range around the central value.

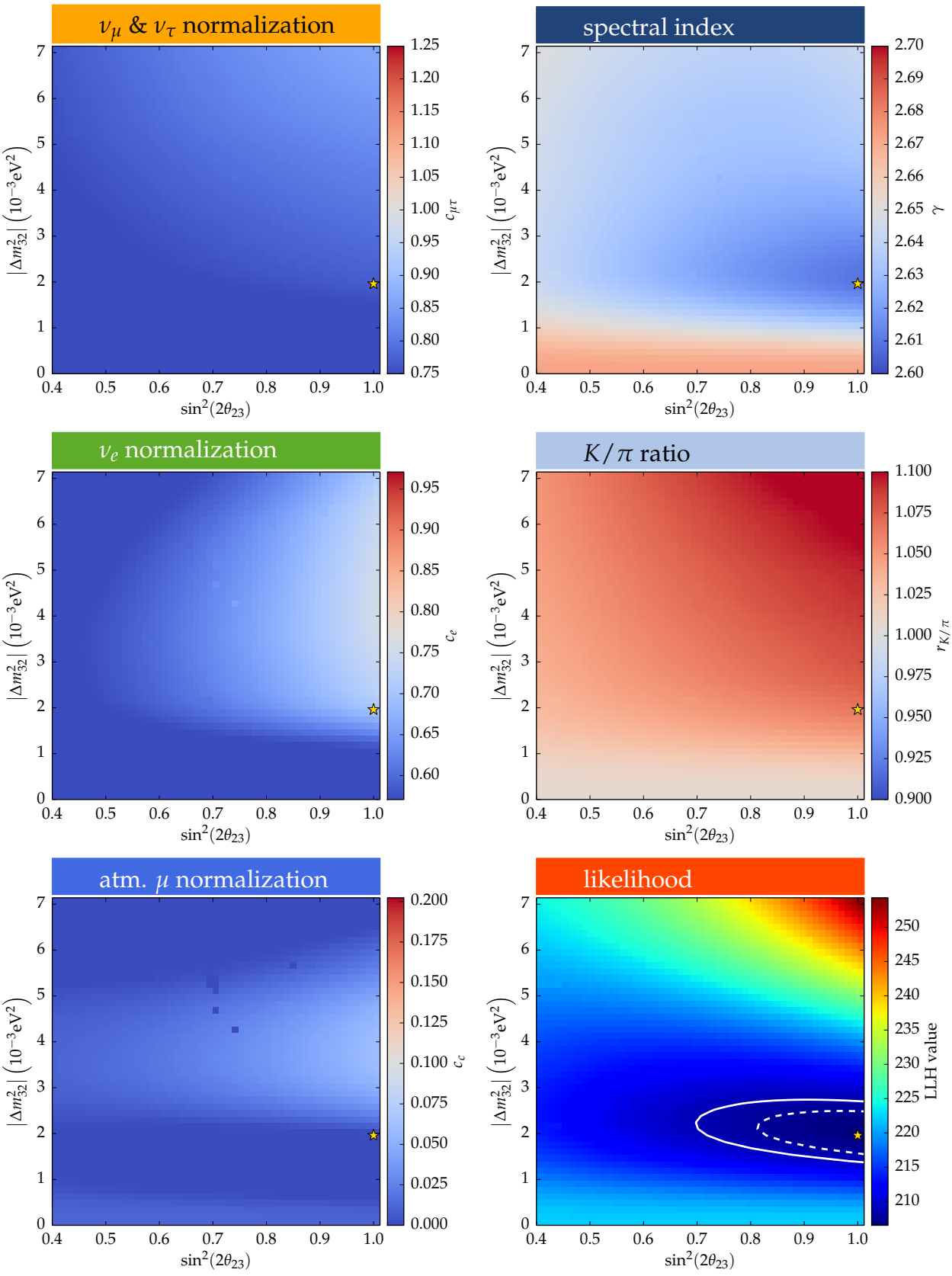

Figure B.7: Fit results for the simulation with an increased optical efficiency of 120%. Bottom right panel: likelihood landscape with 68% and 90% contours. The star marks the position of the best-fit point. Other panels: Fitted values of the nuisance parameters. The z-axis is aligned to the Gaussian priors (if applicable), and covers the 1σ-range around the central value.

Bibliography

[1] M. Aartsen et al. Improvement in Fast Particle Track Reconstruction with Robust Statistics. *Nucl.Instrum.Meth. A*, 736:143–149, 2014. DOI: 10.1016/j.nima.2013.10.074.

[2] M. G. Aartsen et al. Evidence for High-Energy Extraterrestrial Neutrinos at the IceCube Detector. *Science*, 342(6161):1242 856, 2013. DOI: 10.1126/science.1242856.

[3] M. G. Aartsen et al. Measurement of Atmospheric Neutrino Oscillations with IceCube. *Phys. Rev. Lett.*, 111:081 801, Aug 2013. DOI: 10.1103/PhysRevLett.111.081801.

[4] M. G. Aartsen et al. Measurement of South Pole ice transparency with the IceCube LED calibration system. *Nucl.Instrum.Meth. A*, 711:73–89, 2013. DOI: 10.1016/j.nima.2013.01.054.

[5] M. G. Aartsen et al. Measurement of the Atmospheric ν_e Flux in IceCube. *Phys. Rev. Lett.*, 110:151 105, Apr 2013. DOI: 10.1103/PhysRevLett.110.151105.

[6] M. G. Aartsen et al. Measurement of the cosmic ray energy spectrum with IceTop-73. *Phys. Rev. D*, 88:042 004, Aug 2013. DOI: 10.1103/PhysRevD.88.042004.

[7] M. G. Aartsen et al. Search for Dark Matter Annihilations in the Sun with the 79-String IceCube Detector. *Phys. Rev. Lett.*, 110:131 302, Mar 2013. DOI: 10.1103/PhysRevLett.110.131302.

[8] M. G. Aartsen et al. South Pole glacial climate reconstruction from multi-borehole laser particulate stratigraphy. *Journal of Glaciology*, 59:1117–1128, 2013.

[9] M. G. Aartsen et al. Search for a diffuse flux of astrophysical muon neutrinos with the IceCube 59-string configuration. *Phys. Rev. D*, in press.

[10] R. Abbasi et al. The IceCube data acquisition system: Signal capture, digitization, and timestamping. *Nucl.Instrum.Meth. A*, 601(3):294–316, 2009. DOI: 10.1016/j.nima.2009.01.001.

[11] R. Abbasi et al. Calibration and characterization of the IceCube photomultiplier tube. *Nucl.Instrum.Meth. A*, 618(1-3):139–152, 2010. DOI: 10.1016/j.nima.2010.03.102.

[12] R. Abbasi et al. The design and performance of IceCube DeepCore. *Astroparticle Physics*, 35(10):615–624, 2012. DOI: 10.1016/j.astropartphys.2012.01.004.

[13] R. Abbasi et al. Cosmic ray composition and energy spectrum from 1-30 PeV using the 40-string configuration of IceTop and IceCube. *Astroparticle Physics*, 42:15–32, 2013. DOI: 10.1016/j.astropartphys.2012.11.003.

[14] K. Abe, T. Abe, H. Aihara, Y. Fukuda, Y. Hayato et al. Letter of Intent: The Hyper-Kamiokande Experiment — Detector Design and Physics Potential —. *arXiv:1109.3262 [hep-ex]*, 2011.

[15] K. Abe et al. Evidence of electron neutrino appearance in a muon neutrino beam. *Phys. Rev. D*, 88:032 002, Aug 2013. DOI: 10.1103/PhysRevD.88.032002.

[16] S. Abe et al. Precision Measurement of Neutrino Oscillation Parameters with KamLAND. *Phys. Rev. Lett.*, 100:221 803, Jun 2008. DOI: 10.1103/PhysRevLett.100.221803.

[17] Y. Abe et al. Indication of Reactor $\overline{\nu}_e$ Disappearance in the Double Chooz Experiment. *Phys. Rev. Lett.*, 108:131 801, Mar 2012. DOI: 10.1103/PhysRevLett.108.131801.

[18] M. A. Acero, C. Giunti, and M. Laveder. Limits on ν_e and $\overline{\nu}_e$ disappearance from Gallium and reactor experiments. *Phys. Rev. D*, 78:073 009, Oct 2008. DOI: 10.1103/PhysRevD.78.073009.

[19] M. Ackermann et al. Optical properties of deep glacial ice at the South Pole. *Journal of Geophysical Research: Atmospheres*, 111(D13), 2006. DOI: 10.1029/2005JD006687.

[20] C. Adams et al. Scientific Opportunities with the Long-Baseline Neutrino Experiment. *arXiv:1307.7335 [hep-ex]*, 2013.

[21] P. Adamson et al. Search for Muon-Neutrino to Electron-Neutrino Transitions in MINOS. *Phys. Rev. Lett.*, 103:261 802, Dec 2009. DOI: 10.1103/PhysRevLett.103.261802.

[22] P. A. R. Ade et al. Planck 2013 results. XVI. Cosmological parameters. *Submitted to A&A*.

[23] S. Adrián-Martínez et al. Measurement of atmospheric neutrino oscillations with the ANTARES neutrino telescope. *Physics Letters B*, 714(2-5):224–230, 2012. DOI: 10.1016/j.physletb.2012.07.002.

[24] M. Agostini et al. Results on neutrinoless double beta decay of ^{76}Ge from GERDA Phase I. *Phys. Rev. Lett.*, 111:122 503, Sep 2013. DOI: 10.1103/PhysRevLett.111.122503.

[25] A. Aguilar et al. Evidence for neutrino oscillations from the observation of $\overline{\nu}_e$ appearance in a $\overline{\nu}_\mu$ beam. *Phys. Rev. D*, 64:112 007, Nov 2001. DOI: 10.1103/PhysRevD.64.112007.

[26] A. Aguilar-Arevalo et al. A Combined $\nu_\mu \to \nu_e$ and $\overline{\nu}_\mu \to \overline{\nu}_e$ Oscillation Analysis of the MiniBooNE Excesses. *arXiv:1207.4809 [hep-ex]*, 2012.

[27] B. Aharmim et al. Combined analysis of all three phases of solar neutrino data from the Sudbury Neutrino Observatory. *Phys. Rev. C*, 88:025 501, Aug 2013. DOI: 10.1103/PhysRevC.88.025501.

[28] Q. R. Ahmad et al. Direct Evidence for Neutrino Flavor Transformation from Neutral-Current Interactions in the Sudbury Neutrino Observatory. *Phys. Rev. Lett.*, 89:011 301, Jun 2002. DOI: 10.1103/PhysRevLett.89.011301.

[29] J. K. Ahn et al. Observation of Reactor Electron Antineutrinos Disappearance in the RENO Experiment. *Phys. Rev. Lett.*, 108:191 802, May 2012. DOI: 10.1103/PhysRevLett.108.191802.

[30] J. Ahrens et al. Muon track reconstruction and data selection techniques in AMANDA. *Nucl.Instrum.Meth. A*, 524(1-3):169–194, 2004. DOI: 10.1016/j.nima.2004.01.065.

[31] E. K. Akhmedov. Parametric resonance of neutrino oscillations and passage of solar and atmospheric neutrinos through the earth. *Nuclear Physics B*, 538(1-2):25–51, 1999. DOI: 10.1016/S0550-3213(98)00723-8.

[32] E. K. Akhmedov, M. Maltoni, and A. Y. Smirnov. 1-3 leptonic mixing and the neutrino oscillograms of the earth. *Journal of High Energy Physics*, 2007(05):077, 2007. DOI: 10.1088/1126-6708/2007/05/077.

[33] F. P. An et al. Observation of Electron-Antineutrino Disappearance at Daya Bay. *Phys. Rev. Lett.*, 108:171 803, Apr 2012. DOI: 10.1103/PhysRevLett.108.171803.

[34] C. Andreopoulos, A. Bell, D. Bhattacharya, F. Cavanna, J. Dobson et al. The GENIE Neutrino Monte Carlo Generator. *Nucl.Instrum.Meth. A*, 614:87–104, 2010. DOI: 10.1016/j.nima.2009.12.009.

[35] I. Asimov. Franchise. In *The Complete Stories, Vol.1*, p. 43. Broadway Books, New York, 1990.

[36] J. Beringer et al. Review of particle physics. *Phys. Rev. D*, 86:010 001, Jul 2012. DOI: 10.1103/PhysRevD.86.010001.

[37] J. Bonn et al. The Mainz neutrino mass experiment. *Nuclear Physics B - Proceedings Supplements*, 91:273–279, 2001. DOI: 10.1016/S0920-5632(00)00951-8.

[38] H. Chen, J. Chen, and J. D. Kalbfleisch. A modified likelihood ratio test for homogeneity in finite mixture models. *Journal of the Royal Statistical Society. Series B (Statistical Methodology)*, 63(1):19–29, 2001.

[39] P. A. Cherenkov. Visible Radiation Produced by Electrons Moving in a Medium with Velocities Exceeding that of Light. *Phys. Rev.*, 52:378–379, Aug 1937. DOI: 10.1103/PhysRev.52.378.

[40] D. Chirkin. Neutrino search with IceCube. *IceCube internal report*, icecube/200807006, 2008.

[41] D. Chirkin. Likelihood description for comparing data with simulation of limited statistics. *arXiv:1304.0735 [astro-ph.IM]*, 2013.

[42] D. Chirkin and W. Rhode. Propagating leptons through matter with Muon Monte Carlo (MMC). *arXiv:hep-ph/0407075*, 2004.

[43] C. L. Cowan, F. Reines, F. B. Harrison, H. W. Kruse, and A. D. McGuire. Detection of the Free Neutrino: a Confirmation. *Science*, 124(3212):103–104, 1956. DOI: 10.1126/science.124.3212.103.

[44] G. Cowan, K. Cranmer, E. Gross, and O. Vitells. Asymptotic formulae for likelihood-based tests of new physics. *Eur. Phys. J.*, C71(2):1–19, 2011. DOI: 10.1140/epjc/s10052-011-1554-0.

[45] R. Davis, D. S. Harmer, and K. C. Hoffman. Search for Neutrinos from the Sun. *Phys. Rev. Lett.*, 20:1205–1209, May 1968. DOI: 10.1103/PhysRevLett.20.1205.

[46] G. L. Fogli, E. Lisi, A. Marrone, D. Montanino, A. Palazzo, and A. M. Rotunno. Global analysis of neutrino masses, mixings, and phases: Entering the era of leptonic *CP* violation searches. *Phys. Rev. D*, 86:013 012, Jul 2012. DOI: 10.1103/PhysRevD.86.013012.

[47] I. Frank and I. Tamm. Coherent visible radiation from fast electrons passing through matter. *C. R. Acad. Sci. USSR*, 14:109–114, 1937.

[48] Y. Fukuda et al. Evidence for oscillation of atmospheric neutrinos. *Phys. Rev. Lett.*, 81:1562–1567, Aug 1998. DOI: 10.1103/PhysRevLett.81.1562.

[49] T. K. Gaisser. *Cosmic Rays and Particle Physics*. Cambridge University Press, 1990.

[50] T. K. Gaisser. Cosmic Rays at the Knee. In K. Sato and J. Hisano, editors, *Energy Budget in the High Energy Universe*, pp. 45–55. March 2007. DOI: 10.1142/9789812708342_0006.

[51] T. K. Gaisser and M. Honda. Flux of Atmospheric Neutrinos. *Annual Review of Nuclear and Particle Science*, 52(1):153–199, 2002. DOI: 10.1146/annurev.nucl.52.050102.090645.

[52] A. Gazizov and M. P. Kowalski. ANIS: High energy neutrino generator for neutrino telescopes. *Comput.Phys.Commun.*, 172:203–213, 2005. DOI: 10.1016/j.cpc.2005.03.113.

[53] M. Gonzalez-Garcia, M. Maltoni, J. Salvado, and T. Schwetz. Global fit to three neutrino mixing: critical look at present precision. *Journal of High Energy Physics*, 1212:123, 2012. DOI: 10.1007/JHEP12(2012)123.

[54] K. Hanson and O. Tarasova. Design and production of the IceCube digital optical module. *Nucl.Instrum.Meth. A*, 567(1):214–217, 2006. DOI: 10.1016/j.nima.2006.05.091.

[55] D. Heck, G. Schatz, T. Thouw, J. Knapp, and J. Capdevielle. CORSIKA: A Monte Carlo code to simulate extensive air showers. *FZKA Report*, 6019, 1998.

[56] M. Honda, T. Kajita, K. Kasahara, S. Midorikawa, and T. Sanuki. Calculation of atmospheric neutrino flux using the interaction model calibrated with atmospheric muon data. *Phys. Rev. D*, 75:043 006, Feb 2007. DOI: 10.1103/PhysRevD.75.043006.

[57] J. R. Hörandel. On the knee in the energy spectrum of cosmic rays. *Astroparticle Physics*, 19(2):193–220, 2003. DOI: 10.1016/S0927-6505(02)00198-6.

[58] J.-P. Hülß. P_{Hit}-P_{noHit} likelihood identification of starting muons. Talk at the IceCube Collaboration Meeting, Brussels, 2007. https://events.icecube.wisc.edu/contributionDisplay.py?contribId=98&sessionId=42&confId=1.

[59] P. O. Hulth. Results from the IceCube video camera system at 2455 meters ice depth. *Proceedings of VLVνT 2013, to be published*.

[60] IceCube internal gallery. Array Graphics. https://gallery.icecube.wisc.edu/internal/v/graphics/arraygraphics2011/, accessed 30-July-2013.

[61] IceCube wiki. DOM Acceptance. https://wiki.icecube.wisc.edu/index.php?title=DOM_Acceptance_Table_for_Photonics_and_Romeo&oldid=190506, accessed 28-September-2013.

[62] IceCube wiki. Plogl. https://wiki.icecube.wisc.edu/index.php?title=Plogl&oldid=113008, accessed 05-October-2013.

[63] IceCube wiki. Problem DOMs. https://wiki.icecube.wisc.edu/index.php?title=Problem_DOMs&oldid=204056, accessed 28-September-2013.

[64] IceCube wiki. SLC hit cleaning. https://wiki.icecube.wisc.edu/index.php?title=SLC_hit_cleaning&oldid=126846, accessed 02-October-2013.

[65] IceCube wiki. TFT 2010 Season Planning. https://wiki.icecube.wisc.edu/index.php?title=TFT_2010_Season_Planning%&oldid=122189, accessed 02-October-2013.

[66] A. Kappes, J. Hinton, C. Stegmann, and F. A. Aharonian. Potential Neutrino Signals from Galactic Gamma-Ray Sources. *Astrophys.J.*, 656:870–896, 2007. DOI: 10.1086/508936, 10.1086/518161.

[67] A. Karle and K. Woschnagg. Hole Ice Studies with YAG data/MC. `http://icecube.berkeley.edu/kurt/interstring/hole-ice/yak.html`.

[68] H. V. Klapdor-Kleingrothaus and I. V. Krivosheina. The evidence for the observation of $0\nu\beta\beta$ decay: The identification of $0\nu\beta\beta$ events from the full spectra. *Modern Physics Letters A*, 21(20):1547–1566, 2006. DOI: 10.1142/S0217732306020937.

[69] A. Koob. Master's thesis, RWTH Aachen University, in preparation.

[70] D. Koskinen. Removing Pure Noise Events With TrackEngine. Talk at the IceCube Collaboration Meeting, Uppsala, 2011. `https://events.icecube.wisc.edu/getFile.py/access?contribId=58&sessionId=20&resId=0&materialId=slides&confId=36`.

[71] M. Kowalski. Search for Neutrino-Induced Cascades with the AMANDA-II Detector. Ph.D. thesis, Humboldt-Universität Berlin, 2004.

[72] A. Kriesten. Master's thesis, RWTH Aachen University, in preparation.

[73] K. Krings. Studies on the Measurement of Atmospheric Neutrino Oscillations with the PINGU Detector. Master's thesis, RWTH Aachen University, 2013.

[74] Y.-F. Li, J. Cao, Y. Wang, and L. Zhan. Unambiguous determination of the neutrino mass hierarchy using reactor neutrinos. *Phys. Rev. D*, 88:013 008, Jul 2013. DOI: 10.1103/PhysRevD.88.013008.

[75] M. Lindner, T. Ohlsson, and G. Seidl. Seesaw mechanisms for Dirac and Majorana neutrino masses. *Phys. Rev. D*, 65:053 014, 2002. DOI: 10.1103/PhysRevD.65.053014.

[76] J. Lundberg et al. Light tracking through ice and water—Scattering and absorption in heterogeneous media with PHOTONICS. *Nucl.Instrum.Meth. A*, 581(3):619–631, 2007. DOI: 10.1016/j.nima.2007.07.143.

[77] Z. Maki, M. Nakagawa, and S. Sakata. Remarks on the Unified Model of Elementary Particles. *Progress of Theoretical Physics*, 28(5):870–880, 1962. DOI: 10.1143/PTP.28.870.

[78] K. McFarland. Neutrino Interactions (Published in *Neutrinos in Particle Physics, Astrophysics and Cosmology*, CRC Press, 2009). *arXiv:0804.3899 [hep-ex]*, 2008.

[79] G. Mention et al. Reactor antineutrino anomaly. *Phys. Rev. D*, 83:073 006, Apr 2011. DOI: 10.1103/PhysRevD.83.073006.

[80] S. Mikheyev and A. Y. Smirnov. Resonance Amplification of Oscillations in Matter and Spectroscopy of Solar Neutrinos. *Sov.J.Nucl.Phys.*, 42:913–917, 1985.

[81] P. Minkowski. $\mu \to e\gamma$ at a rate of one out of 10^9 muon decays? *Physics Letters B*, 67(4):421–428, 1977. DOI: 10.1016/0370-2693(77)90435-X.

[82] G. Morlino and D. Caprioli. Strong evidence for hadron acceleration in Tycho´s supernova remnant. *A&A*, 538:A81, 2012. DOI: 10.1051/0004-6361/201117855.

[83] PDG. Atomic and nuclear properties of materials: Water. `http://pdg.lbl.gov/2013/AtomicNuclearProperties/HTML_PAGES/276.html`, accessed 27-September-2013.

[84] B. Pontecorvo. Mesonium and Antimesonium. *Soviet Journal of Experimental and Theoretical Physics*, 6:429, 1958.

[85] P. B. Price, K. Woschnagg, and D. Chirkin. Age vs depth of glacial ice at South Pole. *Geophysical Research Letters*, 27(14):2129–2132, 2000. DOI: 10.1029/2000GL011351.

[86] L. Rädel and C. Wiebusch. Calculation of the Cherenkov light yield from low energetic secondary particles accompanying high-energy muons in ice and water with Geant4 simulations. *Astroparticle Physics*, 38:53–67, 2012. DOI: 10.1016/j.astropartphys.2012.09.008.

[87] C. Rott, P. Toale, D. Grant, and V. Viscomi. String Trigger Proposal. *IceCube internal document*, 2008.

[88] A. Schukraft. Search for a diffuse flux of extragalactic neutrinos with the IceCube Neutrino Observatory. Ph.D. thesis, RWTH Aachen University, 2013.

[89] M. Stahlberg. Optimization of the data selection for the neutrino oscillation analysis with IceCube. Bachelor's thesis, RWTH Aachen University, 2013.

[90] M. Tavani et al. Direct Evidence for Hadronic Cosmic-Ray Acceleration in the Supernova Remnant IC 443. *The Astrophysical Journal Letters*, 710(2):L151, 2010. DOI: 10.1088/2041-8205/710/2/L151.

[91] The ANTARES Collaboration. A Deep Sea Telescope for High-Energy Neutrinos. *arXiv:astro-ph/9907432*, 1999.

[92] The IceCube Collaboration. Measurement of neutrino oscillations with the full IceCube detector. *Proceedings of the 33rd International Cosmic Ray Conference 2013, Rio de Janeiro, arXiv:1309.7008 [astro-ph.HE].*

[93] The MINOS Collaboration. *Proceedings of Neutrino 2012, to be published*.

[94] The PINGU Collaboration. PINGU Sensitivity to the Neutrino Mass Hierarchy. *Submitted to the Snowmass 2013 Proceedings, arXiv:1306.5846 [astro-ph.IM]*.

[95] The Super-Kamiokande Collaboration. *Proceedings of Neutrino 2012, to be published*.

[96] The T2K Collaboration. *Proceedings of EPS HEP 2013, to be published*.

[97] M. Vehring. Ph.D. thesis, RWTH Aachen University, in preparation.

[98] M. Wallraff. nuCraft. `http://nuCraft.hepforge.org`.

[99] C. Weinheimer and K. Zuber. Neutrino Masses. *Annalen der Physik*, 525:565–575, 2013. DOI: 10.1002/andp.201300063.

[100] C. Wiebusch and S. Euler. IC79 ν_μ Disappearance Analysis: Results. Talk at the IceCube Collaboration Meeting, Madison (WI), 2013. `https://docushare.icecube.wisc.edu/dsweb/Get/Document-65382/Christopher_Wiebusch_IC79OscillationResults_Parallel_Madison2013.pptx`.

[101] Wikipedia. KATRIN. `http://en.wikipedia.org/w/index.php?title=KATRIN&oldid=549530840`, accessed 7-August-2013.

[102] S. Wilks. The Large-Sample Distribution of the Likelihood Ratio for Testing Composite Hypotheses. *Annals Math.Statist.*, 9(1):60–62, 1938. DOI: 10.1214/aoms/1177732360.

[103] J. Wolf. The KATRIN neutrino mass experiment. *Nucl.Instrum.Meth. A*, 623(1):442–444, 2010. DOI: 10.1016/j.nima.2010.03.030.

[104] J. P. Yanez. private communication, 2013. `https://docushare.icecube.wisc.edu/dsweb/Get/Document-63681/OscillationsCall_Jan2013_CascadeParametrizationIssue.pdf`.

[105] Y. S. Yoon et al. Cosmic-ray Proton and Helium Spectra from the First CREAM Flight. *The Astrophysical Journal*, 728(2):122, 2011.

[106] L. Zhan, Y. Wang, J. Cao, and L. Wen. Determination of the neutrino mass hierarchy at an intermediate baseline. *Phys. Rev. D*, 78:111 103, Dec 2008. DOI: 10.1103/PhysRevD.78.111103.

[107] K. Zuber. *Neutrino Physics*. Series in high energy physics, cosmology, and gravitation. Taylor & Francis, 2012.

Acknowledgements

This thesis would have not been possible (or at least be very different) without certain people and I would like to thank them:

- First of all, Christopher Wiebusch for giving me the opportunity to write this thesis. Your enthusiasm and support carried this project through very different – but always exciting – times. I would do it again.
- The whole IceCube Aachen group. You always manage to create a familiar and enjoyable working atmosphere.
- This is especially true for the Kinderzimmer: Anne Schukraft, Jan Blumenthal and Marius Wallraff. Thank you for being much more than just office mates.
- Marius Wallraff deserves special thanks for making me appreciate the beauty of Python.
- Laura Gladstone for double-, triple- and quadruple-checking my scripts, until we could trace back every single event.
- Per Olof Hulth and the Swedish IceCube groups for a more than memorable time working on DOM testing and the TrackEngine, and especially for giving me the chance to spend some unforgettable time at the South Pole.
- Elisa Resconi for agreeing to be the second reviewer of this thesis.
- Last but not least my family: Without your continuing support, the turbulent last few weeks would certainly have led straight into disaster...
- F3GA2B♭2A